Correlated dynamics of ultracold bosonic atoms in three dimensions:

Facing the challenge with a multi-configurational approach

Dissertation

zur Erlangung des Doktorgrades

an der Fakultät für Mathematik,

Informatik und Naturwissenschaften

der Universität Hamburg,

Fachbereich Physik

vorgelegt von

Valentin Jonatan Bolsinger

geboren am 26. Juni 1985 in Esslingen

Hamburg
2017

Eingereicht am:
28.08.2017

Gutachter der Dissertation: Prof. Dr. Peter Schmelcher
                                                                 Prof. Dr. Mathey

Datum der Disputation: 20.11.2017

Gutachter der Disputation: Prof. Dr. Peter Schmelcher
                                                                 Prof. Dr. Mathey
                                                                 Prof. Dr. Hemmerich
                                                                 Prof. Dr. Moritz
Vorsitzende/r der Prüfungskommission: Prof. Dr. Schnabel

Vorsitzender Fach-Promotionsausschusses PHYSIK: Prof. Dr. Wolfgang Hansen
Leiter des Fachbereichs PHYSIK: Prof. Dr. Michael Potthoff
Dekan der Fakultt MIN: Prof. Dr. Heinrich Graener

Abstract

In general, the understanding of microscopic physical processes in many-body systems needs an investigation starting from first principles, especially taking the impact of dimensionality and correlations into account. However, designing numerical ab-initio algorithms, which can handle the dimensional crossover and correlations is a very challenging task and strongly limited with respect to computational power. Because of this, most of the available algorithms in the literature focus on either one of these challenges.

In this thesis, nevertheless, we tackle these challenges by designing a highly optimized algorithm taking both all correlations and the dimensional crossover into account and show its efficient application for confined, interacting bosonic ensembles. In doing so, the exponential scaling of complexity w.r.t. the number of particles can be tackled by the ab-initio Multi-Configuration Time-Dependent Hartree methods for Bosons (MCTDHB) [PRL **77**, 033613 (2008)]. However, further different challenges occur when trying to model three-dimensional interaction potentials and in order to determine the most feasible interaction potential, we discuss different implementations for zero- as well as finite-range interaction potentials and rate them with respect to (i) the possibility to resolve correlations, (ii) a numerically efficient implementation and acceptable runtimes for desktop computers and (iii) numerically created artefacts due to approximations made. We show that repulsive short-range interaction potentials given as a product with respect to the dimensions are most suited for an implementation. Despite being most suitable, the use of these interaction potentials is highly challenging because they introduce a small length scale and, hence, need large number of grid points in a numerical treatment. We deal with this challenge by developing an efficient algorithm with respect to the number of grid points based on the Multi-Layer MCTDHB (ML-MCTDHB) method for ultracold bosons. In doings so by using a particularly tailored wave function ansatz, we derive equations of motion by using the Dirak-Frenkel variational principle and implement them in a highly optimized way, e.g., using parallel-processing. With our new wave function ansatz, the total numbers of grid point scales linear with the dimensions and not exponential as in the MCTDHB method. The algorithm is validated by comparison with possible analytical results and with other numerical methods available in the literature.

The beneficial scaling of our approach is used to study the impact of dimensionality on bosonic ensembles in different trap geometries. This is achieved by changing the trap aspect ratio, defined as the quotient between the transversal and longitudinal trap frequencies, leading to a crossover from a quasi 1D to an isotropic confinement. Especially, we are interested in the interplay between spatial and particle correlations and, thereby, we employ the following three systems. (i) Two bosons interact in a harmonic trap with various aspect ratios: This system serves as a prototype in order to determine suitable numerical and physical parameters and to study the time scale on which the interaction can induce significant spatial and particle correlations. Furthermore, we study the general convergence behaviour, which indicates an algebraic decay of the natural populations in three dimensions. (ii) A bosonic ensemble tunnels between two wells separated in the longitudinal direction, which are embedded in an elongated harmonic trap: We show that at least two transversal modes are needed in order to resolve the time-dependent density profile correctly and identify the influence of the dimensionality on the evolution of the population imbalance. In addition, we study the validly of different approximation of the many-body wave function, such as the mean-field approximation or the adiabatic separation of the spatial dimensions. (iii) A bosonic ensemble, initially displaced from the trap centre, scatters off a barrier, placed in the trap centre: By studying the mechanisms of coherence loss, interesting for matter-wave interferometers, we find that for nearly isotropic traps, loss of coherence occurs between the region close to the barrier and outer regions, due to spatial correlations while for

quasi one-dimensional traps incoherences rise between the two density fragments of the left and right side of the barrier, due to particle correlations. Furthermore, we can show how spatial and particle correlations modify the decay of the centre of mass oscillation. All these effects are enhanced if the aspect ratio is integer valued.

Zusammenfassung

Um mikroskopische Prozesse in quantenmechanischen Vielteilchensystemen richtig zu verstehen, benötigt man eine ab-initio Beschreibung, welche insbesondere den Einfluss sowohl von Korrelationen als auch der Dimensionalität berücksichtigt. Es ist jedoch sehr anspruchsvoll einen solchen ab-initio Algorithmus zu entwickeln, der nicht dramatisch von der verfügbaren Rechenleistung abhängt. Deshalb beschränken sich die meisten der gängigen Methoden auf eine der beiden Problemstellungen.

Trotzdem nehmen wir in dieser Arbeit diese Herausforderung an, indem wir einen hochoptimierten Algorithmus entwickeln, der sowohl Korrelationen als auch Systeme im Übergang zwischen unterschiedlicher räumlicher Dimensionalität numerisch auflösen kann. Wir zeigen die Effizienz unseres Algoritnmus, indem wir interagierende, bosonische Ensembles im Übergang von drei zu einer räumlichen Dimension simulieren. Dabei verwenden wir die Herangehensweise der ab-initio Multi-Configuration Time-Dependent Hartree Methode für Bosonen (MCTDHB) [PRL **77**, 033613 (2008)], welche den expotentiellen Anstieg der numerischen Komplexität in Bezug auf die Teilchenanzahl optimal handhabt. Dabei treten jedoch weitere Herausforderungen auf, bei dem Versuch Wechselwirkungspotentiale in drei Dimensionen zu modellieren. Um das geeignetste Wechselwirkungspotential zu finden, diskutieren wir unterschiedliche Implementierungen von Kontaktwechselwirkungen wie auch Wechselwirkungen mit endlicher Reichweite und bewerten diese Potentiale in Bezug auf die folgenden Fähigkeiten: (i) Korrelationen richtig aufzulösen, (ii) einen numerisch effizienten Algorithmus mit annehmbaren Rechenlaufzeiten für Desktop-Computer zu ermöglichen und (iii) numerische Artefakte zu minimieren, die von eventuellen Approximationen herrühren könnten. Wir zeigen, dass rein abstoßende Wechselwirkungspotentiale mit endlicher Reichweite, welche zusätzlich in den Dimensionen separieren, am besten für eine effiziente Implementierung geeignet sind. Dennoch stellen solche Wechselwirkungspotentiale numerische eine Herausforderung dar, weil sie eine kleine Längenskala im System induzieren, welche numerisch aufgelöst werden muss, so dass viele Gitterpunkte rechentechnisch gehandhabt werden müssen. Wir begegnen dieser Herausforderung, indem wir einen effizienten Algorithmus entwickeln, der für viele Gitterpunkte ausgelegt ist, basierend auf einer Multi-Layer Methode für MCTDHB. Dabei verwenden wir einen maßgeschneiderten Ansatz für die Mehrteilchen-Wellenfunktion und leiten spezielle Bewegungsgleichungen mit Hilfe des Dirak-Frenkel-Variations-Prinzip her. Die Implementierung der Bewegungsgleichungen wurde stark optimiert, unter anderem, durch Parallelisierung des Programmes. Mit unserem neuen Ansatz erreichen wir, dass die Gesamtzahl der Gitterpunkte linear bezüglich der Dimensionen skaliert und nicht exponentiell wie z.B. in der MCTDHB Methode. Der entwickelte Algorithmus wurde mit analytischen Ergebnissen und anderen gängigen Methoden in der Literatur verglichen.

Wir verwenden das vorteilhafte Skalierungsverhalten, um den Einfluss der Dimensionen auf ein bosonisches Ensemble zu untersuchen, induziert durch unterschiedliche Fallengeometrien. Dies erreichen wir, indem wir das Fallenfrequenzverhältnis, definiert aus dem Quotienten der transversalen zur longitudinalen Fallenfrequenz, kontinuierlich von einer isotropen Falle zu einer zigarrenförmigen Falle verändern. Uns interessiert besonders der Einfluss und das Zusammenspiel von Teilchen- und räumlichen Korrelationen. Wir untersuchen dabei die folgenden drei Systeme: (i) Zwei interagierende Bosonen befinden sich in einer dreidimensionalen, harmonischen Falle mit variablem Fallenfrequenzverhältnis. Dieses System dient als Prototyp, um geeignete numerische sowie physikalische Parameter zu finden, und erlaubt die Zeitskala auf der Teilchen- und räumliche Korrelationen erzeugt werden zu studieren. Des Weiteren untersuchen wir das Konvergenzverhalten und die natürlichen Populationen, welche in drei Dimensionen einen algebraischen Abfall aufweisen. (ii) Ein bosonisches Ensemble tunnelt zwischen zwei Potentialtöpfen, welche in longitudinaler Richtung in einer länglich ausgedehnten harmonischen Falle eingebettet

sind. Wir zeigen, dass man mindestens zwei transversale Moden benötigt, um das zeitabhängige Dichteprofil richtig wiederzugeben. Außerdem untersuchen wir den Einfluss der Dimensionen auf die zeitliche Entwicklung des Ungleichgewichts der Besetzungsverteilung. Zusätzlich studieren wir die Gültigkeit unterschiedlicher Approximationen der Mehrteilchen-Wellenfunktion, wie zum Beispiel einer Mean-field Näherung oder einer adiabatische Separation bezüglich der räumlichen Dimensionen. (iii) Ein bosonisches Ensemble, anfänglich in einer harmonischen Falle ausgelenkt, streut an einer zentrierten Barriere. Wir erforschen unterschiedliche Mechanismen, bezüglich des Verlustes von Kohärenz, was für Atom-Interferometer von zentraler Bedeutung ist. Dabei finden wir heraus, dass für näherungsweise isotrope Fallen Kohärenz zwischen der Region in der Nähe der Barriere und sowohl links als auch rechts davon verloren geht. Für fast eindimensionale Fallen hingegen erkennen wir, dass sich die Kohärenz zwischen den beiden Dichteanteilen der linken und der rechten Seite der Barriere reduziert. Der erste Prozess lässt sich mit Hilfe von räumlichen Korrelationen und der zweite mit Hilfe von Teilchenkorrelationen beschreiben. Des Weiteren ermitteln wir, wie Korrelationen die Oszillation des Masseschwerpunktes modifizieren können. Interesanterweise werden die obigen Effekte für ganzzahlige Fallenfrequenzverhältnisse verstärkt.

CONTENTS

PREFACE

This thesis is based on the following list of publications, which throughout the thesis will be referenced with double brackets [[···]].

List of publications this thesis is based on

[[1]] V. Bolsinger, S. Krönke, P. Schmelcher *Beyond mean-field dynamics of ultra-cold bosonic atoms in higher dimensions: facing the challenges with a multi-configurational approach*, J. Phys. B **50**, 034003 (2017).

[[2]] V. Bolsinger, S. Krönke, P. Schmelcher *Ultracold bosonic scattering dynamics off a repulsive barrier: coherence loss at the dimensional crossover*, Phys. Rev. A. **96**, 013618 (2017)

Further publications

[[3]] L. Cao, V. Bolsinger, S. I. Mistakidis, G. M. Koutentakis, S. Krnke, J. M. Schurer, P. Schmelcher *A unified ab-initio approach to the correlated quantum dynamics of ultracold fermionic and bosonic mixtures.* J. Chem. Phys **147**, 0044106 (2017)

Objectives   The aim of this thesis is to study the dimensional crossover from three to one dimension for ultracold bosonic ensembles in different trap geometries from first principles, especially taking all correlations into account. The exponential scaling of complexity with respect to the number of atoms can be tackled with the Multi-Configuration Time-Dependent Hartree method for Bosons (MCTDHB). However, in three dimensions, a further challenge consists in the modelling of the three-dimensional interaction potential, and we are going to find the most suitable finite-range interaction potential. Due to the different participating length scales occurring due to both the dimensional crossover and the usage of finite-range interactions, a large number of grid points will be needed numerically. We are going to solve this challenge by developing a highly efficient algorithm with respect to the number of grid points based on the Multi-Layer MCTDHB method for ultracold bosons. By using this algorithm, we study the crossover from three to one dimension from first principles and analyse (i) the interplay between spatial and particle correlations, (ii) the validly of different approximation of the many-body wave function such as the mean-field approximation or the adiabatic separation of the dimensions, (iii) the loss of coherence, or (iv) the influence of the different kinds of correlations

on observables. We are going to analyse these properties for three setups; two particles in elongated trap, the dynamics of bosons tunnelling in a double well and scattering off a barrier.

Overall outline In chapter 1, we give a brief introduction in the field of three- and one-dimensional ultracold bosonic gases and the dimensional crossover. Since interactions in three dimensions play a significant role in this thesis, we review definitions and concepts of the scattering theory in chapter 2. Prepared with this knowledge, we discuss possible interaction potentials in three dimensions and their implementation within the framework of the Multi-Layer Multi-Configuration Time-Dependent Hartree method for Bosons, in chapter 3. For the resulting, efficient interaction potentials, we derive, by using the variational principle, equations of motion and discuss their implementation and numerical effort in chapter 4. In chapter 5, 6 and 7, we study the interplay between spatial and particle correlations. However, the focus of chapter 5 is about different aspects of the convergence behaviour for two bosons in three dimensions while the focus of chapter 6 is about the analysis of different regimes occurring while the dimensional crossover. The results of chapter 3, 4 and 6 have been published in the publication [[1]]. Next, we study bosons scattering off a barrier in an elongated trap in chapter 7 and analyse the loss of coherence, important for the studies of matter-wave interferometers. This chapter is based on the publication [[2]]. We end with a summary of our results in chapter 8 and an outlook in chapter 9.

Declaration of Personal Contributions to the Publications [[1-3]] The projects resulting in [[1,2]] were conducted entirely by myself, including the specification of the research questions, numerical work and analytical approximate models. In project [[3]], I contributed by active participation of the discussions rewarding the derivation of the equations of motion and the design of the algorithm as well as consulted the implementation and code development. In all cases, the project progress and some problems were discussed on a regular basis with Dr. Sven Krönke and Prof. Dr. Peter Schmelcher.

CHAPTER

ONE

INTRODUCTION

Quantum many-body physics, as for example, occurring in solid state devices, is a complex and challenging research field not only theoretically, due to the many degrees of freedom, but also experimentally due to the interactions with the environment and among the different constituents. A structured way to experimentally analyse quantum many-particle systems has been started by the achievement of condensed alkali metals in magnetic traps at extremely low temperatures[1] [3–8]. The condensates, being defined by the property that all particles populate the same physical state, have been theoretical predicted by Bose [9] and Einstein [10] in 1924/1925 and are hence named Bose-Einstein Condensates (BEC). The condensation can be achieved in experiments, in which lasers isolate the system from the environment and control motional as well as internal degrees of freedom. Different types of interaction can be chosen by taking e.g., charged, neutral or dipolar atoms (or combinations among them), creating Coulomb, Van-der-Walls or dipole interaction [11], respectively, or taking different spin states and spin interactions into account. E.g., for neutral atoms, the strength of the interaction can be tuned by external magnetic fields applying the concept of Fano-Feshbach resonances [12, 13]. These resonances occur if a closed scattering channel is energetically near the so-called threshold of an open scattering channel. In this way, the unitary regime, defined by infinitely strong interactions, can be achieved [14–17]. Furthermore, laser beams can be used to created different confinement geometries, e.g., harmonic and anharmonic trap potentials, double and triple wells, or different lattices geometries (e.g., square or honey comb lattice) in one, two or three dimension [18]. In addition, the number of trapped particles can be modified by changing the chemical potential. So, in experiments with cold gases a plethora of parameters can be tunes. Detailed summaries about these topics can be found in the standard textbooks [19–22] and reviews [23–25].

Equipped with these experimental tools, BECs can be used for a large variety of different physical applications, e.g. the improvement of quantum measurements, the so called quantum metrology [26–28], by using "Schrödinger's cat" like states, which can be created e.g. with the help of Bose-Einstein condensates [29, 30]. These "Schrödinger's cat" like states can reduce the shot to noise limit [31, 32], or can be used for measurements using matter-waves interferometry [33].

A further application of BECs can be found for the quantum computer. The BEC plays a major role in the three main parts of a quantum computer: quantum transport, quantum calculations and quantum storage/memory (see [34–36] and references therein). Quantum transport can be achieved in lattice systems, by hopping of atoms among the lattices sites [37, 38] or on atom

---

[1]honoured with noble prize in physics 2001 for C. E. Wieman, W. Ketterle and E. A. Cornell [1, 2]

chips by changing electromagnetic fields created by small wires [39]. Quantum computation can be realized by using e.g. ultracold trapped ions [40, 41] or neutral atoms with internal states either in a double well [36] or in lattices [42, 43]. Proposals for the quantum information storage have been made in references [44, 45], using the coupling of quantum particles to an environment in order to drive the system to a steady state, which contains the quantum information.

Furthermore, BECs can not only be used as a constituent for a quantum computer but also to emulate or rather mimic quantum many-body systems for a diversity of condensed matter problems [46–49]. In doing so, a Hamiltonian can be mapped onto a many-body system, which can be mimicked with the help of ultracold atoms. For example, single-particle potentials can be mimicked by external laser fields or the variety of the interaction strength by using a Feshbach resonance. One of the most prominent representative examples is the Bose-Hubbard model [50]. In doing so, the crossover from a Mott insulating state to a superfluid state has been demonstrated [50–53]. Another example is the BEC-BCS[2] crossover for a fermionic system [54]. For weak attractive interaction, Cooper pairs are created [55]. By increasing the interaction strength, the fermions become bounded and create bosonic molecules, which interact repulsively. The last example, we like to mention, is the creation of artificial gauge fields [56] using neutral bosons, where the centre of mass motion can mimic the dynamics of charged particles in a magnetic field. Historically, the usage of an easy-tunable quantum system in order to emulate a more complicated many-body quantum system has been already proposed by R. Feynman in 1982:

> "Nature isn't classical, dammit, and if you want to make a simulation of nature, you'd better make it quantum mechanical, and by golly it's a wonderful problem, because it doesn't look so easy."
>
> R. Feynman, 1982 [57]

However, quantum mechanical emulations or a quantum computer are under construction nowadays and for their construction a microscopic physical understanding is needed, which can be gained by analytical or numerical many-particle studies. Although the fundamental laws of physics are well known theoretically, they are almost impossible to treat analytically as already pointed out by P. Dirac:

> "The underlying physical laws necessary for the mathematical theory of a large part of physics and the whole of chemistry are thus completely known, and the difficulty is only that the exact application of these laws leads to equations much too complicated to be soluble. "
>
> P. Dirac, 1929 [58]

Even numerical solutions quickly become infeasible, since the computational effort of quantum mechanical simulations scales exponentially w.r.t. to the number of particles N, e.g. 2^N for a two-state spin system or $(N + M - 1)!/(M - 1)!N!$ for a bosonic gas, where M is the number of single-particle modes. However, in classical simulations, the scaling is only linear w.r.t. the number of particles, $2dN$, where d represents the dimensionality. This is why R.B. Laughlin and D. Pines wrote in their paper "The theory of everything":

> "However, it (the many-body Hamiltonian) cannot be solved accurately when the number of particles exceeds about 10. No computer existing, or that will ever exist,

---

[2]Named after the inventors of the BCS theory: J. Bardeen, L. N. Cooper und J. R. Schrieffer

> *can break this barrier because it is a catastrophe of dimension"*
>
> R.B. Laughlin and D. Pines, 2000 [59]

However, by restricting ourselves to zero-temperature, trapped, dilute, bosonic systems, the challenge of the exponential scaling w.r.t. the number of particles can be tackled by the recently developed ab-initio *Multi-Configuration Time-Dependent Hartree* method *for Bosons* (MCT-DHB) [60]. For these systems, the two-body van-der-Waals interaction is the dominant interparticle interaction, which can be numerically modelled in one dimension by zero-range interaction potentials. The advantage of using a zero-range interaction potential is that the interaction range Σ must not be resolved numerically. However, in *three* dimensions, a description of the interaction by a zero-range interaction potential within the MCTDHB framework is not possible and a finite-range interaction potential has to be used with the characteristic length scale Σ (see chapter 3). In the crossover from one to three dimension, an additional length scale emerges, namely, the transversal confinement length scale, $l_\perp$. Therefore, a second numerical challenge occurs: the numeral resolution of all these length scales and therefore the need to simulate a large number of grid points. This second numerical challenge is tackled in this thesis (see chapter 4). The MCTDHB method is expanded to an efficient implementation for three dimensions, calling *Multi-Layer Multi-Configuration Time-Dependent Hartree* method *for Bosons* (ML-MCTDHB) based on an idea mentioned in [61, 62]. In doing so, we have improved the exponential scaling of the number of grid point w.r.t. the dimensionality used in MCTDHB to a linear scaling in ML-MCTDHB, and a large number of grid points, approximately an order of magnitude more grid points per dimension, can be handled while executing the algorithm on desktop computers. With this ab-initio algorithm, we are able to simulate few- to many body bosonic ensembles in three dimensions by taking all kinds of correlations into account. Furthermore, we can numerically perform the crossover from three to one dimension and explore the interplay between particle and spatial correlation w.r.t. the dimensionality for different physical systems, e.g., a double well (see chapter 6) or with a local disturber (see chapter 7). We can verify the validity of certain approximations of the many-body wave functions, such as a mean-field approximation or an adiabatic separation of the dimensionality.

The introduction is structured as follows: First, in section 1.1, we briefly discuss different characteristics of three- and one-dimensional systems, for example the possibility of condensation, the occurrence of particle correlations, resonances in the scattering length and bound states. Thereby, we identify the various characteristics which the dimensionality imprints on the system. In doing so, we motivate the study of the crossover from three to one dimension, which links the above quite complementary characteristics. In the following section 1.2, we introduce the physics of the dimensional crossover by reviewing theoretical and experimental studies. In section 1.3, the basic idea of our numerical method is briefly presented. Afterwards in section 1.4, we define particle and spatial correlations, and describe the concept of natural orbitals and natural populations. These definitions are used throughout the thesis. Finally in section 1.5, we describe the further structure of the thesis in order to guide the reader.

1.1. Differences between three and one dimension

It is well known that three-dimensional in contrast to one-dimensional bosonic systems behave in some respects completely different, making the analysis of a crossover between dimensions a fascinating subject to study. In the following section, we want to list some of the striking differences occurring between a three-dimensional and a one-dimensional system.

First, bosons in a three-dimensional trap can condense below a critical temperature T_c, since

phase and density fluctuations are suppressed, whereas, the condensation is absence in one dimension [63–65] due to phase fluctuations [66]. The one-dimensional correlation function decays exponentially [67] on the length scale of the coherence length l_c. Even at absolute zero temperature, there are still phase fluctuations present, however, the decay of the correlation function is algebraic [64, 68, 69]. The one-dimensional phase space w.r.t. the temperature and particle numbers have been derived in reference [70] and experimentally verified in reference [71–74]. However, even in one dimension, if the coherence length l_c is much larger than the healing length $\xi = \hbar/\sqrt{m\rho g}$, where ρ is the density, m the mass of one boson and g is the interaction strength, different condensed blocks can be formed, which lead to a quasi-condensation.

As a consequence for three dimensions, a good approximation is to assume that all bosons reside in a mean-field orbital $\Phi_{GP}(\mathbf{r})$ due to their condensation,

$$\Psi(\mathbf{r}_1,\ ...,\ \mathbf{r}_N, t) = \prod_{i=1}^{N} \Phi_{GP}(\mathbf{r}_i, t) \qquad (1.1)$$

By varying these mean-field orbitals, one obtains a non-linear differential equation, known as the Gross-Pitaevskii equation (GPE) [75, 76]. Within the GPE framework, one can describe the ground state of a BEC in a harmonic trap [77] and its energy spectrum [78] for weak interactions and low densities. Different dynamical properties like the breathing, dipole, or quadrupole mode [78–81] have been derived, using a hydrodynamic formulation of the GPE. Furthermore, the dynamics of vortices [82] can be studied (see also [83] and references therein). However in one dimension, the fluctuations prevent the condensation of the bosons and deviations from mean-field results as well as new effects can arise, for example, fragmentation of the wave function [84], fermionization of the bosons [84–88], the decay of dark solitons due to dynamical quantum depletion [89, 90], or correlated pair tunnelling in a double well [91–93].

Second, the relation between the interaction energy and the kinetic energy is different w.r.t. the dimensions in the thermodynamical limit. In a box of size L^d with N bosons inside, the only length scale, which governs the system, is defined by the interparticle distance, $\bar{l} = \rho^{-1/d}$, where $\rho = N/L^d$ is the density and d denotes the number of dimension. The unitless Hamiltonian can be written as

$$\frac{\hbar^2}{2m}\rho^{\frac{2}{d}}\left[-\int d^d\mathbf{r}\ \hat{\Psi}^\dagger(\mathbf{r})\nabla_\mathbf{r}^2\hat{\Psi}(\mathbf{r}) + \frac{\gamma}{2}\int\int d^d\mathbf{r}\ d^d\mathbf{r}'\ \hat{\Psi}^\dagger(\mathbf{r})\hat{\Psi}^\dagger(\mathbf{r}')W(\mathbf{r},\mathbf{r}')\hat{\Psi}(\mathbf{r})\hat{\Psi}(\mathbf{r}')\right], \qquad (1.2)$$

where $\hat{\Psi}^\dagger(\mathbf{r})$ [$\hat{\Psi}(\mathbf{r})$] are the bosonic creation [annihilation] field operators at position $\mathbf{r}$. For a more concrete calculation, we have assumed an interaction potential, which scales like ρ^{-1} and which is linear in the interaction strength g, e.g., the regularized delta interaction potential $g\partial_\mathbf{x}\mathbf{x}$ [94], where, here, $\mathbf{x}$ is the distance between two particles $\mathbf{x} = |\mathbf{r} - \mathbf{r}'|$. The only remaining tunable parameter, depending on the dimensionality, is then

$$\gamma_d = \frac{mg}{\hbar^2}\rho^{1-\frac{2}{d}}, \qquad (1.3)$$

which is similar to the Lieb-Lininger parameter [95]. We call γ the effective interaction strength, in order to distinguish it from the interaction strength g. In three dimension the effective interaction strength is increased if the density becomes more dense, $\gamma_{3D} = mg\ \rho^{1/3}/\hbar^2$, whereas in one dimension, the effective interaction strength increases if the system becomes more diluted, $\gamma_{1D} = \frac{mg}{\hbar^2}/\rho$.

Third, due to strong transversal confinements [96,97], virtual transversal states can be existed, which modify the interaction strength. The interaction strength for a reduced one-dimensional system is then given as

$$g_{1D} = \frac{g}{\pi l_\perp^2}\left(1 - C\frac{a_0}{l_\perp}\right)^{-1} \qquad (1.4)$$

where $C = 1.4603...$ is a numerical factor and $a_0 = mg/4\pi\hbar^2$ is the zero-energy scattering length (a proper definition of a_0 is given in chapter 2). For a zero-energy scattering length of the order of the transversal confinement, resonances in the one-dimensional interaction strength occur. The resonances only occur due to the dimensional reduction to one-dimensional systems and are called *confinement induced resonances*.

Fourth, in a one-dimensional systems, one encounters new regimes if the reduced one-dimensional interaction strength g_{1D} is increased. Especially, for infinite-strong hard-core interactions, the interacting bosonic system can be mapped onto a non-interacting fermionic systems [85, 98]. In this regime, the so-called Tonks-Girardeau (TG) regime, local bosonic properties, such as the atomic density, behave as that of non-interacting fermions. However, non-local properties, such as the momentum distribution, are different. A full characterization of the one-dimensional phase space in the thermodynamic limes is given in reference [99], where five different regimes have been identified (see figure 1.1). In reference [99] in order to reduce the system to one dimension, the three-dimensional ground state energy is related to the one-dimensional energy functional in dependence on the number of particles and interaction strength $\gamma \equiv g_{1D}/\rho_{1D}$, where ρ_{1D} is the mean one-dimensional density. The five regimes are:

i. $\gamma \ll N^{-2}$: the system can be described by a non-interacting bose gas (NI-BG)

ii. $\gamma \sim N^{-2}$: this regime can be well described by the one-dimensional GPE (1D GP)

iii. $N^{-2} \ll \gamma \ll 1$: the one-dimensional GPE (1D GP) can be further simplified using the Thomas-Fermi (TF) approximation, where the kinetic term is neglected.

iv. $\gamma \sim 1$: for strongly interacting systems, the analytic solution by Lieb and Lining (LL) [95, 100] has to be used.

v. $\gamma \gg 1$: this regime can be described by the Tonks-Girardeau (TG) gas, a bosonic gas, with impenetrable bosons.
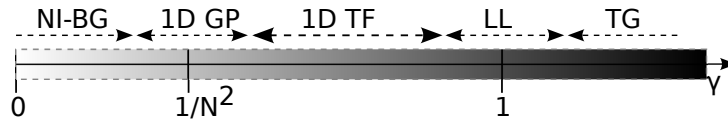
Figure 1.1.: Phase diagram for N particles in one dimensions [99] in dependence of the interaction strength $\gamma = g_{1D}/n_{1D}$. The abbreviations stand for: non interacting, bosonic gas (NI-BG), one-dimensional GPE (1D GP), one-dimensional Thomas-Fermi (1D TF), the Lieb-Lininger (LL) and the Tonks-Girardeau (TG) regime.

1.2. Crossover from three to one dimension

We consider the crossover from three to one dimension for harmonically trapped, bosonic systems at zero temperature. The first part is dedicated to a theoretical discussion, and in the second part we refer to existing experimental studies.

Theory: The crossover from three towards one dimension can be performed by tightening the transversal trap frequency, i.e. increasing the aspect ratio η, defined as the ratio between the transversal $\omega_\perp$ and longitudinal $\omega_\parallel$ trap frequencies, $\eta = \omega_\perp/\omega_\parallel$. For $\eta = 1$, both trap frequencies are equal and an isotropic trap is obtained. If the transversal frequency is decrease ($\eta \to 0$), a pancake-like potential is created and the system becomes two-dimensional. If the transversal frequency is increased ($\eta \to \infty$), a cigar shaped potential is formed and the system becomes one-dimensional. If the energy gap between the transversal ground and transversal

first excited states is much larger than any other energy scale, such as thermal excitations or the chemical potential, the system effectively behaves one-dimensional. Commonly, systems which are studied in three dimensions but behave almost one-dimensional are called *quasi-one dimensional* systems. For quasi-one dimensional systems, static ground state properties [101, 102], the creation of collective excitations [103, 104] or the occurrence of the scissor modes [105] have been studied using the GPE framework. Furthermore, the decay of dark solitons into vortex rings or solitonic vortices [106], and the dynamical characteristics of the ground and excited states [107–110] have been investigated.

In order to reduce the computational effort for quasi-one dimensional systems, one can assume that the Gross Pitaevskii (GP) mean-field wave function $\Phi_{GP}(\mathbf{r})$ can be decomposed into a product of the transversal and longitudinal direction, calling *adiabatic separation* $\Phi_{GP}(\mathbf{r}) = \phi_\perp(x,y)\phi_\parallel(z)$. Here, x and y mark the transversal position and z the longitudinal one. For strong transversal confinements, the transversal state is nearly undisturbed and can be approximated by the harmonic oscillator ground state, $\phi_\perp(\rho) = \exp(-\rho^2/2l_\perp^2)/\sqrt{\pi l_\perp^2}$, where $\rho^2 = x^2 + y^2$ and $l_\perp$ is the transversal characteristic trap length, defined below. In this most simple case, one can integrate out the transversal degrees of freedom directly and receives an *effective one-dimensional* GPE. In order to improve the above approximations, more sophisticated methods have been proposed in the literature and roughly summarized, they all use the adiabatic separation and apply a trial wave function transversally, for example with a Gaussian or Thomas-Fermi (TF) profile which are optimized variationally [111–117]. Using the effective one-dimensional GPE framework, the properties of the ground-state in a harmonic trap [65], collective excitations [118] or dark and bright solitons (see [119] and references therein) has been studied for weak interactions. However, also analytical calculations beyond the adiabatic separation have been performed, taking dimensional entanglement[3] into account [120, 121] via a pertubative Schmidt decomposition [122] of the GP mean-field wave function. In doing so, they showed that the dimensional entanglement stays "remarkably" small.

For harmonically trapped, ultracold bosons, a rough phase diagram can be derived [118], using a zero-range interaction potential. The phase diagram is replotted in figure 1.2 in dependence on the particle number N and the ratio between the transversal and longitudinal characteristic trap length, $l_\perp$ and $l_\parallel$, respectively. For a harmonic confinement, the characteristic trap lengths are given by $l_{\perp,(\parallel)} = \sqrt{\hbar/m\omega_{\perp,(\parallel)}}$, where $\omega_{\perp,(\parallel)}$ are the transversal (longitudinal) trap frequencies respectively. The zero-energy scattering length a_0 is kept constant. The ratio $l_\perp/l_\parallel$ ranges from zero (one-dimensional) towards one (isotropic harmonic trap in three dimensions). In a more one-dimensional system (low $l_\perp/l_\parallel$), we recover the Tonks-Girardeau regime (TG gas) for low number of particles. Increasing the number of particles, the size of the phase space of the Tonks-Girardeau regime is reduced and a regime is found, where a one-dimensional mean-field (1D MF) description is sufficient to describe the system. This phenomenon is also reflected by equation (1.3), where we have observed that in one dimension the effective interaction strength behaves as $\gamma_{1D} \propto 1/N$. For a system closer to three-dimensions ($l_\perp/l_\parallel \sim 1$), we observe that for low number of particles a regime is found, which can be described by a non-interaction bosonic gas (NI-BG). Increasing the number of bosons, the interaction among the particles gets important and must be taken into account. This regime can be solved by the three-dimensional GPE for cigar shaped traps (3D cigar). This feature can be also explained by equation (1.3), where we have found that for three dimensions the effective interaction strength behaves as $\gamma_{3D} \propto N$. A further increase of the number of particles (not shown), would lead to the Thomas-Fermi regime, where the kinetic term in the Hamiltonian can be neglected. Keeping the number of particles fixed and chancing the ratio $l_\perp/l_\parallel$, we see by going from three to one dimension that

---

[3] We will call dimensional entanglement also spatial correlations.

the non-interacting regime is transformed into a weakly correlated regime (1D MF) and finally into the Tonks-Girardeau regime, where strong correlations are present. This feature is reflected by equation (1.4), where the interaction strength is increased if the transversal characteristic length is decreased. However for a large number of particles, the crossover from three to one dimension is not clearly understood and especially the influence and interplay of particle and spatial correlations in higher dimensions is of actual interest. Studies in two dimensions, which
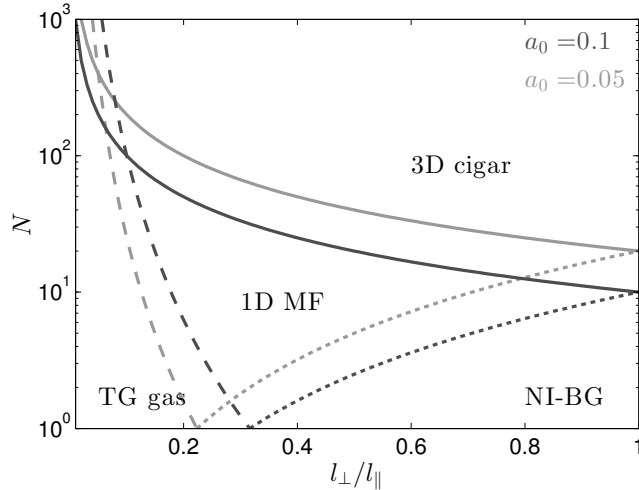

Figure 1.2.: Approximate phase diagram for the crossover from three dimension $l_\perp = 1$ towards one dimension $l_\perp \sim 0$ in dependence on the particle number N but with two different fixed scattering length $a_0 = 0.1$ (dark grey) and $a_0 = 0.05$ (light grey). The lines separate the single regimes (see reference [118]). Four regimes are identified: Tonks Girardeau (TG) gas, 1D mean-field (MF), 3D MF and the non-interacting bose gas (NI-BG).

take all correlations into account, have already been performed (see references [123–127]). For example, vortex nucleation is analysed beyond the mean-field framework, where strong correlations as well as entanglement are observed at a critical rotation frequency [123, 127]. The vortices are proposed to be fragmented objects [126, 127] and not collective excitations as in the mean-field framework. Even if in the density no vortices can be observed, vortex similar structures arise in higher natural orbitals [125], which may be linked to the formation of the Abrikosov lattice and the onset of turbulence in superfluids. Another example is the analysis of the ground state of an interacting bosonic ensemble in a two-dimensional radial split potential [128, 129] (and for three dimensions [130]), where fragmentation of the ground state wave function is predicted. Furthermore, quench dynamics has been studied for one to three-dimensional systems [131] using beyond mean-field methods. However, a structured way to simulations of the dimensional crossover is still missing and, within this thesis, we are going to tackle this challenge.

Experiment: Up to now, condensation of the following elements has been observed in three dimensions Na [3, 6, 132], Rb [133], Li [134], H [135], He [136], K [137], Cs [138], Yb [139], Cr [140], Ca [141], Sr [142], Dy [143] and Er [144]. The condensation of these elements have be achieved after the development of cunning cooling and trapping methods for neutral atoms using laser light (honoured with the noble prize for Steven Chu [145], Claude Cohen-Tannoudji [146] and William D. Philips [147] in 1997). Only four years later, in 2001, the first achievements of a BEC in 1995 have been also dignified with the noble prize for Eric A. Cornell [1], Wolfgang Ketterle [2] and Carl E. Wieman [1]. In a typical experimental setup, an element is heated up to approximately $\sim 600K$ in order to create vapour. In order to cool the vapour, the vapour

is then slowed down by a Zeeman slower and loaded into a magneto-optical trap (MOT). By using further optical cooling techniques with laser beams, some hundreds of micro Kelvin can be achieved. However, this temperature is limited w.r.t. the momentum recoil induced by the laser beams. In order to achieve lower temperature, evaporative cooling [148] can be used, and therefore, the cold gas must be loaded into a pure magnetic trap. A review on different trapping and cooling techniques can be found in references [18,149–152]. In order to perform the crossover from three to one dimension experimentally, the transversal trap frequencies must be increased, for example by changing the current on atom chips [153], by changing the magnetic fields in an Ioffe-Pritchard trap [74], or by superimposing different laser beams, which form cigar shaped traps side by side [154].

1.3. The numerical method: Multi-Layer Multi-Configuration Time-Dependent Hartree for Bosons

As we have already stressed, numerical quantum methods suffer from the exponential scaling of the configuration space w.r.t. the number of particles and a large number of grid points are needed in three dimensions, due to the necessary separation of the characteristic length scales in the system. Furthermore, it is of advantage if the numerical methods are as flexible as the experimental setups; i.e., they can be used for different, time-dependent, various external trap potentials, for mixtures of different bosonic or fermionic species and for the whole range of interaction strength, from weak to strong coupling. It is very demanding to satisfy all of these requests at the same time, and therefore, most of the numerical methods just focus on some of them. Apart from a classification on the various request, an algorithm can also be classified w.r.t. structural differences in its implementation, and in the following section, we want to present three possible criteria. Then, we sketch very briefly the general idea of the Multi-Configuration Time-Dependent Hartree (MCTDH) method, which is the foundation of our method, the Multi-Layer Multi-Configuration Time-Dependent Hartree for Bosons (ML-MCTDHB). The latter is a generalization of the MCTDHB algorithm to multi-species or higher dimensions (as demonstrated in this thesis). A detailed derivation of the equation of motions is given in chapter 4.

We describe three possible criteria, where we partly follow the lines of reference [155]. Somehow, the number of criteria are arbitrary, but we have chosen these three criteria, since they give a reasonable classification for our purposes.

(a) Degree of approximation:
   In general, a physical system can be modelled by a Hamiltonian, which incooperates all the necessary physics. Non-interesting effects or less important parts in the Hamiltonian are neglected or simplified by reasonable model terms, for example, normally, for ultracold interacting neutral bosons, the "true" Van-der-Walls interaction potential is replaced by a much simpler short- or zero-range interaction potential. Then, having the "working" Hamiltonian, one can distinguish two classes of approaches:
   (i) In the first class, no direct approximation is made to the many-body wave functions. The only approximation, which is made, is a truncation of the infinite size of the Hilbert space, necessarily in every numerical calculation, leading to a finite-size subspace. By increasing the size of the subspace, the result becomes more and more *numerically "exact"*. Commonly, the size of the subspace is limited by the resources of computational power and thus either a few numbers of particles or moderate number of grid points can be used. We call these kinds of algorithms *ab-initio* methods, since they simulate the physics from first principles. Some examples are the Exact Diagonalization (ED) [156], the Density-Matrix Renormalization

Group (DMRG) [157–161], Quantum Monte Carlo (QMC) [162, 163] and the family of the MCTDH(B) methods .

(ii) In the second class, one simplifies the many-particle wave function by assuming a particular functional shape. For example, we have already encountered the wave function approach used to derive the GPE, where all the particles occupy the identical orbital. Further examples are the adiabatic separation, where the wave function can be separated into the dimensions (see section 1.2) or the *Gutzwiller* wave function approach applied to lattice systems [164, 165]. In the latter, the many-particle wave function is separated w.r.t. a combination of single modes.

(b) Representation of the number states:

There are two possibilities to represent a number state in a given many-particle Hilbert space $\mathcal{H}$:

(i) On the on hand, the many-particle Hilbert space can be represented as a direct product of the single-particle Hilbert spaces $\mathcal{H}_i$, $\mathcal{H} = \otimes_{i=1}^N \mathcal{H}_i$, where the product runs over all numbers of particles. If the many-body wave function $|\Psi\rangle \in \mathcal{H}$ cannot be factorized in the single particle states of the i-th particle $|\phi^{(i)}\rangle$, $|\Psi\rangle \neq \otimes_{i=1}^N |\phi^{(i)}\rangle$ than *particle correlations* are present in the system. Instead, if $|\Psi\rangle = \otimes_{i=1}^N |\phi^{(i)}\rangle$ no particle correlations exist. This construction is similar to the wave function approach used to derive the GPE.

(ii) On the other hand, the many-particle Hilbert space can be constructed out of single-mode Fock spaces $\mathcal{F}_j = \mathrm{span}\{|n\rangle_j, n \in \mathbb{N}_0\}$, where $|n\rangle_j$ labels the state j with n particles inside, such that $\mathcal{H} = \otimes_{j=1}^M \mathcal{F}_j$, where M is the maximal number of modes. The many-body wave function can be expressed into these modes leading, for example, to the Gutzwiller wave function ansatz. Non-factorization into the modes is a signature of mode correlations.

(c) Temporal Evolution:

At least, two different strategies can be followed in order to solve the temporal evolution of the many-body wave function. The first one determines the time-evolution operator directly and the second one solves the Schrödinger equation by integration. The reason for choosing these tow strategies is that we focus on them in a later discussion. In the following, we have a closer look on them.

(i) There are different ways, to calculate the time-evolution operator, e.g., using the split-operator method [166] or using path integrals [167]. In case of a time-independent, many-particle Hamiltonian H, the temporal evolution of an initial wave function $|\Psi(0)\rangle$ is governed completely by the time-independent many-body eigenstates $\{|E_n\rangle\}_{n=1}^M$ and eigenenergies E_n defined by

$$H|E_n\rangle = E_n|E_n\rangle \qquad |\Psi(t)\rangle = \sum_{n=1}^M c_n \exp(-iE_n t/\hbar)|E_n\rangle$$

with the coefficients $c_n = \langle E_n|\Psi(0)\rangle$. The task is now to solve the eigenvalue equation, for example by exact diagonalization or many-particle perturbation theory. Due to the exponential scaling of the Hilbert space w.r.t. the number of particles, exact diagonalization algorithms needs a lot of computational resources and are only feasible for a few number of particles ($N \sim 5$) [168].

(ii) This is in contrast to methods, which propagate the initial wave-function $|\Psi(0)\rangle$ forward in time. This class allows explicit time-dependent Hamiltonians. For example, one can expand the wave function into a basis set of (well-chosen) many-body functions $\{|\tilde{\chi}_i\rangle\}_{i=1}^{\tilde{M}}$ such that $|\Psi(t)\rangle = \sum_{i=1}^{\tilde{M}} c_i(t)|\tilde{\chi}_i\rangle$ with the yet unknown, time-dependent coefficients $c_i(t)$. If $|\Psi(t)\rangle$ is inserted into the Schrödinger equation, equation of motions for the coefficients can be derived $i\hbar\dot{c}_i(t) = \sum_{j=1}^{\tilde{M}} \langle\tilde{\chi}_i|H(t)|\tilde{\chi}_j\rangle c_j(t)$, which form a coupled system of first-order

ordinary differential equations. Representatives of this class are the family of MCTDH method and the Configuration Interaction.

Summarizing, the MCTDH(B) method is an ab-initio method, which expresses the many-body Hilbert space as a direct product of single-particle Hilbert spaces. The Schrödinger equation is solved by propagating an initial wave function in time and therefore MCTDH(B) can handle time-dependent external as well as interaction potentials. However, instead of using time-independent many-body basis functions, MCTDH(B) uses time-dependent, many-body basis functions. The time-dependent many-body basis functions are determined variationally and thus cover always the optimal subspace of the many-particle Hilbert space. In the following, we further sketch this grave idea of MCTDH(B): In MCTDH(B), a *time-dependent* basis set of single-particle functions $\{|\chi_i(t)\rangle\}_{i=1}^{M}$ is used in order to express the many-particle wave function. The number of single-particle functions is usually much smaller than the number of single-particle functions needed with a time-independent basis $\{|\tilde{\chi}_i\rangle\}_{i=1}^{\tilde{M}}$. The $\chi_i(t)$ are determined variationally and thus cover always the optimal sup-Hilbert space (see figure 1.3). This subspace moves in dependence on time so that the best possible representation of the time-dependent many-particle wave function $|\Psi\rangle$ is always guaranteed. In doing so, the number of basis functions can be reduced and large system can be studied [169].
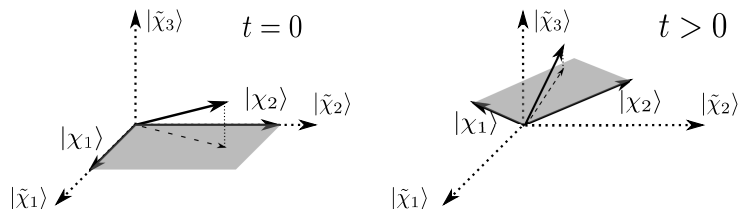
Figure 1.3.: Schematic representation of the MCTDH algorithm. The time-dependent single-particle basis used in the MCTDH algorithm is given by $\{|\chi_i(t)\rangle\}_{i=1}^{M=2}$ (grey area) and for comparison a time-independent basis is given by $|\tilde{\chi}_i\rangle\}_{i=1}^{\tilde{M}=3}$. The dynamics of the time-dependent single-particle wave function is marked by a black solid line, which moves somehow in the (multi-dimensional) single-particle Hilbert space. The basis states $|\tilde{\chi}_i(t)\rangle$ move also in time and due to their variational optimization they cover always the best possible sub-Hilbert space in order to represent the "truth" dynamics of the wave function.

1.4. Using natural orbitals and natural populations: Particle versus spatial correlations

One central issue of this thesis is the occurrence of correlations in an interacting bosonic ensemble in the crossover from three to one dimension for various trap geometries. With *correlations*, we mean the entanglement on the wave function between different degrees of freedom, or in other words, the lack of the possibility to represent the wave functions in a product form. In this way, correlations depend on the chosen coordinate system. In the following, we regard all the correlations w.r.t. the laboratory frame. Let us give some examples for particle and spatial correlations: We define that a wave function contains *particle correlations* if it cannot be separated into a product form:

$$\Psi(\mathbf{r}_1, ... \mathbf{r}_N) \neq \prod_{i=1}^{N} \psi(\mathbf{r}_i)$$

In doing so, we identify that the solution of the GPE cannot contain particle correlations per construction. *Spatial correlations* are defined if the many-particle wave function cannot be

expressed in product form w.r.t. the dimensions.

$$\Psi(\mathbf{r}_1, ... \mathbf{r}_N) \neq \psi_1(x_1, ..., x_N)\psi_2(y_1, ..., y_N)\psi_3(z_1, ..., z_N)$$

This approximation is called *adiabatic separation*.

We quantify spatial and particle correlations with the help of the concept of natural populations, which is presented in the following. The three-dimensional natural orbitals $|\alpha_i\rangle$ and natural populations $a_i^{(3D)}$ are defined as the eigenfunctions and eigenvalues of the three-dimensional reduced one-body density operator ρ^{3D}, namely

$$\rho^{(3D)}|\alpha_i\rangle = a_i^{(3D)}|\alpha_i\rangle, \tag{1.5}$$

which is obtained by

$$\rho^{(3D)} = tr_{N-1}|\Psi\rangle\langle\Psi| \tag{1.6}$$

integrating over $N-1$ particles, denoted by the notation of the trace. Both the natural populations and natural orbitals are time-dependent. In this work, the natural orbitals are normalized to one as well as orthogonal and the natural populations are sorted in decreasing order $a_1^{(3D)} \geq a_2^{(3D)} \geq a_3^{(3D)} \geq ...$ with $\sum_i a_i^{(3D)} = 1$. Furthermore, due to equation (1.5), the reduced one-body density operator can be decomposed into the natural orbital basis using $\mathbb{1} = \sum_i |\alpha_i\rangle\langle\alpha_i|$

$$\rho^{(3D)} = \sum_i a_i^{(3D)}|\alpha_i\rangle\langle\alpha_i|. \tag{1.7}$$

Unoccupied natural orbitals with $a_i = 0$ do not contribute in the above sum and can be neglect for physical considerations, e.g., in the calculation of the expectation value of single-particle observable $\hat{O}$, $\langle\hat{O}\rangle = tr(\hat{\rho}^{(3D)}\hat{O})$. In case only one natural orbital is occupied $a_1^{(3D)} = 1$ and $a_{i>1}^{(3D)} = 0$ (as in condensed systems [170]), the one-body density matrix is composed of only one natural orbital. Here, all the bosons share the same orbital and the bosonic system can be described by the GP mean-field theory. If the second or more natural orbitals are significantly populated, particle correlations are present in the system, which can be quantified by the *depletion*, $D = \sum_{i>1} a_i = 1 - a_1$.

In order to classify spatial correlations, we integrate out all but one coordinate s of the three-dimensional reduced one-body density operator ρ^{3D},

$$\rho^{(s)} = tr_{\{1,2,3\}\backslash s}\ \rho^{(3D)}, \tag{1.8}$$

denoted by the trace $tr_{\{1,2,3\}\backslash s}$. Similar as above, we can construct one-dimensional "natural" orbitals and "natural" populations $|\beta_i^{(s)}\rangle$ and $b_i^{(s)}$, respectively. The deviations of $b_1^{(s)}$ from unity, namely the depletion, can indicate correlations between the spatial coordinate s and the other two remaining coordinates. If $b_1^{(s)} = 1$ (and thus $b_{i>1}^{(s)} = 0$), two important conclusions can be made. First, the s coordinate can be adiabatically separated from the many-body wave function and, second, that all particles share the same orbital ϕ_s w.r.t. the coordinate s, i.e., $\Psi(\mathbf{r}_1, ..., \mathbf{r}_N) = \prod_{i=1}^{N} \phi(x_i)\Phi(y_1, ..., y_N, z_1, ..., z_N)$.

Next, we want to study coherence properties [171, 172] of the bosonic system described by the one-body density operator. The one-body density matrix, namely the one-body density operator given in position space representation, can be normalized in order to obtain the one-body correlation function $g_1(\mathbf{r}, \mathbf{r}')$

$$g_1(\mathbf{r}, \mathbf{r}') = \rho^{(3D)}(\mathbf{r}, \mathbf{r}')/\sqrt{\rho(\mathbf{r})\rho(\mathbf{r}')}. \tag{1.9}$$

where $\rho(\mathbf{r}) = \rho^{(3D)}(\mathbf{r}, \mathbf{r})$ is the single-particle density. It has the property $|g_1(\mathbf{r}, \mathbf{r}')| \leq 1$ and describes the degree of coherence of particles distributed in space. Complete (spatial) coherence

is implied by $|g_1(\mathbf{r}, \mathbf{r}')| = 1$ for all positions $\mathbf{r}$ and $\mathbf{r}'$. The length scale on which the off-diagonal terms of the one-body density matrix significantly differ from one is defined as the coherence length ξ_C. Beyond ξ_C, the condensation of the bosonic system is destroyed [170, 173]. ξ_C gives the length scale on which an atom is smeared out in space.

Furthermore, these mentioned natural populations give a clue about the convergence of our numerical simulation. A necessary condition for convergence is that the highest natural orbital must be sufficient small, even though this condition is not sufficient. In order to judge convergence, a more sophisticated convergence analysis has to be performed (see chapter 4 and the following chapters).

1.5. Structure of the thesis

This thesis is structures as follows: In chapter 2, a short review of two particles scattering at low energies is given, focusing on the solution for different three-dimensional interaction potentials. Thereby, we give a connection between the interaction potentials parameters and the physical zero-energy scattering length. The results from this chapter are needed throughout the following parts of the thesis. In chapter 3, we continue by analysing the numerical applicability of these three-dimensional interaction potentials w.r.t. an efficient numerical implementation within the framework of the MCTDHB algorithm. In doing so, we determine the most suitable interaction potential for our purpose. In order to implement the interaction potential efficiently, we come up with the idea of introducing an additional layer in the MCTDHB algorithm. In chapter 4, we derive the special equations of motion and give details of the concrete implementation of the interaction potential. These equations of motions form a coupled set of first-order integro-differential equations. We discuss the efficient implementation as well as the convergence behaviour. In chapter 5, the first numerical study on the crossover from three to one dimension is executed for the case of two bosons in elongated traps. Afterwards in chapter 6, we study the tunnelling dynamics of an interacting bosonic ensemble in an initial tilted double well, and analyse features, such as the density profile, in dependence on the transversal confinement. Furthermore, we study spatial and particle correlations. In chapter 7, an initially displaced bosonic ensemble scatters off a barrier. The study is similar to the double well scenario, but with higher initial energies, in order to allow for an energy transfer between the longitudinal and transversal dimensions. After describing the physics of these systems, we give a summary in chapter 8, and we end with an outlook of further interesting scenarios in chapter 9.

CHAPTER

TWO

SCATTERING THEORY

Particle interactions are important in order to properly describe a bosonic ensemble, and due to the interaction new (counter-intuitive) effects can arise, as we have seen in the introduction, for example the compensation of dispersion for a free BEC, leading to stable solitons or novel phenomena such as fermionization if the interaction strength between the particles goes to infinity. Therefore, it is worth to have a closer look at the interactions between the particles in a condensate in more detail.

In the following, we briefly review the physics of two particle interactions. The density of dilute BECs is normally seven orders in magnitude smaller than for air ($\rho_{air} \sim 10^{19} cm_{-3}$). Due to the strong diluteness, the mean-particle distance, $\bar{l} = \rho^{-1/3}$, is much larger than the range of the interaction potential Σ, and three-body interactions can be neglected. Usually, the interaction between two neutral alkali-atoms is described by the Van-der-Waals interaction, which consists of a repulsive and an attractive part. Having a closer look at the Van-der-Waals interaction potential, we can divide it into three spatial regions w.r.t. the relative distance between two bosons r (see figure 2.1): In region (A) the interaction is purely repulsive, which is caused by both the atomic core and the centrifugal barrier. Its natural length scale l_{core} is of the order of the Bohr radius i.e., some hundred pico meters large (see table 2.1). Region (B) is mainly attractive. This attractive part is created, due to an induced electrical dipole-dipole interaction between the alkali-atoms and described by α/r^6, where α is the strength of the attractive part. In order to estimate the length scale of the attractive potential Σ, we equate the kinetic energy $\hbar^2/(2\mu\Sigma^2)$ with α/Σ^6 leading to $\Sigma \sim (\alpha\mu/\hbar^2)^{1/4}$ where μ is the reduced mass. The length scale Σ is naturally of the order of some nano meters (see table 2.1). The interaction potential created by both the repulsive part and the attractive part is called the Van-der-Waals interaction potential $U_{VdW}(r)$. Region (C) is the remaining part, where the interaction potential is set to zero. Since the mean-particle distance $\bar{l}$, which is of the order of micro meters, is much larger than the length of the Van-der-Waals potential Σ, the Van-der-Waals potential can be modelled as a (zero- or) short-range interaction potential. Having a short-range interaction potential, only the far-field scattering solution is of interest.

The far-field solution is an outgoing spherical wave [see equation (2.4)], with energy dependent scattering amplitude, causing a phase shift of the outgoing spherical wave. For ultracold collisions, the scattering amplitude can be approximated by a single parameter, the zero-energy scattering length a_0. The zero-energy scattering length describes the interactions between two particles completely and can be tuned from very attractive towards very strong repulsive scattering lengths via virtual excitations, the so called Feshbach resonances [13], by changing internal states of the atom with an external magnetic field.

One well established method in theoretical physics is the replacement of the interatomic potential by some simpler model potential which delivers computational advantage and produces the same phase shift of the outgoing spherical wave in the far field. These simpler model potentials can be divided into two groups: (i) finite-range interaction potentials such as the hard or soft wall interaction potential or (ii) zero-range interaction potentials such as the bare or regularized[1] delta interaction potential. In chapter 3, we show that zero-range interaction potentials cannot be used for numerical simulations in three dimensions within the framework of the MCTDHB method (see chapter 4).

In experimental setups, the condensates have to be trapped and thus an additional length scale emerges, the characteristic lengths scale of the trap, $l_{trap} = \sqrt{\hbar/m\omega}$, with the trap frequency ω. Characteristic length scales for various traps are given in table 2.1. The influence of the trap on the zero-energy scattering length has been studied by several authors and a breakdown of the validity for a short-range interaction potential has been found at $a_0 \sim l_{trap}$ [175–179]. As we will show in section 5.1, our results are in agreement with the limitation. In order to study systems with arbitrary trap geometry, or in other words to neglect the influence of the trap, one has to operate in the regime of $a_0 \ll l_{trap}$ or even better $\Sigma \ll l_{trap}$ [177].

In this dissertation, we want to operate in the latter mentioned regime, and once calculated the zero-energy scattering length in dependence of the parameters of the interaction potential in free space, the zero-energy scattering length can be applied to various trap geometries, e.g. a double well (see chapter 6) or for a local barrier (see section 7). In order to calculate the zero-energy scattering length in dependence of the trap geometry, advanced theories such as the Quantum Defect Theory [180–182] have to be used.
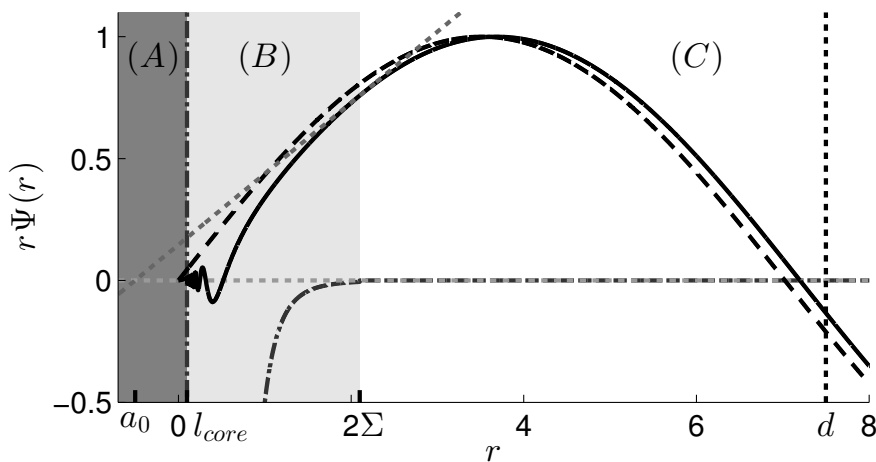
Figure 2.1.: The amplitude of the wave function of a particle in a Van-der-Waals potential (dark grey dash-dotted line) is sketched exemplary (black solid line). The Van-der-Waals potential is composed of the repulsive part [dark grey region (A)] of range l_{core} and attractive part [light grey region (B)] with range Σ. In region (C), the interaction potential is set to zero. For comparison, a non-interacting wave function is plotted (black dashed line) as well. The phase shift between the two wave functions can be calculated using the contact condition at a single point $r = d$ [see equation (2.10)], marked by a dotted black line. The light grey dashed line represents $\chi_{k=0}^{\infty}(r)$, which is the wave function at zero energy in the far field. For zero energy, the zero-energy scattering length can be determined graphically by determine the intersection of the wave function $\chi_{k=0}^{\infty}(r)$ with the abscissa.

The remainder of this chapter is structured as follows: First a short review of the framework

---

[1]The regularized delta-interaction potential as described by Fermi [174] and Huang [94] ensures the right boundary conditions for $r \to 0$ in three dimensions.

Table 2.1.: Different characteristic length scales for a BEC of different alkali earth metals in units of the Bohr radius $a_{Bohr} \simeq 0.529 \, 10^{-10} m$. Shown are the size of the hard core l_{core}, the size of the interaction potential Σ, the inter particle distance $\bar{l}$ and the characteristic trap length l_{trap} used in characteristic experiments. Values are taken from [183].

Elements	$l_{core}[a_{Bohr}]$	$\Sigma[a_{Bohr}]$	$\bar{l}\,[a_{Bohr}]$	$l_{trap}\,[a_{Bohr}]$
Li-Li	2.7	64.7	$41\dot{1}0^3$	$140\dot{1}0^3$
Na-Na	3.4	89.9	$4\dot{1}0^3$	$35\dot{1}0^3$
K-K	4.2	129.1	$41\dot{1}0^3$	$53\dot{1}0^3$
Rb-Rb	4.4	164.4	$18\dot{1}0^3$	$47\dot{1}0^3$
Cs-Cs	5.0	201.8	$18\dot{1}0^3$	$26\dot{1}0^3$

of three-dimensional scattering theory is given in section 2.1. The limit of zero energy scattering is discussed in section 2.2. Then, in section 2.3, the zero-energy scattering length for different model potentials is calculated. Section 2.4 ends with a discussion of the tunability of the zero-energy scattering length for different interaction potentials.

2.1. Review of the scattering theory

In this section, the elastic scattering between two particles in free space is briefly reviewed. A more detailed discussion can be found in text books such as [20, 184–188].

Usually, binary interaction potentials depend only on the relative distance between two particles at position $\mathbf{r}_1$ and $\mathbf{r}_2$, respectively, $W(\mathbf{r}_1, \mathbf{r}_2) = W(r)$, with $|\mathbf{r}_1 - \mathbf{r}_2| = r$, and therefore, the stationary Schrödinger equation separates into relative $\mathbf{r} = \mathbf{r}_2 - \mathbf{r}_1$ and centre of mass $\mathbf{R} = (\mathbf{r}_2 + \mathbf{r}_1)/2$ coordinates. For two particles, with equal mass m, the separated Schrödinger equation reads

$$\left(-\frac{\hbar^2}{2M} \nabla_{\mathbf{R}}^2 - E_{CM} \right) \phi_{CM}(\mathbf{R}) = 0 \tag{2.1}$$

$$\left(-\frac{\hbar^2}{2\mu} \nabla_{\mathbf{r}}^2 + W(r) - E_{\mathbf{k}} \right) \phi_{\mathbf{k}}(\mathbf{r}) = 0 \tag{2.2}$$

where $M = 2m$ is the total mass and $\mu = m/2$ is the reduced mass. The solution for the centre of mass (CM) are just a plain waves. The formal solution for the relative coordinate, $\phi_{\mathbf{k}}(\mathbf{r})$, is given by the Lippmann-Schwinger equation for a particle with energy $E_{\mathbf{k}} = \hbar^2 \mathbf{k}^2/2\mu$

$$\phi_{\mathbf{k}}(\mathbf{r}) = e^{\pm i\mathbf{k}\mathbf{r}} - \frac{2\mu}{\hbar^2} \int d^3\mathbf{r}' G(|\mathbf{r} - \mathbf{r}'|) W(r') \phi_{\mathbf{k}}(\mathbf{r}') \tag{2.3}$$

with the Green's function $G(x) = -\exp(\pm ikx)/4\pi x$, where $k = |\mathbf{k}| = \sqrt{2\mu E_{\mathbf{k}}/\hbar^2}$ has been used. As already stated, we are mainly interested in the far-field solution, $r' \ll r$ and therefore the Green's function can be approximated by $G(|\mathbf{r} - \mathbf{r}'|) \simeq \exp(\mp ikr' \cos\theta) \exp(\pm ikr)/r$ [185], where θ is the angle between $\mathbf{r}$ and $\mathbf{r}'$, leading to

$$\phi_{\mathbf{k}}(\mathbf{r}) = e^{i\mathbf{k}\mathbf{r}} + f(k, \theta) \frac{\pm e^{ikr}}{r} \tag{2.4}$$

with the scattering amplitude

$$f(k, \theta) = -\frac{\mu}{2\pi\hbar^2} \int d^3\mathbf{r}' e^{-ikr' \cos\theta} W(r') \phi_k(\mathbf{r}'). \tag{2.5}$$

Regarding only elastic scattering processes, the scattering amplitude is just a function of the initial energy $\sim k^2$ as well as the deflection angle θ and can be expanded into partial waves [184, 185]

$$f(k, \theta) = \sum_{l=0}^{\infty} (2l + 1) f_l(k) P_l(\cos \theta) \tag{2.6}$$

with the Legendre polynomials $P_l(\theta)$ and partial scattering amplitude $f_l(k)$, depending on the angular momentum quantum number and initial energy[2].

In the following an alternative framework is set up in order to describe two particle interactions. We proceed as before by separating the two-particle Schrödinger equation into a centre of mass and a relative part [see equations (2.1) and (2.2)]. In general, the relative wave function can be expressed as a sum over partial waves, $\phi_{\mathbf{k}}(r) \sim \sum_{l=0}^{\infty} P_l(\cos \theta) \chi_{lk}(r)$, where

$$\chi_{kl}(r) = c_1 j_l(kr) - c_2 n_l(kr) \tag{2.7}$$

is a superposition of the spherical Bessel j_l and Neumann function n_l (see appendix B.1), and $\chi_{kl}(r)$ solves the differential equation

$$\left(-\left[\frac{1}{r^2} \partial r \left(r^2 \partial r \right) - \frac{l(l+1)}{r^2} \right] + \frac{2\mu}{\hbar^2} W(r) - k^2 \right) \chi_{kl}(r) = 0. \tag{2.8}$$

In the far field, the (short-range) interaction potential W is zero, and the scattering solution (2.7) can be written by inserting the asymptotic expressions of the spherical Bessel and Neumann functions (see appendix B.1). For the coefficients c_1 as well as c_2, we use the expression $c_1 = \cos \delta_l(k)$ as well as $c_2 = \sin \delta_l(k)$ in order to fulfil automatically the normalization condition of χ_{kl}. By using the angle addition theorem, the resulting expression reads

$$\chi_{kl}^{\infty}(r) = \frac{\sin(kr - \frac{l\pi}{2} + \delta_l(k))}{kr}. \tag{2.9}$$

Equation (2.9) describes an outgoing spherical wave, where the phase is shifted by $\delta_l(k)$. The phase shift $\delta_l(k)$ can be determined by sticking the asymptotic wave function $\chi_{kl}^{\infty}(r)$ to the true solution $\chi_{lk}(r)$ at a fixed but arbitrary point d, which must be far away w.r.t. the size of the interaction potential, $d \gg \Sigma$. Usually, $\chi_{lk}(r)$ has to be determined numerically (see section 2.3.4) but for special interaction potentials, such as the soft and hard wall interaction potentials, an analytic solution is known (see section 2.3.3). By matching the two wave functions together, the contact condition has to be ensured

$$\left. \frac{\partial_r \chi_{lk}^{\infty}}{\chi_{lk}^{\infty}} \right|_{r=d} = \left. \frac{\partial_r \chi_{lk}}{\chi_{lk}} \right|_{r=d} \equiv B(k). \tag{2.10}$$

Using equation (2.9), the upper equation can be solved for $\delta_l(k)$

$$\cot \delta_l(k) = \frac{[B(k) + \frac{1}{d}] \cot(kd - \frac{l\pi}{2}) + k}{k \cot(kd - \frac{l\pi}{2}) - [B(k) + \frac{1}{d}]}. \tag{2.11}$$

In order to relate the scattering amplitude with the phase shift, we insert equation (2.6) into equation (2.4) and express the result into partial waves. A comparison with (2.9) leads then to

$$f_l(k) = \frac{1}{k \cot(\delta_l(k)) - ik} \tag{2.12}$$

---

[2] The Legendre polynomials $P_l(\theta)$ as well as the factor $(2l + 1)$ originates by using the addition theorem for the spherical harmonics.

2.2. Low-energy and zero-energy scattering limit

The collision energy in ultracold gases is low, and therefore, the wave length of the relative scattering particle is the largest length scale in the system ($\sim 1/k$). The wave function cannot "resolve" the concrete structure of the interaction potential anymore and the interaction potential can be regarded as short-ranged in comparison to the wave length, for $k\Sigma \ll 1$. In order to find an approximation for the scattering amplitude $f_l(k)$ in dependence of the wave length [189], the wave functions $\phi_{\mathbf{k}}(\mathbf{r})$ in the integral (2.5) can be decomposed into partial waves. Due to the effectively short-range interaction potential, the support of the integral (2.5) is limited and the inserted partial waves can be approximated through Bessel functions in the limit $r \to 0$ (see appendix B.1). One obtains for the partial scattering amplitudes the following energy dependence

$$f_l \sim k^{2l}. \tag{2.13}$$

In the following discussion, we focus on very small scattering energies, where only the $l = 0$ term contributes to the scattering amplitude. Such scattering events are named *s-wave scattering*. In order to define s-wave scattering, another line of arguments can be given: For small energies $kr \ll 1$, the centrifugal barrier $l(l+1)/r^2$ in equation (2.8) is so strong that the wave function cannot "penetrate" through and the original interaction potential W is shielded by the centrifugal barrier. The wave function gets a trivial phase shift of $\frac{\pi}{2}l$ in the far-field. Only for $l = 0$, wave function feels the interaction potential and acquires the non-trivial phase shift $\delta_0(k)$

Apart for resonances, the $\cot(\delta_0(k))$ can be expanded for small energies leading to [190]

$$\cot(\delta_0(k)) = \frac{1}{a_0 k} + \frac{1}{2}r_0 k + \dots. \tag{2.14}$$

with the *zero-energy scattering length* $a_0^{-1} \equiv \lim_{k\to 0} k\cot(\delta_0(k))$ and the effective range $r_0 \equiv 2\partial_k \cot(\delta_0(k))|_{k=0}$. The partial scattering amplitude (2.12) is then

$$f_0(k) \equiv a(k) \simeq \frac{1}{\frac{1}{a_0} + \frac{1}{2}r_0 k^2 - ik} \tag{2.15}$$

with the energy dependent scattering length $a(k)$. By taking the zero-energy limit of expression (2.15), we get the zero-energy scattering length again

$$a_0 = \lim_{k\to 0} f_0(k) \tag{2.16}$$

Finally, we note that one can directly perform the zero-energy limit of the Schrödinger equation (2.8) by directly setting $k = 0$. Then, the far field solution is $\chi_{k=0}^{\infty}(r) = 1 - c/r$ with the constant c. By comparing $\chi_{k=0}^{\infty}(r)$ with equation (2.4), the constant c can be determined to be the zero-energy scattering length, $c = a_0$. For zero energy, the zero-energy scattering length can be determined graphically (see figure 2.1) by determining the intersection of the wave function with the abscissa $\chi_{k=0}^{\infty}(r) = 0 \Longleftrightarrow r = a_0$.

2.3. Calculation of the zero-energy scattering length for various interaction potentials

In this section, we analytically derive (if possible) expressions for the zero-energy scattering length for different interaction potentials: the bare delta interaction (section 2.3.1), the regularized delta interaction (section 2.3.2) as well as hard and soft wall interaction potentials (section 2.3.3). In the last section 2.3.4, a numerical algorithm is presented, which determines the zero-energy scattering length for arbitrary interaction potentials.

2.3.1. Bare delta interaction potential

The bare delta interaction potential leads to no scattering in three dimensions. We give a proof of this statement, following the lines of reference [191]. Additionally, further proofs are given in section 3.1.1 or in the appendix B.2.

The Lippmann-Schwinger equation (2.3) can be analytically solved for the bare delta interaction potential $W(\mathbf{r}) = g\delta(r)\delta(\theta)\delta(\varphi)/r^2 \sin\theta$ with the interaction strength g

$$\phi_k(\mathbf{r}) = \frac{e^{i\mathbf{kr}}}{1 - gG(r)}$$

where G is the Green's function. For $r = 0$, the Green's function diverges and one obtains $\phi_k(\mathbf{r} = 0) = 0$. But solving (2.3) with the constraint $\phi_k(\mathbf{r} = 0) = 0$ reveals $\phi_k(\mathbf{r}) = 1$, which does not fulfil the constraint $\phi_k(\mathbf{r} = 0) = 0$. Concluding, the bare delta interaction potential leads to an ill-defined scattering process in three dimensions, in contrast to one-dimensional problems, where the bare delta interaction can be used successfully. To achieve non-trivial scattering, the bare delta interaction potential has to be regularized, in order to include the right boundary condition at $r = 0$.

2.3.2. Regularized delta interaction potential

The regularization of the bare delta interaction potential, invented by Fermi [174], takes the appropriated boundary condition $r \to 0$ into account and reproduces the correct scattering behaviour in the far field. Furthermore, it allows a direct link between the interaction strength g and the zero-energy scattering length a_0. The regularized delta interaction potential can be derived in different ways, e.g. by ensuring the right boundary conditions at $r = 0$ [94, 192], by letting either the diameter of a hard-sphere interaction potential [193] or the size of a delta shell interaction potential [194] tends towards zero, by using the rigorous framework of distribution theory [195], or by applying the Hadamard finite part regularization [196, 197]. We regard only scattering processes for low enough energy, the so called s-wave scattering. For the s-wave scattering, the spherical momentum quantum number l is zero and the regularized delta interaction potential is then given by (see references [94, 192])

$$g\delta(\mathbf{r})\frac{\partial}{\partial r}r \tag{2.17}$$

where g is the interaction strength. We see that the regularization operator $\frac{\partial}{\partial r}r$ regularizes the $1/r$ divergence occurring in the three-dimensional wave function $\chi_{k0}(\mathbf{r})$ [see equation (2.9)]. Following the lines of reference [188], the scattering amplitude for the regularized delta interaction potential can be calculated by inserting equation (2.17) into equation (2.3).

$$\phi_{\mathbf{k}}(\mathbf{r}) = e^{-i\mathbf{kr}} - C\frac{e^{-i\mathbf{kr}}}{r} \tag{2.18}$$

with

$$C = \frac{\mu g}{2\pi\hbar^2}\left[\frac{\partial}{\partial r'}r'\phi_{\mathbf{k}}(\mathbf{r}')\right]_{r'=0} \tag{2.19}$$

First, multiplying equation (2.18) by r, second differentiating it w.r.t. r and last taking the limit $\lim_{r\to 0}$ for both sides of equation (2.18), we obtain

$$C = 1 - aCik \qquad \Longleftrightarrow \qquad C = \frac{a}{1 + ika}. \tag{2.20}$$

The scattering solution (2.18) is then

$$\phi_{\mathbf{k}}(\mathbf{r}) = e^{-i\mathbf{k}\mathbf{r}} - \frac{a}{1+ika}\frac{e^{-i\mathbf{k}\mathbf{r}}}{r}. \tag{2.21}$$

Comparison with equation (2.4) gives the scattering amplitude as well as the partial scattering amplitude

$$f(k) = f_0(k) = -\frac{a}{1+ika} \tag{2.22}$$

and the phase shift can be determined via equation (2.12). In order to derive a relation between the zero-energy scattering length a_0 and the interaction strength g, we perform the zero-energy limit $k \to 0$ on both sides of equation (2.19), leading to

$$g = \frac{2\pi\hbar^2}{\mu}a_0 \tag{2.23}$$

2.3.3. Soft-wall and hard-wall interaction potentials

For the soft as well as the hard wall interaction potential, $W_S(r) = g\Theta(r - \Sigma)$ and $W_H(r) = \lim_{g\to\infty} g\Theta(r - \Sigma)$, respectively, analytical solution of the wave function $\chi_{kl}(r)$ can be found in the area $r < \Sigma$ [185–187]. Here, g is the height of the soft wall interaction potential. The wave function $\chi_{kl}(r)$ can be linked to the far field solution using equation (2.10) and the phase shift as well as the scattering amplitude can be obtained. In doing so, B is determined at $r = \Sigma$ leading to $B = \kappa \cot(\kappa\Sigma - \frac{l\pi}{2})$, with $\kappa = \sqrt{2\mu(E - g)/\hbar^2}$ and the initial energy $E = \hbar^2\mathbf{k}^2/2\mu$. Inserting the expression for B in equation (2.11) and regarding only s-wave scattering, we obtain

$$\cot(\delta_0) = \begin{cases} \frac{\kappa\cot(\kappa\Sigma)\cot(k\Sigma)+k}{k\cot(k\Sigma)-\kappa\cot(\kappa\Sigma)} & \text{for} \quad E > g \\[2mm] \frac{\kappa\coth(\kappa\Sigma)\cot(k\Sigma)+k}{k\cot(k\Sigma)-\kappa\coth(\kappa\Sigma)} & \text{for} \quad E < g \end{cases} \tag{2.24}$$

In the special case of hard wall interaction potential $g \to \infty$, the phase shift is proportional to the size of the interaction potential $\cot\delta = 1/k\Sigma$ and in the zero-energy limit, the zero-energy scattering length (2.16) is equal to the size of the interaction potential Σ

$$\lim_{k\to 0} f_0(k) = \Sigma = a_0 \tag{2.25}$$

where we have used equation (2.12).

2.3.4. General interaction potentials

Usually, equation (2.8) cannot be analytically solved for general interaction potentials and $\chi_{kl}(r)$ has to be determined numerically. Equation (2.8) can be simplified using the transformation $\chi_{kl}(r) = u_{kl}(r)/r$, but in doing so, attention must be paid, since the Laplace operator induces a singular behaviour at $r = 0$ [198, 199]. In order to avoid the singularity, we set $\chi_{kl}(r)\,r|_{r=0} = 0$ and hence get the boundary condition $u(0) = 0$. This boundary condition can be motivated with that the scattering atoms have an impenetrable core and the relative wave function has to drop to zero at $r = 0$ (see also appendix B.2 for a mathematical motivation). The radial part of the relative wave function reads then

$$\left[\frac{1}{2}\frac{d^2}{dr^2} - \frac{2\mu}{\hbar^2}W(r) + k^2\right]u(r) = 0 \tag{2.26}$$
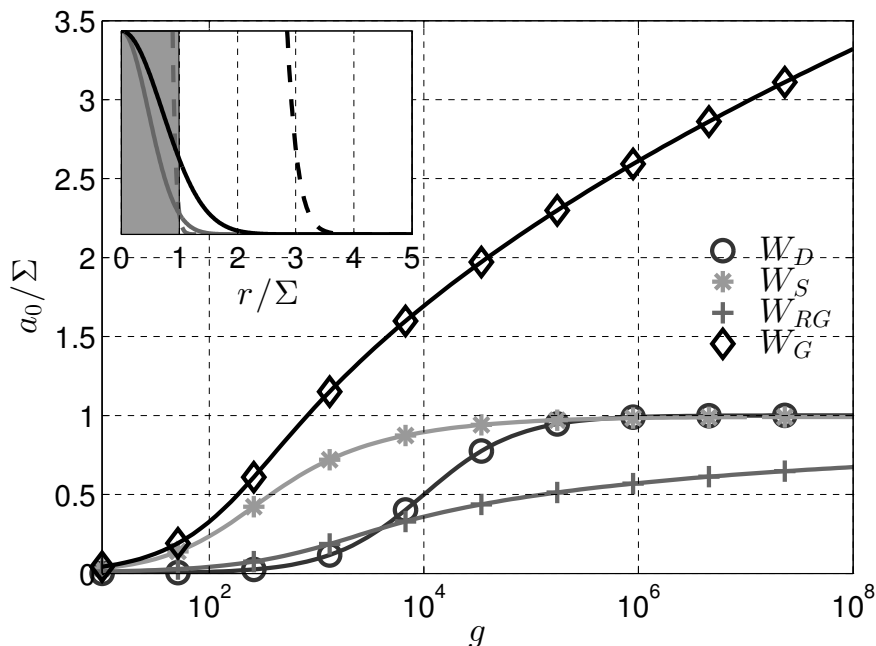
Figure 2.2.: Shown is the zero-energy scattering length for different interaction potentials: The soft wall interaction potential $W_S(r) = g\Theta(r - \Sigma)$ (asterisk), the delta shell interaction potential $W_D(r) = g\delta(\Sigma - |\mathbf{r}|)$ (circles), the Gaussian interaction potential $W_G(r) = g\exp(r^2/\Sigma^2)$ (diamonds) and the renormalized Gaussian interaction potential $W_{RG}(r) = g\exp(r^2/\sigma^2)$ in dependence of the interaction strength g. Please note the logarithmic scaling of the x-axis. The inset shows the shape of different interaction potentials for the two different interaction strength $g = 10$ (grey) and $g = 2000$ (black): $W_S(r)$ (shaded area), $W_G(r)$ (dashed lines) and W_{RG} (solid lines). Figure is taken from [[1]].

which can be solved numerically, e.g. using Numerov's method [200]. Knowing $\chi_{kl}(r)$, the parameter B [see equation (2.10)], the phase shift [see equation (2.11)], the scattering amplitude [see equation (2.12)], the scattering length [see equation (2.15)] and the zero-energy scattering length [see equation (2.16)] can be determined.

In order to illustrate the behaviour of the zero-energy scattering length a_0 in dependence on the interaction strength g, we numerically solve equation (2.26) for the following four interaction potentials and show the results in figure 2.2:

1. Soft wall interaction potential $W_S(r) = g\Theta(r - \Sigma)$:
   The zero-energy scattering for the soft wall interaction potential reaches an upper bound at $a_0 = \Sigma$ for $g \to \infty$, as expected from the analytical calculation (see equation (2.25)).

2. Delta shell interaction potential $W_D(r) = g\delta(\Sigma - |\mathbf{r}|)$:
   The zero-energy scattering length for the delta shell interaction potential reaches an upper bound for larger interaction strengths, $a_0 = \Sigma$ for $g \to \infty$. An infinite strong delta potential causes a node in the wave function at Σ and thus the zero-energy scattering length has the same size.

3. The Gaussian interaction potential $W_G(r) = g\exp(r^2/\Sigma^2)$:
   By increasing g and keeping Σ fixed, the zero-energy scattering length of the Gaussian interaction potential increases unlimited (see the inset of figure 2.2), since the effective width of the Gaussian interaction potential increases unlimited as well, $\propto \sqrt{g}$ and may violate other length scales in the system. We like to note that the effective width of the Gaussian interaction potential may destroy the condition for short-range interaction

potentials.

4. The renormalized Gaussian interaction potential $W_{RG}(r) = g \exp(r^2/\sigma_{\text{eff}}^2)$:
   The renormalized Gaussian interaction potential is renormalized so that the effective width of the Gaussian is independent of g, $W_{RG}(r = \Sigma) = \epsilon$, where ϵ is a small and arbitrary energy scale of the system. In doing so σ_{eff} can be calculated, $\sigma_{eff} = \Sigma[\ln(g/\epsilon)]^{-1/2}$. The renormalized Gaussian interaction potential unifies two advantageous features, which are extremely helpful in order to perform numerical simulations in three dimensions (see chapter 3 and 4). The first one is that $W_{RG}(r)$ is restricted on the range Σ, like the soft wall interaction potential. This can be seen by regarding the limit $g \to \infty$ (graphically shown in the inset of figure 2.2):

$$\lim_{g \to \infty} W_{RG}(r) = \begin{cases} \infty & |r| < |\Sigma| \\ \epsilon & |r| = |\Sigma| \\ 0 & |r| > |\Sigma| \end{cases} \overset{(\epsilon = 1)}{=} \lim_{g \to \infty} W_T(r) \tag{2.27}$$

The restriction of the width helps to avoid the penetration of other length scales appearing in the system, and the zero-energy scattering length reaches an upper bound at $a_0 = \Sigma$ for infinite interaction strength. The second advantage is that $W_{RG}(r)$ is separable into the dimensions, like the standard Gaussian interaction potential, which is extremely helpful for an efficient numerical implementation (as we will see in chapter 3 and 4).

2.4. Tunability of the interaction potentials

The maximal zero-energy scattering length is limited to $a_0 \leq \Sigma$ for an arbitrary, but purely repulsive short-range interaction potentials $W_A(r)$; $W_A(r) > 0$ for $r \leq \Sigma$ and $W_A(r) = 0$ for $r > \Sigma$. To proof this statement, we approximate $W_A(r)$ into a sum of theta functions $W_A(r) \simeq \sum_{i=1}^{I_{max}}[\Theta(r - i\Delta) - \Theta(r - (i-1)\Delta)]g_i$ with $\Delta = \Sigma/I_{max}$ and $g_i = W_A(i\Delta)$. For $I_{max} = \infty$ the interaction potential $W_A(r)$ is recovered, but numerically I_{max} can be arbitrary large but must be finite. Performing the limit of infinite interaction strength i.e. $g_i \to \infty$, we can separate the $i = I_{max}$ term from the remainder of the sum, leading a hard wall interaction potential $W_A(r) \simeq \lim_{g_{I_{max}} \to \infty} \Theta(r - \sigma) + remainder$. This hard wall interaction potential is responsible for the limitation of the zero-energy scattering length, $a_0 \leq \Sigma$, as seen in section 2.3.4

Larger scattering lengths can be created in three different ways:

i. If a bound state is close to the threshold of the incoming energy, scattering resonances occur. As much as we know, there is no combination of pure repulsive interaction potentials, which causes a similar resonant scattering behaviour.

ii. If the bound state of an internal closed scattering channel (occurring for $l > 0$ or taking the electronic structure of the atom into account) is near to the threshold of the incoming energy, resonances, i.e., divergences in the scattering length, can be observed [13]. Such resonances are called Fano-Feshbach and by experimentally tuning external magnetic fields, the levels of the closed channels can be shifted and arbitrary scattering length can be obtained, both negative and positive. Neglecting the electronic structure of the scattering atom and taking only s-wave scattering into account, as we do in this thesis, Fano-Feshbach do not occur.

iii. If the scattering occurs in a strong transversal confinement, virtual transversal modes can be excited, leading to confinement induced resonances [96, 97]. For example, in the case of a harmonic wave guide, one can sum over these transversal modes, leading to a

modification in the scattering length [96]

$$a_{1D} = -\frac{l_\perp^2}{2a_0}\left(1 - C\frac{a_0}{l_\perp}\right) \qquad (2.28)$$

with the characteristic transversal trap length $l_\perp = \sqrt{\hbar/\omega_\perp\mu}$, where $\omega_\perp$ is the harmonic transversal trap frequency, C is a numerical factor $C = 1.4602...$ and a_0 is the three-dimensional zero-energy scattering length.

Part I.

Development of an efficient algorithm

EFFICIENT NUMERICAL MODEL FOR THE TWO-BODY INTERACTION POTENTIAL

Due to the complexity w.r.t. the many degrees of freedom of an interacting bosonic ensemble in three dimensions, it is as good as impossible to solve the time-dependent many-particle Schrödinger equation analytically. However, analytic solutions can be found, e.g., for two bosons in an isotropic (anisotropic) harmonic trap with the regularized delta interaction potential [201] ([202]) or many particles interacting with the harmonic interaction potential [203–207]. However, the harmonic interaction potential is unphysical, due to its boundary conditions at infinity. In general, bosonic ensembles interacting with realistic interaction potentials have to be solved numerically.

Because of the freedom to choose the special shape of a short-range interaction potential in the zero-energy limit (see chapter 2 and reference [177]), various interaction potentials can be created and used. A list of possible interaction potentials is given in table 3.1. All of these interaction potentials depend on a global interaction strength[1] h and on a parameter σ corresponding to the width of the interaction potential. The connection between the parameters h and σ of the interaction potential and the physical measurable zero-energy scattering length a_0 can be obtained by solving the scattering problem in three dimensions (see section 2.3.4).

In this chapter, we address the questions, what is the preferable interaction potential for numerical application and which special mathematical features of the interaction potential can be used in order to simplify the numerical effort. These questions have been already shortly answered in our publication [[1]]. First, three-dimensional zero-range interaction potentials such as the bare delta interaction (section 3.1.1), the regularized delta interaction (section 3.1.2) and the bare delta interaction with a renormalized interaction strength (section 3.1.3) are discussed w.r.t. the possibility to resolve correlations and a feasible numerical implementation. We find that none of these zero-range interaction potentials can be used properly for an "correct" numerical simulation with the ML-MCTDHB method, working within a single particle basis in the laboratory frame and taking particle correlations into account[2]. However, the bare delta interaction potential is fine for mean-field calculations and the regularized delta interaction can be used correctly if a correlated two particle basis is used. Concluding, we have to use finite-range interaction potentials, which introduce a new length scale to the system. This new length scale

---

[1]For finite interaction potentials, we call the interaction strength g also interaction height and label it with h.

[2] Already here, we comment on a constraint given by the numerical ML-MCTDHB method. The ML-MCTDHB algorithm implies the language of second quantization, in order to represent an ensemble of bosons, which restricts the implementation to a formulation in the laboratory frame. Therefore, we look for interaction potentials with nice mathematical and numerical features in the laboratory frame.

Table 3.1.: Examples of possible interaction potentials.

Gaussian interaction potential	$W_G(\mathbf{r}) = h \exp(-\mathbf{r}^2/\sigma^2)$
Cosh interaction potential	$W_S(\mathbf{r}) = h/\cosh(|\mathbf{r}|/\sigma)$
Lorentz interaction potential	$W_L(\mathbf{r}) = h/(1 + \mathbf{r}^2/\sigma^2)$
Exponential potential	$W_E(\mathbf{r}) = h \exp(-|\mathbf{r}|/\sigma)$
Theta interaction potential	$W_T(\mathbf{r}) = h\Theta(\sigma - |\mathbf{r}|)$
Delta interaction potential	$W_D(\mathbf{r}) = h\delta(\sigma - |\mathbf{r}|)$
Fermi interaction potential	$W_F(\mathbf{r}) = h/(\exp(|\mathbf{r}| - \sigma) + 1)$

is some orders of magnitudes smaller than other characteristic length scales in the system (see table 2.1) and has to be resolved numerically. In section 3.2, we look for a short-range interaction potential, which is most handy for a numerical implementation within the ML-MCTDHB algorithm. Finally, in section 3.3, we give a summary of the main outcome of this chapter: The most suitable short-range interaction potential for our propose is a renormalized Gaussian interaction potential, which we have already met in section 2.3.4.

3.1. Zero-range interactions potentials

The main advantage of zero-range interaction potentials is that the length scale of the interaction does not have to be resolved numerically and thus less grid points are needed, leading to a huge reduction of the computational effort. Furthermore, a possible interference of the interaction length with the characteristic trap lengths, important in the crossover from three towards one dimension, does not have to be considered and the scattering can be regarded as taking place in free space. The simplest zero-range interaction potential is the bare delta interaction operator (in position space representation)

$$g\delta(\mathbf{r}) \tag{3.1}$$

where $\mathbf{r} = \mathbf{r_2} - \mathbf{r_1}$ is the relative position vector of two colliding particles, with length $|\mathbf{r}| = r$ and g is the interaction strength for the bare delta interaction. The interaction strength can be related to the zero-energy scattering a_0 length by $g = 2\pi\hbar^2/\mu a_0$, where μ is the reduced mass (see section 2.3.2). Because in some cases, a_0 can be experimentally tuned from minus towards plus infinity via a Feshbach resonance, the interaction range extends to the same infinite interval.

As we have already seen in section 2.3.1, the bare delta interaction $g\delta(\mathbf{r})$ is ill defined in three dimensions and thus cannot describe scattering in three dimensions. To support this crucial statement, a new line of argumentation is given in section 3.1.1 in order to formulate the error caused by the bare delta interaction. Usually, two corrections to the bare delta interaction potential are used. The first one, described in section 3.1.2, is a regularization of the bare delta interaction operator w.r.t. to the boundary condition at $r = 0$. The second, presented in section 3.1.3, is a renormalization of the interaction strength w.r.t. a truncation of the single-particle Hilbert space.

3.1.1. Bare delta interaction potential

In order to support the statement that the bare delta interaction does not properly describe scattering in three dimensions, we give a line of argument, which follows the papers [201,208,209]. In doing so, we make a comparison between $D = 1$ and $D = 3$ dimensions and between particles in free space and trapped in an isotropic harmonic trap.

The relative Schrödinger equation in D dimensions is given by $(H_0 + g\delta - E_{rel})|\phi_{rel}\rangle$, where δ is the bare delta operator and H_0 is the Hamiltonian describing one particle either in free space or trapped in an isotropic harmonic trap. We expand the relative D-dimensional wave function $|\phi_{rel}\rangle = \sum_{\mathbf{i}} c_{\mathbf{i}}|\varphi_{\mathbf{i}}\rangle$ into a complete set of eigenfunctions $H_0|\varphi_{\mathbf{i}}\rangle = \epsilon_{\mathbf{i}}|\varphi_{\mathbf{i}}\rangle$, where all quantum numbers are summarized in $\mathbf{i}$. Projecting onto $\langle\varphi_{\mathbf{j}}|$ leads to

$$c_{\mathbf{j}}(\epsilon_{\mathbf{j}} - E_{rel}) + g\sum_{\mathbf{i}} c_{\mathbf{i}}\langle\varphi_{\mathbf{j}}|\delta|\varphi_{\mathbf{i}}\rangle = 0 \tag{3.2}$$

which can be solved for $c_{\mathbf{j}}$, using the position space representation for the delta operator

$$c_{\mathbf{j}} = \mathcal{A}\frac{\langle\varphi_{\mathbf{j}}|\mathbf{r} = 0\rangle}{\epsilon_{\mathbf{j}} - E_{rel}}, \tag{3.3}$$

where $\mathcal{A} = -g\sum_{\mathbf{i}} c_{\mathbf{i}}\langle\mathbf{r} = 0|\varphi_{\mathbf{i}}\rangle$ is some unknown constant. Inserting equation (3.3) into (3.2), leads to the general equation for the bare delta interaction potential

$$\sum_{\mathbf{i}=0}^{\mathbf{M}=\infty} \frac{\langle\mathbf{r} = 0|\varphi_{\mathbf{i}}\rangle\langle\varphi_{\mathbf{i}}|\mathbf{r} = 0\rangle}{\epsilon_{\mathbf{i}} - E_{rel}} = -\frac{1}{g}, \tag{3.4}$$

where the summation labels a summation over all quantum numbers.

Next, we want to study the validation of this equation w.r.t. dimensionality and apply both plain waves and harmonic oscillator wave functions in D dimensions for the eigenfunctions $|\varphi_{\mathbf{i}}\rangle$.

First, $\langle\mathbf{r}|\varphi_{\mathbf{i}}\rangle$ are $D-$dimensional plain waves with momentum $\mathbf{q}$. The sum in equation (3.4) can be transformed into an integral, $(2\mu/\hbar^2)\int d^D q \frac{1}{\mathbf{q}^2 - \mathbf{k}^2} = -1/g$, where $E_{rel} = \hbar^2 k^2/2\mu$ and $\epsilon_{\mathbf{q}} = \hbar^2\mathbf{q}^2/2\mu$ have been used. In one dimension, this integral is convergent, which justifies the use of the bare delta interaction potential in numerical simulations [88,90,210–214] and analytical calculations [208, 215]. In three dimensions, however, the integral is ultra-violet divergent and the interaction strength has to be zero $g = 0$, otherwise, the equation is ill defined.

Second, using three-dimensional spherical harmonic oscillator wave functions $\langle\mathbf{r}|\varphi_{\mathbf{i}}\rangle$ with the quantum numbers $\mathbf{i} = \{k, l, m\}$ and assuming a symmetrical setup so that $l = 0$, one can also show after some algebra that equation (3.4) is divergent and only meaningful for $g = 0$ (see appendix C.1 for the calculation).

In order to "heal" equation (3.4) from its divergence, one can follow two strategies: The first one is a regularization of the bare delta interaction operator (see section 3.1.2), and the second one is a truncation of the sum in equation (3.4) i.e. a renormalization of the interaction strength (see section 3.1.3) in order to compensate for the truncation. In the following, we have a closer look at these two strategies.

3.1.2. Regularization of the bare delta interaction potential

The first strategy is to regularize the bare delta interaction operator, by incorporating the right boundary conditions at $r = 0$. Roughly speaking, since the wave function is zero at $r = 0$, the Dirichlet boundary condition in three dimensions has no influence on the wave function (see also appendix B.2). However, we can modify the slope of the wave function at $r = 0$ (Neumann boundary condition), in order to create a phase shift in the far-field (see chapter 2). Incorporating the Neumann boundary condition by rewriting the interaction operator leads to an additional term $\partial_r r$, named, the regularization operator [94,192]. The regularized interaction potential reads in position space representation

$$g\delta(\mathbf{r})\partial_r r. \tag{3.5}$$

This regularization operator "kills" the $1/r$ divergent part of the wave function $\phi_{rel}(\mathbf{r})$, which naturally occurs in three dimensions. This can be proven by a fast calculation assuming $\phi_{rel}(\mathbf{r}) = u(\mathbf{r})/r$ where $u(\mathbf{r})$ is a general polynomial (up to infinite order).

The numerical ML-MCTDHB method, as most numerical many-body methods, operates with three-dimensional single particle functions given in the laboratory frame $\{\chi_i(\mathbf{r})\}_{i=1}^{M}$ and therefore a Hartree product can be formed, which can be symmetrized. The regularized delta interaction potential (given in the relative frame) acts on these Hartree products (given in the laboratory frame). Without loss of generality, we can analyse the action of the regularized delta interaction potential on only two particles (for a transformation of the regularized delta interaction potential into the laboratory frame, see appendix C.2)

$$g\delta(\mathbf{r})\partial_r\left(r\chi_i(\mathbf{r}_1)\chi_j(\mathbf{r}_2)\right) = g\delta(\mathbf{r_1}-\mathbf{r_2})\Big[\chi_i(\mathbf{r}_1)\chi_j(\mathbf{r}_2) + \frac{\mathbf{r}_1-\mathbf{r}_2}{2}\left(\nabla_{\mathbf{r}_1}-\nabla_{\mathbf{r}_2}\right)\chi_i(\mathbf{r}_1)\chi_j(\mathbf{r}_2)\Big], \quad (3.6)$$

Performing the limit $\mathbf{r}_1-\mathbf{r}_2 \to 0$, this equation leads to $g\delta(\mathbf{r})\partial_r\left(r\chi_i(\mathbf{r}_1)\chi_j(\mathbf{r}_2)\right) = g\delta(\mathbf{r})\chi_i(\mathbf{r}_1)\chi_j(\mathbf{r}_2)$, which is a direct consequence of the fact that a single Hartree product, defined in laboratory frame, cannot feature a $1/r$ singularity in the relative frame, although the single particle functions $\chi_j(\mathbf{r}_i)$ can possess a $1/|\mathbf{r}_i|$ divergence in the laboratory frame. Due to the commutation of $\partial_r r$ with any finite sum, the regularization operator has no effect on any combination of two or more Hartree products and thus on any numerically available two-body state.

This has three important consequences:

1. The action of the regularization operator is identical to the action of the bare delta interaction and can be replaced by it if it acts on a finite Hartree product basis in laboratory frame, as for example in a mean-field approach used to derive the Gross-Pitaevskii equation. But a Hartree product basis cannot feature non-trivial correlations, e.g. particle correlations.

2. If non-trivial correlations are present, increasing the size of basis function, χ_i, does not help, since one converges to the non-interacting solution, as discussed in section 3.1.1.

3. The regularized delta interaction potential is not only of use for analytical solutions [201, 202] but can also be used numerically if and only if a *correlated two-body basis* is employed. For example, an effective interaction potential can be constructed from the exact two body solution [201], which gives good predictions for the eigen-energies of the many-boson problem (e.g. see references [216, 217] and references therein). These correlated basis functions live in a six-dimensional space and the numerical calculations of matrix elements (if not known analytically) are six-dimensional and hence very sensitive on the applied number of grid points. Especially, in the crossover from three towards one dimension, as studied in this thesis, a large number of grid points are needed. If time-dependent correlated basis function would be used, then these six-dimensional matrix elements have to be evaluated at every instance in time, which is computationally very costly and nearly infeasible.

As a consequence, we do not follow this approach any further.

3.1.3. Renormalized bare delta interaction potential

We focus on the second strategy, namely, the truncation of the sum in equation (3.4) and a corresponding renormalization of the interaction strength $g \to g_R = g_R(M, g)$. Only in this section, we name g the "true" interaction strength in order to distinguish it from the renormalized interaction strength g_R. A renormalization theory can be decomposed into two steps; first, to

regularize[3] the divergence occurring by introducing a cut-off and, second, to renormalize the interaction strength g w.r.t. this cut-off.

In this section, first, we discuss our requirements for a proper renormalization theory and then describe the general steps of a renormalization procedure. Then, two renormalization procedures, suitable for the ML-MCTDHB algorithm, are discussed, however their developments and derivations are done in the appendix C.3, since knowledge of the MCTDHB method is needed. We end by a characterization of the two renormalization theories for our developed requirements and a short summary.

The requirements are:

  i. The renormalization theory must handle arbitrary and time-dependent potentials in order to be flexible for different trap geometries.

 ii. Not only the ground state of a two-particle systems, but also excited as well as many-particle states must be described correctly.

iii. Since the ML-MCTDHB method is an ab-initio method, the renormalization procedure is not allowed to use any further approximation, except the "natural" numerical truncation of the single particle basis set or the discretization of space used by the method anyway.

 iv. The renormalization theory must be numerically feasible, and its computational costs must be small in comparison with the rest of the algorithm.

General steps of a renormalization procedure: In different physical fields, different ideas of how divergences can be regularized have been developed, for example, using dimensional regularization [220], introduction of a high-momentum cut-off [221–224], self-adjoint extension [225], subtraction of the divergent part of the wave function [223], perturbative regularization [222], discretization in coordinate space [208] and many more [221, 226–228]. Most of these ideas have in common that the underlying single-particle Hilbert space, here, spanned by three-dimensional single particle functions $\{|\varphi_i\rangle\}_{i=0}^{M}$, is truncated by M and therefore equation (3.4) can be written as

$$\sum_{\mathbf{i=0}}^{\mathbf{M}} \frac{\langle \mathbf{r} = 0 | \varphi_{\mathbf{i}} \rangle \langle \varphi_{\mathbf{i}} | \mathbf{r} = 0 \rangle}{\epsilon_{\mathbf{i}} - E_{rel}} = -\frac{1}{g_R(M)}, \tag{3.7}$$

with the 'renormalized' interaction strength g_R which depends on M. The true interaction strengths g, encrypted in $E_{rel} = E_{rel}(g)$, must be linked with the 'renormalized' interaction strength g_R. E_{rel} has to be calculated analytically, however, this is only possible for rare scenarios in three-dimensions, such as for an isotropic [201] or anisotropic [202] harmonic confinement.

Another possible way to derive a correspondence between the g_R and g is the following: Usually, a physical quantity, e.g. the ground state energy [229], the centre of mass [230] or the T-matrix [208] can be calculated, on the one hand, in the truncated single-particle Hilbert space while using the bare delta interaction potential and, on the other hand, in the full single-particle Hilbert space while using the regularized delta interaction potential. The results are set equal in order to derive the correspondence between the true and renormalized interaction strength $g_R = g_R(M, g)$. Here, we calculate the T-matrix elements given in a truncated Hilbert space

---

[3] In this section, regularization has a different meaning than in section 3.1.2. Here, by regularization, we denote the introduction of a cut-off parameter, which truncates either the sum in equation (3.4) or a corresponding integral. This cut-off parameter is used for the regularization, similar to the renormalization group theory by Wilson [218, 219], leading to cut-off parameter free theory [167]. In contrast, in section 3.1.2, the crossover from $\delta(r) \to \delta(r)\partial_r r$ is denoted as regularization.

and set them equal to the analytical known solution [see equation $(2.22)^4$]

$$\langle \mathbf{k}|T|\mathbf{k}'\rangle = \delta_{\mathbf{k},\mathbf{k}'} \frac{2\pi\hbar^2}{\mu} \frac{a_0}{1 + a_0 k}, \tag{3.8}$$

where a_0 is the zero-energy scattering length and $\mathbf{k}$, $\mathbf{k}'$ are the incoming and outgoing wave vectors, respectively, with $k = |\mathbf{k}|$. In doing so, we follow the lines of reference [208] and start with the three-dimensional single-particle Hamiltonian $H_0 + W$, where H_0 is the relative kinetic operator and $W = g_R \delta$ the delta interaction operator. In position space representation, the delta interaction operator is given by $W = g_R|\mathbf{r} = 0\rangle\langle\mathbf{r} = 0|$. The energy dependent T-matrix is defined as

$$T(E) = W + WGW \tag{3.9}$$

with the Green's function $G(E) = 1/(E - H)$ and the energy $E = \hbar^2\mathbf{k}^2/2\mu$. The Green's function can be calculated from the free Green's function $G_0(E)$

$$G(E) = G_0(E) + G_0(E)WG(E) \tag{3.10}$$

Projecting equations (3.9) and (3.10) onto plain waves, leads to

$$T_{\mathbf{k},\mathbf{k}'}(E) = \frac{g_R}{1 - g_R\Omega(E, M)} \tag{3.11}$$

with $\Omega(M, E) = \langle\mathbf{r} = 0|G_0|\mathbf{r} = 0\rangle$ evaluated in the truncated basis set $\{\langle\mathbf{r}|\varphi_i\rangle\}_{i=0}^{M}$. Equating equation (3.8) and equation (3.11) leads to a connection between the true and renormalized interaction strength, and in the zero-energy limit, we get

$$g(g_R, M) = \lim_{E \to 0} \frac{g_R}{1 + g_R\Omega(M, E)}. \tag{3.12}$$

$\Omega(M, E \to 0)$ is a monotonically increasing function w.r.t. M, e.g. if $\langle\mathbf{r}|\varphi_i\rangle$ are plane waves then $\Omega \sim M$ or if $\langle\mathbf{r}|\varphi_i\rangle$ are harmonic oscillator functions then $\Omega \sim \psi_0(M + 5/2)$, where ψ_0 is the polygamma function. In order to get a feeling for the renormalization procedure, the true interaction strength $g = g(g_R, M)$ is plotted in dependence of the renormalized interaction strength, applying a three-dimensional harmonic oscillator basis (see figure 3.1). We can see that for very small g_R and small M the renormalization of g has no significant influence and thus the bare delta interaction can be used. In this regime, a mean-field approximation is sufficient and one expects only trivial correlations ruling the system. For a larger renormalized interaction strength g_R, the true interaction strength g saturates $g_{max}(M) = \lim_{g_R \to \infty} g(g_R, M)$. It is not possible to simulate, larger "true" interaction strength than $g_{max}(M)$ and $g_{max}(M)$ decreases if M is increased. Increasing M, leads to a zero true interaction strength g, $\lim_{M \to \infty} g(g_R, M) = 0$, since the polygamma function at infinity is infinity. Again, we recover the result that the bare delta interaction potential does not induce scattering in three dimensions.

Developed renormalization procedures: We present two renormalization procedures and discuss them w.r.t. our described requirements. A detailed derivation of the renormalization procedures is given in the appendix (see appendix C.3), since a deeper understanding of the ML-MCTDHB algorithm is needed.

The first renormalization procedure (appendix C.3.1) is the simpler one. Regarding only two interacting particles, the Hamiltonian can be separated into a centre of mass and a relative part.

---

[4]The connection between the scattering amplitude and the T-matrix elements is given by $f(\mathbf{k}, \mathbf{k}') = 4\pi^3\mu/\hbar^2\langle\mathbf{k}|\hat{T}|\mathbf{k}'\rangle$, where μ is the relative mass and $\mathbf{k}$, $\mathbf{k}'$ are the incoming and outgoing wave vectors, respectively.
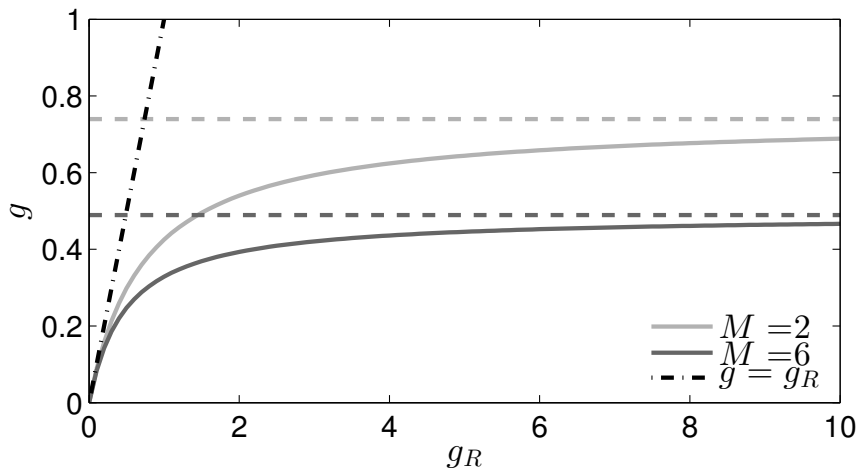
Figure 3.1.: Shown is the true interaction strength, calculated using a three-dimensional harmonic oscillator basis for the two different truncations $M = 2$ (light grey line) and $M = 6$ (dark grey line) in equation 3.7. E_{rel} is approximated for small interaction strengths and linear in the interaction strength [201]. The dashed line shows the values for $g_R \to \infty$. As a reference, the black dash-dotted line shows $g = g_R$.

The ground state energy E_{rel} of the relative Hamiltonian can be obtained either analytically for a harmonic confinement [201, 202] or numerically if the trap geometry is more advanced in dependence of the 'true' interaction strength g, $E_{rel} = E_{rel}(g)$. The single particle functions $|\varphi_\mathbf{i}\rangle$ and eigen energies are known from the non-interacting problem, $H_0|\varphi_\mathbf{i}\rangle = \epsilon_\mathbf{i}|\varphi_\mathbf{i}\rangle$ and equation (3.7) can be solved either analytically (if possible) or numerically in order to get a dependence between the true and renormalized interaction strength. This renormalization procedure can handle arbitrary potentials. However, the introduced truncation does not corresponds to the truncation made by the ML-MCTDHB algorithm since the single particle basis in the ML-MCTDHB algorithm is time-dependent and is given in laboratory coordinates. Therefore, the truncation gets time-dependent, which is not reflected by this renormalization procedure. Another weak point of this renormalization procedure is that the ground state energy is used to link the true and the renormalized interaction strengths and thus excited states or many particle scattering events are not renormalized correctly.

The second developed renormalization procedure tries to circumvent the last mentioned point. Instead of assuming the correspondence between the ground state energies, the T-matrix, including already multiple two-body scattering events, can be used as a starting point [208]. Merging the general idea of reference [208] with the constrains of the ML-MCTDHB method by using time-dependent single-particle functions in the relative frame $|\varphi_i\rangle$ and by linking them to the finite single-particle basis in the laboratory frame $\{\chi_i\}_{i=1}^M$ used in ML-MCTDHB, a second renormalization theory has been derived (appendix C.3.2)[5]. Due to the time-dependence of the single-particle functions $|\varphi_i\rangle$, $\Omega(M, E)$ has to be evaluated at every instance in time and due to the coordinate transformation between the relative frame and the laboratory frame, six dimensional integrals have to be evaluated at every instance in time. This is far too cumbersome for a dynamical application. Nevertheless, as we have shown, this renormalization theory can reproduce the right ground state energy in an isotopic harmonic trap (see appendix C.3.2).

In summary, no suitable renormalization procedure has been found, which fulfils all our requirements. The following list summarizes the conceptual problems, we have encountered thereby:

---

[5] In order to make the point clear. The main problem is that the regularization theory is derived in the relative coordinates, however, the ML-MCTDHB methods works in the laboratory frame.

- A renormalization procedure is limited to a maximal achievable 'true' interaction strength and therefore not the whole interaction range which is experimentally feasible, can be simulated numerically.

- In ML-MCTDHB, the single-particle basis states $|\varphi_i\rangle$ are dynamically determined at each instant in time, and therefore the renormalization procedure gets time-dependent, especially $g_R = g_R(t)$. However, a simulation with a time-dependent renormalized interaction strength is not assured to converge to the right result, given by the true interaction strength.

- Due to the description of ML-MCTDHB in second quantization, it operates in the laboratory frame, whereas the renormalization is formulated in the relative frame. That is why a coordinate transformation between these two frames has to be performed, leading to a six-dimensional integration. Paired with the time-dependence of the single-particle basis, the integration has to be performed at every instant in time, which is numerically very costly. This is in complete contrast to the philosophy and basic idea of the ML-MCTDHB method, which is designed to avoid exactly these six dimensional integrations.

- Generally speaking, a renormalization procedure is just a shift of the interaction strength $g \rightarrow g_R$ and excited states are shifted the same way as ground states. Therefore, it is not expected that excited states are renormalized correctly.

- The ML-MCTDHB method does not only truncate the three-dimensional single-particle Hilbert space once, in fact a truncation happens on different "layers" (see chapter 4). In the ML-MCTDHB method, the three-dimensional single-particle Hilbert space is separated into one-dimensional single-particle Hilbert spaces, which are truncated on their own. All these truncations influence each other (see figure C.1a in the appendix) and has to be included in a proper renormalization theory.

As a consequence, we have given up the effort to improve or develop new renormalization procedures, due to the many conceptual difficulties and challenges.

Summary: Describing numerically non-trivial correlations, neither the regularization of the delta interaction nor renormalization of the interaction strength can be used in order to circumvent the problems of the three-dimensional bare delta interaction. As a consequence, we have to give up the great advantage of zero-range interaction potentials, namely the independence of the simulation on the interaction range, and focus on finite-range interaction potentials in the following.

3.2. Finite-range interaction potential

As a consequence of the discussion in the previous section, the interactions in three dimensions must be modelled by a finite-range potential W if we want non-trivial correlations to be taken into account. But not all finite-range interaction potentials are suitable for a numerical implementation. Therefore, we demand the following requirements to be satisfied for the finite-range potential used in the ML-MCTDHB algorithm:

1. The interaction potential must be short-range:

   In order that a short-range interaction potential is well defined, it must obey certain constraints: (i) It must be isotropic in space, in order to model s-wave scattering. (ii) At a finite distance i.e. the size of the interaction potential Σ, the short-range interaction potential must drop to zero, $W(|\mathbf{r}| > \Sigma) = 0$, or is forced to be zero. (iii) Σ must constitute the smallest physical length scale in the problem at hand, and especially it must be smaller

than the characteristic lengths scales of the trap length l_{trap}. The trap is not allowed to influence the scattering process so that the scattering process gets independent of the trap geometry i.e. the scattering can be regarded as taking place in free space, similar to the delta interaction potential. (iv) Furthermore, Σ must be smaller than the typical inter-particle distance to avoid three-body scattering. (v) The short-range interaction potential must be resolved numerically by a grid with grid distance $\Delta_s = L_s/q_s$, where L_s is the total grid length and q_s is the number of grid points in the s-th dimension. Because of isotropy, the grid spacing must be the same in every dimension, and since the scattering is homogeneous in space, the grid must be equidistant. (vi) The scattering process, in detail the far-field phase shift, is not allowed to depend on the special shape of the short-range interaction potential.

Summarizing, we have the following relations for the length scales:

$$\Delta_s < \Sigma < l_{trap} < L_s \tag{3.13}$$

To satisfy all these constraints of equation (3.13), a large number of grid points are needed, which causes a numerical challenge (see chapter 1). A list of some possible interaction potentials is given in table 3.1, with interaction height/strength h and width σ. Of cause attractive ($h < 0$) and repulsive ($h > 0$) interaction potentials, and any combination between them, are possible.

2. The interaction potential must be linked with the s-wave scattering length a_0:

The zero-energy scattering length a_0 must be easily tunable via the interaction potential parameters h and σ. In principle, the whole range for the scattering length from $a_0 = -\infty \dots \infty$ can be covered if the interaction potential features a bound state (see section 2.4). Bound states, however, simulated in the laboratory frame, feature strong particle correlations, which are in general difficult to handle numerically and challenging to bring to convergence [231]. Furthermore, the resonance is strongly energy-dependent and thus resulting in an energy-dependent scattering length, which has to be handled numerically in a many-particle simulation. In order to avoid these difficulties, we focus on pure repulsive interaction strengths, with the disadvantage that the maximal achievable scattering length is limited to $a_0 \leq \Sigma$ (see section 2.4).

The only relevant physical scattering parameter is the zero-range interaction length a_0, which can be calculated numerically from the interaction potential in dependence of h and σ (see section 2.3.4). In order to reduce the dependence of a_0 to one parameter, which is numerical easier to handle, an additional normalization condition can be introduced, which couples h and σ.

3. The interaction potential must lead to the lowest possible computational effort:

As in many numerical method, the interaction matrix element

$$W_{ijkl} = \langle \chi_i \chi_j | W | \chi_k \chi_l \rangle \tag{3.14}$$

has to be calculated[6], created by the three-dimensional single-particle functions $\{\chi_k(\mathbf{r}_i)\}_{k=1}^M$, where k is the mode index and i the particle index.

(i) Using a brute force implementation, a six-dimensional spatial integration has to be performed, requiring $q_1^2 q_2^2 q_3^2$ operations at each instant in time (if the χ_i are time-dependent as in the ML-MCTDHB method), where q_s are the number of grid points in the dimensions $s = \{1, 2, 3\}$. The numerical effort per iteration step is given by $q_1^2 q_2^2 q_3^2$, which can be

---

[6]Here, we regard only the implementation of local interaction potentials, such as the ones given in table 3.1.

improved a little by using Monte Carlo integration. As we have seen, a large number of grid points are necessary to resolve short-range interaction potentials, and therefore a brute force implementation is not feasible numerically. A different implementation has to be imagined with a better numerical performance.

(ii) The interaction potential W can be approximated by a sum of single particle potentials, using a Schmidt decomposition [122, 232, 233],

$$W(\mathbf{r}_1, \mathbf{r}_2) = W(\mathbf{r}_1 - \mathbf{r}_2) \sim W_P(\mathbf{r}_1 - \mathbf{r}_2) = \sum_{p=1}^{P} c_p w_p^{(1)}(\mathbf{r}_1) w_p^{(2)}(\mathbf{r}_2) \tag{3.15}$$

which becomes exact for $P = q_1 q_2 q_3$. If W_P approximates W well for much less terms, i.e. $P \ll q_1 q_2 q_3$, the calculation of the interaction matrix element W_{ijkl} can be separated into two steps, first, the calculation of $T_{ikp}^{(\kappa)} = \langle \chi_i | w_p^{(\kappa)} | \chi_k \rangle$, where κ is the particle index and then $W_{ijkl} = \sum_{p=1}^{P} c_p T_{ikp}^{(1)} T_{jlp}^{(2)}$. The numerical performance scales in dependence on the number of grid points with $\sim q_1 q_2 q_3$, which is numerically more feasible, but still out of range of an efficient implementation. Furthermore, we have found empirically that for too few terms P, the potential W_P exhibits long-range interaction and unphysical oscillations, which can feature bound states. Although these oscillation can be damped manually by considering the average $\propto \sum_{p=1}^{P_{max}} W_p$ as the interaction potential (see Appendix C.4), the resulting interaction potential is not satisfactory and the performance is still too costly.

(iii) The three-dimensional single-particle functions $|\chi_j\rangle$ can be expanded by one-dimensional basis functions $|\phi_j^{(s)}\rangle$ for the different spatial directions s (as we will do in our implementation, see section 4), $|\chi_j\rangle = \sum_{j_1 j_2 j_3} B_{j j_1 j_2 j_3} |\phi_{j_1}^{(1)}\rangle \phi_{j_2}^{(2)}\rangle \phi_{j_3}^{(3)}\rangle$ and the interaction potential can be decomposed into the spatial directions,

$$W(\mathbf{r}_1, \mathbf{r}_2) \sim W_{P_1 P_2 P_3}(\mathbf{r}_2 - \mathbf{r}_1) = \sum_{p_1=1}^{P_1} \sum_{p_2=1}^{P_2} \sum_{p_3=1}^{P_3} c_{p_1 p_2 p_3} \tilde{w}_{p_1}^{(1)}(x_1 - x_2) \tilde{w}_{p_2}^{(2)}(y_1 - y_2) \tilde{w}_{p_3}^{(3)}(z_1 - z_2)$$

$$\tag{3.16}$$

which can be achieved by the POT-FIT algorithm [232, 233] for a finite number of P_s. In doing so, the computational task is split into a subtask, first, to calculate $\tilde{W}_{p_s i_s j_s k_s l_s}^{(s)} = \langle \phi_{i_s}^{(s)} \phi_{j_s}^{(s)} | \tilde{w}_{p_s}^{(s)} | \phi_{k_s}^{(s)} \phi_{l_s}^{(s)} \rangle$ and second $W_{ijkl} = \sum_{P}^{\mathcal{P}} c_P \sum_{IJKL} B_{iI}^* B_{jJ}^* B_{kK} B_{lL} \prod_{s=1}^{3} \tilde{W}_{p_s i_s j_s k_s l_s}^{(s)}$, where we have used the multi-index $I = (i_1, i_2, i_3)$ as well as $\mathcal{P} = (P_1, P_2, P_3)$, and where we have used the abbreviation for the sum sign $\sum_I = \sum_{i_1} \sum_{i_2} \sum_{i_3}$. In this way, the computational effort in dependence of the number of grid points scales with $\sum_{s=1}^{3} q_s^2$, which is still computationally very challenging for large number of gird points. The efficiency of this scheme depends on $P_i < q_s$ as well as on how many one-dimensional basis states $|\phi_j^{(s)}\rangle$ are needed for convergence. We notice that only for the Gaussian interaction potential (see table 3.1) $P_1 = P_2 = P_3 = 1$.

(iv) Applying symmetry arguments: The matrix element (3.14) has got the computational effort, scaling with $\propto m_s^4 q_1^2 q_2^2 q_3^2$. If the interaction potential W (i.e. $\tilde{W}_{pijkl}^{(s)}$) depends only on the relative coordinate and is real valued, symmetry arguments of the matrix elements can be used to improve the scaling. We obtain:

$$\tilde{W}_{pijkl}^{(s)} = \tilde{W}_{pjilk}^{(s)} = \tilde{W}_{pklij}^{*(s)} = \tilde{W}_{plkji}^{*(s)} \tag{3.17}$$

Furthermore $\tilde{W}_{pijkl}^{(s)}$ can be Fourier transformed and then evaluated using the IMEST-algorithm [234] (see also appendix C.5). In doing so, the scaling in dependence of the number of grid points is reduced from $\propto q_1^2 q_2^2 q_3^2$ to $\propto q_1 q_2 q_3 \log(q_1 q_2 q_3)$.

Table 3.2.: Numerical effort to determine the matrix element W_{ijkl} for the various implementations. q_s is the number of grid points in dimension $s = \{1, 2, 3\}$, M is the number of three-dimensional single-particle functions and m_s is the number of one-dimensional single-particle functions in dimension s. The parameter of the POT-FIT algorithm are P or P_s for dimension s, depending on the context (see main text).

brute force implementation	
Determine W_{ijkl}	$M^4 q_1^2 q_2^2 q_3^2$
Expansion into particles	
Determine T_{ikp}	$M^2 P q_1 q_2 q_3$
Determine W_{ijkl}	PM^4
Expansion into dimensions	
Determine $\tilde{W}^{(s)}_{p, i_s j_s k_s l_s}$	$p_s m_s^4 q_s^2$
Determine W_{ijkl}	$P_1 P_2 P_3 M^4 m_1^4 m_2^4 m_3^4$

Since the ML-MCTDHB method aims at an efficient representation of $|\chi_i\rangle$ in terms of the $|\phi_j^{(s)}\rangle$, we follow the third strategy in combination with the fourth strategy for evaluating the matrix elements. Moreover, we restrict ourselves to interaction potentials, which are separable in Cartesian coordinates, $W(\mathbf{r}_1 - \mathbf{r}_2) = W^{(1)}(x_1 - x_2) W^{(2)}(y_1 - y_2) W^{(3)}(z_1 - z_2)$, to further reduce the number of P summations. Demanding isotropy, a natural choice for W is the Gaussian interaction potential in three dimensions $W_G(\mathbf{r}_1 - \mathbf{r}_2) = he^{-(\mathbf{r}_1 - \mathbf{r}_2)^2/\sigma^2}$. The interaction strength can be adjusted by h, however, increasing the height of the Gaussian potential increases also its range $\Sigma(h, \sigma)$ and thus the length scale of the Gaussian may interfere with other length scales, for example the trap size. Then, short-range interactions are not ensured anymore. Therefore, we renormalize the width of the Gaussian w.r.t. a small energy scale of our system ϵ (as already done in section 2.3.4) by demanding $W_{RG}(\mathbf{r}) = \epsilon$ if $|\mathbf{r}| = \sigma$, such that Σ is independent of the height h :

$$ W_{RG}(\mathbf{r}_1 - \mathbf{r}_2) = he^{-\ln(h/\epsilon) \frac{(\mathbf{r}_1 - \mathbf{r}_2)^2}{\sigma^2}} . \tag{3.18} $$

Increasing the height, the renormalized Gaussian W_{RG} approaches the shape of a hard wall interaction potential, whose width is limited by $\sigma = \Sigma$. In contrast to this, the range of W_G grows unlimited with increasing h such that the assumptions of both free space scattering and short-range interactions would be violated (see figure 2.2).

3.3. Summary

In summary, we have analysed the implementation of zero-range interaction potentials in three dimensions, which all produce insuperable problems, especially, they cannot resolve non-trivial correlations if a single-particle basis is used. Because of this, we have to use finite-range interaction potentials in a numerical implementation, which introduce a new length scale into the system. This length scale must be the shortest length scale in the problem at hand and has to be resolved numerically making to a large number of grid points necessary. After formulating requirements for the finite-range interaction potential (e.g. the interaction potential must be short-ranged), we have analysed the efficiency to calculate interaction matrix elements, i.e. the scaling w.r.t. the number of grid points for different implementations of short-range interaction potentials. We have found that the renormalized Gaussian interaction potential (3.18) fulfils our requirements for the finite-range interaction potential and causes the most efficient implementation.

CHAPTER

FOUR

THE ALGORITHM: ML-MCTDHB

As already worked out in the introduction, two grave numerical challenges have to be solved for an efficient implementation of an ab-initio method for bosons in three dimensions taking all correlations into account. We repeat them shortly: (i) the exponential scaling w.r.t. the number of particles (ii) the large amount of grid points in order to simulate short-range interaction potentials. The Multi-Configuration Time-Dependent Hartree method for Bosons (MCTDHB) [235] is well suited to tackle the first challenge and numerous applications [90, 212–214, 236–245] show its success. In order to tackle the second challenge, a Multi-Layer expansion of the MCTDHB algorithm (ML-MCTDHB) can be used as already pointed out in reference [62]. In reference [[1]], we have developed and implemented an algorithm for the efficient simulation of ultracold many-body systems in three dimensions. In this chapter, we discuss this multi-layer expansion and its concrete numerical implementation based on reference [[1]].

This chapter is structured as follows: We begin in section 4.1 with a short introduction into the family of MCTDH methods, highlighting the main developments. Afterwards, we introduce the Hamiltonian of the physical system (section 4.2), which we have in mind for the following discussion. One of these developments has been the specialization of MCTDH to bosonic systems (MCTDHB), which we describe in section 4.3. In section 4.4, we present our Multi-Layer expansion (ML-MCTDHB), suitable for bosonic systems with the need of high spatial resolution. Then, a comparison between MCTDHB and ML-MCTDHB, which benchmark our implementation, is given in section 4.5. Numerical tricks and solutions to numerical problems, which occur during the concrete implementation are discussed in section 4.6. We end this chapter by a validation of the implementation of ML-MCTDHB in section 4.7.

4.1. The family of MCTDH-methods

In the year 1990, H.-D. Meyer, U. Manthe and L. Cederbaum have numerically solved the many-particle Schrödinger equation of distinguishable particles[1] by expanding the wave function into a sum over configurations, created by Hartree products of time-dependent one-dimensional single-particle functions [246, 247]. They have named their method Multi-Configuration Time-Dependent Hartree (MCTDH). The time-dependent single particle functions are variationally optimized at every instance in time. In doing so, MCTDH has achieved a better numerical convergence behaviour with a smaller numerical effort. Further reductions of the computational effort by selecting only the most relevant configurations (Selective-MCTDH), have made the

---

[1] To be more exact the Schrödinger equation is solved for many distinguishable degrees of freedom.

study for even larger systems possible [248]. The next crucial step has been the development of a multi-layer structure, named ML-MCTDH, where the many-body wave function is expanded into sums of configurations, created by products of time-dependent multi-dimensional functions. This multi-dimensional function can be recursively expanded into time-dependent functions of lower dimensions, until one reaches the level of one-dimensional single-particle functions. This multi-layer structure allows treating systems with even more degrees of freedom [249]. Applications of the ML-MCTDH method to a plethora of systems can be found for example in references [235, 250, 251].

Apart from the formulations for distinguishable particles, the MCTDH algorithm has been specialized to indistinguishable particle such as fermions (MCTDHF) [252–254] or bosons (MCT-DHB) [60, 255] or even mixtures (see references [256–258] and [[3]]). In short, one replaces the Hartree product with symmetrized products, i.e., determinants and permanents for fermionic and bosonic system, respectively. Another approach to include distinguishable particles into the MCTDH algorithm is to express the many-particle Hilbert space in terms of direct products of single-mode Fock spaces. This approach is based on the second quantization framework and called the MCTDH in Second Quantization Representation (MCTDH-SQR) [259–261]. Further developments include the usage of Wannier basis states for lattice systems [262, 263], the treatment of internal degrees of freedom [264] and the formulation of a linear-response theory on top of MCTDHB [265, 266]. Reviews about the MCTDH, ML-MCTDH, and MCTDHB can be found in [169, 267–271].

In the following, we focus onto a purely bosonic system. The ideas of the expansions of MCTDH to bosonic systems [60] and the multi-layer structure for distinguishable particles can be merged, which is named the Multi-Layer Multi-Configuration Time-Dependent Hartree for Bosons (ML-MCTDHB) [61, 62]. Due to the computational challenges w.r.t. the number of grid points, the MCTDHB algorithm has been primarily used in one dimension for the study of processes such as tunnelling in a double well [214, 236–239], breathing dynamics [212], soliton dynamics [90, 240], quench induced dynamics in lattice systems [241, 242], hybrid atom systems [213, 214], and dipolar systems [243, 244]. Simulations in two and three dimensions are rare and limited to a few grid points [123–129, 131, 240, 272] (for a review see reference [273]). Our work enlarge the maximal number of grid points, which can be used per dimension, by a factor of 10 for every dimension, thus huge systems can be simulated.

4.2. Setup and Hamiltonian

We want to solve the time-dependent three-dimensional Schrödinger equation for an ultracold bosonic ensemble of N bosons with mass m

$$i\hbar\partial_t\Psi(\mathbf{r}_1, \mathbf{r}_2, ..., \mathbf{r}_N, t) = \mathcal{H}\Psi(\mathbf{r}_1, \mathbf{r}_2, ...\mathbf{r}_N, t)$$
$$= \left[\sum_{i=1}^{N} H_0(\mathbf{r}_i) + \sum_{1 \le i < j \le N} W(\mathbf{r}_i, \mathbf{r}_j)\right]\Psi(\mathbf{r}_1, \mathbf{r}_2, ..., \mathbf{r}_N, t). \quad (4.1)$$

where the single particle Hamiltonian $H_0(\mathbf{r}_i)$ acts on the i-th boson and is composed of a kinetic and an arbitrary, possible time-dependent, external potential $V(\mathbf{r}_i, t)$ term[2].

$$H_0(\mathbf{r}_i) = -\frac{\hbar^2}{2m}\nabla_{\mathbf{r}_i}^2 + V(\mathbf{r}_i, t) \quad (4.2)$$

---

[2]We use position space representation.

The position of the i-th boson is given by $\mathbf{r}_i = (x_i,\ y_i,\ z_i)^T$ in Cartesian coordinates and $r_{ij} = |\mathbf{r}_i - \mathbf{r}_j|$ is the distance between the i-th and the j-th atom, appearing in the interaction potential

$$W(\mathbf{r}_i, \mathbf{r}_j) = W(|\mathbf{r}_i - \mathbf{r}_j|) = W(r_{ij}) \tag{4.3}$$

with $j \neq i$. For the interaction potential, we assume the following properties, which have been derived and discussed in the chapter 3: (i) The interaction potential W is local and (ii) is separable w.r.t. to its dimensions, $W(\mathbf{r}_i - \mathbf{r}_j) = W^{(1)}(x_i - x_j)W^{(2)}(y_i - y_j)W^{(3)}(z_i - z_j)$.

4.3. The basic idea of MCTDHB in higher dimensions

The main idea of MCTDHB [60] is to express the many-body wave function into a sum over configurations, created by time-dependent permanents. These permanents are again represented by time-dependent single-particle functions, which can be expressed by a time-independent set of basis functions. These different expansions are divided into different layers. In the following, we have a closer look on each expansion i.e. on each layer.

The first layer or top layer is dedicated to the N-body wave functions Ψ. The N-body wave function Ψ is expanded into a set of time-dependent permanents $|\vec{n}\rangle_t$ in order to include the bosonic symmetry directly into the N-body wave function approach,

$$|\Psi(t)\rangle = \sum_{\vec{n}|N} A_{\vec{n}}(t)|\vec{n}\rangle_t, \tag{4.4}$$

where the sum runs over all N-body permanents and $A_{\vec{n}}(t)$ are time-dependent expansion coefficients. The permanent is labelled by the integer vector $\vec{n} = (n_1,\ ...,\ n_i,\ ...,\ n_M)$, where n_i is the occupation number of the i-th three-dimensional, time-dependent single-particle function (3D-SPF), $|\chi_i(t)\rangle$. The 3D-SPFs are already member of the next layer, the so-called particle -layer. The maximal number of supplied 3D-SPFs is M, which can be regarded as a numerical control parameter. This expansion gets exact in the limit of $M \to \infty$. The time-dependent 3D-SPFs can be expanded once more, but this time, onto a time-independent set of primitive function $|U_J\rangle$.

$$|\chi_j(t)\rangle = \sum_{J=1}^{Q} \tilde{B}_{jJ}(t)|U_J\rangle \tag{4.5}$$

where $\tilde{B}_{jJ}(t)$ are the time-dependent expansion coefficients and the sum runs over the total number of grid points $Q = q_1 q_2 q_3$. The primitive function $|U_J\rangle$ are members of the lowest layer, the so called primitive or physical layer. For example, the set of primitives function can be a discrete variable representation (DVR) [267, 274] or a grid based on a Fast-Fourier Transformation [166, 275]. In future, we name the number of primitive functions also number of grid points. In order to get a better understanding of the expansion of the N-body wave function, we sketch our expansion in figure 4.1.

If we count the number of needed expansion coefficients, we get for the top layer coefficients

$$\binom{N + M - 1}{M - 1} \tag{4.6}$$
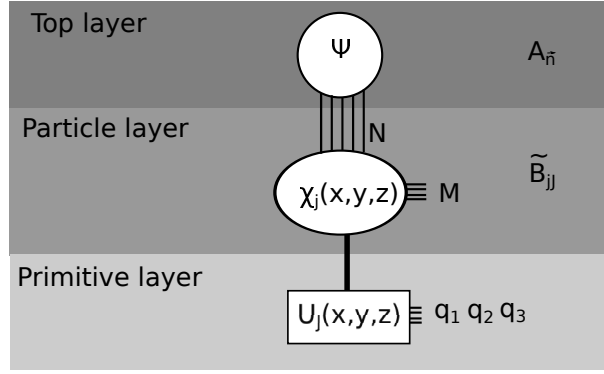
and

$$M \prod_{s=1}^{3} q_s \tag{4.7}$$

Figure 4.1.: Expansion of the N-body wave function used for MCTDHB in higher dimensions. On the *top-layer*, the N-particle wave function Ψ is expressed by permanents with expansion coefficients $A_{\vec{n}}(t)$. These permanents are constructed by the M 3D-SPFs χ_i. The 3D-SPFs χ_i are assigned to the (single) particle layer and are expanded by time-independent functions U_J with coefficients $\tilde{B}_{jJ}$. The U_J are collected on the primitive layer.

for the $\tilde{B}_{jJ}$ coefficients, where we have assumed a direct product grid of time-independent basis functions per dimension, with Q number of grid points.

Next, we derive the equations of motions for the time-dependent expansion coefficients $A_{\vec{n}}(t)$ and $\tilde{B}_{jJ}(t)$ using the variational principle. Different variational principles can be applied in order to derive the equations of motion, for example, Lagrange, Dirac-Frenkel [276, 277] or McLachlan's [278]. The equivalence between them has been shown in reference [279, 280]. Finally, the equations of motions are solved numerically by the MCTDHB algorithm using a common integrator (for example the zvode solver [281–283] for a system of complex differential equations of first order).

We use the Dirac-Frenkel variational principle, namely $\langle\delta\Psi|\,i\partial_t - H\,|\Psi\rangle = 0$, and insert the expansion of the N-body wave function (4.4) as well as the expansion of the 3D-SPFs (4.5) into it (see also appendix D.4). Orthonormality of the 3D-SPFs are ensured by the constrain $\langle\chi_j|i\partial_t|\chi_k\rangle = 0$ only if the 3D-SPFs are already orthogonal at $t = 0$. Performing the variation leads to the following equations of motion [60]

$$i\hbar\partial_t A_{\vec{n}} = \sum_{\vec{m}|N} \langle\vec{n}|\,H\,|\vec{m}\rangle A_{\vec{m}} \tag{4.8}$$

$$i\hbar\partial_t \tilde{B}_{iI} = \sum_{k,l=1}^{M}\sum_{L=1}^{Q} \langle U_I|\left[\left(1 - P^{(\chi)}\right)\left(H_0 + \left[\rho^{(\chi)}\right]_{ik}^{-1}\langle W\rangle_{kl}^{(\chi)}\right)\right]|U_L\rangle \tilde{B}_{lL} \tag{4.9}$$

Let us first explain the notation and significance of the single terms in these two equations of motions. In order to shorten our notation, we drop the time-dependence here and in the following. Equation (4.8) is a complete expansions over all possible permanents and the matrix element $\langle\vec{n}|H|\vec{m}\rangle$ has to be calculated at every instance in time. Using the language of second quantization, the matrix element is $\langle\vec{n}|H|\vec{m}\rangle = \sum_{ij}\hat{a}_i^\dagger\hat{a}_j h_{ij} + \sum_{ijkl}\hat{a}_i^\dagger\hat{a}_j^\dagger\hat{a}_k\hat{a}_l w_{ijkl}$, where $\hat{a}_i^\dagger$ ($\hat{a}_i$) creates (destroys) a boson in the i-th state with,

$$h_{ij} = \langle\chi_i|H_0|\chi_j\rangle, \tag{4.10}$$

and

$$w_{ijkl} = \langle\chi_i^{(1)}|\langle\chi_j^{(2)}|W^{(ij)}|\chi_k^{(1)}\rangle|\chi_l^{(2)}\rangle. \tag{4.11}$$

A more complex structure is observed in equation (4.9). The projector, $P^{(\chi)} = \sum_{i=1}^{M} |\chi_i\rangle\langle\chi_i|$, projects onto the co-moving subspace spanned by the instantaneous 3D-SPFs $\{\chi_i\}_{i=1}^{M}$. According to equation (4.9), the 3D-SPF can only rotate into the orthogonal complement of the subspace which they are spanning. The dynamics of the 3D-SPFs is driven by both the one-body Hamiltonian H_0 and the interactions among the atoms, which are represented by the second term in the bracket on the right-hand-side of equation (4.9). Here, $\rho_{ik}^{(\chi)}$ denotes the one-body density matrix[3] in the 3D-SPF representation, which can be calculated by

$$\rho_{ik}^{(\chi)} = \langle\Psi|a_i^\dagger a_k|\Psi\rangle/N \tag{4.12}$$

The inverse of the one-body density matrix causes that weakly occupied single particle-functions rotate faster than strongly occupied ones [267] so that they get stronger populated by the equation of motion. Finally, $\langle W\rangle_{ik}^{(\chi)}$ refers to the so-called mean-field operator matrix, which can be written as

$$\langle W\rangle_{ik}^{(\chi)} = \sum_{j,l=1}^{M} \rho_{ijkl}^{(2)} \sum_{I,K=1}^{Q} W_{IjKl}^{(\chi)}|U_I\rangle\langle U_K| \tag{4.13}$$

with $W_{IjKl} = \sum_{JL} \tilde{B}_{jJ}^* \tilde{B}_{lL} \langle U_I U_J|W|U_K U_L\rangle$ and the two-particle density matrix $\rho_{ijkl}^{(2)} = \langle\Psi|a_i^\dagger a_j^\dagger a_k a_l|\Psi\rangle/N$. Thus, the interaction couples different 3D-SPF, weighted by the corresponding two body density matrix elements.

A numerical challenge is to determine the two ingredients W_{IjKl} for the particle layer and w_{ijkl} for the top layer, since they are both time-dependent and scale w.r.t. the number of grid points $\propto (q_1 q_2 q_3)^2$. However, the elements $\langle U_I U_J|W|U_K U_L\rangle$ are time-independent and have to be calculated only once either numerical or analytically. (The basis functions U_I can be chosen in such a way that the evaluation is easy.) Although the scaling w.r.t. the number of grid points can be improved by applying symmetry arguments (see section (3.17)) or by evaluating the integrals in Fourier space (see appendix C.5), the algorithm is still numerical infeasible for a large number of grid points ($q_i \sim 100$).

Summarizing, we have performed two truncation of the many-body Hilbert space. The first truncation has been performed by supplying only M orbitals in order to build-up the permanent. In the limit of only one 3D-SPFs $M = 1$, the equations of motion (4.4) and (4.5) recover the GPE again. The proof is given in the appendix D.1. If only M orbitals are supplied, the simulations corresponds to a M-mode approximation and if convergence is achieved using M orbitals, or in the limit $M \to \infty$ the calculation gets *numerically exact* (for sufficient large number of grid points). The second truncation, which has been made, is a discretization of the Hamiltonian (4.2). In the limit $M = \prod_{s=1}^{3} q_s$, the full Configuration Interaction (CI) method is recovered and the discretization of space is the only truncation. Of cause, the algorithm is only of use if convergence can be achieved for situations $M \ll \prod_{s=1}^{3} q_s$.

4.4. Multi-Layer extension: the ML-MCTDHB algorithm

Apart from the computational effort of the exponential scaling w.r.t. the number of particles, we have discussed the numerical unfavourable scaling w.r.t. the number of grid points in the MCTDHB algorithm (see section 4.3), which restricts numerical simulations to a small number of grid points. However, the scaling of w_{ijkl} and $\langle W\rangle_{ik}^{(\chi)}$ w.r.t. the number of grid points can be significantly improved if both the interaction potential and the basis function $|U_J\rangle$ can be

---

[3]We note that in the (ML-)MCTDHB terminology, the one- and two-body density matrix are proportional to the transposed of the physical reduced one- and two-body density matrix
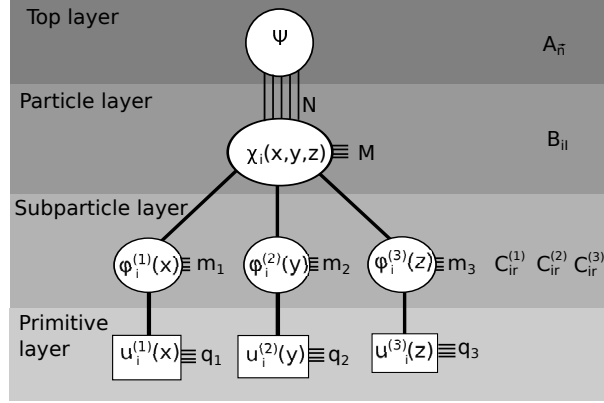
Figure 4.2.: Expansion of the N-body wave function as done in ML-MCTDHB. On the *top-layer*, the N-particle wave function Ψ is expressed by permanents with expansion coefficients $A_{\vec{n}}(t)$. These permanents are constructed by the M time-dependent 3D-SPFs χ_i, which are located on the so-called *particle layer* with coefficients B_{iI}. These time-dependent wave functions are expanded once more into time-dependent 1D-SPFs $\phi_i^{(s)}$ with expansion coefficient $C_{ir}^{(s)}$, on the *subparticle layer*. Finally on the *primitive layer*, the 1D-SPFs are expanded onto a time-independent grid $u_i^{(s)}$.

decomposed into the spatial dimensions. In order to decompose an arbitrary interaction potential, the POT-FIT algorithm can be used [see section 3.2, in particular equation (3.16)]. The basis function $|U_J\rangle$ are replaced by three time-dependent, one-dimensional single particle functions (1D-SPFs) $|U_J\rangle \rightarrow |\Phi_\mathbf{J}(t)\rangle = \bigotimes_{s=1}^{3} |\phi_{j_s}^{(s)}(t)\rangle$, where we have introduced the multi-index $\mathbf{J} = (j_1, j_2, j_3)$ with $j_s = 1, ..., m_s$ and $m_s \leq q_s$ as well as the dimensions $s = 1, 2, 3$. This expansion is linked with the *subparticle layer* as illustrated in figure 4.2.

In this way, the 3D-SPFs are given by

$$|\chi_i(t)\rangle = \sum_{j_1=1}^{m_1} \sum_{j_2=1}^{m_2} \sum_{j_3=1}^{m_3} B_{ij_1j_2j_3}(t) \bigotimes_{s=1}^{3} |\phi_{j_s}^{(s)}(t)\rangle \qquad (4.14)$$
$$\equiv \sum_\mathbf{J} B_{i\mathbf{J}}(t)|\Phi_\mathbf{J}(t)\rangle,$$

and the 1D-SPFs are expanded into a time-independent, one-dimensional set of basis functions $|u_r^{(s)}\rangle$, $r = 1, ..., q_s$

$$|\phi_j^{(s)}(t)\rangle = \sum_{r=1}^{q_s} C_{jr}^{(s)}(t)|u_r^{(s)}\rangle. \qquad (4.15)$$

The wave function is not only expanded, but also the acronym MCTDHB, where an ML- is added at the beginning, due to the expansion into the sub-particle layers. In the limit of as many numbers of 1D-SPFs as time-independent basis functions, $(m_s = q_s)$, just a rotation of the basis is performed and, finally, nothing is gained by the ML-MCTDHB algorithm and the MCTDHB method is recovered. This expansion is only of use if the number of 1D-SPFs can be chosen much smaller than the number of basis functions, $m_s \ll q_s$. Usually, a few 1D-SPFs are enough to represent the dynamics of elongated systems correctly. Only for systems with very strong spatial correlations, many 1D-SPFs are needed and the algorithm losses its advantage. For example, regarding the crossover from three to one dimension, the spatial correlations between the transversal and longitudinal direction becomes smaller, due to the separation of the transversal and longitudinal energy scale, such that less transversal 1D-SPFs are needed $(m_1, m_2 < m_3)$, with $s = 3$ the longitudinal direction. For these systems, the here presented

algorithm is most suitable. For a very strong transversal confinement, there are no spatial correlations between the longitudinal and transversal dimension anymore and all particle correlations are handed over to the longitudinal direction. In this case, one can set the number of transversal 1D-SPFs $m_1 = m_2 = 1$. This choice represents an initial wave function ansatz $\Psi(\mathbf{r}_1, \mathbf{r}_2, \ldots, \mathbf{r}_N) = \Phi^{(z)}(z_1, z_2, \ldots z_N) \prod_{i=1}^{N} \phi^{(x)}(x_i)\phi^{(y)}(y_i)$, where (i) the wave function separates into its dimensions, (ii) the longitudinal part carries all the correlations as well as the bosonic symmetry and (iii) the transversal wave functions are determined variationally.

In order to derive the equations of motion, the Dirac-Frenkel variational principle is consulted again. The top layer coefficients $A_{\vec{n}}$ still obey equation (4.8), whereas the equations of motion for the particle and subparticle layer become

$$i\hbar\partial_t B_{i\mathbf{I}} = \sum_{k,l=1}^{M} \sum_{\mathbf{L}} \langle \Phi_{\mathbf{I}} | \left[\left(1 - P^{(\chi)}\right) \left(H_0 + \left[\rho^{(\chi)}\right]_{ik}^{-1} \langle W \rangle_{kl}^{(\chi)} \right) \right] | \Phi_{\mathbf{L}} \rangle B_{l\mathbf{L}} \qquad (4.16)$$

$$i\hbar\partial_t C_{ir}^{(s)} = \sum_{r'=1}^{q_s} \sum_{j,k=1}^{m_s} \langle u_r^{(s)} | (1 - P^{(s)}) \left(h_0^{(s)} + \left[\rho^{(s)}\right]_{ik}^{-1} \left[\langle \bar{V} \rangle_{kj}^{(s)} + \langle W \rangle_{kj}^{(s)} \right] \right) | u_{r'}^{(s)} \rangle C_{jr'}^{(s)} \qquad (4.17)$$

Both equations of motion have got the same structure as equation (4.9), which has been already explained in section 4.3. Next, we define the ingredients of these equations of motion, starting with equation (4.17). The projector $P^{(s)} = \sum_{i=1}^{m_s} |\phi_i^{(s)}\rangle\langle\phi_i^{(s)}|$ projects onto the one-dimensional subspace, spanned by the 1D-SPFs $|\phi_i^{(s)}\rangle_{i=1}^{m_s}$. Here, $h_0^{(s)}$ is dismantle into a part, which acts non-trivially on the s-th coordinate, and by a unit operators on all the others s'-th coordinate, $s' \neq s$, as well as a part, which couples the s-th direction to the other ones, $\bar{V}$. In other words: A single particle operator in s dimensions can be decompose into $T_1 \otimes \mathbb{1}_2 \otimes \mathbb{1}_3 + \mathbb{1}_1 \otimes T_2 \otimes \mathbb{1}_3 + \mathbb{1}_1 \otimes \mathbb{1}_2 \otimes T_3 + \bar{V}$, where T_s is a one-particle, one-dimension operator and $\bar{V}$ is a one-particle operator, which couples the dimension. For example, the operator T_s can be the kinetic operator plus a potential in dimension (s) and $\bar{V}$ can be a Gaussian potential, i.e., $\exp(-\mathbf{r}_i^2/2)$. Projecting onto the s-th dimension by integrating out the complementary dimensions, we obtain an operator acting only on the s-th dimension, namely the mean-field operator matrix

$$\langle \bar{V} \rangle_{ik}^{(s)} = \sum_{q,p} \rho_{qp}^{(\chi)} \sum_{\mathbf{Q}^s, \mathbf{P}^s} B_{q\mathbf{Q}_i^s}^* B_{p\mathbf{P}_k^s} \langle \Phi_{\mathbf{Q}^s} | \bar{V}^{(s)} | \Phi_{\mathbf{P}^s} \rangle \qquad (4.18)$$

with $|\Phi_{\mathbf{P}^s}\rangle \equiv \bigotimes_{s' \neq s} |\phi_{p_{s'}}^{(s')}\rangle$ and $\rho_{qp}^{(\chi)}$ already defined in equation (4.12), but with respect to a different basis. The next unknown element in equation (4.17) is the density matrix of the s-th degree-of-freedom of a single boson $\rho_{ik}^{(s)}$:

$$\left[\rho^{(s)}\right]_{ik} = \sum_{q,p} \rho_{qp}^{(\chi)} \sum_{\mathbf{Q}^s, \mathbf{P}^s} B_{q\mathbf{Q}_i^s}^* B_{p\mathbf{P}_k^s} \qquad (4.19)$$

where $\sum_{\mathbf{Q}^s}$ abbreviates a summation over all $q_{s'}$ with $s' \neq s$ and $\mathbf{Q}_i^s$ equals (q_1, q_2, q_3) with q_s replaced by i. As in equation (4.9), the two-body interaction is expressed with the mean-field operator matrix $\langle W \rangle_{kl}^{(\chi)}$, which is calculated by

$$\langle W \rangle_{ik}^{(s)} = \sum_{j,l,q,p} \rho_{qjpl}^{(2)} \sum_{\mathbf{J}, \mathbf{L}, \mathbf{Q}^s, \mathbf{P}^s} B_{q\mathbf{Q}_i^s}^* B_{j\mathbf{J}}^* B_{p\mathbf{P}_k^s} B_{l\mathbf{L}} \left[\prod_{s' \neq s} W_{q_{s'} j_{s'} p_{s'} l_{s'}}^{(s')} \right] \langle \phi_{j_s}^{(s)} | W^{(s)} | \phi_{l_s}^{(s)} \rangle, \qquad (4.20)$$

where $W_{q_{s'} j_{s'} p_{s'} l_{s'}}^{(s')} = \langle \phi_{q_{s'}}^{(s')} \phi_{j_{s'}}^{(s')} | W^{(s')} | \phi_{p_{s'}}^{(s')} \phi_{l_{s'}}^{(s')} \rangle$ and $\langle \phi_{j_s}^{(s)} | W^{(s)} | \phi_{l_s}^{(s)} \rangle$ constitute a single particle one-dimensional operator. For simplicity in the notation, we set the number of POT-FIT terms

equal to one i.e., the interaction potentials can be represent as a direct product w.r.t. the dimensions $W = \prod_{s=1}^{3} W^{(s)}$.

In equation (4.16), all ingredients are similar to equation (4.9), except for the mean-field operator matrix $\langle W \rangle_{kl}^{(\chi)}$, which can be written as a product made out of $W_{q_s j_s p_s l_s}^{(s)}$.

$$\langle W \rangle_{ik}^{(\chi)} = \sum_{j,l} \rho_{ijkl}^{(2)} \sum_{\mathbf{I},\mathbf{J},\mathbf{K},\mathbf{L}} B_{j\mathbf{J}}^* B_{l\mathbf{L}} \prod_s W_{i_s j_s k_s l_s}^{(s)} |\Phi_{\mathbf{I}}\rangle \langle \Phi_{\mathbf{K}}| \tag{4.21}$$

Furthermore, the calculation of the interaction element of the top layer w_{ijkl} can be also expressed as a product of $W_{q_s j_s p_s l_s}^{(s)}$

$$w_{ijkl} = \sum_{IJKL} B_{iI}^{\star} B_{jJ}^{\star} B_{kK} B_{lL} \left\langle \Phi_I^{(1)} \right| \left\langle \Phi_J^{(2)} \right| W \left| \Phi_K^{(1)} \right\rangle \left| \Phi_L^{(2)} \right\rangle \tag{4.22}$$

After having all ingredients together, we see that the number of grid points only enter the calculation of the ingredients $W_{i_s j_s k_s l_s}^{(s)}$, which scale w.r.t. the number of grid points as $\propto q_s^2$ and can be improved to $\propto q_s \log(q_s)$ if the IMEST algorithm is applied (see appendix C.5). Having derived $W_{i_s j_s k_s l_s}^{(s)}$, the other two mean-field operator matrices $\langle W \rangle_{kl}^{(\chi)}$ and w_{ijkl} for the particle and top layer, respectively, can be constructed without any further summations on the number grid points [see equation (4.21) and (4.22)], which is in contrast to the MCTDHB algorithm. In total, the scaling w.r.t. the number of grid points is

$$\mathcal{C} \sum_{s=1}^{3} q_s \log(q_s) \tag{4.23}$$

where the prefactor $\mathcal{C}$ strongly depend on the numbers of 3D-SPFs M, 1D-SPFs m_s and the number of expansion term needed in the POT-FIT algorithm $\mathcal{P}$ [compare with equation (3.16)]. An approximation for $\mathcal{C}$ is given in section 4.5 in dependence of M, m_s and $\mathcal{P}$. Due to this advantageous scaling w.r.t. the number of grid points, the ML-MCTDHB algorithm can face larger number of grid points, making it possible to study either a finer grid spacing or larger grid length, respectively.

Notes about the symmetry conservation of the equations of motion: The here presented equations of motion do only conserve symmetries, including transformations of two or three coordinates e.g. rotations or reflections if the simulation is fully converged w.r.t. the expansion into 1D SPFs (m_1, m_2, m_3) [62]. In general, symmetry conservation can be ensured if symmetry-adapted coordinates are chosen, but this can lead to the non-separability of the interaction potential w.r.t. to these new coordinates. In such new coordinates, the interaction potential has to be transformed into a product form again by using the POT-FIT algorithm, which increases the computational effort, or a new appropriate interaction potential must be found, which is separable w.r.t. to these new coordinates if feasible at all. Furthermore, the new coordinates can lead to a non-equidistant grid spacing, which distorts the interaction in the laboratory frame.

ML-MCTDHB as an efficient GPE solver: If convergence w.r.t. the expansion into 1D-SPFs (m_1, m_2, m_3) is achieved and only one 3D-SPF is supplied $(M = 1)$, the ML-MCTDHB equations of motion reduces to the GPE (see appendix D.1). Actually the bare delta interaction $W(\mathbf{r}_1, \mathbf{r}_2) = g\delta(\mathbf{r}_1 - \mathbf{r}_2)$ can be used for such mean-field calculations, as we have discussed in section 3.1.2. It has the advantage that it is separable w.r.t. the dimensions and, thus, the algorithm of ML-MCTDHB, with its advantageous scaling w.r.t. the number of grid points, can

be used. Furthermore, the bare delta function reduces the computational effort w.r.t. the number of grid points to approximately a linear scaling $\sum_{s=1}^{3} m_s^4 q_s$, since one integration w.r.t. to the grid points of equation (4.20) can be performed analytically in order to calculate the mean-field operator matrix $\langle W \rangle_{ik}^{(s)}$. In contrast to the linear scaling of the interaction potential w.r.t. the number of grid points for ML-MCTDHB, the scaling of the MCTDHB algorithm (applying a product grid) behaves cubic $\sim q_1 q_2 q_3$. Thus, ML-MCTDHB is an efficient algorithm, which can be used to solve the GPE, in case minor spatial correlations are present in the system and $m_s \ll q_s$ can be applied.

4.5. Comparison between MCTDHB and ML-MCTDHB

This section deals with a comparison of the numerical effort between the MCTDHB method (see section 4.3) and the ML-MCTDHB method (see section 4.4). Here, *numerical effort* is defined as the number of floating point operations, which have to be performed at each instance in time in order to build up the equations of motions [see equations (4.8), (4.9) (4.17) and (4.16)]. We focus thereby on the numerical effort building-up the mean-field operator matrix for the two-body interaction operator between the MCTDHB and ML-MCTDHB algorithm since the computation of the remaining ingredients e.g., the one and two body density matrix as well as the projector, are computationally small and can be neglected. Furthermore, we only analyse a "brute force"[4] implementation for both the MCTDHB and ML-MCTDHB algorithm, since a concrete implementation can be quite tricky. Especially, we do not take symmetry arguments, parallelization or any other trick (see section 4.6) into account.

Table 4.1.: Shown is the numerical effort calculating the mean-field operator matrix for the two-body interaction operator using a brute force implementation for the MCTDHB and ML-MCTDHB algorithms. M (m_s) is the number of 3D-SPFs (1D-SPFs) and q_s is the number of grid points for the s-th degree of freedom. $\mathcal{P}$ is the total number of used POT-FIT terms (see equation (3.16)). The two abbreviations have been used $\mathbf{m} \equiv \prod_{s=1}^{3} m_s$ as well as $\mathbf{q} \equiv \prod_{s=1}^{3} q_s$.

Layer	Ingredient	method	Equation	Numerical effort
Top	v_{ijkl}	MCTDHB	(4.11)	$M^4 \mathbf{q}^4$
	v_{ijkl}	ML-MCTDHB	(4.22)	$\mathcal{P} M^4 \mathbf{m}^4$
Particle	$\langle W \rangle_{kl}^{(\chi)}$	MCTDHB	(4.13)	$M^4 \mathbf{q} + M^2 \mathbf{q}^4$
	$\langle W \rangle_{kl}^{(\chi)}$	ML-MCTDHB	(4.21)	$\mathcal{P}\left(M^4 \mathbf{m} + M^2 \mathbf{m}^4\right)$
Subparticle	$\langle W \rangle_{ik}^{(s)}$	ML-MCTDHB	(4.20)	$\mathcal{P} \sum_{s=1}^{3} m_s^4 q_s^4$

In table 4.1, we regard the numerical effort for building-up the mean-field operator matrix for the two-body interaction operator, which are needed in the equation of motions for both MCTDHB and ML-MCTDHB. We see that in comparison between the MCTDHB algorithm and ML-MCTDHB algorithm, the scaling of the total number of grid points ($\mathbf{q} \equiv \prod_{s=1}^{3} q_s$) for both the top and particle layer is substituted by the scaling w.r.t. the 1D-SPFs ($\mathbf{m} \equiv \prod_{s=1}^{3} m_s$)[5]. As already mentioned, if $m_s \ll q_s$, the ML-MCTDHB algorithm is much more efficient as the MCTDHB algorithm, however the computational effort of the ML-MCTDHB algorithm exceeds the computational effort of the MCTDHB algorithm if $m_s \sim q_s$, since, the additional, mean-field operator matrix elements for the subparticle layer have to be created. Furthermore, we see that

---

[4]With brute force implementation, we mean a direct implementation of the above equations of motions and ingredients.

[5]Here, $\mathbf{q}$ and $\mathbf{m}$ are not vectors.

the exponential scaling of the total number of grid points w.r.t. the dimensions $\propto \prod_{i=1}^{3} q_s^4$ in the MCTDHB algorithm is replaced by a linear scaling w.r.t. the dimensionality, $\propto \sum_{i=1}^{3} q_s^4$ in the ML-MCTDHB algorithm.

Table 4.2.: Number of coefficients for the MCTDHB and ML-MCTDHB method. The same notation as in table 4.1 is used. N is the number of bosons.

Layer	Method	Equation	Number of expansion coefficients
Top	MCTDHB	(4.4)	$\binom{N+M-1}{M-1}$
	ML-MCTDHB	(4.4)	$\binom{N+M-1}{M-1}$
Particle	MCTDHB	(4.5)	$M\mathbf{q}$
	ML-MCTDHB	(4.16)	$M\mathbf{m}$
Subparticle	ML-MCTDHB	(4.15)	$\sum_{s=1}^{3} m_s q_s$

Next, we have a look at the number of expansion coefficients (see table 4.2). Adding the subparticle layer does not mean necessarily that more expansion coefficients have to be propagated in time. Due to the product grid used in the MCTDHB algorithm, the MCTDHB algorithm needs $\binom{N+M-1}{M-1} + M\prod_{s=1}^{3} q_s$ expansion coefficients and this number of expansion coefficients can be larger than the number of expansion coefficients needed in the ML-MCTDHB algorithm $\binom{N+M-1}{M-1} + M\prod_{s=1}^{3} m_s + \sum_{s=1}^{3} m_s q_s$. Knowing the number of expansion coefficients, the computational effort can be determined for calculating the equations of motions (see table 4.3). We want to emphasise again that we regard only a brute force implementation, while using sophisticated algorithms this scaling can be improved significantly for both the MCTDHB and ML-MCTDHB algorithm[6].

Summarizing, two main differences between the MCTDHB and ML-MCTDHB algorithm can be recognized: First, the substitution from the scaling w.r.t. the number of grid points towards a scaling w.r.t. the number of 1D-SPFs and second the replacement of the exponential scaling of the total number of grid points to a linear scaling w.r.t. the dimensions.

Table 4.3.: Numerical effort for determining the equations of motion for the MCTDHB and ML-MCTDHB algorithm. The same notation as in table 4.1 is used. N is the number of bosons.

Layer	Method	Equation	Numerical effort
Top	MCTDHB	(4.8)	$\binom{N+M-1}{M-1}^2$
	ML-MCTDHB	(4.8)	$\binom{N+M-1}{M-1}^2$
Particle	MCTDHB	(4.9)	$M^3\mathbf{q}$
	ML-MCTDHB	(4.16)	$M^3\mathbf{m}$
Subparticle	ML-MCTDHB	(4.17)	$\sum_{s=1}^{3} m_s^3 q_s$

Analysing the total computational effort, we can identify three different computational "bottlenecks".

i. The exponential scaling w.r.t. the number of particles, occurring both in MCTDHB and ML-MCTDHB. This scaling additionally depends on the number of 3D-SPFs [see equation (4.6)].

---

[6]E.g., the numerical effort for propagating the top layer coefficients can be reduced to $\binom{N+M-1}{M-1}M^2 + \binom{N+M-3}{M-3}M^4$ (see reference [62]).

ii. Although the scaling of the number of grid points has been improved in ML-MCTDHB, it still enters the computational effort with the fourth power for non-local interaction potentials.

iii. The evaluation of the mean-field operator matrix for the two-body interaction operator scales w.r.t. both 3D and 1D SPFs as M^{16}, where we have set $M = m_s$.

In the next section, we report how these bottle necks can be circumvented.

4.6. Implementation of the algorithm

In this section, we report on specific problems, which occur when implementing the ML-MCTDHB algorithm. As already mentioned in section 4.5, the algorithm suffers from three numerical bottlenecks. We show how these bottlenecks can be circumvented and how further approximations can be used to additionally reduce the numerical effort.

i. **The exponential scaling w.r.t. the number of particles:**
The exponential scaling w.r.t. the number of particles can be reduced either by a selection of the most important configurations [248,284] or by introducing a coherent-tail [285]. This coherent tail takes care of contributions from higher number states and the algorithm need less number states in order to obtain the same accuracy in comparison to a simulation without using the concept of the coherent-tail. Furthermore, the calculation of the matrix element $\langle \vec{n}|H|\vec{m}\rangle$ can be parallelized using high performance computing tools such as OpenMP [286] or OpenMPI [287]. With characterized parameters for our simulations (see chapters 5-7), we have not reached this kind of bottleneck and therefore, we do not focus on this bottleneck any further.

ii. **Scaling w.r.t. number of grid points:**
If the interaction potential obeys $W(\mathbf{r}_1, \mathbf{r}_2) = W(|\mathbf{r}_1 - \mathbf{r}_2|)$ and is real valued, some serve consequences can be drawn resulting in a huge reduction of the numerical effort. Both requirements are usually fulfilled for all physical two-body short-range interaction potentials (see table 3.1). A first consequence is that the interaction potential is local, resulting in an enormous reduction of the numerical effort w.r.t. the number of grid points by $q_s^4 \to q_s^2$ for the calculation of the mean-field operator matrix for the two-body interaction operator $\langle W \rangle_{ik}^{(s)}$. A second consequence is that symmetry properties exist $W_{ijkl}^{(s)} = W_{jilk}^{(s)} = W_{klij}^{*(s)} = W_{lkji}^{*(s)}$ leading to another reduction of the numerical effort w.r.t. the number of 1D-SPFs. Lastly, one can use a very efficient algorithm, called the Interaction Matrix Evaluation by Successive Transforms (IMEST) [234]. Using IMEST, the interaction potential is transformed via a Fast Fourier Transformation (FFT) into Fourier space, and then, the integration over the two dimensional grid declines into two separate integrations. A short description of the algorithm is given in the appendix C.5. In doing so, the numerical effort can be reduced further from q_s^2 to $\propto 3q_s \log q_s$.

iii. **Scaling w.r.t. the number of both 3D and 1D SPFs:**
The calculation of the mean-field operator matrix for the two-body interaction operator scales with M^{16} (setting $M = m_s$) w.r.t. the number both 3D and 1D SPFs. In order to reduce the numerical effort, two different strategies can be followed. The first strategy is to perform the summation over each index individually and store the resulting higher dimensional matrix temporarily. We illustrate this by a small example, which calculates

$S = \sum_{ij} A_{ij} B_i C_j$:

$$D_j = \sum_i A_{ij} B_i$$

$$\text{save} \quad D_j$$

$$S = \sum_j D_j C_j$$

In doing so, we can reduce the scaling w.r.t. to the number of both 3D and 1D SPFs to M^{10}, as long as that the time of storing and loading the temporary data is tolerable. The second strategy is the parallelization of summation using OpenMP in order to reduce the numerical effort further to $M^{10-\eta}$, where η is the number of parallelized summations.

In the ML-MCTDHB algorithm, we have implemented the second and third mentioned strategies. The first strategy is not implemented, since it is a further approximation to our wave function, which we try to avoid. All in all, the ML-MCTDHB algorithm can be used on desktop computers with efficient runtimes (see figure 4.3).
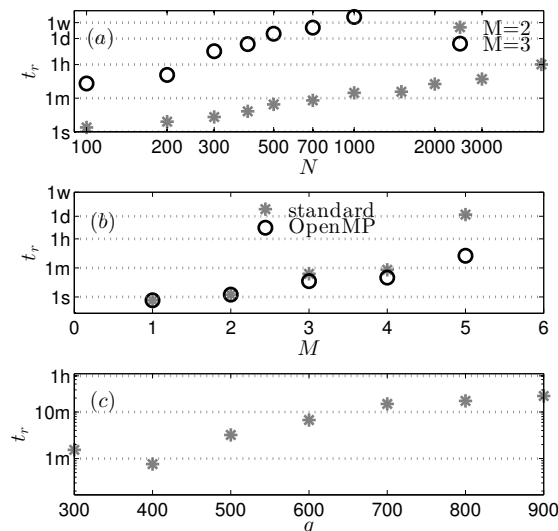
Figure 4.3.: Numerical effort in dependence of (a) number of particles N, (b) 3D-SPFs M and (c) grid points per dimensions $q = q_s$. For the time axis, a logarithmic scale is used and the time is scaled w.r.t. the harmonic trap frequency. We used the abbreviations 1s (one second), 1m (one minute), 1h (one hour), 1d (one day) and 1w (one week).

In order to get a better feeling for the performance of the ML-MCTDHB algorithm, we measure the numerical effort by comparing the real(wall time) time t_r, which the ML-MCTDHB algorithm needs to propagate an initial wave function up to a certain time point t_s, i.e., a certain number of iterations steps. The number of iteration steps is large enough that initialization processes of the algorithm can be neglected. The system, which we regard, consists of two bosons in a three-dimensional, isotropic, harmonic trap. We prepare the systems ground state and induce dynamics by a sudden quench of the two-particle interaction strength from $h = 0$ to $h = 1000$. The two-particle interaction is modelled by the Gaussian interaction potential [see equation (3.18)]. The reference calculation has the numerical parameters $M = m_1 = m_2 = m_3 = 2$, $n = q_1 = q_2 = qn_3 = 128$ and we study deviations from this reference calculation in the following. We change the number of particles, the number of 3D-SPFs and the number of grid points separately in figure 4.3(a), (b), and (c), respectively. In figure 4.3(a), the computational effort

is plotted in dependence of the number of particles N for both $M = 2$ (grey stars) and $M = 3$ (black circles). For $M = 2$, the scaling $\binom{N+M-1}{M-1}$ becomes linear, while for $M = 3$, one recognize the exponential growth of the number of configurations. For example, approximately two weeks are needed in order to simulate 1000 particles with $M = 3$. In figure 4.3(b), we compare a parallelized implementation (black circles) with a non- parallelized (grey stars). Parallelization is implemented by demanding $\eta = 1$ parallel processes. The computational overhead has been analysed using Intel VTunes [288] and has been reduced whenever it was possible. The parallelized implementation significantly reduces the numerical effort for larger values of 3D-SPF M (for example for $M = 4$ by a factor of 3). Fluctuations in the processor frequency, the waiting times for the I/O streams, spin times and overhead times are reduced by performing the measurements several times and calculating their average. In the last figure 4.3(c), the advantage scaling w.r.t. the number of grid points of ML-MCTDHB is shown. A MCTDHB calculation, based on a product grid, cannot achieve these large number of grid points, for example for $q = 900$, the product grid has 729.000.000 grid points, whereas with the linear scaling of the ML-MCTDHB algorithm, we obtain only 2700 grid points.

4.7. Validation of the algorithm

In order to validate the implementation of our algorithm presented in section 4.4, we compare the energy, wave function and density w.r.t. either known analytical solutions or other established numerical algorithms available in literature. Both the ground state properties as well as the dynamical properties are analysed.

i. **Comparison with analytical solutions:**
The many-body Hamiltonian with harmonic interaction (given in length units of $\sqrt{\hbar/m\omega}$, where m is the mass and ω is the trap frequency for an isotropic harmonic trap)

$$ H = \sum_{i=1}^{N} \left(-\frac{1}{2} \nabla_{\mathbf{r}_i}^2 + \frac{1}{2} \mathbf{r}_i^2 \right) \pm g \sum_{1 \leq i < j \leq N} (\mathbf{r}_i - \mathbf{r}_j)^2 \tag{4.24} $$

can be solved analytically and the ground state energy is $E_{ana} = 3(N-1)/2 \sqrt{1 \pm 2Ng} + 3/2$ [203, 205]. The analytical solution is used as a benchmark for our simulations. Numerically, the ground state energy can be obtained by an imaginary time propagation of the ML-MCTDHB equations of motion and we compare the numerical with the analytical results in table 4.4. We see that increasing the number of 3D-SPFs, the numerical result converges to the analytical one. For an interaction strength of $g = 0.01$, we obtain a good agreement with the analytical result already at $M = 8$.

ii. **Comparison with other mean-field implementation:**
We compare the mean-field results obtained by ML-MCTDHB ($M = 1$, solving the GPE), with the established MATLAB tool GPELab [289–291] for different anharmonic trap geometries and a bare delta interaction potential. The Hamiltonian is

$$ H = \sum_{i=1}^{N} \left(-\frac{1}{2} \nabla_{\mathbf{r}_i}^2 + \frac{\eta}{2} (\mathbf{x}_i^2 + \mathbf{y}_i^2) + \frac{1}{2} \mathbf{z}_i^2 \right) + g \sum_{1 \leq i < j \leq N} \delta(\mathbf{r}_i - \mathbf{r}_j) \tag{4.25} $$

where η is the aspect ratio between the transversal and longitudinal trap frequency. We compare in table 4.5 the ground state energy obtained for two particles and different interaction strengths. Independent of the interaction strength or the aspect ratio, the obtained ground state energies agree very well.

iii. **Comparison with MCTDHB:**
We can use the MCTDHB method [60] with artificial interaction potential (which are already given in a product form w.r.t. dimensions), in order to validate the ML-MCTDHB algorithm. In doing so, we have to reduce the number of grid points, in order to make the simulation feasible. We have checked the following interaction potentials in an isotropic harmonic trap, with $\mathbf{r}_i$ being the vector $\mathbf{r}_i = (x_i, y_i, z_i)^T$:

(a) $W(\mathbf{r}_1, \mathbf{r}_2) = g(\mathbf{r}_1 - \mathbf{r}_2)^2 = g(\mathbf{r}_1^2 - 2\mathbf{r}_1\mathbf{r}_2 + \mathbf{r}_2^2)$, with $g = 0.1$ and for two particles. The numerical parameters are $M = m_1 = m_2 = m_3 = 3$ and $q_1 = q_2 = q_3 = 20$.

(b) $W(\mathbf{r}_1, \mathbf{r}_2) = g\exp(x_1^2/S^2 + x_2^2/S^2 + y_1^2/S^2 + y_2^2/S^2 + z_1^2/S^2 + z_2^2/S^2)$, with $g = 10$ and $S = 1$ for two particles. The numerical parameters are $M = m_1 = m_2 = m_3 = 3$ and $q_1 = q_2 = q_3 = 10$.

(c) $W(\mathbf{r}_1, \mathbf{r}_2) = g\delta(\mathbf{r}_1 - \mathbf{r}_2)$, which can also be brought into a product form using a trick, presented in the appendix D.2. The interaction strength is set to $g = 0.1$ for two particles and the numerical parameters are $M = m_1 = m_2 = m_3 = 3$ and $q_1 = q_2 = q_3 = 11$.

(d) $W(\mathbf{r}_1, \mathbf{r}_2) = g$, with $g = 1$ and same parameter as above.

Due to the artificial interaction potentials and the reduced number of grid points, the obtained results are quite unphysical and not converged. We have checked the difference of the two methods for the energy and density profile and for both relaxation and propagation, where dynamics have been induced by a quench in the interaction strength. The maximal observed relative deviation in all these simulations is smaller than 10^{-6}, which is quite satisfying.

Table 4.4.: Comparison of the ground state energy between the ML-MCTDHB and the analytic solution of the harmonic interaction potential with two particles and the interaction strengths $g = 0.1$ as well as $g = 0.01$ in dependence of the number of 3D-SPFs $M = \{2, 4, 6, 8\}$.

	$g = 0.01$	$g = 0.1$
E_{ana}	3.029705854	3.2748239349
$E_{M=8}$	3.029705858	3.274**64469**
$E_{M=6}$	3.029705860	3.2748**77909**
$E_{M=4}$	3.029705865	3.274**904647**
$E_{M=2}$	3.029**802938**	3.**282511714**

Table 4.5.: Comparison of the ground state energies between GEPLab and the ML-MCTDHB implementation for two particles with $M = 1$ and $m = m_1 = m_2 = m_3 = 3$. In the left column a harmonic isotropic trap $\eta = 1$ is assumed and the interaction strength g is varied. In the right column the interaction strength is constant $g = 4$ and the aspect ratio is increased, deforming the trap into a more cigar shaped potential.

g	GPELab	ML-MCTDHB	η	GPELab	ML-MCTDHB
1	3.0617826	3.0617826	1	3.2301755	3.2301755
3	3.176498**5**	3.176498**6**	3	7.655996**5**	7.655996**6**
6	3.331509**2**	3.331509**5**	6	14.231841	14.231841
9	3.4712339	3.4712339	9	20.75375**3**	20.75375**5**

Part II.

Preparations and Applications

TWO PARTICLES IN AN ELONGATED TRAP

After working out an efficient numerical algorithm in order to study many-particle correlations in three dimensions in chapter 4, we have to tackle new questions, concerning the numerical parameters for a concrete implementation and the convergence behaviour of the algorithm. In this section, we give answers to the following questions:

  i. How fine resolved must be the grid spacing $\Delta_s = L_s/q_s$ in order to model the interaction potential properly, where L_s and q_s are the grid length and the number of grid points, respectively, where s denotes the different dimensions $s = \{1, 2, 3\}$? How large must be the grid length L_s so that the wave function drops to zero at the boundary?

  ii. How large can be the zero-energy scattering length a_0, created by the interaction potential, until the transversal confinement, characterized by the length scale $l_\perp$, influences the interaction? Can the unitary interaction regime [14, 15] be reached and can Confinement Induced Resonances (CIR) be numerically observed for a large enough aspect ratio? Is it possible to obtain a strong fragmented ground state for a tight transversal confinement, still ensuring short-range interactions between the particles?

  iii. How fast does the numerical result converge and how large must be the numbers of SPFs in order to get the numerical error tolerable?

  iv. On which time scale can the interaction induce spatial correlations?

  v. How large has to be the aspect ratio η so that the transversal degrees of freedom can be integrated out and one ends up with a pure one-dimensional description of the system?

In order to answer these questions, we analyse two interacting bosons in an either isotropic or anisotropic harmonic trap. The dimensionless Hamiltonian equation reads then[1]

$$\mathcal{H} = \sum_{i=1}^{N=2} \left[H_\parallel(z_i) + H_\perp(x_i, y_i) \right] + W_{RG}(\mathbf{r}_1, \mathbf{r}_2), \tag{5.1}$$

with $\mathbf{r_i} = (x_i, y_i, z_i)^T$ the position of the i-th boson. The longitudinal and transversal single-particle Hamiltonians are given by

$$H_\parallel(z) = -\frac{1}{2}\nabla_z^2 + \frac{1}{2}z^2$$

$$H_\perp(x, y) = -\frac{1}{2}\nabla_x^2 - \frac{1}{2}\nabla_y^2 + \frac{1}{2}\eta^2(x^2 + y^2),$$

---

[1]We use position representation for the operators.

Table 5.1.: List of used numerical and physical parameters. The index s stands for the three dimension $s = \{1, 2, 3\}$.

numerical parameters	physical parameters
L_s grid length	η aspect ratio
q_s number of grid points	h height of the interaction in 3D
m_s number of 1D-SPFs	σ width of the interaction both in 3D and 1D
M number of 3D-SPFs	N number of particles

where η is the aspect ratio between the transversal $\omega_\perp$ and longitudinal $\omega_\parallel$ trap frequencies, $\eta = \omega_\perp / \omega_\parallel$. For $\eta = 1$, an isotropic three-dimensional harmonic trap potential is recovered. In this case, if the transversal characteristic trap length $l_\perp = \sqrt{\hbar / \omega_\perp m}$ equals the longitudinal characteristic trap length $l_\parallel = \sqrt{\hbar / \omega_\parallel m}$, we set $l_{trap} = l_\perp = l_\parallel$. For $\eta < 1$ we obtain pancake like traps, performing a crossover towards two dimensions and for $\eta > 1$ cigar shaped, i.e. elongated, traps are obtained. We are interested in the crossover from three to one dimension and vary the aspect ratio form 1 towards 100. The units of energy and length are given in $\hbar \omega_\parallel$ and $l_\parallel$, respectively. The interaction potential is given by the renormalized Gaussian interaction potential [see equation (3.18)]

$$W_{RG}(\mathbf{r}_1, \mathbf{r}_2) = h \exp(-r_{12}^2 / \sigma_{eff}^2), \tag{5.2}$$

where $r_{12} = |\mathbf{r}_{12}|$ is the relative distance between the 1-st and 2-nd boson and $\sigma_{eff} = \sigma / \ln(h/\epsilon)$ is the effective width of the Gaussian, depending on the width σ and height h, renormalized to a small energy scale, $\epsilon = 1$. Due to the renormalization, the width of the Gaussian is limited and independent of the height. The advantages for using the renormalized interaction potential have been already discussed in section 3.2. In order not to confuse the reader, we give an overview of the used numerical and physical parameters in table 5.1.

The upper setup has the advantage that the two-body Hamiltonian can be separated into a relative and centre of mass (CM) part using the transformation $\mathbf{R} = (\mathbf{r}_1 + \mathbf{r}_2)/\sqrt{2}$ and $\mathbf{r} = (\mathbf{r}_2 - \mathbf{r}_1)/\sqrt{2}$. The relative and centre of mass Hamiltonians read then

$$H_{CM} = -\frac{1}{2}\nabla_{\mathbf{R}}^2 + \frac{1}{2}\mathbf{R}^2 \tag{5.3}$$

$$H_{rel} = -\frac{1}{2}\nabla_{\mathbf{r}}^2 + \frac{1}{2}\mathbf{r}^2 + h e^{-2\frac{\mathbf{r}^2}{\sigma_{eff}^2}}. \tag{5.4}$$

This separation has two serious consequences: First, the Hamiltonian (5.4) is a one-particle Hamiltonian and can be numerically solved easily. Second, the variance for the ground state of the CM $var(\mathbf{R}) = \sqrt{\langle \mathbf{R}^2 \rangle - \langle \mathbf{R} \rangle^2}$ can be calculated analytically and serves us as an additional strict tool to check convergence for the simulation [292].

The remaining of the chapter is structured as follows: In section 5.1, we discuss the length scales of the system. In doing so, we give an answer to the upper questions (i) and (ii). In section 5.2, the convergence behaviour of the two particle system is studied in detail and upper limits for the physical parameters, i.e., the interaction height, are determined [see question (iii)]. Section 5.3 provides the answers to the questions (iv) and (v). In doing so, a quench of the transversal trap frequency is used to induce spatial correlations. Next, in section 5.4, we discuss the conditions to obtain a pure one-dimensional system. Finally, a summary of this section is given in section 5.5.

5.1. Numerical resolution of different length scales

In this section, we give an estimation of the order of magnitude of the various length scales in the system, which appear for interacting bosons in an isotropic harmonic trap. The grid spacing Δ_s is the finest length scale and must be fine enough in order to resolve the width of the interaction potential correctly, $\Delta_s < \sigma$. Furthermore, in comparison with experimental achievable values, the range of the interaction potential must be smaller than the characteristic length scale of the trap $\sigma \ll l_{trap}$ in order to model short-range interactions correctly. At the boundary of the grid, the density must drop to zeros, in order to avoid that boundary effects affect the simulation results, giving an additional constrain to the grid length L_s, $l_{trap} < L_s$. Summarizing, the occurring length scales in the system must satisfy

$$\Delta_s < \sigma \ll l_{trap} < L_s. \tag{5.5}$$

In the following, we discuss in more detail the influence of each length scale and estimate their minimal and/or maximal values.

Influence of the grid spacing: We want to answer the question, how fine must be the grid spacing in order to resolve the interaction potential correctly. In doing so, we chose a large grid length $L = L_s = 12$ so that the density drops to zero at the boundary. The behaviour of the ground state energy is analysed in dependence of the grid spacing $\Delta = \Delta_s$ and we define the maximal valued of the grid spacing, when the ground state energy becomes constant in dependence on Δ. The grid spacing Δ is decreased by increasing the number of grid points $q = q_s$, while keeping the other numerical parameters ($M = 2$, $m_1 = m_2 = m_3 = 3$) and physical parameters (h, $\sigma = 0.1$) fixed. We perform four different simulations with the interaction heights $h = \{27, 125, 512, 1000\}$, respectively. The results are shown in figure 5.1a. We note that the ground state energy converges to a constant value w.r.t. h for a grid spacing approximately smaller than the half of the interaction width σ, namely $\Delta = 0.05$. Due to the advantageous property of the renormalized interaction potential (that it approaches the shape of the hard-core interaction potential with size σ for $h \to \infty$), the interaction height can be arbitrary increased, without any significant influence on the convergence behaviour.

Influence of the grid length: Again, we look for a converged ground state energy, however this time in dependence of the grid length L keeping the grid spacing $\Delta = 0.02$ and the other numerical parameters constant (same parameters as above). We perform the three simulations for different number of particles $N = \{2, 5, 10\}$, respectively, since more particles cause a broader wave function, which may interfere with the boundary. The parameters for the interaction potential are $h = 10$ and $\sigma = 0.1$. Figure 5.1b shows the ground state energy divided by the particle number, and we observe that a grid length of $L > 7$ is sufficient to ensure a converged ground state energy. Furthermore, it seems that the expected broadening of the wave function in dependence on the number of particles is a minor effect and is neglected in the following discussion.

Influence of the transversal characteristic trap length: We want to estimate the influence of the trap onto the short-range scattering properties. In doing so, we increase the aspect ratio η, starting from one, and analyse the interaction energy $E_{int} = \langle W_{RG} \rangle$ in dependence of η. The result is shown in figure 5.2a for different interaction widths $\sigma = \{0.1, 0.2\}$ and a constant interaction height $h = 10$ both for a mean-field ($M = 1$) and a beyond mean-field ($M = 4$) simulation. In the mean-field simulation, the interaction energy increases unlimited if η is increased. However, in the beyond mean-field simulation, the interaction energy drops
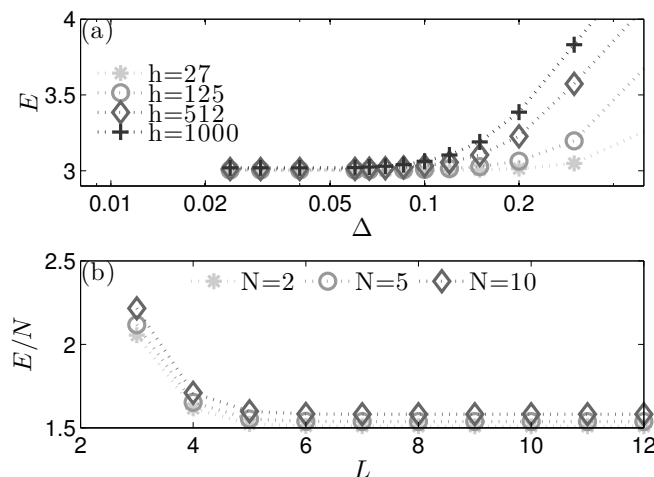
Figure 5.1.: Panel (a) shows the ground state energy E in dependence on the grid spacing Δ for different interaction heights $h = \{27, 125, 512, 1000\}$, labelled by asterisk, circles, diamonds and crosses, respectively. Panel (b) shows the ground state energy E in dependence on the grid length L for different number of particles $N = \{2, 5, 10\}$, marked by asterisk, circles and diamonds respectively.

towards zero if the aspect ratio is increased, because for strong transversal confinements (quasi-one dimensional case) and strong interactions, two different particles can repel each other and the overlap of their wave functions approaches zero, and thus the interaction energy is reduced as well. This fragmentation of the wave function can be observed in one dimension [84,87,129,210]. We observe fragmentation at an aspect ratio larger than $\eta > 10$ for $\sigma = 0.2$ and $\eta > 50$ for $\sigma = 0.1$. As we will see in section 5.4, at these large aspect ratios, we are already in a pure one-dimensional regime, and therefore, the observed fragmentation process is an artefact induced by the finite-range interaction potential.

However, we are interested in a *direct* influence of the aspect ratio on the interaction energy, since by changing the transversal confinement, the density is modified in the trap, and therefore also the scattering properties. In the following, we try to eliminate this effect from the interaction energy: For a very tight transversal confinement, due to the separation of the longitudinal and transversal energy scale, the transversal degrees of freedom can be integrated out (assuming transversally a harmonic oscillator wave function), leading to a renormalization of the interaction height in dependence of the aspect ratio $h_{1D} = h f(\eta, \sigma_{eff})$ with $f(\eta, \sigma_{eff}) = \eta \sigma_{eff}^2 / (2 + \eta \sigma_{eff}^2)$. The interaction energy depends on η via $f(\eta, \sigma_{eff})$ and we renormalize the interaction energy w.r.t. $f(\eta, \sigma_{eff})$ and furthermore normalize the outcome to unity, $\bar{f} = f(\eta, \sigma_{eff}) \max(E_{int})$. The resulting interaction energy is shown in figure 5.2b. We identify a regime for $\sigma = 0.1$, from $\eta = 1$ towards $\eta \sim 10$, in which the renormalized interaction energy $E_{int}/\bar{f}$ is constant in dependence of η. In this regime, the trap potential has no *direct* influence on the short-range interaction and the scattering between the two particles can be assumed to take place in free space. For $\sigma = 0.2$, however, we do not find such a regime.

Summary: We have found the following values for the different length scales in the system in order to ensure convergence w.r.t. the grid spacing and grid length and furthermore in order to ensure short-range interaction w.r.t. the transversal confinement.

$$\Delta = 0.05 \quad < \quad \sigma = 0.1 \quad \ll \quad l_\perp = (0.3 \dots 1) \quad \leq \quad l_\| = 1 \quad < \quad L = 7.$$
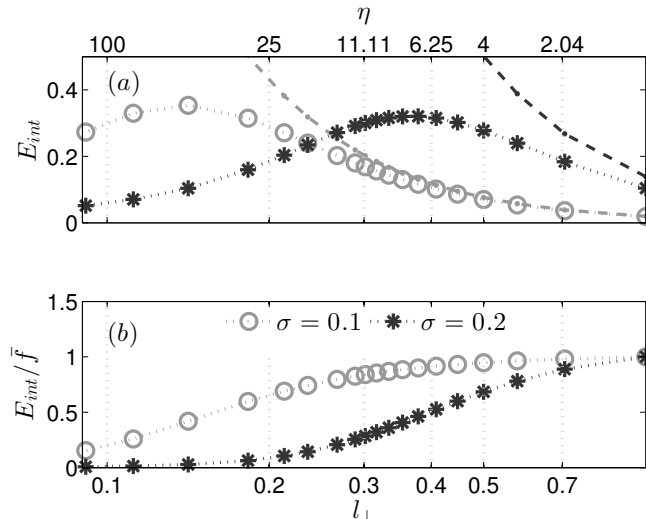
Figure 5.2.: (a) Interaction energy E_{int} for $\sigma = 0.1$ (both light grey lines) and $\sigma = 0.2$ (both dark grey lines) for a BMF calculation (circles and stars) and a MF calculation (dashed lines). (b) Interaction energy divided by $\bar{f} = \max(E_{int})\eta\sigma_{eff}^2/(2 + \eta\sigma_{eff}^2)$. Same labels as in panel (a).

At least 140 grid points are needed in every dimension. In order to avoid convergence problems w.r.t. the number of grid points, we chose a significantly higher number of grid points, at least twice the number of grid points, namely 280. We note that the ML-MCTDHB algorithm can handle even more grid points without any significant loss of efficiency (up to 1000 grid points per dimension).

5.2. Convergence with respect to the 3D single particle functions

Due to the special choice of our short-range interaction potential, the maximal zero-energy scattering length a_0 is limited by $a_0 \leq \sigma$, where the zero-energy scattering length depends on the two interaction potential parameters h and σ. But how large can a_0 be made, ensuring converged simulations? How many 3D-SPFs are needed in order to obtain converged simulations and how fast do the numerical simulations converge w.r.t. the 3D-SPFs? To answer these questions, we simulate again two particles in an isotropic three-dimensional, harmonic trap and change the zero-energy scattering length by changing the height of the interaction from $h = 8$ to $h = 1000$ for a fixed width $\sigma = 0.1$. We compare the numerical ground state energy with the analytical result, which has been derived using the regularized delta interaction potential [201], calling E_{ana}. Due to the shape independence of the short-range interaction potential, this interaction potential can be used, or alternatively, the relative Hamiltonian can be also solved numerically with the regularized interaction potential [see equation (5.4)], which leads to similar results as the analytical calculation. Here, we define a simulation as converged if the ground state energy does not differ more than 0.1 % from the analytical solution[2].

In figure 5.3a, the ground state energy is given in dependence of the zero-energy scattering length a_0 (i.e. the interaction height h) for different numbers of 3D-SPFs $M = \{1, 2, 3, 4\}$. The number of 1D-SPFs are set to $m = m_1 = m_2 = m_3 = 3$, which is sufficient in order to ensure convergence w.r.t. the 1D-SPFs, as can be seen by simulations with $m = 4$ (not shown). Increasing a_0 leads to a larger deviation between the analytic solution E_{ana} and the numerical

---

[2]In general, we define a simulation converged if the observable of interest does not modified by changing the number of single particle functions.
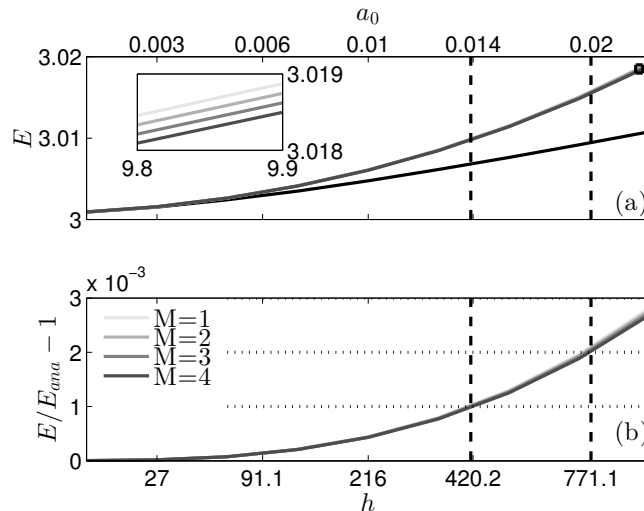
Figure 5.3.: (a) Ground state energy E for two particle in a three-dimensional, isotropic harmonic trap with the interaction potential W_{RG} [see equation (3.18)] in dependence of the zero-energy scattering length a_0 (i.e., interaction height h) and w.r.t. different numbers of 3D-SPFs M. The number of 1D-SPFs are $m = m_1 = m_2 = m_3 = 3$. Light grey towards dark grey lines correspond to $M = \{1, 2, 3, 4\}$, respectively. The black line is the analytic solution E_{ana} [201]. The inset in panel (a) is a magnification of the small black square in the right upper corner. (b) Relative deviation of the ground state energy in dependence of the zero-energy scattering length.

results. However, increasing the number of 3D-SPFs M, the difference is not significantly reduced. The worse convergence behaviour in dependence on M can be seen in the inset of figure 5.3a, which shows a zoom of the interaction height in the range between $h = 941$ and $h = 970$ (right upper rectangle in the main plot of figure 5.3). We approximately see a linear behaviour of the convergence in dependence on M. This bad convergence behaviour is intrinsic and studied in the next paragraph in more detail. A linear extrapolation would lead to approximately $M \sim 85$ numbers of 3D-SPFs so that the numerical solution would agree with the analytical one, which is numerically infeasible. Therefore, here, we define a simulation as converged if the relative error $E/E_{ana} - 1$ is smaller than 0.1%. The relative error is plotted in figure 5.3b. In doing so, we can reach a maximal zero-energy scattering length of $a_0 = 0.014$ i.e. an interaction height of $h \sim 420$.

The enormous deviation between the numerical and analytical ground state energy comes from the fact that MCTDHB has difficulties, as many numerical methods, to correctly resolve kinks occurring in the relative wave function into a finite set of smooth basis functions defined in the laboratory frame. This problem of coordinate transformation is quite general and does not depend on the dimensions [212]. Examples for wave functions with a kink are: high correlated one-dimensional, bosonic systems [229], or in general three-dimensional wave functions, where the relative wave function behaves as $\propto 1/|r|$ and has a kink at $r = 0$. In reference [293], Giesbertz and van Leeuwen have shown that for a relative wave function with a kink, the natural populations decay algebraically, whereas for smooth relative wave functions they find an exponential decay of the natural populations. For two particles in an isotropic harmonic trap, the decay of the natural populations can be estimated (using a similar calculation as in reference [293]). The relative Hamiltonian can be solved analytically [201], and in the limit for $kr < 1$, the two-body wave function can be approximated by $u(\mathbf{r})u(\mathbf{R})/|\mathbf{r}|$, where $u(r) > 0$ is a
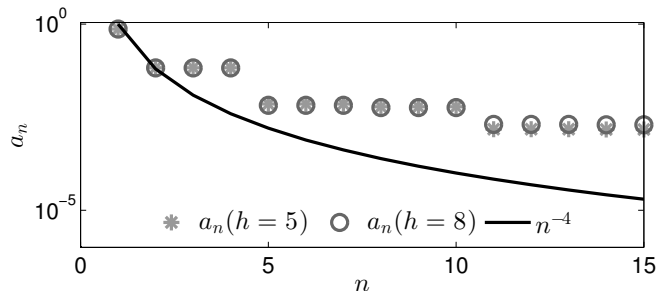
Figure 5.4.: Shown are the first 15 natural populations for two different interaction strengths $h = 5$ (light grey stars) and $h = 8$ (dark grey circles). The solid black line corresponds to the approximation [see equation (5.10)] $a_n \propto n^{-4}$. Note the logarithmic scale on the y-axis.

Gaussian $u(r) = \pi^{-1/4} \exp(-\mathbf{r}^2/2)$. Transforming the wave function into laboratory frame gives

$$\Psi(\mathbf{r}_1, \mathbf{r}_2) = \frac{u(\mathbf{r}_1)u(\mathbf{r}_2)}{|\mathbf{r}_1 - \mathbf{r}_2|}. \tag{5.6}$$

The eigenvalues a_n and eigenfunction $|\alpha_n\rangle$, which are linked to the one-body reduced density matrix (see appendix D.3), can be determined directly [see equation (D.7)] from equation (5.6)

$$\int d^3\mathbf{r}_2 \ \Psi(\mathbf{r}_1, \mathbf{r}_2)\alpha_n(\mathbf{r}_2) = \sqrt{a_n}\alpha_n(\mathbf{r}_1). \tag{5.7}$$

We insert equation (5.6) into equation (5.7) and use the definition $A_n(\mathbf{r}) = \alpha_n(\mathbf{r})/u(\mathbf{r})$, namely a renormalization of the natural orbitals

$$\int d^3 r_2 \ \frac{u^2(\mathbf{r}_2)}{|\mathbf{r}_1 - \mathbf{r}_2|} A_n(\mathbf{r}_2) = \sqrt{a_n}A_n(\mathbf{r}_1). \tag{5.8}$$

We let act the Laplace operator ∇_1^2 on $\mathbf{r}_1$ for both sides of the equation and use the relation $\nabla_1^2(1/|\mathbf{r}_1 - \mathbf{r}_2|) = -4\pi\delta(\mathbf{r}_1 - \mathbf{r}_2)$,

$$\nabla_1^2 A_n(\mathbf{r}_1) = -\frac{4\pi}{\sqrt{a_n}}u^2(\mathbf{r}_1)A_n(\mathbf{r}_1). \tag{5.9}$$

This differential equation can be solved for hard wall boundary conditions and further for small values of $\mathbf{r}_1$, leading to the approximation $u(\mathbf{r}) \sim 1$. We see that the natural populations in dependence of n decays algebraically

$$a_n \propto n^{-4}. \tag{5.10}$$

In order to get a deeper insight into the intrinsic problem of transforming a kinked wave function from the relative frame into the laboratory frame, we numerically determine the natural populations a_n for the analytical solution $\Psi_{ana}(\mathbf{R}, \mathbf{r})$, given by reference [201]. We note that $\Psi_{ana}(\mathbf{R}, \mathbf{r})$ is separable in the CM and relative coordinates, however, the natural orbitals are given in the laboratory frame. The natural populations are determined by using the POT-FIT algorithm [232, 233] up to the $I = 30$ order, $\Psi_{ana}(\mathbf{R}, \mathbf{r}) = \sum_{i=1}^{I} \sqrt{a_i}\alpha_i(\mathbf{r}_1)\alpha_i(\mathbf{r}_2)$. The result is shown in figure 5.4, where we compare the natural populations for two different interaction strengths, $h = 5$ and $h = 8$ with the approximation (5.10). As expected, the natural populations decay algebraically (note the logarithmic scale in figure 5.10) and they are three fold degenerated, due to the symmetry of the isotropic harmonic trap. For larger interaction strengths, the decay of the natural populations is even worse. In conclusion, due to the algebraic decay of the natural populations, it is very challenging to achieve convergence for large interaction strengths. In order to circumvent this challenge, we have to come up with a new strategy:
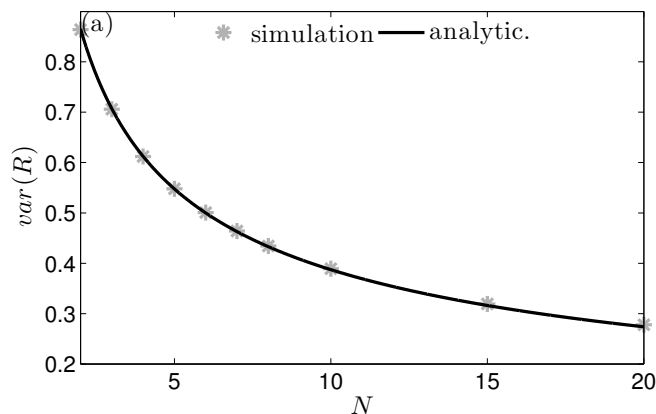
Figure 5.5.: Variance of the CM ground state $var(R)$ with $h = 125$ in dependence of the number of particles.

The strength of correlations can be defined as $\gamma = N^{1/3}a_0$ (see section 1.1), and therefore, there are two ways in order to increase γ: The first one is to increase the zero-energy scattering length a_0 (i.e. the interaction strength), as we have done before, and the second one is to increase the number of particles N. In order to see that increasing the number of particles does not influence our intrinsic convergence problem discovered before, we increase the number of particles N from two to twenty and keep the interaction strength fixed $h = 125$, therefore increasing γ. In order to judge the convergence of our simulations, we compare the variance of the CM, $var(R) = \sqrt{\langle R^2 \rangle + \langle R \rangle^2}$, for the numerical obtained ground state with the analytical solution in dependence of the number of particles (see figure 5.5). We find a good agreement between the analytical and computational result. This strategy paves the way to systems with higher correlations.

In summary, due to the intrinsic convergence problem of expressing a kink in the relative wave function into the laboratory frame, and thus the corresponding algebraic decay of the natural populations, the interaction strength must be limited to $h < 470$ in order to ensure a relative error of the ground state energy smaller than 0.1%. Higher correlated systems can be achieved by increasing the number of particles. This strategy is followed in the upcoming chapters.

5.3. Interaction induced spatial correlations

In the following section, we give an estimation of the various time scales in the system induced solely by the interaction. In doing so, we quench five bosons in an elongated harmonic trap from the aspect ratio $\eta = 4$ to $\eta = 5$. The longitudinal dimension is untouched. For one particle, the time-evolution of the wave function can be solved analytically, see appendix E.1. Since we are not interested in particle correlations, convergence is achieved with the numerical mean-field configuration $\mathcal{C} = (1; 2, 2, 3)$ with 250 and 300 number of grid points in the longitudinal and transversal dimensions, respectively. The grid spacing Δ_s is given by 0.02.

The three terms of the Hamiltonian (5.1), the longitudinal single-particle term $H_\parallel$, the transversal single-particle term $H_\perp$ and the interaction term W induce three different time scales in the system. For the first two terms, we get the following estimations by neglecting the influence of the interaction: $T_\perp = 2\pi/\Delta E_\perp \sim 0.6$ and $T_\parallel = 2\pi/\Delta E_\parallel \sim 3.1$, where $\Delta E_\perp = 10$ and $\Delta E_\parallel = 1$ are the eigenenergy differences between the ground and the second and first excited eigenstates for

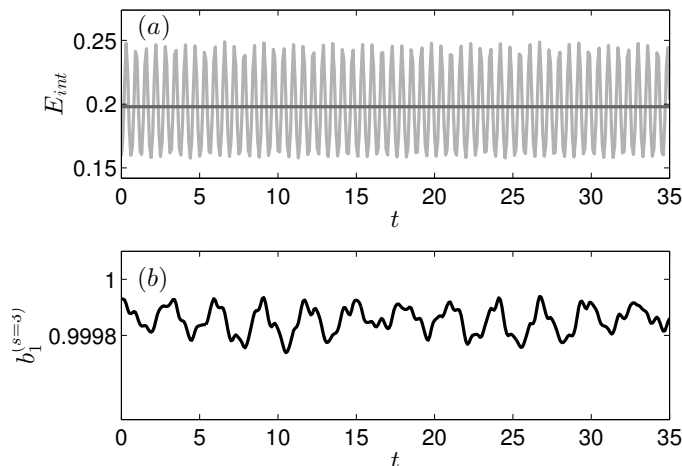**Figure 5.6.:** (a) Interaction energy E_{int} in dependence of time (light grey solid line) and the mean value of the interaction energy $\bar{E}_{int}$ (dark grey solid line). (b) Natural population of $b_1^{(s=3)}$ in dependence of time (black solid line). For a definition of $b_1^{(s=3)}$ see section 1.4.

the transversal and longitudinal single particle Hamiltonians, respectively[3]. In order to estimate the time scale governed by the interaction, and which is responsible for the induction of spatial correlations, we determine the mean value of the interaction energy $\bar{E}_{int} = \int_0^T \langle W_{RG} \rangle dt / T$, where T is the total simulation time (see figure 5.6a), $T_{int} = 2\pi / \bar{E}_{int} \sim 31.4$. In order to resolve these different time scales a fine temporal grid spacing is needed, leading to an enormous data volume.

Next, we are interested in the induced spatial correlations by the interaction, which is manifested by the deviation of the natural populations $b^{(s=3)}$ from one (see figure 5.6b). The deviation is very small, and a significant coupling between the dimensions can be achieved by the following three different strategies:

i. Add an additional external potential, which couple the dimensions, e.g. an anharmonic confinement potential or double well potential.

ii. Increase the simulation time. Comparing the shortest with the longest time scale, we see T_{int} is roughly a factor 50 larger than $T_\perp$.

iii. Increase the number of particles.

In the last two strategies, not only the coupling between the dimensions is increased, but also other correlations in the system, e.g. the particle correlations. Therefore, in the following, we focus on the first strategy in order to increase the spatial correlations in the system.

5.4. Dimensional reduction

In general, if the wave function separates into its dimensions

$$\Psi(\mathbf{r}_1, ... \mathbf{r}_N) = \Phi_\perp(x_1, ... x_n, y_1 ... y_N) \cdot \varphi(z_1, ... z_N) \tag{5.11}$$

an effective one-dimensional Hamiltonian, for the longitudinal dimension, can be obtained by integrating out the transversal dimensions, calling it a *pure* one-dimensional system. Obviously,

---

[3]Due to symmetry, only the second transversal excited eigenstate is used.

this product form of the wave function (5.11) w.r.t. the dimensions can be obtained if the Hamiltonian is already given as a sum composed by a transversal and longitudinal Hamiltonian, $\tilde{H}_\perp$ as well as $\tilde{H}_\parallel$, respectively, $\tilde{H} = \tilde{H}_\perp + \tilde{H}_\parallel$. For a harmonic confinement, the wave function is restricted in the transversal direction $\sim 1/(2\eta)$ and the relative distance between the two particles can be approximated by $(x_2 - x_1) = (y_2 - y_1) \sim 1/2\eta$, which can be smaller than the width of the Gaussian interaction potential for very tight confinements, $(x_2 - x_1) = (y_2 - y_1) \sim 1/2\eta \ll \sigma$. In this regime, the Gaussian interaction potential can be Taylor expanded, and regarding only the first terms of the Taylor expansion, the Hamiltonian decay into a transversal and a longitudinal part, and therefore the wave function separates into the dimensions. Other short-range interaction potentials (e.g. as presented in 3.1) have a similar behaviour. Summarizing, for finite-range interaction potential, a crossover to a pure one-dimensional regime can be always obtained if the confinement in on the length scale of the interaction width.

Another way to define a one-dimensional regime is if the wave function can be expanded into only one transversal natural orbitals β, $\Psi(\mathbf{r}_1, ... \mathbf{r}_N) = \prod_{i=1}^{N} \beta(x_i, y_i) \varphi(z_1, ... z_N)$. This definition of one-dimensional systems depends strongly on the concrete setup i.e., the particle number, the interaction strength and the external single-particle potential.

5.5. Summary

We have found that the parameters for the renormalized Gaussian interaction potential are limited to $\sigma \leq 0.1$ and $h < 470$, in order to ensure convergence. The restriction to these parameters limits the correlations in the system. Stronger correlating systems can be achieved by increasing the number of particles.

For the numerical parameters, the grid spacing must be $\Delta \leq 0.04$ so that the renormalized Gaussian interaction potential is modelled properly. In order to ensure short-range interactions (for $\sigma \leq 0.1$), which are not affected by the confinement, we get the range of the transversal characteristic trap length $0.3 \leq l_\perp \leq 1$ (i.e. for the aspect ratio $11 \geq \eta \geq 1$). In order to fulfil all these constrains, we end up with a grid length of $L = 7$ for a characteristic trap length of $l_\parallel = 1$.

Performing the crossover from three to one dimension, we see that at approximately $\sigma \sim l_\perp$, the interaction energy approaches zero, as expected for a fragmented state. However, this parameter regime, $\sigma \sim l_\perp$, does not assure short-range interactions any more. Furthermore, confinement induced resonances are 'out-of range', since the zero-energy scattering length, obtained with the above parameters for the interaction potential is given by $a_0 = 0.0068$, and the confinement induced resonance would occur at a transversal trap length $l_\perp = 0.007$ [see equation (1.4)]. This parameter is again not in the valid regime, which has been set above.

We have seen that the interaction term is too weak (even at weak transversal confinement) to induce significant spatial correlations. One way to circumvent this restriction is to add an external single-particle potential, which couples the dimensions directly.

DOUBLE WELL TRAP

Due to the high degrees of tunability of external parameters as well as the interaction strength and the separability from the environment, BECs are ideal candidates in order to study physical many-body phenomena such as the Josephson junctions [294, 295]. One of the first experimental realization of a single bosonic Josephson junction has been achieved in 2005 [296] within a double well, observing macroscopic quantum self-trapping, which has been already predicted in references [297, 298] using a two-mode, mean-field description. Theoretical extensions to higher-mode, mean-field models have been performed [299], and a rich dynamics has been predicted, including chaotic behaviour [300], enhanced tunnelling [93, 211] as well as a quantum collapse and revival [91]. Especially, it has been shown that for strong interactions a mean-field description of the Josephson junction fails and particle correlations have to be taken into account [92, 93, 211, 301, 302]. All these studies have been performed in one dimension, and a proper analysis w.r.t. particle and spatial correlations is still missing for three-dimensional Josephson junctions. Since, the zero-energy scattering length is limited by the usage of three-dimensional, repulsive short-range interaction potentials (see chapters 2 and 3), not the whole range of the dynamical regimes for a Josephson junction can be explored with ML-MCTDHB. Therefore, we focus on the study of the validity of the (i) mean-field and (ii) adiabatic separation approximations of the wave function and show that the obtained results are fully converged using ML-MCTDHB.

First, we describe the setup of our three-dimensional double well in section 6.1 and repeat the definitions of the mean-field and adiabatic separation approximation. Then in section 6.2, the ground state properties of a tilted double well are analysed w.r.t. both mean-field and adiabatic separation approximations. Since, as we will see, the ground state differs significantly for the different approximations, the resulting dynamics, induced by switching off the tilt, differ also significantly and therefore they are hard to compare. However, characteristic differences between the mean-field as well as adiabatic separation approximations and the full numerical result can be identified and are studied in section 6.3. We end this chapter with a summary in section 6.4. We notice that this chapter is literally based in parts on our publication [[1]].

6.1. Setup and numerical parameters

Fourteen bosons, $N = 14$, are loaded in an elongated trap $V_{trap}(\mathbf{r}_i) = \frac{\eta^2}{2}(x_i^2 + y_i^2) + \frac{1}{2}z_i^2$, where η is the aspect ratio between the transversal $\omega_\perp$ and longitudinal $\omega_\parallel$ trap frequencies, respectively, $\eta = \omega_\perp/\omega_\parallel$. All units are scaled w.r.t. to the length $l_\parallel = \sqrt{\hbar/m\omega_\parallel}$ and energy $\hbar\omega_\parallel$. E.g. by shining a blue detuned laser beam in the trap centre, or by using an immobile impurity, both
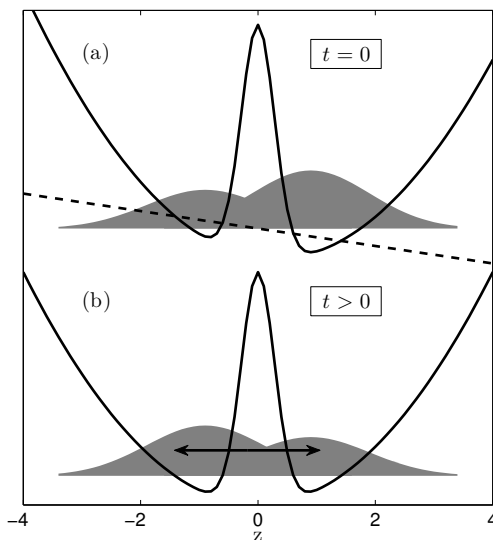
Figure 6.1.: (a) Sketch of the external potential $V(\mathbf{r}_i)$ (black solid line) at time instant $t = 0$. In order to emphasize the tilt, only $V_{tilt}(\mathbf{r}_i)$ is shown as a black dashed line. The initial density is sketched as a grey shaded area. (b) Sketch of the external potentials $V(\mathbf{r}_i)$ (black solid line) at time instant $t > 0$.

theoretically modelled by $V_{barrier}(\mathbf{r}_i) = H \exp(-\mathbf{r}_i^2/S^2)$ with fixed height $H = 10$ and width $S = 0.4$, a double well is created which separates the trap into a left and a right half. In order to get an initial population imbalance between the right and left well, an additional linear potential is added in the longitudinal direction in order to tilt the two potential wells, $V_{tilt}(\mathbf{r}_i) = dz_i$ with $d = -0.1$. The full external potential is then given by

$$V(\mathbf{r}_i) = V_{trap}(\mathbf{r}_i) + V_{barrier}(\mathbf{r}_i) + V_{tilt}(\mathbf{r}_i).$$

The interaction is modelled by the renormalized Gaussian interaction potential [see equation (3.18)]

$$W_{RG}(\mathbf{r}_1, \mathbf{r}_2) = he^{-\ln\left(\frac{h}{\epsilon}\right)\frac{(\mathbf{r}_1-\mathbf{r}_2)^2}{\sigma^2}},$$

where the width $\sigma = 0.1$, the height $h = 125$ and the small reference energy $\epsilon = 1$ are fixed. By solving equation (2.26), we obtain a zero-energy scattering length of $a_0 = 0.0048$. Then, the full many-body Hamiltonian is given by

$$H = \sum_{i=1}^{N=14} \left(-\frac{1}{2}\nabla^2_{\mathbf{r}_i} + V(r) \right) + \sum_{1 \leq i < j \leq 14} W(r_i, r_j) \tag{6.1}$$

We are interested in a crossover from three to one dimension and thus, we vary the aspect ratio between two and eight. The characteristic transversal trap lengths $l_\perp(\eta) = \sqrt{\hbar/m\eta}$ ranges from $l_\perp(2) \simeq 0.70$ to $l_\perp(8) \simeq 0.35$. The other physical parameter are chosen such that short-range interaction can be ensured (see chapter 5 for a discussion). We use

$$\Delta = 0.02 \quad < \quad \sigma = 0.1 \quad < \quad l_\perp = (0.35 \dots 0.7) \quad < \quad l_\parallel = 1 \quad < \quad L_\perp = 6, L_\parallel = 8$$

where Δ is the grid spacing, which has been chosen in order to resolve the interaction potential properly. In doing so, we simulate $q_z = 400$ and $q_x = q_y = 300$ grid points in the longitudinal and each transversal dimension, respectively. The total angular momentum w.r.t. to the longitudinal

directions (z-direction) commutes with the Hamiltonian (6.1) and in principle this can be used to simplify the Hamiltonian to a two dimensional problem. However, we do not apply this symmetry, since otherwise the interaction term is not separable w.r.t. the dimensions anymore and the interaction potential model has to be approximated (see chapter 3 for a discussion).

In order to obtain the ground state, the ML-MCTDHB equations of motions (4.8), (4.16) and (4.17) are propagated in imaginary time until convergence is reached. Then V_{tilt} is switched off and the dynamics is obtained by a real time propagation (see figure 6.1).

In the following, we repeat the definitions of the mean-field and adiabatic separation approximations, respectively. By a mean-field approximation, we define that all particles share the same orbital.

$$\Psi(\mathbf{r}_1, ..., \mathbf{r}_N) = \prod_{i=1}^{N} \psi_{MF}(\mathbf{r}_i).$$

The same approximation is used when deriving the GPE. If the transversal and longitudinal dimensions separate and if transversally a mean-field approximation can be applied, we call the approximation adiabatic separation:

$$\Psi(\mathbf{r}_1, ..., \mathbf{r}_N) = \left(\prod_{i=1}^{N} \psi_\perp(x_i, y_i) \right) \psi_\parallel(z_1, ...z_N).$$

Numerically both approximation can be obtained by either using only one 3D-SPF ($M = 1$) or by using transversally only one 1D-SPF ($m_1 = m_2 = 1$), for the mean-field and adiabatic separation, respectively (for a discussion see chapter 4). As a reminder, the number of 3D-SPFs, and 1D-SPFs are summarized in the so-called numerical configuration defined as $\mathcal{C} = (M; m_1, m_2, m_3)$. We are interested in the differences between these two approximations and a fully converged simulation, where no approximations to the wave function are taken into account. Convergence for each approximation has been achieved by the following numerical parameters:

1. Mean-field approximation by solving the three-dimensional GPE with the numerical configurations $\mathcal{C}_{MF} = (1; 3, 3, 4)$. In this approximation no particle correlations are present.

2. Adiabatic separation of the transversal dimensions can be achieved with the numerical configuration $\mathcal{C}_{q1D} = (4; 1, 1, 4)$. In the adiabatic separation approximation no spatial correlations are taken into account and we call this the *quasi 1D* simulation.

3. Fully converged solution, which is obtained with the numerical configuration $\mathcal{C}_{FC} = (4; 3, 3, 4)$

6.2. Ground-state analysis

First, we discuss properties of the ground state. Since we have already said much about convergence (see chapter 5) and the ML-MCTDHB methods (see chapter 4), we refer to a detailed convergence analysis given in the appendix F.1 and give here only the converged results.

For the ground state, we compare the population imbalance between the two wells, $I_z = (N_R - N_L)/N$, where $N_{L,R} = \sum_{i=1}^{N} \langle \Theta(\pm z_i) \rangle$, for these three different numerical configurations in dependence on the aspect ratio η (figure 6.2). One can clearly see that the 3D GPE agrees well with the fully converged results for $\eta < 4$, while the mean-field results deviate for more anisotropic traps since interparticle correlations become important. In contrast to this, the configuration $\mathcal{C}_{q1D}$ corresponds to an adiabatic separation of the transversal degrees-of-freedom while resolving interparticle correlations by bringing the simulation to convergence w.r.t. $M = m_3$. This quasi one-dimensional simulation approaches the fully converged results for increasing η, but even for $\eta = 8$, significant deviations remain.
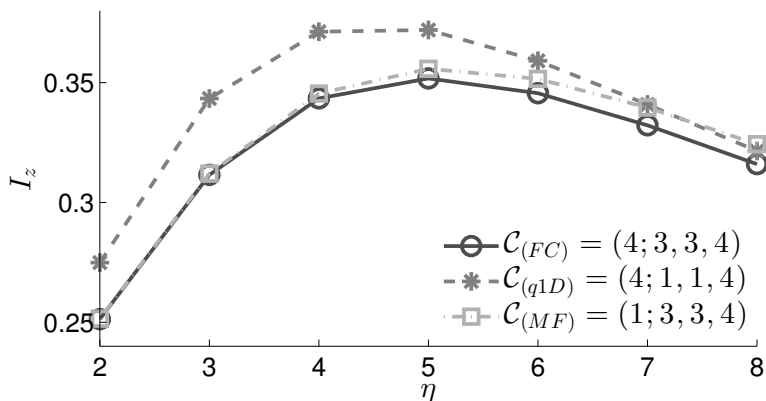
Figure 6.2.: Shown are the population imbalances for different numerical configurations $\mathcal{C}$ with respect to the aspect ratio. The lines connecting the points are plotted as a guide to the eye for the three numerical configurations: the mean-field $\mathcal{C}_{MF} = (1; 3, 3, 4)$ (light grey dashed-dotted with squares), quasi-1D $\mathcal{C}_{(q1D)} = (1; 3, 3, 4)$ (grey dashed asterisk) and fully converged $\mathcal{C}_{(FC)} = (4; 3, 3, 4)$ (dark grey solid line with circles). Figure is taken from reference [[1]].

Configuration dependent ground state properties
Validation of the approximations

Next, we explore in some detail the validity of the adiabatic separation of the transversal degrees of freedom and the mean-field approximation. Let us consider a cut of the three-dimensional ground state density $\rho(x, y = 0, z)$ for the three numerical configurations $\mathcal{C}_{MF}$, $\mathcal{C}_{q1D}$ and $\mathcal{C}_{FC}$, shown in figure 6.3 for the two aspect ratios $\eta = 2$ and $\eta = 8$.

For $\eta = 2$, the mean-field (figure 6.3a) and fully converged (figure 6.3c) density profiles agree well, whereas they differ significantly in their geometry from the quasi 1D simulation $\mathcal{C}_{q1D}$ (figure 6.3e). This is interesting, since the second dominant transversal natural orbital is only weakly populated with $b_2^{(1)} = b_2^{(2)} \sim 4 \cdot 10^{-3}$ (see figure F.1 in the appendix), indicating low spatial correlations. Nevertheless, these further orbitals are necessary to describe the dip in the density induced by the barrier $V_{barrier}(\mathbf{r}_i)$. This is an example that small values of the natural populations are not a sufficient condition in order to justify convergence. This density dip cannot be resolved in the quasi 1D simulation due to the crude adiabatic separation, i.e. the single variationally optimized SPF in each transversal direction has a shape independent of the longitudinal position.

Increasing the transversal trap frequency restricts the wave function stronger in the transversal direction, $\langle x^2 + y^2 \rangle \sim 1/(\eta)$, and if it is smaller than the width of the barrier, the barrier can be Taylor expanded $V_{barrier}(\mathbf{r}_i) \sim H \exp(-z_i^2/S^2)$, as already worked out in section 5.4. No spatial correlations are induced by this approximated barrier any more, and the adiabatic separation is a good approximation, as can be seen by comparing the density profiles for $\mathcal{C}_{MF}$ (figure 6.3b), $\mathcal{C}_{FC}$ (figure 6.3d) and $\mathcal{C}_{q1D}$ (figure 6.3f) for the aspect ratio $\eta = 8$. In this regime, only the interaction could induce spatial correlations, which however is prevented by the transversal excitation gap.
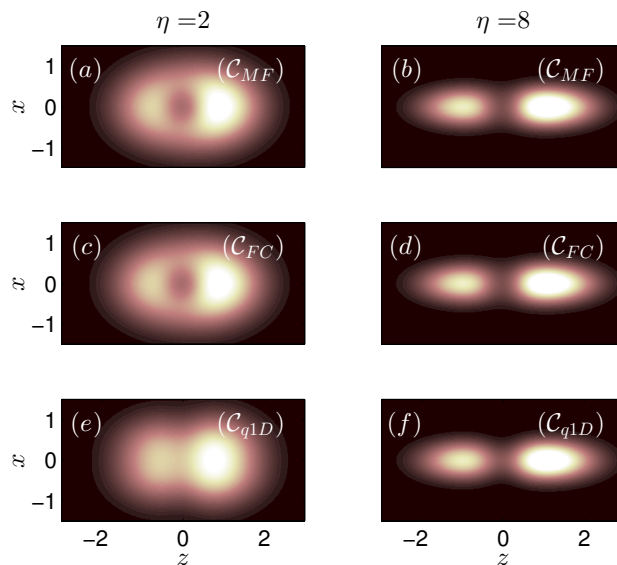
Figure 6.3.: Cut through the density $\rho(x, y = 0, z, t)$ for different aspect ratios $\eta = 2$ (left column), $\eta = 8$ (right column) and configurations $\mathcal{C}_{MF}$ (first row), $\mathcal{C}_{FC}$ (second row) and $\mathcal{C}_{q1D}$ (third row) in dependence of the longitudinal z and transversal dimension x. The range of the colour bar goes from zero (black) to 0.2 (white) for the plots (a, c, and e) and to 0.8 for (b, d, and f). Figure is taken from reference [[1]].

6.3. Tunnelling dynamics

To trigger the tunnelling dynamics, we switch off the tilted potential $V_{tilt}(z)$ at $t = 0$ and propagate the many-body wave function in real time, with the intention to study its dynamical features (results have been published in [[1]]). We compare the two approximations, namely the adiabatic separation and the mean-field approximation with the fully converged solution. Snapshots of the temporal evolution of the density cut $\rho(x, y = 0, z, t)$ for the two different numerical configurations $\mathcal{C}_{q1D}$ (see figures 6.4a,d,e) and $\mathcal{C}_{FC}$ (see figure 6.4b,d,f) show how the particles tunnel from right ($t = 0$) (see figure 6.3) to left ($t = 5.3$) and back ($t = 10.6$). The aspect ratio has been set to $\eta = 2$. We observe again that the quasi one-dimensional configuration can not resolve the right geometry of the temporal evolution of the density. This has a direct consequence on the population imbalance I_z (see figure 6.5). For weak aspect ratios $\eta = 2$, we see an excellent agreement in the population imbalance of the mean-field approximation with the fully converged simulation and a significant phase shift is observed for the adiabatic separation approximation (quasi 1D configuration). However, at the aspect ratio $\eta = 8$, we observe that the mean-field approximation fails, which cannot describe the collapse and revival of the population imbalance, whereas the adiabatic separation approximation shows this feature. The collapse and revival is a clear signature of the necessity to include particle correlations in the system. Additionally, the phase of the adiabatic separation approximation is shifted, which is caused by the different initial population imbalances.

In order to quantify particle and spatial correlations, respectively, and therefore the validity of the adiabatic separation and mean-field approximation, we analyse the integrated depletions
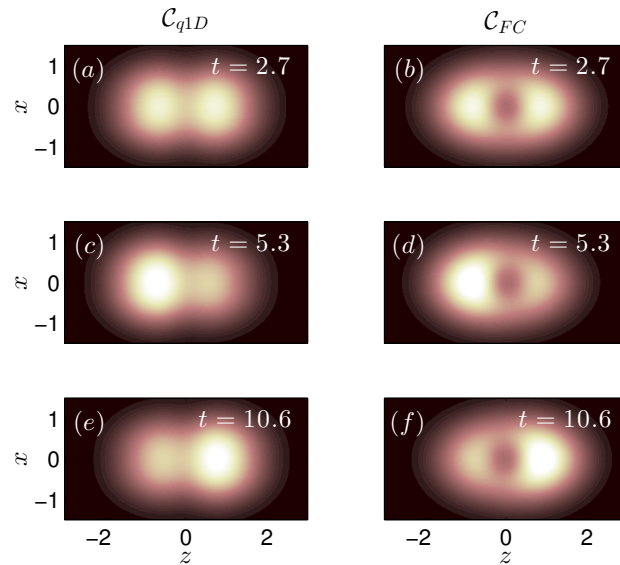
Figure 6.4.: Cut through the density $\rho(x, y = 0, z, t)$ for different times, $t = 2.9$, $t = 5.3$, $t = 10.6$ and configurations $\mathcal{C}_{q1D}$ (left column) and $\mathcal{C}_{FC}$ (right column) in dependence of the longitudinal z and transversal dimension x. The aspect ratios is $\eta = 2$. The range of the colour bar is from zero (black) to 0.2 (white). Figure is taken from reference [[1]].
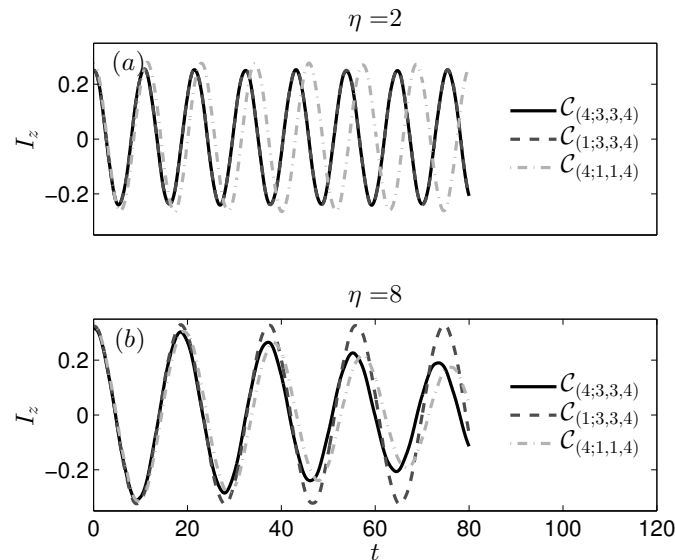

Figure 6.5.: Temporal evolution of the population imbalance $I_z(t)$ for the two aspect ratios $\eta = 2$ (a) and $\eta = 8$ (b). Shown are the following numerical configurations $\mathcal{C} = (4; 3, 3, 4)$ (black solid line), $\mathcal{C} = (1; 3, 3, 4)$ (dark grey dashed line), $\mathcal{C} = (4; 1, 1, 4)$ (light grey dashed dotted line). Note that in (a) the grey dashed line is covered by the black solid line. Figure is taken from reference [[1]].
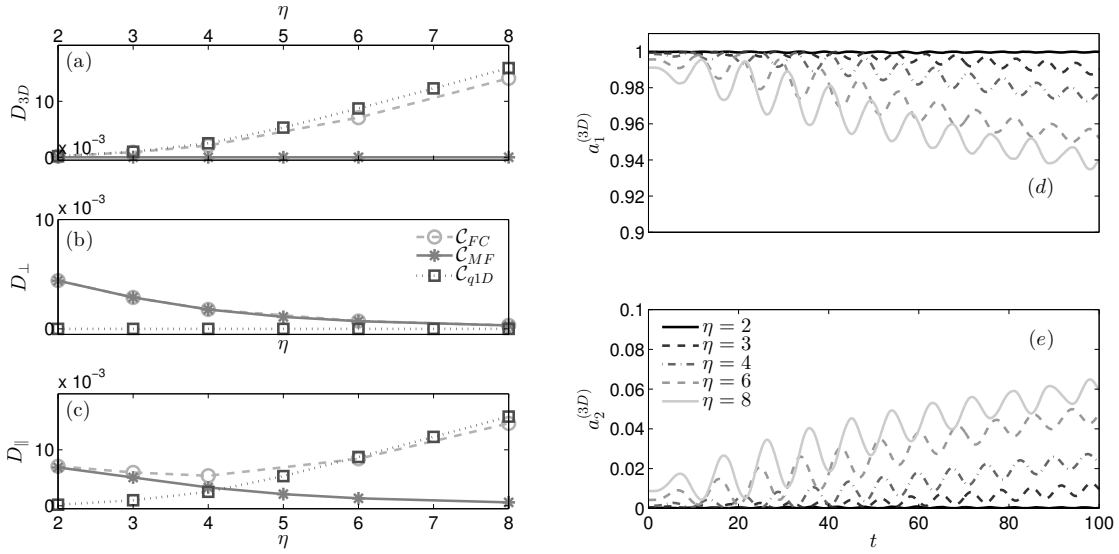
Figure 6.6.: The natural populations $a_1^{(3D)}$ (a) and $a_2^{(3D)}$ (b) w.r.t. time for different aspect ratios. Both subfigures have the same colour coding. Figures are taken from reference [[1]]

in dependence of η,

$$D_{(3D)}(\eta) = 1 - \frac{1}{T_{max}} \int_0^{T_{max}} a_1^{(3D)} dt$$

$$D_\perp(\eta) = D_{(s=1)}(\eta) = D_{(s=2)}(\eta) = 1 - \frac{1}{T_{max}} \int_0^{T_{max}} b_1^{(s=1)} dt$$

$$D_\parallel(\eta) = 1 - \frac{1}{T_{max}} \int_0^{T_{max}} b_1^{(s=3)} dt$$

where $a_1^{(3D)}$ and $b_1^{(s)}$ are the first natural populations of $\rho^{(3D)}$ and $\rho^{(s)}$ for the dimension $s \in \{1, 2, 3\}$, respectively, and T_{max} is the maximal simulation time (see section 1.4 for definitions of the natural populations and density matrices). These quantities may be interpreted as followed: The larger the averaged depletion $D_{(3D)}(\eta)$, $D_{(s)}(\eta)$ is, the more important correlations are between the atoms and between the spatial dimension s and the other two spatial dimensions in the dynamics, respectively. For example if $D_{(3D)}(\eta) = 0$, no particle correlations are present and the mean-field approximation is suitable, as well as for $D_{(1)}(\eta) = D_{(2)}(\eta) = 0$, the transversal dimensions can be adiabatically separated in the many-body wave function. In figure 6.6a, b and c, we see $D_{(3D)}(\eta)$, $D_\perp(\eta)$ and $D_\parallel(\eta)$, respectively. For a weak transversal confinement, we have less particle correlations $D_{(3D)}(\eta) \sim 0$ but spatial correlations $D_\perp(\eta) \sim D_\parallel(\eta) > 0$, which justify the use of the mean-field approximation. For tighter traps $\eta = 8$, the particle correlations increase while spatial correlations decrease, $D_\perp(\eta) \sim 0$. All correlations are well described by the adiabatic separation approximation $\Psi(\mathbf{r}_1, \ldots \mathbf{r}_N) = [\prod_{i=1}^N \phi(x_i)\phi(y_i)]\varphi(z_1, \ldots z_N)$, which shows that particle correlations are visible in $\varphi(z_1, \ldots z_N)$ and also in $D_\parallel(\eta)$, $D_\parallel(\eta) \simeq D_{(3D)}(\eta)$. In between these two aspect ratios, we find a regime, where both particle and spatial correlations are present.

Next, we have a look at the natural populations $a_1^{(3D)}$ and $a_2^{(3D)}$ for the fully converged simulation in dependence of time for different aspect ratios (figure 6.6d and e). For weak transversal confinement $\eta = 2$, the first natural populations is very close to one $a_1^{(3D)} \sim 1$ (as already discussed), indicating that no particle correlations are present in the system. For tighter traps, the second natural population $a_2^{(3D)}$ increases (see figure 6.6e), leading to higher particle
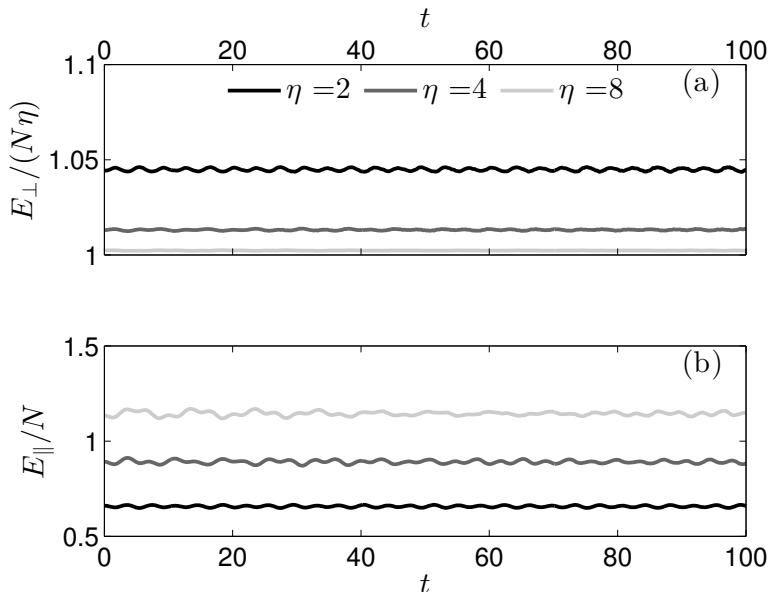
Figure 6.7.: Transversal $E_\perp$ (panel a) and longitudinal $E_\parallel$ (panel b) energy in dependence of time for different aspect ratios, $\eta = 2$ (dark grey), $\eta = 4$ (grey) and $\eta = 8$ (light grey). The physical parameters are: $H = 10$, $S = 0.4$, $h = 5$ and $\sigma = 0.1$. For the simulation, we used the numerical configuration $\mathcal{C} = (4; 3, 3, 4)$.

correlations and thus to beyond mean-field effects. Therefore, the mean-field configuration fails to describe the system, which possesses damping as well as a different frequency in the population imbalance (see figure 6.5b).

Last, we have a look at the transversal and longitudinal energy scales in the double well (see figure 6.7). The transversal (longitudinal) energy $E_\perp$ ($E_\parallel$) is defined as the expectation value of the transversal (longitudinal) Hamiltonian, $E_\perp = \langle H_\perp \rangle$ ($E_\parallel = \langle H_\parallel \rangle$) with

$$H_\perp(x_i, y_i) = -\frac{1}{2}\left(\frac{\partial^2}{\partial x_i^2} + \frac{\partial^2}{\partial y_i^2}\right) + \frac{\eta}{2}\left(x_i^2 + y_i^2\right) \tag{6.2}$$

$$H_\parallel(z_i) = -\frac{1}{2}\frac{\partial^2}{\partial z_i^2} + \frac{1}{2}z_i^2. \tag{6.3}$$

For low aspect ratios, we see a sinusoidal oscillation both in the transversal and longitudinal energy and for larger aspect ratios, more frequencies take part, however, we do not observe any energy transfer between the longitudinal and transversal motion. In order to increase the energy transfer between the dimensions, a different initial condition has to be chosen, which will be done in the next chapter, where we will increase the initial energy in order to yield a scattering off the barrier instead of a tunnelling trough the barrier.

6.4. Summary

We have studied particle and spatial correlations in a three-dimensional double well. The mean-field as well as the adiabatic separation approximation for the wave function have been checked and compared to a fully converged simulation, taking all correlations into account. We have seen that increasing the aspect ratio towards quasi 1D leads to stronger particle and weaker spatial correlations. For low aspect ratios, the properties of the ground state as well for the dynamics can be well-described by the mean-field ansatz, whereas for high aspect ratios (quasi

1D) an effective one-dimensional but beyond mean-field theory is needed. Especially, at least two transversal modes are needed, in order to approximate the true topology of the ground state density. We have seen that for the studied system, there is little energy transfer between the transversal and longitudinal dimensions. In order to increase the energy transfer, a different initial condition has to be chosen.

Concluding, with the ML-MCTDHB method (see chapter 4), we are able to simulate the crossover from quasi one-dimensional to three-dimensional behaviours taking all correlations into account.

<div style="text-align: right">

CHAPTER

SEVEN

</div>

SCATTERING OFF A BARRIER

In the previous chapter, where we have analysed the dynamics of a bosonic ensemble tunnelling in a double well, and where we have seen that no energy is transferred between the transversal and longitudinal direction, no higher transversal modes are excited. In order to increase the population of higher transversal modes, enough initial energy must be provided, e.g., spatially displacing the initial ground state (in a harmonic trap). For sufficiently high initial energies, the bosonic ensemble does not tunnel between the left and right well anymore, but rather scatters off the barrier multiple times. Such setups are used in interferometers [33], where the barrier can split or recombine [303] an atomic beam or a single soliton [304], similar to light impinging on a half-silvered mirror. Another possibility of building interferometers is the free-oscillation atom interferometer, where the ground-state wave function in a harmonic trap is excited by a laser pulse into a left and right moving part, which collides again after half an oscillation period similar to a Michelson interferometer [305–310]. When the trapped condensate is initially spatially displaced and impacts with a centred impurity dissipative transport [311], dipole oscillations [312] as well as effects of the inter-particle interactions can be studied [310]. In both interferometric setups above, a coherent splitting and recombination is important in order to obtain the contrast of the interference fringes. Sources of coherence loss are particle correlations, excitations of transversal modes or coupling to an environment as well as finite temperature. The splitting and recombination process of interferometers is described using a quasi-one dimensional mean-field approach [312], which cannot cover, per construction, loss of coherence via particle correlations. In order to study coherence losses in the complete crossover from three to one dimension, particle correlations and coupling to higher transversal modes have to be taken into account. Furthermore, in interferometers, observables of interest are the probability of reflection and transmission of the matter wave beam or the oscillation of the centre of mass (CM) [303].

The following chapters based on our publication [[2]], where we have explored the quantum dynamics of a bosonic ensemble in an elongated trap, which is initially displaced and exposed to a centred Gaussian barrier, experimentally realizable by a blue-detuned laser beam [313] or an impurity [314–316]. We vary the aspect ratio of the trap, thereby providing a smooth transition from three to one spatial dimension. The initial displacement is large enough, such that, by the dimensional coupling induced by the barrier, higher excited transversal modes can be populated in a controlled manner. In this way, this chapter is a natural extension of the previous chapter, where the three-dimensional tunnelling of few bosons in a double well has been explored at low energies (see also reference [[1]]). We analyse the influence of particle and spatial correlations on the coherence, measured by the first-order correlation function in longitudinal direction, and on
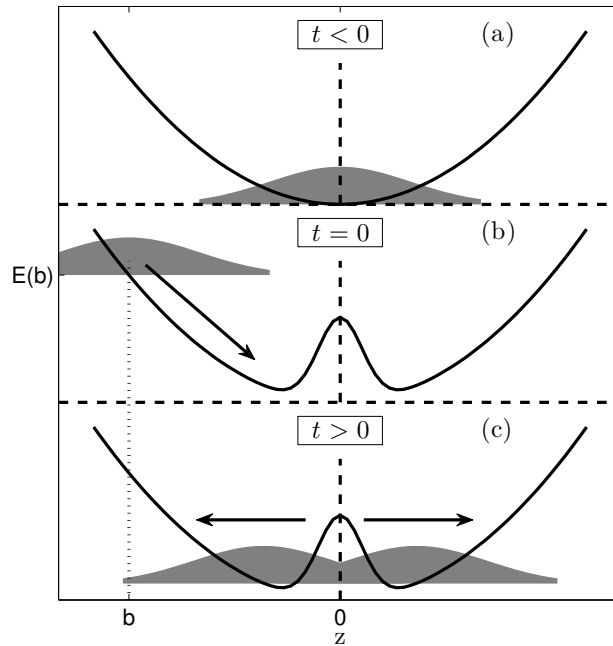
Figure 7.1.: Schematic representation of the setup and preparation of the initial state. The black solid line is the longitudinal external trap potential and the grey areas give sketches of the respective many-body densities.

the decay of the CM motion. The strength of the particle and the spatial correlations depend strongly on the aspect ratio of the trap. Two mechanisms of coherence loss are identified. In the first one, present for small aspect ratios, we observe a loss of coherence between the region close to the barrier and outer regions, due to the excitations of transversal modes. The second one, at larger aspect ratios, is an incoherence between the density fragments to the right and the left of the barrier, emerging due to particle correlations and becoming manifest in the occupation of the second natural orbital. Furthermore, the damping of the CM oscillation is reduced if particle correlations become dominant, whereas it is enhanced if spatial correlations are present. When the aspect ratio is integer valued, we see a quantitative enhancement of these effects.

The remaining sections follow very closely reference [[2]], which is mainly cited literally, and is structured as follows: In section 7.1, the setup and the preparation of the initial state are introduced. To thoroughly understand the case of interacting bosons in three dimensions, we proceed in three steps. First, presented in section 7.2, we focus on few atoms in a one-dimensional trap, where only particle correlations can occur. Second, in section 7.3, we study a single atom and change the aspect ratio continuously to cover the transition from three to one dimension. We show how the coupling between the dimensions reduces the amplitude of the CM oscillation and how the coherence is modified, due to incoherent spherical scattering off the barrier. If the aspect ratio is integer, the damping of the CM motion and the loss of coherence are enhanced. In section 7.4, we then combine our findings for the few boson case in the crossover from three to one dimensions, taking both particle and spatial correlations into account. Finally, a conclusion is given in section 7.5.

7.1. Setup and numerical parameters

Let us repeat the setup here again for completeness, even if it is very similar to the previous chapter. We consider $N = 5$ interacting, ultracold bosons each of mass m in a cylindrically symmetrical harmonic trap with aspect ratio, $\eta = \omega_\perp/\omega_\parallel$, between the transversal and longitudinal trap frequency. The one-particle Hamiltonian for the i-th particle at position $\mathbf{r}_i = (x_i, y_i, z_i)^T$ reads in harmonic oscillator units (energy scale $\hbar\omega_\parallel$ and length scale $l_\parallel = \sqrt{\hbar/m\omega_\parallel}$)

$$H_0(\mathbf{r}_i) = H_\perp(x_i, y_i) + H_\parallel(z_i) \tag{7.1}$$

with the transversal and longitudinal components

$$H_\perp(x_i, y_i) = -\frac{1}{2}\left(\frac{\partial^2}{\partial x_i^2} + \frac{\partial^2}{\partial y_i^2}\right) + \frac{\eta^2}{2}\left(x_i^2 + y_i^2\right), \tag{7.2}$$

$$H_\parallel(z_i) = -\frac{1}{2}\frac{\partial^2}{\partial z_i^2} + \frac{1}{2}z_i^2. \tag{7.3}$$

The short-range interaction between the i-th and j-th atom is modelled by the renormalized Gaussian interaction potential (3.18), and is given here as a reminder

$$W(\mathbf{r}_i, \mathbf{r}_j) = W_{RG}(\mathbf{r}_i, \mathbf{r}_j) = he^{-\frac{(\mathbf{r}_i - \mathbf{r}_j)^2}{\sigma_{eff}^2}} \tag{7.4}$$

with the interaction height h and effective width $\sigma_{eff} = \sigma/ln(h/\epsilon)$, where ϵ is a small energy scale of the system and set to one (see the discussion in chapter 3) and $\sigma = 0.1$ the width of the short-range interaction potential. The initial state is obtained by letting the bosonic ensemble relax to its ground states by an imaginary time propagation of the ML-MCTDHB equations of motion (see figure 7.1a). Then the wave function is displaced by a distance $b = 3$ in the elongated direction and instantaneously a barrier is switched on, which can be experimentally realizable by a blue-detuned laser beam or by adding an impurity (see figure 7.1b). The barrier (impurity) is modelled by an external Gaussian potential

$$V(\mathbf{r}_i) = He^{-\frac{r_i^2}{S^2}} \tag{7.5}$$

with height H and width $S = 0.2$. The displacement of the wave function is chosen large enough such that its overlap with the barrier is negligible and its gained potential energy is larger than the barrier height H, which ensures that we operate in the over-barrier and not in the tunnelling regime. The obtained displaced wave function is then propagated (see figure 7.1c) in time with the following many-particle Hamiltonian

$$\mathcal{H}_{3D} = \sum_{i=1}^{N}\left[H_0(\mathbf{r}_i) + V(\mathbf{r}_i)\right] + \sum_{1 \leq i < j \leq N} W(\mathbf{r}_i, \mathbf{r}_j). \tag{7.6}$$

7.2. Few bosons ensembles in one dimension

In this section, mainly taken from our publication [[2]], we analyse the scattering dynamics of a small ensemble of interacting bosons, displaced initially (by a distance $b = 3$) in a purely one-dimensional harmonic trap off a centred barrier. In the first part (section 7.2.1), we derive a pure one-dimensional Hamiltonian by adiabatically reducing the three-dimensional Hamiltonian (7.6) in order to derive corresponding one-dimensional physical parameters such as the interaction

height h_{1D} or barrier height H_{1D} in dependence on the aspect ratio η. We do so, since up to now, we have studied only quasi 1D systems (three-dimensional simulations with a sufficient large aspect ratio), however here, we are going to study a pure one-dimensional system. In the second part (the first part of section 7.2.2), we focus on weak particle and spatial correlations, created by a weak interaction strengths and moderate barrier heights. This allows us to describe analytically the collision dynamics by means of a time-dependent two-mode approximation within the mean-field theory. In the third part (the remaining part of this section), we increase the interaction strength as well as barrier height in order to create more correlations and numerically study the effects of these correlations on the oscillation of the CM and the loss of first-order coherence.

7.2.1. Dimensional reduction

We derive an effective one-dimensional Hamiltonian from the three-dimensional one by applying the framework already presented in section 5.4. In the limit of large aspect ratios $\eta \to \infty$, the energy of the first excited transversal mode is much larger than any other energy scale in our system, and thus, the wave functions separates into the dimensions. Transversally, a ground state $\sqrt{\eta/\pi}\exp(-\eta\rho^2)$, where $\rho = \sqrt{x^2 + y^2}$, can be assumed and the three-dimensional Hamiltonian (7.6) reads then

$$\mathcal{H}_{1D} = \sum_{i=1}^{N}\left[H_0(z_i) + V_{1D}(z_i)\right] + \sum_{1 \le i < j \le N} W_{1D}(z_i, z_j) \tag{7.7}$$

with $H_0(z_i) = (-\partial_{z_i}^2 + z_i^2)/2$, $V_{1D}(z_i) = H_{1D}\exp(-z_i^2/S^2)$ and $W_{1D}(z_i, z_j) = h_{1D}\exp[-(z_j - z_i)^2/\sigma_{eff}^2]$. The resulting one-dimensional parameters are $H_{1D} = H\eta S^2/(1 + \eta S^2)$ and $h_{1D} = h\eta\sigma_{eff}^2/(2 + \eta\sigma_{eff}^2)$. For a pure one-dimensional setup ($\eta \to \infty$), the three-dimensional parameters are recovered again, $H_{1D}(\eta \to \infty) = H$ and $h_{1D}(\eta \to \infty) = h$.

7.2.2. Quantum dynamics in one spatial dimension

We analyse the quantum dynamics of five bosons in a one-dimensional trap following the Hamiltonian (7.7). In doing so, the interacting ground state is displaced by $b = 3$ and gains an additional potential energy of $E = b^2/2 = 4.5$, which is larger than H_{1D}, and thus the bosons reveal dipole oscillations [318–322], which are modified by the presence of the barrier. This setup is in contrast to chapter 6, where the initial state gains only a small potential energy. Here, first, we consider weak interactions and small barrier heights, where a mean-field approximation is justified, and then we switch to stronger interactions and larger barrier heights, where particle correlations become important.

Small barriers and weak interactions

In order to understand the basic scattering behaviour, we first focus on five very weakly interacting ($h_{1D} = 0.13$, $\sigma = 0.1$) bosons and a shallow barrier ($H_{1D} = 0.38$, $S = 0.2$). In this regime, a fraction of the initially displaced bosons is reflected at the barrier and cause a counter oscillating wave-packet, which interferes with the transmitted wave-packet (see figure 7.2a). In particular, we do not find any major difference between the results of the *ab-initio* ML-MCTDHB simulation and a mean-field calculation, which assumes that all bosons reside in the same orbital
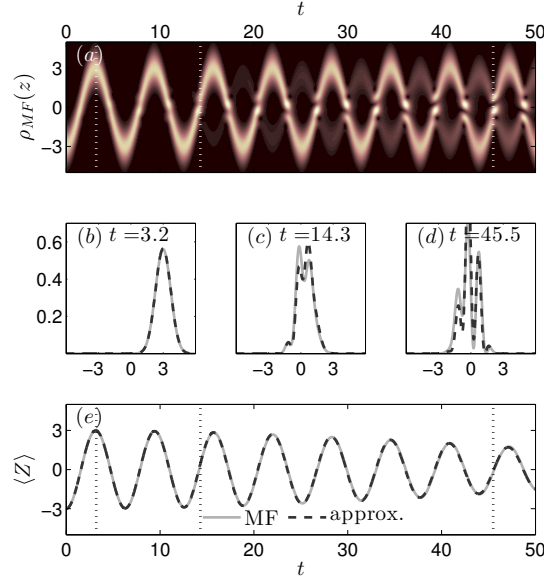
Figure 7.2.: Time evolution of the numerically obtained one-body density (first row) for $N = 5$ interacting atoms with $h_{1D} = 0.1293$, $\sigma = 0.1$ and barrier $H_{1D} = 0.4$, $S = 0.2$. The grey scales are normalized w.r.t. the maximal value of the density. (b)-(d) The numerically exact density profile (light grey line) is compared with the approximation (7.15) (dark grey line) for three instants in time. In figure (e), the corresponding expectation value of the CM is compared with equation (7.14). Vertical dashed lines mark the three instants in time used in sub figures (b)-(d). Figure is taken from reference [[2]].

$\Psi_{GP}(z,t)$ obeying the one-dimensional GPE

$$i\partial_t \Psi_{GP}(z,t) = [H_0(z) + V_{1D}(z)]\, \Psi_{GP}(z,t) + \tag{7.8}$$
$$+ \left((N-1) \int d\mathcal{Z} |\Psi_{GP}(\mathcal{Z},t)|^2 W_{1D}(z,\mathcal{Z}) \right) \Psi_{GP}(z,t).$$

Furthermore, by inspecting at figure 7.2a, we see that the temporal evolution of the density can be modelled by two counter-propagating, stiffly[1] oscillating wave packets, expressed as two different, stiff modes $\{\Phi_i\}_{i=1,2}$. For obtaining analytical insights into the dynamics of the density, namely, into the interference pattern and the decay of the CM oscillation, we assume that the time-dependent Gross-Pitaevskii orbital $\Psi_{GP}(z,t)$ can be expanded into these two modes

$$\Psi_{GP}(z,t) = A_1(t)\Phi_1(z,t) + A_2(t)\Phi_2(z,t). \tag{7.9}$$

As the two modes, we use the solutions of the time-dependent GPE for $V(z) = 0$ with the corresponding GPE ground state φ_{GP} and energy E_{GP}, being displaced by $\pm b$ as the initial state: $\Phi_{1,2}(z,t) = \exp(-i\Theta(t))\exp(\pm i\bar{p}(t)z)\varphi_{GP}(z \mp \bar{z}(t))$ (see appendix G.2 for the derivation and further details). Here, $\Theta(t) = E_{GP}t + \frac{1}{2}\bar{z}(t)\bar{p}(t)$ defines the dynamical phase factor and $\bar{z}(t) = b\cos(t)$ as well as $\bar{p}(t) = -b\sin(t)$ are the classical values for position and momentum of an atom oscillating in a harmonic trap.

These two modes represent two stiff wave packets, displaced in opposite direction and counter-propagating. In order to get an analytic expression for φ_{GP}, we use the Gaussian trial wave function $(\Omega/\pi)^{1/4}\exp(-\Omega z^2/2)$ and determine the parameter Ω, which incorporates the effect

---

[1] In the literature, this motion is also called a coherent motion, but in order not to confuse the reader with our other definition of coherence [172], we call it a stiff moving wave packet, since its shape is maintained during time evolution

of the interaction by minimizing the total energy. For a non-interacting system, Ω is equal to one, and by increasing the repulsive (attractive) interaction leads to a broadening (narrowing) of the trial wave function and thus to a smaller (larger) Ω. Knowing the functional expression for φ_{GP}, the overlap between $\Phi_1(z,t)$ and $\Phi_2(z,t)$ can be calculated analytically and equals $\exp(-b^2(\Omega^2\cos^2(t)+\sin^2(t))/\Omega)$. For large displacements b, as regarded here, these two modes are approximately orthogonal for all times, of which we will make use in the following. Inserting the expansion (7.9) into the time-dependent GPE (7.8), projection onto the two modes, $\Phi_{i=1,2}$, and employing the symmetries $\varphi_{GP}(z)=\varphi_{GP}(-z)$ and $V_{1D}(z)=V_{1D}(-z)$, leads to the equations of motion for the coefficients

$$i\partial_t \begin{pmatrix} A_1 \\ A_2 \end{pmatrix} = \begin{pmatrix} v_{11} & v_{12} \\ v_{12} & v_{11} \end{pmatrix} \begin{pmatrix} A_1 \\ A_2 \end{pmatrix} \tag{7.10}$$

where the matrix elements are $v_{11}=\int dz |\varphi_{GP}(z-\bar{z}(t))|^2 V_{1D}(z)$ and $v_{12}=\int dz \exp(-i2\bar{p}(t)z) \varphi_{GP}(z-\bar{z}(t))\varphi_{GP}(z+\bar{z}(t))V_{1D}(z)$. These last two integrals can be evaluated, and yield

$$v_{11}(t) = \frac{\sqrt{\Omega S^2}}{\sqrt{1+\Omega S^2}} H_{1D} e^{-\frac{\Omega b^2 \cos^2(t)}{1+\Omega S^2}}, \tag{7.11}$$

$$v_{12}(t) = \frac{\sqrt{\Omega S^2}}{\sqrt{1+\Omega S^2}} H_{1D} e^{-b^2\left(\Omega\cos^2(t)+\frac{S^2\sin^2(t)}{1+\Omega S^2}\right)}.$$

The set of equations (7.10) can be solved analytically

$$A_1(t) = e^{-iF(t)}\cos(G(t)) \tag{7.12}$$

$$A_2(t) = -ie^{-iF(t)}\sin(G(t))$$

with $F(t)=\int_0^t v_{11}(\tau)d\tau$ and $G(t)=\int_0^t v_{12}(\tau)d\tau$. Since the modes $\Phi_{1,2}$ couple only during the collisions, $v_{12}(\tau)$ is periodic and strongly peaked such that $G(t)$ increases step-like (see figure 7.3). In order to simplify $G(t)$, we apply a stationary phase approximation for v_{12} piecewise in the time intervals $[n\pi,(n+1)\pi)$, with $n\in\mathbb{N}_0$, and furthermore perform a linear fit $G(t)\approx\tilde{G}(t)=ct$ with

$$c = \frac{1}{\sqrt{\pi}b}\sqrt{\frac{\Omega s}{\Omega-s}} H_{1D} e^{-b^2 s} \tag{7.13}$$

where $s=S^2/(1+\Omega S^2)$. These approximations are quite accurate as can be seen in figure 7.3. Calculating the evolution of the CM $\langle Z\rangle=\sum_{i=1}^N\langle z_i\rangle/N$

$$\langle Z\rangle = b\cos(t)\cos(2ct), \tag{7.14}$$

we find that the classical oscillation of a displaced atom in a harmonic trap $[\langle Z\rangle=b\cos(t)]$ is modified by a slower oscillation $\propto\cos(2ct)$, causing a decay and revival of $\langle Z\rangle$. Thus c determines the time-scale on which the classical CM oscillation 'decays', namely $t_d=\pi/(4c)$, and we therefore called it *decay coefficient* in the following. The decay coefficient c depends strongly on b, and if b is increased, c reduces towards zero, meaning that if the initial wave function is stronger displaced, it has more kinetic energy, travels faster through the barrier and thus the coupling with the barrier is reduced. Similarly, decreasing the barrier height H_{1D}, the coupling to the barrier is reduced, and $c\to 0$, leading to an undamped CM oscillation, $\langle Z\rangle=b\cos(t)$. The influence of the interaction strength on c is rather small in the weak interacting regime, which we have addressed with the Gaussian trial function for φ_{GP}, and in the validity of our model, c can be assumed as constant, $c(h_{1D})\sim const$. Furthermore, the
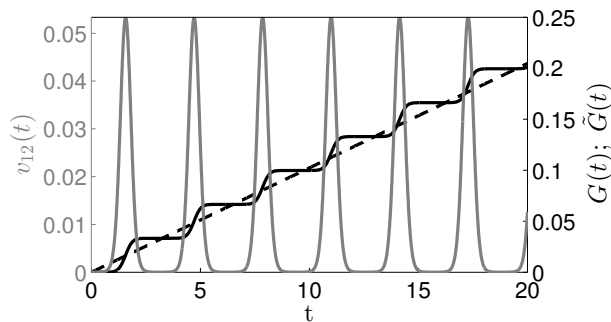
Figure 7.3.: Shown is $v_{12}(t)$ (grey solid line), $G(t)$ (black solid line), $\tilde{G}$ (black dashed line) versus time t, with $c = 0.01$. c and v_{12} are obtained using the parameters $\Omega = 1$, $H_{1D} = 0.38$, $S = 0.2$ and $b = 3$. Figure is taken from reference [[2]].

density $|\Psi(z,t)|^2$ can be calculated analytically

$$
\begin{aligned}
|\Psi(z,t)|^2 &= \cos^2(ct)|\varphi_{GP}(z - \bar{z})|^2 \\
&+ \sin^2(ct)|\varphi_{GP}(z + \bar{z})|^2 \\
&+ \sin(2\bar{p}z)\sin(2ct)\varphi_{GP}(z - \bar{z})\varphi_{GP}(z + \bar{z}),
\end{aligned}
\tag{7.15}
$$

where we have omitted the time-argument for $\bar{z}$ and $\bar{p}$ for better readability. The density (7.15) consists of three parts. The first two terms describe stiff, out-of-phase oscillations of the ground state wave functions $|\varphi_{GP}(z - \bar{z})|$ and $|\varphi_{GP}(z + \bar{z})|$ with a sinusoidal population transfer of frequency $2c$ between these two states. The last term creates an interference pattern with a contrast $\propto \sin(2ct)$ and is strongest at $t = t_d + n\pi/2c$, $n \in \mathbb{N}_0$. In the limit of $c \to 0$, this interference pattern blurs and one is left with a stiff oscillation of a single wave packet.

For different instants in time, we compare the approximate solution (7.15) for the density and (7.14) for the CM with the full mean-field calculation (figure 7.2). Not only the decay of the CM oscillations $\langle Z \rangle$ is well-described by our simple model, but also the interference pattern. Nevertheless, let us finally discuss the implicit assumptions underlying our analytical approach. Deviations in our model occur, since the barrier can scatter atoms into higher excited modes, which are not taken into account by the model. Therefore, the model is only valid for small to moderate barrier heights. Furthermore, while our model assumes elastic scattering off the barrier, the scattering is inelastic in fact, which can be seen in the mean-field calculations showing that the turning points of the reflected density fraction are closer to the trap centre than for the transmitted density fraction (see figure 7.2a). Finally, the assumption of a Gaussian trial wave function limits the model to small interactions and, summarizing, we find empirically that the 'decay' of the CM is slightly decreased in fact if the interaction strength is increased, whereas our model features the opposite trend.

Large barrier amplitude and stronger interactions

For stronger interactions ($h_{1D} = 1.5385$) and larger barrier height ($H_{1D} = 1.5$), the dynamics cannot be described by the GP equation (7.8) anymore, since correlations between the atoms have to be taken into account. Quantitative differences between a MF and a BMF simulation are observed, for example, in the oscillation of the CM, in the interference pattern of the density or in the one-body correlation function. In the following, we explain the occurrence of these quantitative differences, starting with the interference pattern.

While the MF density $\rho_{MF}(z,t)$ reveals a pronounced interference pattern for all times (see figure 7.4a), the interference pattern becomes smeared out as time proceeds if particle correlations are taken into account (see figure 7.4b). The reason for the loss of coherence is a significant depletion of the first natural orbital $\alpha_1(z,t)$ down to 0.65 of the original population (white line in figure 7.4c), which mainly stems from populating the second natural orbital $\alpha_2(z,t)$ up to 0.29 (white line in figure 7.4d) at time $t = 39$. The remaining 0.06 are distributed among further natural populations.

We can approximate the BMF density ρ_{BMF} by the two main contributing natural orbitals, $\rho_{BMF} \approx a_1(t)|\alpha_1(z,t)|^2 + a_2(t)|\alpha_2(z,t)|^2$, with $a_1(t) + a_2(t) \approx 1$. We have observed that the first natural orbital has a qualitatively similar structure as the mean-field density (compare panels 7.4a and 7.4c), $|\alpha_1(z,t)|^2 \sim \rho_{MF}(z,t)$, and the BMF expectation value for the CM can be approximated as

$$\langle Z \rangle_{BMF} \sim (1 - a_2(t))\langle Z \rangle_{MF} + a_2(t) \int dZ \; Z|\alpha_2(Z,t)|^2 \qquad (7.16)$$

Inspecting figure 7.5a, where we show the second part $\delta_{BMF} \equiv \int dZ \; Z|\alpha_2(Z,t)|^2$ multiplied by $a_2(t)$, we notice that δ_{BMF} is in-phase with the classical harmonic oscillation. By increasing $a_2(t)$ this in-phase oscillation becomes more pronounced in $\langle Z \rangle_{BMF}$ and therefore the decay of the CM in reduced and t_d is increased. This effect can be also seen in figure 7.5, where both $\langle Z \rangle_{BMF}$ and $\langle Z \rangle_{MF}$ are presented.
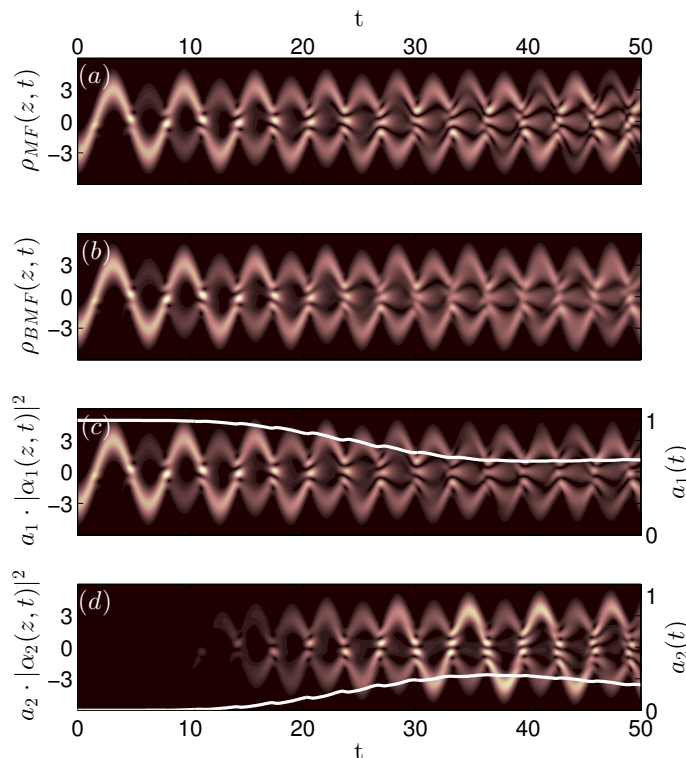

Figure 7.4.: Temporal evolution of the density both within the 1D-GPE (a) and when taking particle correlations into account (b), for $N = 5$ bosons in a harmonic trap with barrier $H_{1D} = 1.54$, $S = 0.2$ and interaction $h_{1D} = 2.01$, $\sigma = 0.1$. (c) and (d) show the first and second natural orbitals $\alpha_{1,2}(z,t)$ weighted with their natural populations $a_{1,2}$, which are shown as white solid lines. The grey scales are normalized w.r.t. the maximal value of the density. Figure is taken from reference [[2]].
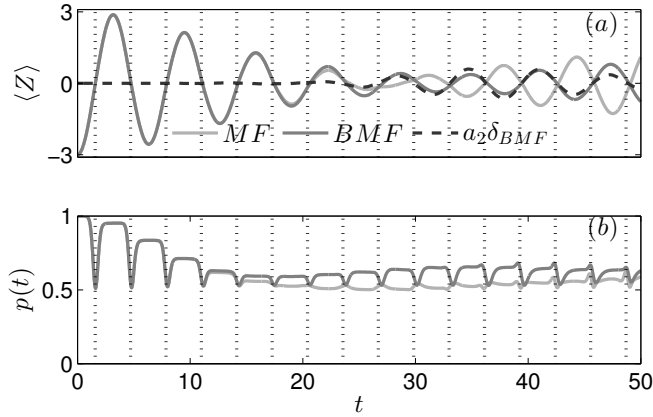
Figure 7.5.: Panel (a) shows the CM oscillation for and panel (b) shows the probability to find two bosons on the same side of the trap, see equation (7.17). Same parameters as in figure 7.4 are used. For both figures, the light grey line represents the mean-field result (7.8) and the darker grey line denotes a ML-MCTDHB result, where particle correlations are taken into account. The black dashed line represents the expectation value of $\delta_{BMF} = \langle z \rangle$ evaluated w.r.t. the second natural orbital and weighted with its population. Figure is taken from reference [[2]].

Next, we study the probability for two bosons being on the same side of the barrier, which effectively measures the probability of pairwise transmission or reflection at the barrier

$$p(t) = \frac{1}{N(N-1)} \sum_{1 \leq i < j \leq N} \left(\langle \Theta(z_i)\Theta(z_j) \rangle + \langle \Theta(-z_i)\Theta(-z_j) \rangle \right), \tag{7.17}$$

where Θ is the Heaviside function. The probability $p(t)$ is enhanced if particle correlations are taken into account (see figure 7.5b), identifying pair correlation. So, the bosons like to be transmitted or reflected pairwise. Pair correlations have already been observed in a double well scenario [211], similar to our setup, but focusing on tunnelling dynamics. This feature of enhanced pair correlation causes a decrease of the one-body coherence in the dynamics, which is consistent with the disappearance of the interference pattern in the temporal evolution of the density.

Finally, we analyse how the emergent particle correlations affect the spatial coherence of the bosonic ensemble by inspecting the first-order correlation function

$$g_1(z, z') = \rho_{1D}(z, z') / \sqrt{\rho(z)\rho(z')}, \tag{7.18}$$

where ρ_{1D} is the one-dimensional one-body density matrix and $\rho(z) = \rho_{1D}(z, z)$ the one-dimensional one-body density. The absolute value of the first-order correlation function equals unity in a MF simulation and features values $|g_1(z, z')| < 1$ if particle correlations are present. In figure 7.6, $|g_1(z, z')|$ is given for three different times $t = 9\pi$, 9.5π and 10π. The first and the last instant in time correspond to the 9-th and 10-th classical turning point of the CM oscillation and $t = 9.5\pi$ refers to the tenth collision with the barrier. At the classical turning points, we find that the coherence between the density fragments to the right and the left of the barrier has been reduced due to the depletion of the dominant natural orbital such that the interference contrast is reduced at the subsequent collision. At the collision times, however, the coherence function features an involved ripple structure, which is difficult to interpret.
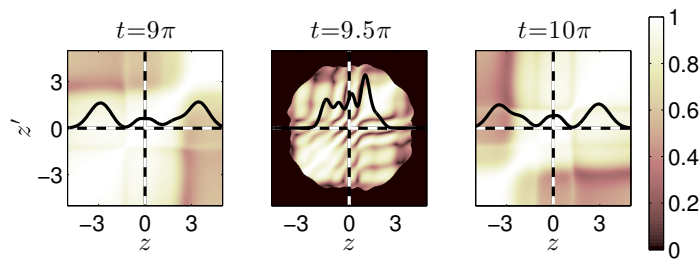
Figure 7.6.: Absolute value of the first-order correlation function for three different times $t = \{9\pi, \, 9.5\pi, \, 10\pi\}$. The black lines indicate the density profiles at the corresponding time instants and the black-white dashed lines mark the position of the barrier. Areas of density smaller than 10^{-6} are coloured in black. Figure is taken from reference [[2]].

7.3. Dynamics of one atom in three dimensions

In this section, mainly based literally on the publication [[2]], we analyse the scattering dynamics of a single atom at the barrier in the crossover from three to one spatial dimension by varying the aspect ratio in order to focus solely on the impact of spatial correlations without any particle correlations. The atom is initially displaced by $b = 3$ in the longitudinal dimension (z-direction i.e. $s = 3$) and oscillates longitudinally back and forth and scatters (approximately spherically) at the cantered barrier ($H = 5$). First, we inspect the temporal evolution of the density in both transversal and longitudinal direction, and then discuss the effect of integer and non-integer aspect ratios on the participating scattering channels, followed by an analysis of the CM oscillation and the loss of longitudinal first-order coherence in the system.

In figures 7.7a and 7.7b, we depict the time-evolution of the longitudinal and transversal density profiles, respectively. No interference pattern is observed in the longitudinal density profile and the density becomes much more delocalized as well as more irregular compared to the one-dimensional simulations (cf. figure 7.4). While in one dimension, the atom can only be transmitted or reflected, in three dimensions also transversal modes may be populated, since the barrier induces a coupling between the longitudinal and transversal modes. The transversal excitations manifest themselves as a breathing of the density (see figure 7.7b) [212, 323, 324]. Scanning the aspect ratio, we empirically find that the transversal breathing excitations are enhanced if the aspect ratio is integer valued, i.e. $\eta \in \mathbb{N}$. The mechanism of breathing mode excitation is discussed later in detail.

In order to analyse the channels participating in the scattering process as well as the influence of the aspect ratio, we project the numerically ML-MCTDHB obtained wave function $\Psi(\mathbf{r}, t)$ onto the following co-moving basis

$$\phi_{n,l,m}(\mathbf{r}, t) = \varphi_{n,l}^{2D}(\rho, \theta) \phi_m(z, t),$$

which are products of the one-dimensional, periodically moving, stiff wave functions $\phi_m(z, t)$ multiplied by static transversal harmonic oscillator eigenfunctions $\varphi_{n,l}^{2D}(\rho, \theta)$. For the complete orthonormal basis states in the longitudinal direction, we take the solutions $\phi_m(z, t)$ of the time-dependent Schrödinger equation for an one-dimensional harmonic oscillator with the m-th harmonic oscillator eigenstate φ_m^{1D} initially at rest and displaced by b as the corresponding initial condition (for a derivation see appendix G.2). The stiff wave functions $\phi_m(z, t)$ have the following functional form $\phi_m(z, t) = e^{-i\Theta_m(t)} e^{+i\bar{p}(t)z} \varphi_m^{1D}(z - \bar{z}(t))$, with $\Theta_m(t) = E_m t + \frac{1}{2}\bar{z}(t)\bar{p}(t)$ and the harmonic oscillator eigenenergies E_m. Both $\bar{z}(t) = b\cos(t)$ and $\bar{p}(t) = -b\sin(t)$ are the classical values for the position and momentum of an atom oscillating in a harmonic trap. Pictorially, one may view this co-moving basis as the instantaneous eigenstates in a harmonic potential with
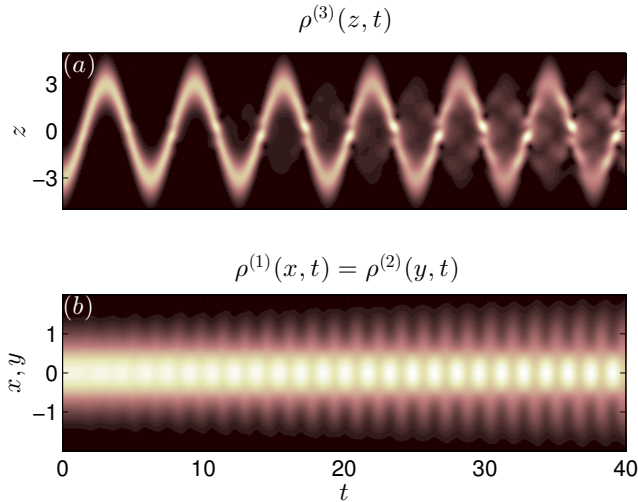
$$\rho^{(3)}(z,t)$$

$$\rho^{(1)}(x,t) = \rho^{(2)}(y,t)$$

Figure 7.7.: Figures (a) and (b) show the longitudinal and transversal density profiles, respectively. Parameters are: barrier height $H = 5$, width $S = 0.2$, displacement $b = 3$ and aspect ratio $\eta = 2$. The grey scales are normalized w.r.t. the respective maximal value of the density. Figure is taken from reference [[2]].

the trap centre $\bar{z}(t)$, which are modified by a momentum boost $\exp(i\bar{p}(t)z)$. By projecting onto this basis, we effectively measure excitations on top of the stiff dipole oscillation of a particle in a harmonic trap.

The initial state of the problem at hand is the Gaussian ground state displaced by $\bar{z}(0) = b$ in the longitudinal direction, i.e. $\Psi(\mathbf{r}, 0) = \phi_{0,0,0}(\mathbf{r}, 0)$. Without the barrier, the stiff Gaussian wave packet $\phi_{0,0,0}(\mathbf{r}, t)$, oscillating in the longitudinal direction, would exactly coincide with the solution of the time-dependent Schrödinger equation. In contrast to this, the barrier $\mathcal{V}$ couples various $\phi_{n,l,m}(\mathbf{r}, t)$ while respecting the following symmetry-induced selection rule. The Hamiltonian $\mathcal{H}_{3D} = H_0 + V$ commutes with the z-component of the angular momentum operator L_z. Since $\phi_{n,l,m}(\mathbf{r}, t)$ is an eigenstate of L_z with eigenvalue l, which holds, in particular, for the initial state $\phi_{0,0,0}(\mathbf{r}, 0)$ with $l = 0$, the barrier may only couple states with vanishing angular quantum number, i.e. $\phi_{n,0,m}(\mathbf{r}, t)$. In order to monitor both transversal excitations and deviations from the stiff Gaussian wave packet oscillation, we show the probabilities

$$d_{n,m}(t) \equiv |\langle \Psi(t) | \phi_{n,0,m}(t) \rangle|^2,$$

for an integer aspect ratio $\eta = 3$ (solid lines) and a non-integer aspect ratio $\eta = 2.5$ (dashed lines) in figure 7.8a. If the aspect ratio is integer valued, the population of the mode $\phi_{0,0,0}$ is transferred both to the second excited transversal harmonic oscillator state $\varphi_{2,0}^{2D}$ measured by $d_2 \equiv \sum_{m=0}^{\infty} d_{2,m}$ as well as to higher excited longitudinal states in the comoving frame with the transversal degrees of freedom being in the ground state, measured by $d_0 \equiv \sum_{m=1}^{\infty} d_{0,m}$, which destroys the stiff oscillation of the wave function. We find that (for our parameter values) essentially no other states participate in the dynamics, i.e. $d_{0,0} + d_2 + d_0 \approx 1$, because the first excited transversal state cannot be excited for symmetry reasons and the excitation energy is not sufficient to populate even higher transversal modes. In the considered time interval, the population d_2 saturates, whereas the population of d_0 monotonously increases. Since these higher excited longitudinal modes are more delocalized, the density becomes more delocalized, too (see figure 7.7).

In contrast to the integer valued case, no significant population of $\varphi_{2,0}^{2D}$ can be observed for the non-integer aspect ratio $\eta = 2.5$, i.e. d_2 is negligible. In total the loss of population of the mode $\phi_{0,0,0}$ is weaker for non-integer aspect ratios. Furthermore d_0 is also decreased for non-

integer aspect ratios, representing a reduced population of higher excited longitudinal states (transversal ground state) and therefore the longitudinal density is more localized compared to the integer aspect ratio case.
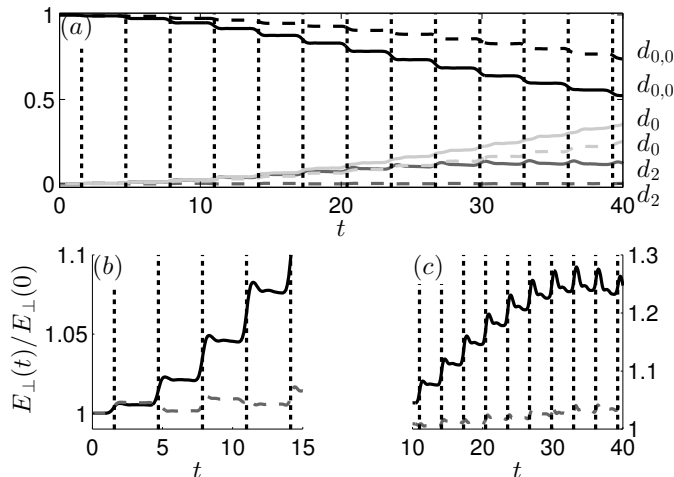

Figure 7.8.: (a) Populations of $d_{0,0}$ (all dark black), $d_2 = \sum_{m=0}^{\infty} d_{2,m}$ (all grey lines), $d_0 = \sum_{m=1}^{\infty} d_{0,m}$ (all light grey lines) for the aspect ratio $\eta = 3$ (solid lines) and for $\eta = 2.5$ (dashed lines). (b) Normalized transversal energy $E_{\perp}(t)/E_{\perp}(0)$ for the integer aspect ratio $\eta = 3$ (dark grey solid line) and the half-integer aspect ratio (light grey solid line) for the first oscillation periods, continued in sub figure (c) for longer times. Black vertical dotted lines mark times, when the atom scatters with the barrier. All other parameters as in figure 7.7. Figure is taken from reference [[2]].

The suppression of transversal excitations for non-integer valued η can be explained by a simple multiple-scattering model, focusing on the transversal degrees of freedom only and assuming instantaneous collisions with the barrier: At the first collision ($t_1 = \pi/2$) of the wave function with the barrier, the second transversal mode $\varphi_{2,0}^{(2D)}$ is excited, since the first transversal mode cannot be populated due to symmetry constraints. Directly afterwards, the time evolution is only governed by H_0. Neglecting correlations between the spatial directions induced by the scattering, the time-dependent transversal wave function for $t \in (\pi/2, 3\pi/2]$ is therefore given by

$$ b_{00}\varphi_{0,0}^{(2D)} + b_{02}e^{-i2\eta(t-t_1)}\varphi_{2,0}^{(2D)} $$

and up to a global phase factor with the amplitudes b_{00} and b_{02}, which determine the transitions $\varphi_{0,0}^{(2D)} \to \varphi_{0,0}^{(2D)}$ and $\varphi_{0,0}^{(2D)} \to \varphi_{2,0}^{(2D)}$, respectively. This excitation leads to a transversal breathing in the density with frequency 2η. After the time interval $\Delta t = \pi$, the wave function collides with the barrier again, leading to a new excitation from the ground state to the second transversal mode and vice versa. Excitations to higher modes are neglected again. At this instant in time ($t_2 = 3\pi/2$), two additional scattering processes have to be taken into account $\varphi_{2,2}^{(2D)} \to \varphi_{2,0}^{(2D)}$ and $\varphi_{2,2}^{(2D)} \to \varphi_{2,2}^{(2D)}$ with the amplitudes b_{20} and b_{22}, respectively. The time-dependent transversal wave function is then

$$ B_0\varphi_{0,0}^{(2D)} + B_2\varphi_{2,0}^{(2D)} $$

with $B_0 = b_{00}b_{00} + b_{02}b_{20}e^{-i2\eta\pi}$ and $B_2 = b_{00}b_{02}(1 + e^{-i2\eta\pi}b_{22}/b_{00})$. Within first-order time-dependent perturbation theory (see appendix G.3), the amplitudes b_{22} and b_{00} are of the same order $b_{22} \simeq b_{00}$ and have the same phase relation. We approximate $B_2 \simeq 2b_{02}b_{00}$ for an integer aspect ratio $\eta = n$ and $B_2 \simeq 0$ for the half integer aspect ratio $\eta = (2n + 1)/2$, with $n \in$

$\mathbb{N}_0$. In other words, the breathing excitations induced by the first and the second collision interfere constructively for integer aspect ratios, whereas they interfere destructively for half-integer valued η.

This feature can also be clearly seen in the transversal energy, $E_\perp = \langle -(\partial_x^2 + \partial_y^2)/2 + \eta^2(x^2 + y^2)/2\rangle$ (see figure 7.8b,c). At the first scattering event off the barrier ($t_1 = \pi/2$), longitudinal kinetic energy is transformed into transversal excitation energy both for the integer and non-integer aspect ratio. But at the second scattering event at $t_2 = 3\pi/2$, the transversal excitation energy is reduced again for the non-integer valued case, whereas in the integer valued case more energy is deposited transversally. This effect causes the step like structure in $E_\perp(t)$ for integer aspect ratios for times $t < 20$. As times goes by, the wave function becomes more and more delocalized and the matrix element $\langle\Psi(t)|V|\Psi(t)\rangle$ couples the transversal and longitudinal dimensions not only at the main scattering events (i.e. at $t = (2n+1)/2\,\pi$ with $n \in \mathbb{N}_0$) but all the time. Thus, following a main scattering event, where energy is pumped into the transversal degrees of freedom, energy can 'flow' continuously back to the longitudinal degree of freedom. This causes the change from the step-like transversal energy increase to a peak-like one (see figure 7.8c). Summarizing, varying the number of oscillation events with the barrier and the aspect ratio might be used for preparing the atom in a certain state involving longitudinal and transversal excited modes.

Due to the spatial coupling (in the case of a low integer aspect ratio), we expect also a modification of the CM oscillation, since the barrier can transfer longitudinal kinetic energy into transversal energy, inducing this way a decay mechanism for the longitudinal CM oscillation $\langle Z\rangle$. In figure 7.9a, we show the CM oscillation for $\eta \in \{2, 2.5, 3\}$ and observe that the CM oscillations decay faster for the integer cases, where significant excitations of the transversal mode are possible. In order to analyse the influence of the aspect ratio on the decay of the CM oscillations, we fit the model (7.14) to our numerical data and extract the decay coefficient c (see figure 7.9b). If the aspect ratio is integer valued, c is peaked, indicating the mentioned decay mechanism w.r.t. the transversal excitation. These peak heights are reduced for larger aspect ratios since a higher initial excitation energy would be needed to populate the transversal modes. For even larger aspect ratios, c saturates and corresponds to a pure one-dimensional simulations with the effective physical parameters stated in section 7.2.1 (not shown).
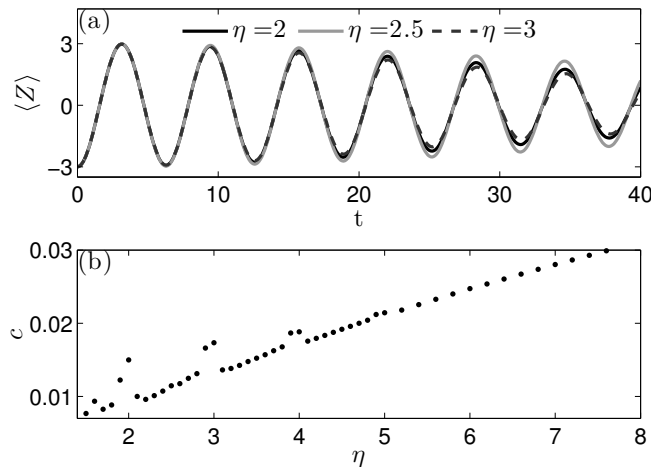

Figure 7.9.: (a) The oscillation of the CM for $\eta = 2$ (dark grey line), $\eta = 2.5$ (light grey line) and $\eta = 3$ (black dashed line). (b) depicts the fitted decay coefficient c of model (7.14) for various aspect ratios. All other parameters coincide with those of figure 7.7. Figure is taken from reference [[2]].
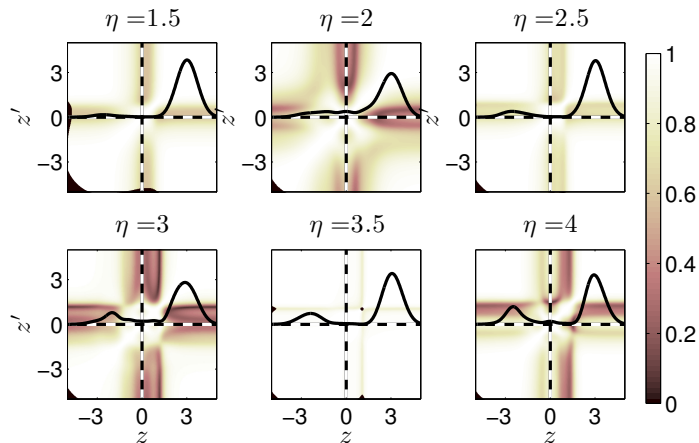
Figure 7.10.: First-order correlation function $|g_1(z, z')|$ for different aspect ratios η at the time instant $t = 9\pi$. Areas of density smaller than 10^{-6} are coloured in black. The black-white dashed line marks the position of the barrier and the black solid line is the longitudinal density profile. Same physical parameters are used as in figure 7.7. Figure is taken from reference [[2]].

To analyse the loss of coherence in the longitudinal direction due to correlations between the spatial directions, we compare the first-order correlation function

$$g_1(z, z') = \frac{\rho^{(s=3)}(z, z')}{\sqrt{\rho^{(s=3)}(z)\rho^{(s=3)}(z')}}$$

where the longitudinal one-dimensional density $\rho^{(s=3)}(z')$ and one-dimensional density matrix $\rho^{(s=3)}(z, z')$ are obtained by integrating out the transversal degrees of freedom, e.g. $\rho^{(s=3)}(z, z') = \int dx dy \, \rho^{(3D)}(x, y, z; x, y, z')$. The absolute value of the first-order correlation function is shown in figure 7.10 for different aspect ratios at the turning point $t = 9\pi$ of the corresponding classical oscillation. For integer aspect ratios, we find a pronounced loss of coherence between the region close to the barrier and outer regions. This incoherent density fraction stems from nearly spherical, incoherent scattering (involving the second excited transversal mode) off the barrier. Due to a stronger coupling of the spatial directions, this loss of coherence is enhanced for decreasing η. Accordingly, there is only a faint incoherent density fraction for non-integer aspect ratios, being hardly visible in the case $\eta = 3.5$. Non-integer aspect ratios are thus favourable if one needs to propagate an initial wave function coherently w.r.t. the longitudinal direction in the presence of a perturber or impurity. We finally remark that $g_1(z, z')$ contains for large aspect ratios an asymmetry w.r.t. the barrier in comparison with smaller aspect ratios at the time instant $t = 9\pi$. A symmetric arrangement of g_1 around the barrier can be found at an earlier time instant in which the time shift increases.

7.4. Dynamics of few bosons in three dimensions

In this section, mainly taken from the publication [[2]], we combine the knowledge, which we have gained for a few atoms in one dimension, with one atom in three dimensions in order to study few atoms in three dimensions taking correlations into account. We simulate the temporal evolution of five interacting bosons, ($h = 91.125$) with a centred barrier ($H = 9$) and vary the aspect ratio η between 1.5 and 8.0 in order to see the influence of the dimensionality on the scattering behaviour. In order to ensure short-range interactions and to resolve the interaction potential properly, a large number of grid points have to be used. The ML-MCTDHB method

is tailored to effectively treat large number of grid points and we perform our simulations with $q_3 = 800$ and $q_1 = q_2 = 200$ grid points in the longitudinal and each transversal direction, respectively. For a convergence study and other numerical parameters, see also appendix G.1.

In order to quantify particle and spatial correlations, we analyse the integrated depletions in dependence of η, as we have done in chapter 6. For completeness, we repeat the definitions of the depletion here (see also section 1.4).

$$D_{(3D)}(\eta) = 1 - \frac{1}{T_{max}} \int_0^{T_{max}} a_1^{(3D)} dt$$

$$D_{(s)}(\eta) = 1 - \frac{1}{T_{max}} \int_0^{T_{max}} b_1^{(s)} dt$$

where $a_1^{(3D)}$ and $b_1^{(s)}$ are the first natural populations of $\rho^{(3D)}$ and $\rho^{(s)}$ for the dimension $s \in \{1,2,3\}^2$, respectively, and T_{max} is the maximal simulation time.

We see that for small integer aspect ratios the system is spatially correlated. Increasing the aspect ratios, particle correlations increase while spatial correlations decrease. Further increasing the aspect ratio, the spatial correlations between the transversal and longitudinal degrees of freedom become negligible and the depletion $D_{(3D)}$ come closer to the $D_{(s)}(\eta)$ one. This is the same characteristic as already observed for the double well trap (see figure 6.6), here, however, the spatial correlations are much stronger. For half-integer aspect ratios (see the inset of figure 6.6), we again observe the general characteristic behaviour, however, in comparison to integer aspect ratios, the spatial correlations are suppressed, as already discovered and explained in section 7.3.
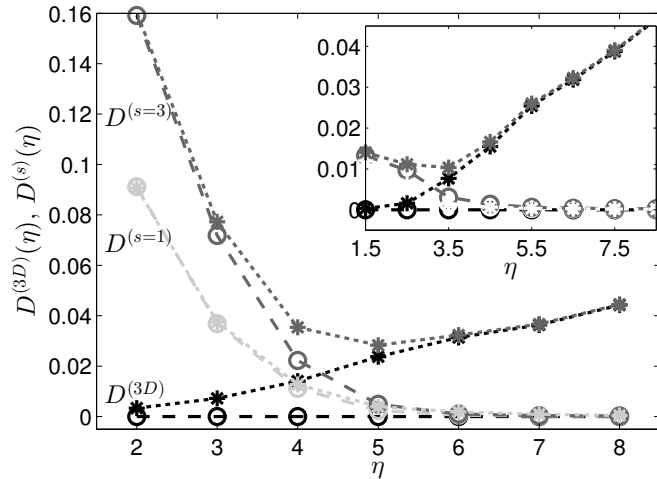

Figure 7.11.: Time-averaged depletions (for a definition see text) for integer (half integer) aspect ratios in the main figure (inset), measuring particle ($D^{(3D)}$, all black lines), spatial transversal ($D^{(s=1,2)}$, all light grey lines) and longitudinal ($D^{(s=3)}$, all grey lines) correlations. Circles denote MF simulations, and stars represent BMF simulations. Physical parameters: $N = 5$, $H = 9$, $S = 0.2$, $h = 91.125$ and $\sigma = 0.1$. Data points are connected by a line in order to guide the eye. Figure is taken from reference [[2]].

The CM dynamics of the few-boson ensemble does not differ qualitatively from the single-atom case discussed in section 7.3 (see figure 7.12a), but only quantitatively due to the presence of interactions. As already observed, the CM oscillation for integer aspect ratios features a stronger

---

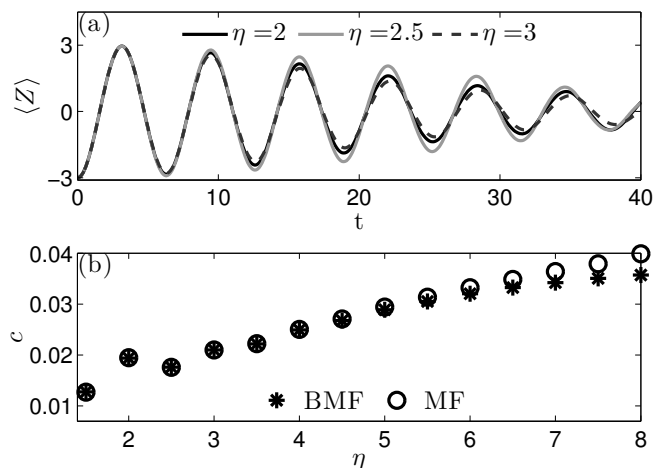² Note $D_{(1)} = D_{(2)}$ due to symmetry.

Figure 7.12.: (a) The CM dynamics is shown for the different aspect ratios $\eta = 2, 2.5, 3$. (b) shows the fitted decay constant c of the model (7.14) in dependence of η. Same physical parameters as in figure 7.11. Figure is taken from reference [[2]].

decay, since energy can be stored in transversal modes. Fitting again the model (7.14) to the numerical data (figure 7.12b), we see that the decay coefficient c features a similar dependence on η as for a single atom (figure 7.9), but the peak structure is less pronounced. Furthermore for larger aspect ratios, a discrepancy in c is observed between MF and BMF simulations. This effect has already been encountered in the purely one-dimensional case, where the second natural orbital becomes populated, leading to a reduction of the decay coefficient (see section 7.2).

In figure 7.13, the absolute value of the first-order correlation functions $g_1(z, z')$ is given for different aspect ratios, at the right classical turning point ($t = 9\pi$). For the aspect ratios $\eta = 1.5, 2$, we see that the correlation function exhibits the characteristic structure observed for a single atom in three dimensions (see figure 7.10), namely the loss of coherence between the region close to the barrier and outer regions. This structure is more pronounced for the integer aspect ratio $\eta = 2$ because of the enhanced population of the second transverse excited mode. Increasing the aspect ratio to $\eta = 3.5, 4$, enhances the overall coherence. For $\eta = 3.5$, we even find almost perfect coherence in the longitudinal direction. This regime is well-suited for propagating the initial wave function coherently in a harmonic trap with the presence of a scatterer, as a beam splitter. For large aspect ratios $\eta = 7.5, 8$, the differences between the integer and non-integer aspect ratios disappears and an incoherent structure emerges, which is similar to the results for few bosons in one dimensions (see figure 7.6), but with a sharp borderline between coherent regions.

7.5. Summary

We have studied the dynamics of an interacting ensemble of bosons, which are initially displaced from the trap centre of an elongated, three-dimensional, harmonic trap. The displacement has been larger than the one performed in chapter 6, so that enough initial energy exists in order to populate transversal modes. As the same time as the start of the temporal evolution of the bosonic ensemble, a trap-centred barrier is switched on of which the bosons can scatter. We have been interested in the influence of spatial and particle correlations on the oscillation of the centre of mass as well as on the loss of first-order coherence in the crossover from three to one dimension. The crossover has been achieved by changing the aspect ratio between the transversal

and longitudinal trap frequencies. In order to perform a structured study, we have divided the analysis into three parts: First, we have regarded only particle correlations by looking at a pure one-dimensional system. Second, the focus has been set to only spatial correlations and we have analysed one boson in three dimensions, and finally, we have studied both particle and spatial correlations by simulating five bosons in three dimensions.

Concluding, two mechanisms of coherence loss have been identified: The first mechanism can be linked to spatial correlations, occurring for low aspect ratios, due to the excitations of transversal modes. We observe a loss of coherence between positions close to the barrier and outer regions. The second mechanism occurs for larger aspect ratios and originates from an incoherence between the density fragments to the right and the left of the barrier, emerging due to particle correlations. At intermediate aspect ratios, e.g., at $\eta = 3.5$, we have found a regime, where both particle and spatial correlations are suppressed, and therefore, this regime is suitable for coherent transport of the wave-function.

Next, we have focused on the damping of the centre of mass oscillation in dependence of the aspect ratio. Apart from the influence of the reflection and transmission, induced by the multiple scattering events of the wave function with the barrier, we have identified two more effects: In the first one, due to the coupling of the dimensions, energy is transferred into the excitation of transversal modes, leading to a decay mechanism for the (longitudinal) CM oscillations. This effect is dominant for small aspect ratios. In the second one, particle correlations become more pronounced which modify the CM oscillations, occurring at large aspect ratios.

Furthermore, we have found out, that all these described effects are stressed for integer aspect ratios and reduced for half-integer aspect ratios. Looking at the depletions, three different regimes have been identified, identical to the ones already studied in chapter 6, however with stronger spatial correlations for integer aspect ratios.
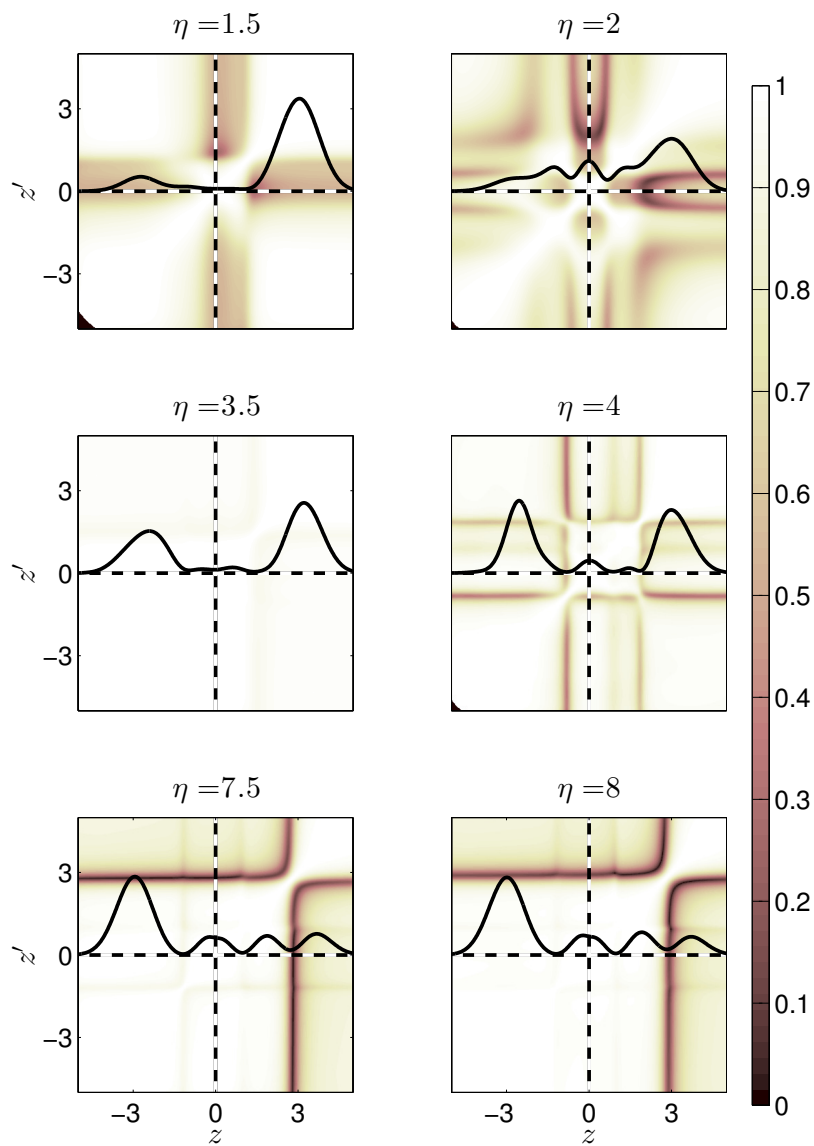
Figure 7.13.: First-order correlation function $|g_1(z, z')|$ for different aspect ratios η at the time instant $t = 9\pi$. Areas of density smaller than 10^{-6} are coloured in black. The black-white dashed line marks the position of the barrier and the black solid line is the longitudinal density profile. Same physical parameters are used as in figure 7.11. Figure is taken from reference [[2]]

<div style="text-align: right">

CHAPTER

EIGHT

</div>

<div style="text-align: right">

SUMMARY

</div>

In this thesis, we have explored the impact of dimensionality on the quantum dynamics of inter-acting bosons in various traps including spatial and particle correlations. In order to tackle this problem, we have extended the state-of-the-art ab-initio Multi-Layer Multi-Configuration Time-Dependent Hartree method for Bosons (ML-MCTDHB), which solves the many-body bosonic Schrödinger equation very efficiently. The working principle of the MCTDHB algorithm is to expand the many-body wave function into a sum over all number states of the bosonic system with time-dependent coefficients. Importantly, the number states are created by variationally optimized time-independent single-particle functions. In doing so, the MCTDHB can tackle the exponential scaling of complexity with respect to the number of bosons. However, it has not been clear how the two-body interaction can be efficiently modelled in three dimensions by taking correlations into account.

First, we have analysed different possibilities of modelling a (time-dependent) two-body inter-action potential in three dimensions, starting with the bare delta interaction potential, which has the advantage that the interaction range has not to be resolved numerically. However, the bare delta interaction in three dimensions can be shown to be an ill-defined interaction, since the increase of the size of basis set reduces the effect of the interaction until, in the limit of an infinite number of basic functions, no scattering remains. This is in contrast to one-dimensional systems, where the bare delta interaction can be used without limitation. A natural correc-tion to the bare delta interaction has been given by the regularized delta interaction potential, which is very successfully used in analytical calculations. However, we prove that the regularized delta interaction reduces to the bare delta interaction if it acts on a finite sum over products of single-particle basis functions, as used in many wave function expansion methods, such as the MCTDHB method. Only if a two-particle basis would be used, the regularized delta interac-tion describes the scattering in three-dimensions correctly. In the Gross-Pitaevskii mean-field theory, however, the bar delta interaction is commonly used. Indeed, we show that bare and regularized delta interactions are equivalent if particle correlations are neglected. In order to fix the problems with the delta interactions in three dimensions, we have developed different renormalization algorithms suitable for the MCTDHB method. However, in doing so, these algo-rithms expose many conceptual problems due to the time-dependent basis used in the MCTDHB method. Therefore, the algorithms have turned out to be numerical impractical as well as con-tradicts to the philosophy of the MCTDHB method. As a consequence, we have decided to use finite-range interaction potentials accepting the challenge of resolving the interaction range nu-merically. We have defined conditions for an efficient numerical implementation for finite-range interaction potentials, e.g., that the finite-range interaction potentials must be short-ranged and

pure repulsive, where the latter is numerically convenient and avoids complications of bound states. We have discussed different interaction potentials and have come up with a renormalized Gaussian interaction potential as the most suitable numerical implementation for a two-body iteration potential. Here, the renormalization keeps the interaction range limited, and therefore, restricts the zero-energy scattering length to the interaction range. As already mentioned, the finite-range interaction potential induces a new physical length scale. By construction, the latter must be the smallest length scale in the system, in particular smaller than the characteristic trap length scale in order to satisfy the short-range criterion. In this case, numerical methods, such as the MCTDHB method requires a large number of grid points in order to cover all the involved lengths scales. Hence, we need an algorithm, which can efficiently handle large number of grid points.

However, the MCTDHB method is not designed to handle these large number of grid points, since it uses a product grid w.r.t. the dimensions as the primitive basis. In order to circumvent this limitation, we have extended the MCTDHB algorithm by expanding the three-dimensional single-particle functions into three, time-dependent, one-dimensional single-particle functions, in the spirit of the Multi-Layer Multi-Configuration Time-Dependent Hartree method for Bosons (ML-MCTDHB) [62]. In doing so, we have derived specially tailored equations of motion by employing the Dirac-Frenkel variational principle and have discussed their efficient numerical implementation in order to cope with the occurring numerical bottlenecks. Among other things, e.g. by using parallel-processing, we have achieved an efficient implementation for desktop computers. Our algorithm does not operate on a product grid anymore, rather the total numbers of grid points q_{tot} scale linear with the dimensions d, $q_{tot} \propto dq$ and not exponential as in the MCTDHB method, $q_{tot} \propto q^d$ The implementation of the new algorithm has been tested and compared with other numerical methods available in the literature. Let us note that apart from solving the full time-dependent Schrödinger equation, this ML-MCTDHB algorithm can be also used to efficiently solve the Gross-Pitaevskii mean-field equation for a large number of grid points by using the bare delta interaction potential.

In the remaining part of the thesis, we have applied the ML-MCTDHB method to three different physical systems in order to study the generation and evolution of spatial and particle correlations in the crossover from three to one dimension:

In the first setup, we have studied the ground state of two interacting bosons in both an isotropic and elongated harmonic trap in order to determine the interesting range of numerical and physical parameters and study the convergence behaviour of the ML-MCTDHB algorithm. By analysing the ground state energy, we have been able to determine the maximal and/or minimal values for the numerical parameters, i.e., the grid spacing and the grid length. By varying the aspect ratio between the transversal and longitudinal trap frequencies, the maximal and minimal value for the aspect ratio has been determined ensuring short-range interactions, i.e., ensuring the disregard of the influence of the trap on the scattering process. Next, we have determined the maximal possible value for the zero-energy scattering length, which we can achieve, while still guaranteeing converged simulations. As we have shown, the maximal zero-energy scattering length of the renormalized Gaussian interaction potential induces only minor particle correlations in the system. However, higher particle correlations can be achieved by increasing the number of particles. Furthermore, we have studied the convergence behaviour of the two-particle system in an isotropic trap, since here the numerical results can be compared with the analytical ones. We have found two main effects w.r.t. the convergence behaviour: (i) In three dimensions, the natural populations decay algebraically. (ii) Even for weak transversal confinement, small spatial correlations are obtained, justifying our wave function ansatz as done in the ML-MCTDHB algorithm.

The second system, which we have studied, consists of a three-dimensional double-well in the

longitudinal direction embedded in an elongated harmonic trap. A surplus of bosons in one well is created by adding a linear potential, and by removing this linear potential the bosons tunnel between the wells. We have studied the influence of particle and spatial correlations in dependence on the transversal confinement, performing a crossover from three to one dimension. Especially, we have been interested in the validity of the following two approximations for the many-body wave function: (i) The many-body wave function is approximated by a mean-field ansatz, in particular, by assuming that all particles occupy the same orbital ψ, $\Psi(\mathbf{r}_1, ...\mathbf{r}_N) = \prod_{i=1}^{N} \psi(\mathbf{r_i})$, known as the Gross-Pitaevskii ansatz. The orbital ψ is determined variationally. This approximation of the many-body wave function cannot resolve particle correlations. (ii) The many-body wave function is separated into a longitudinal and a transversal part, where transversally only one mode is used, $\Psi(\mathbf{r}_1, ...\mathbf{r}_N) = \prod_{i=1}^{N} \psi(x_i, y_i)\varphi(z_1, ...z_N)$. This approximation is the approach for reducing a three-dimensional system to a pure one-dimensional system, where the transversal modes are determined variationally and cannot resolve spatial correlations. We have seen that for weak transversal confinements, minor particle correlations can be found in the system, however, significant spatial correlations both for the ground state and in the dynamics occur. Hence this parameter regime is well described by the mean-field approach. For a strong transversal confinement, the spatial correlations are reduced and significant particle correlations can be only found in the longitudinal direction. In between the weak and strong confinement, we have identified a regime, where both particle and spatial correlations are present such that both of the above approximations fail to describe the many-body wave function correctly. In this regime, all correlations have to be taken into account, which can be done by the ML-MCTDHB algorithm. Furthermore, even for small spatial correlations, there is the need for at least two transversal modes, in order to describe the density profile of the wave function and the tunnelling behaviour correctly. Finally, we want to note that in the regarded system no significant energy transfer from the longitudinal to transversal directions has been observed.

In the third system, we have changed the initial conditions in order to see an energy transfer between the dimensions. In doing so, we have been able to analyse the quantum dynamics of an interacting bosonic ensemble in an elongated trap, initially displaced in the elongated direction. We follow the evolution of the bosonic ensemble in time which scatters multiple times off a centred barrier. Again, we have been interested into the emergence and disappearance of particle and spatial correlations in the crossover from three to one dimension. We have observed a similar behaviour as in the double well scenario; however, spatial correlations are strongly suppressed for half-integer aspect ratios. We have explained this effect by a model which describes destructive interference of transversally excited modes. Furthermore, we have found two mechanisms of loss of the first-order coherence in the longitudinal direction in dependence on the aspect ratio. For weak confinement, we have observed loss of coherence due to an incoherent scattering, manifested between positions close to the barrier and outer regions. For stronger confinement, one can see incoherences between the density fragments to the right and the left of the barrier emerging due to particle correlations. However, for non-integer aspect ratios, coherent transport of the bosonic ensemble even in the presence of the barrier is observed. Therefore, traps with non-integer aspect ratios may be suitable in order to avoid decoherences in beam splitters or matter-wave interferometers. In addition, we have analysed the decay of the amplitude of the oscillation of the centre of mass. Apart from the reflection and transmission of the bosonic ensemble off the barrier, two more effects have been identified, which influence the decay of the centre of mass oscillation. For small aspect ratios, transversal modes can be populated transferring energy from the longitudinal into the transversal direction enabled by the barrier which coupled the dimensions. Afterwards, this energy is missing in the oscillation of the centre of mass and leading to a decay of the oscillation. In contrast for large aspect ratios, the increasing particle correlations weaken the decay of the centre of mass oscillation, since the second natural orbital maintains the dipole oscillation. These effects are pronounced for integer

aspect ratios and attenuated for non-integer (especially for half-integer) aspect ratios. We have shown that by tuning the initial displacement, the simulation time, the parameters of the hump as well as the aspect ratio, we have full control on the spatial fragmentation in the longitudinal directions and the admixture of excited transversal states.

In summary, the presented ML-MCTDHB method is able to cover the whole crossover from three to one dimension by taking all correlation into account in a numerical controlled way, which is notoriously difficult to describe by any numerical method. Since the ML-MCTDHB method evolves the initial wave function in time, the wave function is known at every instant in time and different kinds of observables can be calculated and studied. Especially one- and two-body observables are easy to calculate since the one- and two-body density matrices are anyway calculated in the ML-MCTDHB algorithm. The ML-MCTDHB algorithm is efficiently implemented for one-species bosonic ensembles in three dimensions with (time-dependent) two-body interaction potentials given in a product form such as the delta interaction or the Gaussian interaction.

<div style="text-align: right">

CHAPTER

NINE

</div>

OUTLOOK

 The presented three-dimensional version of the ML-MCTDHB method is able to cover the whole crossover from 3D to 1D and also from 3D to 2D for interacting bosonic ensembles while taking all kinds of correlations into account. Furthermore, arbitrary types of (even time-dependent) three-dimensional interaction potentials can be employed, however, most efficiently is the use of interaction potentials, which are already given in the product from w.r.t. the dimensions. The ML-MCTDHB method, as every MCTDH method, can handle arbitrary time-dependent single-particle potentials either with periodic or hard wall boundary conditions. With this quite general numerical tool, a huge variety of different bosonic systems can be studied not only in the dimensional crossover but also in a pure three- and two-dimensional situation and in which particle correlations are taken into account. In the following, we give some examples for possible setups:

i. The coherent transport through a wave guide [325] can be studied including spatial and particle correlations. For a sufficient strong interaction, transversal mode can be populated, storing kinetic energy, and coherence may be lost due to particle correlations or transversal excitations. The transport can be disturbed by single or multiple obstacles, e.g., a single impurity in order to study polaron physics [315, 326], a chain of ions for the analysis of solid state emulators [327, 328] or random potentials in order to investigate Anderson localization [329–332]. In particular if a large amount of number of grid points is needed, the here presented method fully exploits its advantages. As already mentioned, apart from a static potential, also a time-dependent potential can be used in order to quantum-mechanically study guided quantum transport in elongated traps or wave guides [333–335]. Furthermore, by placing on each end of the wave guide a bosonic ensemble with opposite initial momentum, the quantum dynamics of the many-particle scattering process can be analysed [336, 337]. Using the ML-MCTDHB method, all these studies can be performed by taking particle and spatial correlation into account. These results of the studies of coherent transport through a wave guide may be used in many physical fields, e.g., such as for matter-waves interferometers or for quantum computing.

ii. Another interesting study is the dynamics of the breathing mode in the crossover from three to one dimension and the influence of particle and spatial correlations on the breathing frequency. In particular, differences from the mean-field results [80, 118, 154] are expected or a modification from pure one-dimensional examinations [324, 338]. Furthermore, different quench scenarios can be imagined, where either the interaction strength or an external potential e.g. the longitudinal or transversal trap frequency is quenched, creating

not only a breathing mode, but also a cradle and/or dipole mode[1]. In particular, induced dynamics in the direction orthogonal to the quench direction is of interest in order to observe induced spatial as well as particle correlations.

iii. The three-dimensional ML-MCTDHB algorithm can also be used to study coherence properties of twin-atom beams [340, 341]. Twin-atom beams can be created if a transversally excited ensemble of bosons may decay into a longitudinal right and left moving fraction. These counter-propagating beams provide non-local correlations and feature entanglement, which can be exploited in quantum communication protocols [341].

iv. Owing to the efficiency, the ML-MCTDHB algorithm is suitable for the study of parameter scans. For example, it would be interesting so see the dependency of the Lieb-Lininger parameter, e.g. monitored by the interaction energy, on the crossover from three to one dimension as well as on the number of particles. We remind that for a pure one-dimensional system, the Lieb-Lininger parameter behaves as $\propto 1/N$ whereas in three dimensions $\propto N$.

v. Another interesting study would be the tunnelling between two neighbouring elongated traps (see figure 9.1a). A bosonic ensemble can tunnel w.r.t. the y-directions while many low laying modes can be excited in the longitudinal (orthogonal) z-dimension [303, 342, 343]. This is in contrast to the setup, studied in chapter 6, where no significant orthogonal modes are excited during the tunnelling process, i.e. no significant energy transfer exists between the transversal and longitudinal directions. Here, one can analyse, how these low-energy excitations (in the z-direction) influence the tunnelling frequency taking particle correlations and spatial correlations into account.

Another aspect is that ions could be put between the two neighbouring elongated traps (see figure 9.1b) and the influence of the ions on the tunnelling frequency can be studied and allowing for tuning the tunnelling by changing the interaction between the ion(s) and the boson. The corresponding pure one-dimensional study has been performed in reference [213, 214, 316].
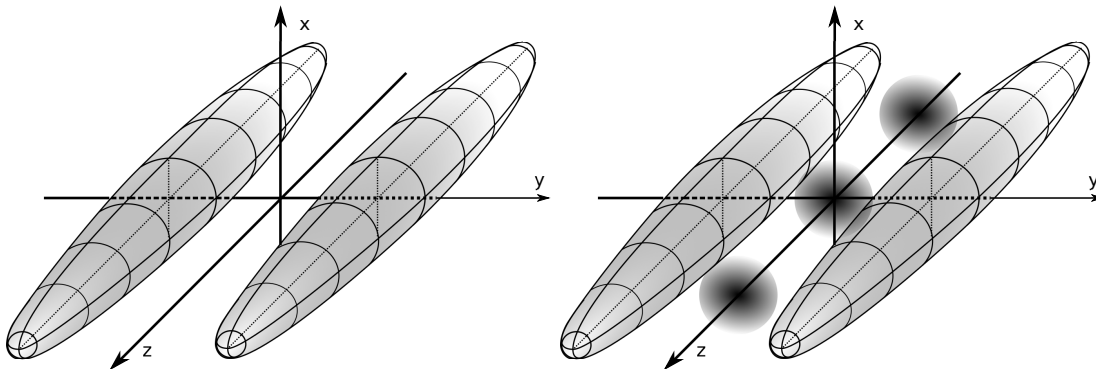

Figure 9.1.: Left panel shows two separated elongated bosonic ensembles (grey shaded area) confined to elongated traps, sketched by the black solid lines. Right panel shows the same as the left panel but with three additional ions between the two elongated traps.

vi. A challenging but in principle possible numerical task would be to study a bosonic ensembles with attractive interactions. The implementation of an attractive interaction potential is straight forward, namely, by using negative prefactors for the renormalized Gaussian interaction potentials in order to model more realistic interaction potentials. Furthermore, one can think of a combination of repulsive and attractive interaction potentials, e.g., by using two nested Gaussian interaction potential. Due to the resonances occurring in an

---

[1]For a one dimensional study see reference [339]

attractive interaction potential, an arbitrary high zero-energy scattering length can be obtained, and maybe even, the unitary limit in three dimensions can be reached, being of current interest in research [15, 344]. However, the convergence behaviour of such simulations has to be studied very carefully since it can be questionable if these simulations can be brought to convergence [231].

vii. Not only various pure three-dimensional setups or studies of the dimensional crossovers from 3D to 1D can be handled by the ML-MCTDHB algorithm but also all the above studies can be performed for a pure two-dimensional bosonic ensembles or crossovers between 2D and 1D. However, we note that the algorithm is optimized for three dimensions, resulting in a computational overhead for two dimensions. The computational overhead can be minimized by a future efficient implementation of the ML-MCTDHB algorithm for two dimensions. Other possible numerical extensions of the three-dimensional algorithm are the extension to multi-species, such as two or more different bosonic or fermionic or mixtures between fermionic and bosonic systems in three dimensions, which we have already derived in reference [[3]]. Furthermore, another possible extension could be to include internal degrees of freedoms, e.g., spin, yielding a four-dimensional problem. These algorithms have to be highly optimized in order to obtain tolerable simulation times and to achieve convergence.

Concluding, we are able to study a plethora of different systems while taking particle and spatial correlations into account with the here developed three-dimensional version of the ML-MCTDHB method. With this optimized algorithm, we have been able to reach new regimes, whose quantum dynamics are notoriously difficult to be studied by any method in the literature. These studies enable to develop a better understanding of microscopic physical processes in many-body systems and can advance the interpretation of physical experiments by illuminating the influence of correlations.

ACKNOWLEDGEMENTS

EIDESSTATLICHE ERKLÄRUNG / DECLARATION ON OATH

Hiermit versichere ich an Eides statt, die vorliegende Dissertationsschrift selbst verfasst und keine anderen als die angegebenen Hilfsmittel und Quellen benutzt zu haben.

Die eingereichte schriftliche Fassung entspricht der auf dem elektronischen Speichermedium.

Die Dissertation wurde in der vorgelegten oder einer ähnlichen Form nicht schon einmal in einem früheren Promotionsverfahren angenommen oder als ungenügend beurteilt.

Hamburg, den _____

_____
Valentin Jonatan Bolsinger

Appendix

APPENDIX

A

GENERAL APPENDIX

A.1. Acronyms

Table A.1.: List of used acronyms

BEC	Bose-Einstein Condensate
BMF	Beyond Mean-Field
CI	Configuration Interaction
CM	Center of Mass
DOF	Degree Of Freedom
EOM	Equations Of Motion
FFT	Fast Fourier Transform
GPE	Gross-Pitaevskii Equation
IMEST	Interaction Matrix Evaluation by Successive Transforms
MCTDH(B)	Multi-Configurational Time-Dependent Hartree method (for Bosons)
MF	Mean-Field
ML-MCTDH(B)	Multi-Layer Multi-Configurational Time-Dependent Hartree method (for Bosons)
1D-SPF(s)	One-Dimensional Single-Particle Functions(s)
3D-SPF(s)	Three-Dimensional Single-Particle Functions(s)
rel	relative
w.r.t.	with respect to

SCATTERING THEORY

B.1. Spherical Bessel and Neumann functions

In the far and near field, the spherical Bessel and Neumann function have the asymptotic representation [345]:

$$\lim_{x \to \infty} j_l(x) = j_l^{\infty}(x) = \frac{\sin(x - \frac{l\pi}{2})}{x} \qquad\qquad \lim_{x \to 0} j_l(x) = j_l^0(x) = \frac{x^l}{(2l+1)!!}$$

$$\lim_{x \to \infty} n_l(x) = n_l^{\infty}(x) = -\frac{\cos(x - \frac{l\pi}{2})}{x} \qquad\qquad \lim_{x \to 0} n_l(x) = n_l^0(x) = -\frac{(2l-1)!!}{x^{l+1}}$$

B.2. Proof that the bare delta interaction does not scatter in three dimensions

Let $p = i\partial_r$ be the radial momentum operator in three dimensions (in position representation) and $T = p^2/2 = -\partial_r^2/2$ the radial kinetic operator as well as $\phi(r) = u(r)/r$ an arbitrary, normalized (well-defined) wave function with the radial coordinate r. The Schrödinger equation can be written for $u(r)$ [see equation (2.26)]. If p is a hermitian operator $\langle u|pu \rangle = \langle pu|u \rangle$ then T is also one, since p can be applied twice. $\langle u|Tu \rangle = \langle u|p^2 u \rangle = \langle pu|pu \rangle = \langle p^2 u|u \rangle = \langle Tu|u \rangle$. Next, we analyse under which conditions p is hermitian in the interval from a to b.

$$\langle u|pu \rangle = |u(r)|^2|_a^b + \langle pu|u \rangle$$

using partial integration to shift the partial derivative to the conjugated part, and therefore, the condition for a hermitian momentum operator is

$$|u(a)|^2 = |u(b)|^2 \tag{B.1}$$

We set the boundary $a \to 0$ and $b \to \infty$ and notice that $u(r)|_{r \to \infty} = 0$, due to the normalization condition of $\phi(r)$, $1|\phi(r)|^2$. Therefore at position $r = 0$, the function u must be zero as well, otherwise p is not hermitian. Because the bare delta interaction is localized at $r = 0$, however $u(0) = 0$, the bare delta interaction has got no effect in three dimensions.

APPENDIX

C

EFFICIENT NUMERICAL MODEL FOR THE TWO-BODY INTERACTION POTENTIAL

C.1. Derivation of equation (3.4)

We show the divergent behaviour of equation (3.4) by using harmonic oscillator functions $\langle r = 0|\varphi_k\rangle$ with $l = 0$.

$$\langle r = 0|\varphi_k\rangle = N_k L_k^{\frac{1}{2}}(0)Y_{00}(\theta, \phi)$$

$$= \sqrt{\pi^{-3/4}2^k k!/(2k-1)!!} \left(\begin{array}{c} k + \frac{1}{2} \\ k \end{array} \right) \tag{C.1}$$

with the generalized Laguerre polynomials $L_k^{\frac{1}{2}}(0) = \left(\begin{array}{c} k + \frac{1}{2} \\ k \end{array} \right)$, the spherical harmonic function $Y_{00}(\theta, \phi) = 1/\sqrt{4\pi}$ and the normalization constant $N_k = (4\pi)^{-1/4}\sqrt{2^{k+3}k!/(2k+1)!!}$. We have set $\hbar = \omega = m = 1$. The left hand side of equation (3.4) is then

$$\sum_{k=0}^{\infty} \frac{|\langle \mathbf{r} = 0|k, l = 0, m = 0\rangle|^2}{\epsilon_{k,l=0} - E_{rel}}$$

$$= \left(\frac{1}{\pi}\right)^{\frac{3}{2}} \sum_{k=0}^{\infty} \frac{2^k k!}{(2k-1)!!} \left(\begin{array}{c} k + \frac{1}{2} \\ k \end{array} \right) \left(\begin{array}{c} k + \frac{1}{2} \\ k \end{array} \right) \frac{1}{\epsilon_{k,l=0} - E_{rel}}$$

$$= \left(\frac{1}{\pi}\right)^{\frac{3}{2}} \frac{1}{2} \sum_{k=0}^{\infty} \frac{(2k+1)!!}{(2k)!!} \frac{1}{k - \mathcal{E}}$$

where we have used the following identities $\Gamma(k + 3/2) = \sqrt{\pi}(2k+1)!!/2^{k+1}$, $(2k)!! = 2^k k!$ and insert the relations $\epsilon_{k,l=0} = 2k + 3/2$ and the definition $\mathcal{E} \equiv E_{rel}/2 - 3/4$. Here, Γ is the gamma function, $\Gamma(k+1) = k!$. With $(2k+1)!!/(2k)!! > 1$, the sum is bounded from below by $\sum_{k=0}^{\infty} \frac{1}{k-\mathcal{E}}$, which is divergent.

C.2. Transformation of the regularized delta interaction to laboratory coordinates

We transform the regularized delta interaction potential $g\delta(\mathbf{r})\partial_r r$, given in spherical relative coordinates with $r = |\mathbf{r}|$, into Cartesian laboratory coordinates. The individual parts of the

regularized delta interaction potential can be transformed separately. We only perform the transformation into Cartesian coordinates for the derivative $\partial/\partial r$ since the other parts are trivial. The coordinate transformation from spherical relative coordinates to Cartesian relative coordinates reads

$$\mathbf{r} = \begin{pmatrix} r_1 \\ r_2 \\ r_3 \end{pmatrix} = \begin{pmatrix} x \\ y \\ z \end{pmatrix} = \begin{pmatrix} r\cos\theta\sin\varphi \\ r\sin\theta\sin\varphi \\ r\cos\varphi \end{pmatrix}$$

leading to

$$\frac{\partial}{\partial r} = \sum_{i=1}^{3} \frac{r_i}{\sqrt{r}}\frac{\partial}{\partial r_i}$$

with $r^2 = x^2 + y^2 + z^2$. After transformation into the laboratory frame ($\mathbf{r} = \mathbf{r}_2 - \mathbf{r}_1$) and putting the parts together, equation (3.6) is recovered.

C.3. Renormalization Theories

As mentioned in the main text, different renormalization theories have been developed in various physical fields. However, these theories cannot be used straight forward in our case, because of the complexity of the ML-MCTDHB algorithm. Before presenting our developed renormalization procedures w.r.t. to the ML-MCTDHB algorithm, we repeat the requirements, which a proper renormalization procedure has to fulfil.

  i. The renormalization theory should handle arbitrary, especially time-dependent, external potentials in order to be flexible for different (experimental) setups.

 ii. Not only the ground state of a two particle systems, but also the renormalization of excited as well as many-particle states should be described correctly.

iii. Since the ML-MCTDHB method is ab-initio, the renormalization procedure should not use any approximation, except the "natural" numerical truncation of the single-particle functions or the discretization of space.

 iv. The renormalization theory should be numerical feasible, and its computational costs should be less in comparison with the remaining part of the ML-MCTDHB algorithm.

C.3.1. Renormalization theory No. 1

The idea of the first renormalization theory is to start with the truncated version of equation (3.2), derived in the main text. As a reminder, equation (3.2) reads:

$$c_{\mathbf{j}}(\epsilon_{\mathbf{j}} - E_{rel}) + g_R \sum_{\mathbf{i}=1}^{M} c_{\mathbf{i}}\langle\varphi_{\mathbf{j}}|\delta|\varphi_{\mathbf{i}}\rangle = 0 \qquad (C.2)$$

We want to determine $E_{rel} = E_{rel}(g)$, in order to derive a relation between the true and renormalized interaction strength, g and g_R, respectively. For two, weakly interacting particle in an isotropic trap, an analytic expression can be obtained [201], $E_{rel}(g) = 1.5 + (2\pi)^{-3/2}g$. Approximating $|\varphi_i\rangle$ by harmonic oscillator functions with spherical symmetry, equation (C.2) can be written as an eigenvalue equation $\underline{\underline{E}}^{-1}\underline{\underline{W}}\mathbf{c} = 1/g_R\,\mathbf{c}$, with the two matrices

$$\underline{\underline{W}} = \begin{pmatrix} W_{0,0} & W_{0,1} & ... \\ W_{1,0} & W_{1,1} & ... \\ ... & ... & ... \end{pmatrix} \qquad \underline{\underline{E}}^{-1} = \begin{pmatrix} \frac{1}{(2\pi)^{3/2}g} & 0 & ... \\ 0 & \frac{1}{(2\pi)^{3/2}g-2} & ... \\ ... & ... & ... \end{pmatrix}$$

where

$$W_{m,n} = \left(\frac{1}{\pi}\right)^{\frac{3}{2}} \sqrt{\binom{n+0.5}{n}} \sqrt{\binom{m+0.5}{m}}$$

The matrix $\underline{\underline{W}}$ is symmetric i.e. can be diagonalized, and the eigenvalue problem can be solved. There is only one eigenvalue, since the rank of $\underline{\underline{W}}$ is one, thus the given renormalization is unique and can be inverted. For example, for only one supplied basis function $M = 1$, one recovers the mean-field solution again,

$$g = g_R.$$

For $M = 2$, we obtain

$$g_R = \pi \left(-\sqrt{\frac{25}{16\pi^2}g^2 + \sqrt{\frac{2}{\pi}}g + 8\pi} + \frac{5}{4\pi}g + \sqrt{8\pi} \right)$$

We skip to write down the expressions for higher M, since they are very lengthy and not further used in this thesis.

In general, for arbitrary trap geometries, E_{rel} and $W_{m,n}$ have to be determined numerically and g_R can be obtained using equation (3.4), where the sum on the right hand side is truncated in dependence of M.

C.3.2. Renormalization theory No. 2

In the ML-MCTDHB method, the three-dimensional single-particle Hilbert space $\mathcal{H}$ is separated into one-dimensional single-particle Hilbert spaces $\mathcal{H}_s$, where s stands for the three dimensions, respectively. Both the $\mathcal{H}$ and the $\mathcal{H}_s$ are truncated by the ML-MCTDHB method. In $\mathcal{H}$, the three-dimensional single-particle functions $\{\chi_i\}_{i=1}^{M}$ form a basis and the $\mathcal{H}_s$ are each spanned by $\{\phi_i^{(s)}\}_{i=1}^{m_s}$. All these truncation are summarized in $\mathcal{C} = (M; m_1, m_2, m_3)$, called numerical configuration. A proper renormalization theory must take all these multiple truncations into account.

Following the lines of [208], our main renormalization formula is obtained in the limit for small energies $E \to 0$, which is discussed in the following

$$g = \lim_{E \to 0} \frac{g_R}{1 + g_R \Omega(E)} \tag{C.3}$$

where the zero-energy limit is already performed on the left hand side and $\Omega(E \to 0) = \lim_{E \to 0} \langle \mathbf{r} = 0 | G_0(E) | \mathbf{r} = 0 \rangle$ is the non-interacting Green's function at $\mathbf{r} = 0$. This result is obtained by comparing the T-matrices, on the one hand, in free space for the truncated and, on the other hand, for the full Hilbert space, respectively[1]. In three dimensions, Ω is infinite and one obtains for the 'true' interaction strength $g = 0$. Only through the truncation of the three-dimensional single-particle basis, Ω gets finite and leads to a useful renormalization formula. We note that the definition of Ω is given in relative coordinates. In order to calculate Ω within the truncated basis of the ML-MCTDHB method (given in laboratory frame), first, Ω has to be transformed into the laboratory frame[2] and second projected onto the numerical single-particle functions $\{\chi_i\}_{i=1}^{M}$ as well as $\{\phi_i^{(s)}\}_{i=1}^{m_s}$, given by the ML-MCTDHB algorithm. In doing so, the multiple truncations of single basis functions of the ML-MCTDHB algorithm are taken into account. By solving the transformation from the relative frame into the laboratory frame, six dimensional integrals over all grid points have to be solved, which are numerically

---

[1] For a consideration of the T-matrix and Green's function in a harmonic oscillator potential see [346–348].

[2] Assuming a Gaussian ground state for the centre of mass.

very costly, and this procedure is in complete contrast with the basic idea of ML-MCTDHB, which avoids these higher-dimensional integrations over the grid points. Furthermore, many conceptual problems occur, which are discussed in the main text (see section 3.1.3). Here, we apply the renormalization procedure[3] to two bosons in an isotropic harmonic trap and compare the ground state with the analytically known solutions [201].

First, we want to study the effect of increasing the number of the three-dimensional single-particle functions $M \in \{1...8\}$ as well as the number of one-dimensional single-particle functions $m = m_1 = m_2 = m_3 \in \{2,3\}$. The interaction strength g_R is set to one and the number of grid points are $n = n_1 = n_2 = n_3 = 200$. In figure C.1a, the ground-state energy is plotted in dependence of M w.r.t. different numerical configurations. We see that increasing both the number of three-dimensional and one-dimensional single particle functions, the ground-state energy tends to the non-interacting limit $E = 3$.

The influence of the renormalization procedure is given in figure C.1b and C.1c, where the ground state energy and width of the radial density profile are compared with the analytical solution [201], respectively. The renormalized energy fits very well to the analytical solution, whereas we find deviations in the width for the density profile. We conclude that the wave function profile is not renormalized correctly. Furthermore, by renormalizing the energy of the first excited states (not shown), we see a discrepancy between the analytic and the renormalized first excited energy, as expected, since the renormalization formula (C.3) gives us only a state-independent shift in the interaction strength.

Concluding, this renormalization can only be used with a high numerical effort, which makes the renormalization theory infeasible. Furthermore, within this renormalization method, conceptual problems occur (discussed in the section 3.1.3).

C.4. Improvement of the POT-FIT algorithm

POT-FIT is an algorithm [232, 233] that represents a multi-dimensional potential W_G with N degrees of freedom $\mathbf{s} = (s_1, \ ... \ s_N)^T$ as a combination of P_i one-dimensional potentials $w_i(s_j)$:

$$W_G(\mathbf{s}) \simeq W_{P_1 \ ... \ P_N}(\mathbf{s}) = \sum_{p_1=1}^{P_1} ... \sum_{p_N=1}^{P_N} c_{p_1 \ ... \ p_N} w_{p_1}(s_1) \ ... \ w_{p_N}(s_N). \tag{C.4}$$

If $N = 2$ and P_i equals the number of grid points, the POT-FIT algorithm reduces to the Schmidt decomposition [122] and becomes exact. In order to simplify the notation, we consider only two degrees of freedom $N = 2$, with $P_1 = P_2 = P$.

Usually, for short-range potentials W_G, many expansions coefficients c are needed in order to approximate W_G properly, since significant oscillations appear in the pot-fitted potential W_P (see figure C.2). Apart from these artificial oscillations, which are slowly damped for short-range interaction potentials, additional artificial bound states can occur. In order to improve the approximation, the different POT-FIT potentials W_P for various P can be averaged, leading to a suppression of the artificial oscillations and a reduction of the depth and number of artificial

---

[3] In order to avoid the mentioned six dimensional integration in every iteration step, we assume that the three-dimensional single-particle functions $\{\chi_i\}_{i=1}^M$ change only little during relaxation, and perform the renormalization procedure only for the final obtained state.
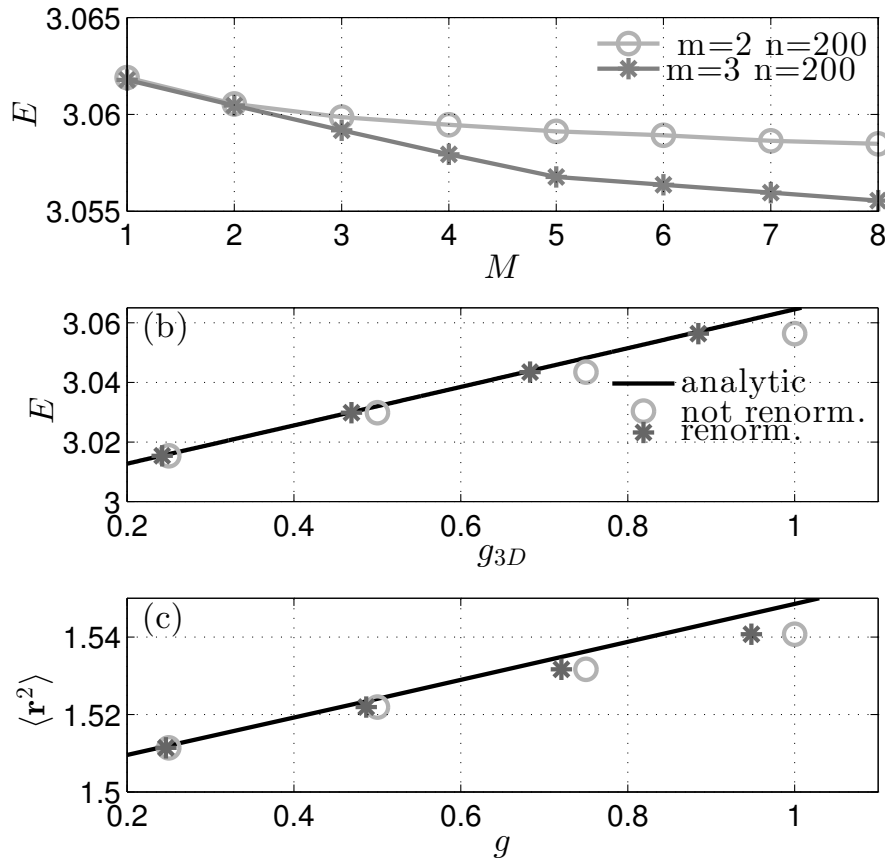
Figure C.1.: (a) Ground state energy in dependence of M for different configurations and $g_R = 1$. (b) Ground state energy in dependence of different 'true' interaction strengths g for the numerical configurations $\mathcal{C} = (6; 3, 3, 3)$. Dark grey stars are the results obtained with renormalization and the light grey circles have been obtained without renormalization. The black solid line is the analytic result given by reference [201]. (c) Radial width of the ground state density profile $\langle \mathbf{r}^2 \rangle$ in dependence of true interaction strength g. Same numerical configuration as in (b).

bound states (see figure C.2). In doing so, we can write:

$$W_G(s_1, s_2) \simeq \frac{1}{N} \sum_{P=1}^{N} W_P(s_1, s_2) = \frac{1}{N} \sum_{P=1}^{N} \sum_{p_1,p_2=1}^{P} c_{p_1 p_2} w_{p_1}(s_1) w_{p_2}(s_2)$$

$$= \frac{1}{N} \left([c_{11} w_1 w_1] + [c_{11} w_1 w_1 + c_{12} w_1 w_2 + c_{21} w_2 w_1 + c_{22} w_2 w_2] + ... \right)$$

where we have dropped the argument of the potential w_p in the second line. The single expansion terms can be rearranged leading to a modification of the expansion coefficients $c_{p_1 p_2}$

$$= \frac{1}{N} \left(N c_{11} w_1 w_1 + (N-1) [c_{12} w_1 w_2 + c_{21} w_2 w_1 + c_{22} w_2 w_2] + (N-2) [c_{13} w_1 w_3 + ...] + ... \right)$$

$$= \sum_{p_1,p_2=1}^{N} c_{p_1 p_2}^{new} w_{p_1} w_{p_2}$$

with

$$c_{p_1 p_2}^{new} = c_{p_1 p_2} \frac{N + 1 - \max(p_1, p_2)}{N}. \tag{C.5}$$

Concluding, the improved POT-FIT algorithm modifies the expansion coefficients, which is of no additional numerical cost and can be implemented very easily. In figure C.2, we plot the improved POT-FIT potential W_{av} (black dashed line). Its oscillations are faster damped and most of the artificial bound states disappear, however, its core width is broader. The approximation can be even further improved (a reduction of the width of the core) if the lowest POT-FIT terms are neglected, which are mainly responsible for the broadening of the core.

$$W_G(s_1, s_2) \simeq \frac{1}{N_2 - N_1} \sum_{p=N_1}^{N_2} W_p(s_1, s_2)$$

After a re-summation, similar as above, the new POT-FIT coefficients are given by

$$W_G(s_1, s_2) \simeq \sum_{p_1,p_2=1}^{N_2} \frac{N_2 + 1 - \max(N_1, p_1, p_2)}{(N_2 - N_1)} c_{p_1 p_2} w_{p_1}(s_1) w_{p_2}(s_2) \tag{C.6}$$
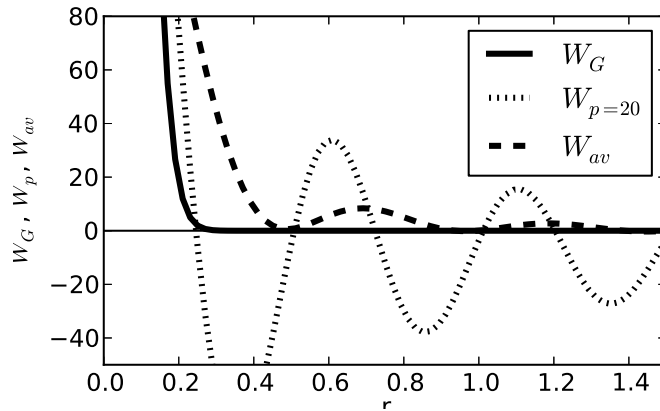

Figure C.2.: The short range potential W_G (black solid line) is compared with its POT-FIT representation $W_{P=20}$ (black dotted lines) for twenty expansion terms and the improved POT-FIT representation W_{av} with $N = 20$ (black dashed line).

C.5. Interaction Matrix Evaluation by Successive Transforms

In this section, we present the Interaction Matrix Evaluation by Successive Transforms (IMEST) algorithm [234], which is an efficient algorithm in order to calculate interaction matrix elements such as $W_{ijlm} = \langle \phi_i \phi_j | \hat{W} | \phi_l \phi_m \rangle$, where ϕ_i can be either three- or one-dimensional functions. In this thesis, ϕ_i is one-dimensional, and therefore, we focus only on the one-dimensional case. The interaction matrix elements are then

$$W_{ijlm} = \int dx \int dx' \ (\phi_i(x))^* \left(\phi_j(x')\right)^* \phi_l(x).\phi_m(x')W(x-x') \tag{C.7}$$

Using the property that the interaction potential $W(x-x')$ depends only on the distance between two particles $\xi = x - x'$, we can reduce the computational effort from q^2 to $\propto q\log(q)$ by using a Fast Fourier Transform (FFT), which obeys a logarithmic scaling w.r.t. the number of grid points q. The forward and backward Fourier Transform of the interaction potential are defined as

$$W(\xi) = W(x - x') = \frac{1}{\sqrt{2\pi}} \int dk \ e^{-ik(x-x')}w(k) \tag{C.8}$$

$$w(k) = \frac{1}{\sqrt{2\pi}} \int d\xi \ e^{ik\xi}W(\xi) \tag{C.9}$$

Inserting (C.8) into (C.7) leads to

$$W_{ijlm} = \frac{1}{\sqrt{2\pi}} \int dx \ (\phi_i(x))^* \phi_l(x) \left[\int dk \ w(k) \left(\int dx' \ \left(\phi_j(x')\right)^* \phi_m(x')e^{-ikx'} \right) e^{ikx} \right]$$

The calculation of this integral can be divided into three steps. The first step is a FFT w.r.t. the x' coordinate, $g_{jm}(k) = \frac{1}{\sqrt{2\pi}} \int dx' \left(\phi_j(x')\right)^* \phi_m(x')e^{-ikx'}$, followed by an inverse FFT, $G_{jm}(x) = \frac{1}{\sqrt{2\pi}} \int dk \ w(k)g_{jm}(k)e^{ikx}$. In the last and third step, one has to perform a one-dimensional integration over the x coordinate, $W_{ijlm} = \sqrt{2\pi} \int dx \ (\phi_i(x))^* \phi_l(x)G_{jm}(x)$. In total, the computational effort is $\propto 2\cdot q\log q + q$ for every time step, instead of the 'brute force' scaling $\propto q^2$.

THE METHOD: ML-MCTDHB

D.1. Reduction of (ML-)MCTDHB algorithm to the Gross-Pitaevskii equation

In this section, we show how the ML-MCTDHB equations of motion can be reduced to the Gross-Pitaevskii equation (GPE) [75, 76]. Therefore, we assume that the simulation is fully converged w.r.t. the numbers of 1D-SPFs (m_1, m_2, m_3) on the sub-particle layer [see equations (4.16) and (4.17)]. Alternatively, we can start directly from equation (4.9), namely, the equations of motion for MCTDHB. On the particle layer, we take only one orbital into account, $M = 1$, corresponding to a mean-field simulation. Same to the derivation of the GPE, the (ML-)MCTDHB method variationally determines the single-particle orbitals. We pick some arbitrary particle (say the first one) and multiply equation (4.16) with $|\phi_{\mathbf{I}}\rangle$, which lead us to

$$i\partial_t |\chi\rangle = \left[(1 - |\chi\rangle \langle \chi|) \left(H_0 + \left[\rho^{(\chi)} \right]^{-1} \langle W \rangle^{(\chi)} |\chi\rangle \right) \right].$$

where H_0 is the single-particle Hamiltonian. By neglecting particle correlations, we have shown (see chapter 3) that the interaction potential can be modelled by the bare delta potential, which is then $W(\mathbf{r}_1, \mathbf{r}_2) = g \sum_{i=2}^{N} \delta(\mathbf{r}_1 - \mathbf{r}_i)$, and the mean field operator becomes $\langle W \rangle^{(\chi)} = g(N-1) |\chi|^2$. In the mean-field picture, the one body-density matrix $\rho^{(\chi)}$ is unity and the equation of motion simplifies to:

$$i\partial_t |\chi\rangle = \left(H_0 + g(N-1) |\chi|^2 \right) |\chi\rangle - c(t) |\chi\rangle, \tag{D.1}$$

with a time dependent term $c(t) = \langle \chi | \left(H_0 + g(N-1) |\chi|^2 |\chi\rangle \right)$, which cancels if one applies an unitary transformation $|\chi\rangle = e^{i \int_0^t c(\tau) \, d\tau} |\tilde{\chi}\rangle$. Finally, one obtains the well-known GPE

$$i\partial_t |\tilde{\chi}\rangle = \left(H_0 + g(N-1) |\tilde{\chi}|^2 \right) |\tilde{\chi}\rangle. \tag{D.2}$$

D.2. Writing the bare delta interaction in product form

In this section, we present a trick how the bare delta interaction potential $\delta(\mathbf{r}) \equiv \delta(\mathbf{r}_2 - \mathbf{r}_1)$ can be transformed into a product w.r.t. its single degrees of freedom, namely, by using the identity

$$\delta(\mathbf{r}_2 - \mathbf{r}_1) = \int d^3\xi \, \delta(\mathbf{r}_2 - \xi)\delta(\mathbf{r}_1 - \xi).$$

For numerical purposes, the integral can be converted into a summation over all grid points, with the weights w_i (the same weights are used for the DVR grid) given by the Gaussian quadrature formula $\int f(\xi)\, d\xi = \sum_{i=1}^{N} w_i f(\xi_i)$. In total, $q_1 q_2 q_3$ terms are created, where q_s is the number of grid points for dimension s. Then, the delta interaction potential is given by weighted kronecker delta function $\delta(a - b) \to \frac{1}{w}\delta_{a,b}$. Finally, one gets the delta-interaction as a sum over simple products

$$\delta(\mathbf{a} - \mathbf{b}) = \otimes_{s=1}^{3} \sum_{q_s=1} D_{q_s}^{(s)},$$

with $D_q^{(s)} = \frac{1}{w_q}\delta_{a_s,\xi_q}\delta_{b_s,\xi_q}$.

D.3. Connection between the many-body wave function and the one-body density operator

In general, a two-component wave function, e.g., two particles or two species, can be decomposed into single-component, orthogonal orbitals

$$|\Psi\rangle = \sum_{n} \sqrt{a_n}|\alpha_n^{(1)}\rangle|\alpha_n^{(2)}\rangle \tag{D.3}$$

using the Schmidt decomposition [122]. In the following, we think of two particle orbitals for these components. In this short section, we proof that $|\alpha_n\rangle$ and a_n are the natural orbitals and natural populations, respectively. The natural populations a_n (natural orbitals $|\alpha_n\rangle$) are defined as the eigenvalues (eigenfunctions) of the one-body density matrix $\rho^{(1)} = tr_2|\Psi\rangle\langle\Psi|$, where tr_2 denotes the sum over the second particle and $|\Psi\rangle$ is the complete two-body wave function,

$$\rho^{(1)} = \sum_{m} \langle\alpha_m^{(2)}|\Psi\rangle\langle\Psi|\alpha_m^{(2)}\rangle. \tag{D.4}$$

Inserting equation (D.3) into equation (D.4), leads to

$$\rho^{(1)} = \sum_{n} a_n|\alpha_n^{(1)}\rangle\langle\alpha_n^{(1)}|, \tag{D.5}$$

where we used the orthogonality of the single particle orbitals. Multiplying the upper equation with $|\alpha_m^{(1)}\rangle$ leads to the eigenvalue equation (D.6).

$$\rho^{(1)}|\alpha_m\rangle = a_m|\alpha_m\rangle. \tag{D.6}$$

with the spectral decomposition (D.3). By projecting equation (D.3) onto the second particle leads to the eigenvalue equation, which determines the natural populations and natural orbitals as well

$$\langle\alpha_m^{(2)}|\Psi\rangle = \sqrt{a_m}|\alpha_m^{(1)}\rangle. \tag{D.7}$$

D.4. Derivation of the equations of motions of the ML-MCTDHB algorithm

In this section, we sketch the derivation of the equations of motion for the ML-MCTDHB implementation in three dimensions. The expansion of the many-body wave function into number states, the expansion of the three-dimensional SPFs into one-dimensional SPFs, and the expansion of the one-dimensional SPFs into a DVR grid have been already given in equations

(4.4), (4.14), and (4.15), respectively. The equations of motion can be derived much easier by introducing the so-called hole-functions for each layer, which are labelled by an upper bar:

$$|\Psi\rangle = \sum_j^M \overline{|\chi_j\rangle_\Psi}|\chi_j\rangle_\eta \qquad\qquad \overline{|\chi_j\rangle_\Psi} := \sum_{\vec{n}}^{N-1} A_{\vec{n}+\vec{j}}\sqrt{\frac{n_j+1}{N}}|\vec{n}\rangle$$

$$|\chi_i\rangle = \sum_q^m |\phi_q^{(s)}\rangle\overline{|\phi_q^{(s)}\rangle_{\chi_i}} \qquad\qquad \overline{|\phi_q^{(s)}\rangle_{\chi_i}} := \sum_{R_s} B_{i,R(r_\sigma\to q_s)}|\phi_{R_s}^{(\sigma)}\rangle$$

$$|\Psi\rangle = \sum_q^m \overline{|\phi_q^{(s)}\rangle_\Psi}|\phi_{q_s}^{(s)}\rangle \qquad\qquad \overline{|\phi_q^{(s)}\rangle_\Psi} := \sum_j^M \overline{|\chi_j\rangle_\Psi}\,\overline{|\phi_q^{(s)}\rangle_{\chi_j}},$$

where we used the terminology from the main text. The sum $\sum_{R_s}$ stands for the summation over the two dimensions σ excluding the s dimension (see table D.1) and $R(r_\sigma \to q_s)$ replaces in the multi-index R the r_σ index with the q_s index. With the help of the hole functions the time-derivative and the variation of the many-particle wave-function can be expressed in a simple way:

$$\partial_t|\Psi\rangle = \sum_{\vec{m}} \partial_t A_{\vec{m}}|\vec{m}\rangle + \sum_{iI} \overline{|\chi_i\rangle_\Psi}|\phi_I\rangle\partial_t B_{i,I} + \sum_{suv} \overline{|\phi_u^{(s)}\rangle_\Psi}|S_v\rangle\partial_t C_{uv}$$

$$\delta|\Psi\rangle = \sum_{\vec{m}} \delta A_{\vec{m}}|\vec{m}\rangle + \sum_{iI} \overline{|\chi_i\rangle_\Psi}|\phi_I\rangle\delta B_{i,I} + \sum_{suv} \overline{|\phi_u^{(s)}\rangle_\Psi}|S_v\rangle\delta C_{uv}$$

where $|S\rangle$ stands for the time-independent primitive grid for the dimensions $S = \{x,y,z\}$. Inserting the time-derivative and the variation of the many-particle wave-function into the Dirac-Frenkel variational principle

$$\langle\delta\Psi|\,i\partial_t - \mathcal{H}\,|\Psi\rangle = 0$$

and by performing the variation w.r.t. $\partial A_{\vec{m}}$, $\partial B_{i,I}$ and ∂C_{uv}, we obtain the equations of motion for the top-, particle-, and sub-particle layer for an arbitrary, many-particle Hamiltonian $\mathcal{H}$. Due to the rotational invariance of the basis spanned by the SPFs, we can set the constraint $\langle\phi_q|\partial_t\phi_q\rangle = 0$ in order to fix the basis and to simplify the equations of motion. From this constraint, it follows: $\langle\chi_i|\partial_t\chi_i\rangle = 0$ and $\langle\vec{n}|\partial_t\vec{m}\rangle = 0$. Finally, we get:

$$i\partial_t A_{\vec{n}} = \sum_{\vec{m}} \langle\vec{n}|H|\vec{m}\rangle A_{\vec{m}}$$

$$i\partial_t B_{i,I} = \sum_{jkJ} \langle\phi_I|\left[\rho^{(\chi)}\right]_{ik}^{-1}\left(1 - P^{(\chi)}\right)\overline{\langle\chi_k|_\Psi}\,H\,\overline{|\chi_j\rangle_\Psi}\,|\phi_J\rangle\, B_{j,J}$$

$$\partial_t C_{wl} = \sum_{vuk} \langle S_l|\left[\rho^{(\phi)}\right]_{wk}^{-1}(1 - P^{(\phi)})\overline{\langle\phi_k^{(s)}|_\Psi}\,H\,\overline{|\phi_u^{(\sigma)}\rangle_\Psi}\,|\Sigma_u\rangle C_{uv},$$

with the one-body density matrices

$$\left[\rho^{(\chi)}\right]_{ik}^{-1} = \overline{\langle\chi_k|_\Psi|\chi_i\rangle_\Psi}, \qquad\qquad \left[\rho^{(\phi)}\right]_{uw}^{-1} = \overline{\langle\phi_u^{(s)}|_\Psi|\phi_w^{(\sigma)}\rangle_\Psi},$$

and the projectors

$$P^{(\chi)} = \sum_i \chi_i\rangle\langle\chi_i|, \qquad\qquad P^{(\phi)} = \sum_I |\phi_I\rangle\langle\phi_I|.$$

Using the Hamiltonian $\mathcal{H}$ [defined via equation (4.1)] with the two-body interaction (see section

if s	then σ	if S	then Σ
1	$\{2,3\}$	x	$\{y,z\}$
2	$\{3,1\}$	y	$\{z,x\}$
3	$\{1,2\}$	z	$\{x,y\}$

4.2), the mean-field operator matrices $\overline{\langle\chi_k|_\Psi}\, H\, \overline{|\chi_j\rangle_\Psi}$ and $\overline{\langle\phi_k^{(s)}|_\Psi}\, H\, \overline{|\phi_u^{(\sigma)}\rangle_\Psi}$ can be determined, leading to equation (4.21) and (4.20) respectively. Finally, we obtain the equations of motion for the top layer [see equation (4.8)], particle layer [see equation (4.16)] and subparticle layer [see equation (4.17)]. By the introduction of two-particle hole functions

$$|\Psi\rangle = \sum_{ij} |\chi_i\rangle|\chi_j\rangle\overline{|\chi_i^{(1)}\chi_j^{(2)}\rangle}_\Psi,$$

$$\overline{|\chi_k^{(1)}\rangle}_\Psi = \sum_{l} |\chi_l^{(2)}\rangle\overline{|\chi_k^{(1)}\chi_l^{(2)}\rangle}_\Psi,$$

$$\overline{|\chi_i^{(1)}\chi_j^{(2)}\rangle}_\Psi = \sum_{\vec{n}}^{N-2} A_{\vec{n}+\vec{i}+\vec{j}}\sqrt{\frac{n_i+1}{N}}\sqrt{\frac{n_j+1+\delta_{ij}}{N-1}}|\vec{n}\rangle,$$

the two-body density matrices can be easily expressed, where the upper index of the 3D-SPF labels the particle index

$$\left[\rho_2^{(\chi)}\right]_{ijkl} = \overline{{}_\Psi\left\langle\chi_i^{(1)}\chi_j^{(2)}\middle|\middle|\chi_k^{(1)}\chi_l^{(2)}\right\rangle_\Psi}.$$

TWO PARTICLES IN AN ELONGATED TRAP

E.1. Derivation of the analytic solution of the breathing mode

We derive the analytic solution of one particle in one dimension, initially in the ground state, which is instantaneously quenched by changing the trap frequency from Ω to ω. We set the mass $m = 1$ and $\hbar = 1$. The initial and final Hamiltonians read in position representation

$$H_\omega = -\frac{1}{2}\frac{d^2}{dx^2} + \frac{1}{2}\omega^2 x^2$$

$$H_\Omega = -\frac{1}{2}\frac{d^2}{dx^2} + \frac{1}{2}\Omega^2 x^2.$$

The initial wave function $\langle x|N=0\rangle$ is the zero order of the harmonic oscillator functions

$$\langle x|N\rangle = \left(\frac{\Omega}{\pi}\right)^{\frac{1}{4}}\frac{1}{\sqrt{2^N N!}}H_N\left(\sqrt{\Omega}x\right)e^{-\frac{\Omega x^2}{2}},$$

where H_N are the Hermite polynomials of order N. We calculate the time-evolution of this initial state, $|\Psi\rangle = e^{-iH_\omega t}|N=0\rangle$, by inserting a complete set of orthogonal functions

$$\langle x|n\rangle = \left(\frac{\omega}{\pi}\right)^{\frac{1}{4}}\frac{1}{\sqrt{2^n n!}}H_n\left(\sqrt{\omega}x\right)e^{-\frac{\omega x^2}{2}}$$

yielding to

$$|\Psi(t)\rangle = \sum_{m=2n=0}^{\infty} c_{2n}e^{-iE_{2n}t}|2n\rangle + \sum_{m=2n+1=0}^{\infty} c_{2n+1}e^{-iE_{2n+1}t}|2n+1\rangle, \tag{E.1}$$

where we have separated the even and odd states and with the coefficients c_m

$$c_m = \langle m|N=0\rangle = \frac{1}{\sqrt{2^m m!}}\left(\frac{\Omega\omega}{\pi^2}\right)^{\frac{1}{4}}\int dx\ H_m\left(\sqrt{\omega}x\right)e^{-\frac{(\Omega+\omega)x^2}{2}}.$$

Substituting $\sqrt{\frac{\Omega+\omega}{2}}x = \frac{x}{\alpha} = \xi$ and using the solution of the integral $\int_{-\infty}^{\infty} dy\ e^{-y^2}H_{2m}(ay)$ with $a = \sqrt{\frac{\Omega+\omega}{\omega}}$ (see reference [349]), lead us to

$$c_{2m} = \frac{(\Omega\omega)^{\frac{1}{4}}}{\sqrt{2^{2m}(2m)!}}\frac{(2m)!}{m!}\alpha(a^2-1)^m$$

$$c_{2m+1} = 0.$$

Inserting the expansion coefficients c_m into the wave function of equation (E.1) and using the formula for generation function for even Hermite polynomials [350][1], we get

$$\langle x|\Psi(t)\rangle = \left(\frac{4}{\pi}\frac{\Omega\omega^2}{(\Omega+\omega)^2}\right)^{\frac{1}{4}} e^{-i\frac{\omega}{2}t}\frac{1}{\sqrt{1+Ae^{-i2\omega t}}}e^{-\frac{\omega x^2}{2}\left(\frac{1-Ae^{-i2\omega t}}{1+Ae^{-i2\omega t}}\right)} \tag{E.2}$$

and for the density

$$\Psi^\star\Psi = \left(\frac{4}{\pi}\frac{\Omega\omega^2}{(\Omega+\omega)^2}\right)^{\frac{1}{2}}\frac{1}{\sqrt{B}}e^{-\frac{4\omega^2\Omega}{B(\omega+\Omega)^2}x^2}, \tag{E.3}$$

with $A = (\omega-\Omega)/(\omega+\Omega)$ and $B = \left(1+Ae^{-i2\omega t}\right)\left(1+Ae^{+i2\omega t}\right) = 1+A^2+2A\cos(2\omega t)$. The wave function is normalized to one as can be shown by a straight forward calculation. Furthermore, the variance can be calculated

$$\langle x^2\rangle = \frac{(\omega+\Omega)^2}{4\omega^2\Omega}B(t) = \frac{1}{2\omega^2\Omega}\left[\left(\omega^2+\Omega^2\right)+\left(\omega^2-\Omega^2\right)\cos(2\omega t)\right]. \tag{E.4}$$

---

[1] $\sum_{n=0}^{\infty}\frac{t^n}{n!}H_{2n}(\omega x) = \frac{1}{\sqrt{1+4t}}e^{\left(\frac{4t}{1+4t}\omega x^2\right)}$

APPLICATION: DOUBLE WELL TRAP

F.1. Convergence studies

In this section, we check the convergence of the simulations performed in chapter 6. The analysis of convergence is mainly taken from [[1]]. In doing so, we vary the number of 3D-SPFs M and 1D-SPFs (m_1, m_2, m_3) for fixed physical parameters, and compare the ML-MCTDHB results for an observables of interest. A simulation is converged if the observables of interest do not change upon increasing the number of SPFs further. One has to check carefully the convergence in the ML-MCTDHB algorithm, because an interdependence between M and m_s can occur.

For the considered cylindrically symmetrical trap, we may choose the number of transversal 1D-SPFs to be equal: $m_1 = m_2$. For nearly isotropic traps, i.e. $\eta \sim 1$, one can use $m_1 = m_2 = m_3$. If the transversal trap is tightened, less transversal 1D-SPF are needed, and all particle correlations, if existent, are handed over to the population of longitudinal 1D-SPFs, thus a good choice is to set $M = m_3 \geq m_1 = m_2$. In the following, each simulation is characterized by the numerical configuration $\mathcal{C} = (M; m_1, m_2, m_3)$.

A first indicator for convergence can be obtained by a spectral analysis of certain reduced density operators, i.e. the eigenvalues (natural populations) $a_i^{(3D)}$ and $b_i^{(s)}$ of the reduced density operator of a single boson $\rho^{(3D)}$ and of the s-th degree-of-freedom of a single boson $\rho^{(s)}$ as well as their eigenvectors (natural orbitals). The smallest natural population $a_i^{(3D)}$ and $b_i^{(s)}$ may serve as a practical measure for how many 3D-SPF and 1D-SPF are needed, respectively, and the natural-population distribution is sensitive to the presence of particle and spatial correlations, respectively. Such conclusions from the natural orbitals are rigorous for already converged simulations and otherwise only indicative (see reference [231] for a critical discussion). Within our normalization, we have $0 \leq a_i^{(3D)}, b_i^{(s)} \leq 1$ and $\sum_i a_i^{(3D)} = \sum_i b_i^{(s)} = 1$. Moreover, we label the natural populations in decreasing sequence.

In figure F.1, we show the natural populations $b_i^{(s)}$ and $a_i^{(3D)}$ for two aspect ratios $\eta = 2$ and $\eta = 8$ and different numerical configurations $\mathcal{C}$. Adding an additional 3D-SPF, the two most dominant natural populations $a_{1,2}^{(3D)}$ change by only $\sim 10^{-4}$, i.e. not significantly (see figure F.1a). A tighter trap depletes $a_1^{(3D)}$ in favour of $a_2^{(3D)}$, indicating already emerging particle correlations. Adding further 1D-SPFs, the two most dominant natural populations of $\rho^{(s)}$, $b_{1,2}^{(s)}$, are not significantly changed and corrections take place of the order of 10^{-4}. As expected, the second dominant natural population $b_2^{(1,2)}$ of the transversal directions is stronger populated for a more isotropic trap, $\eta = 2$, than for $\eta = 8$, which implies stronger spatial correlations (see
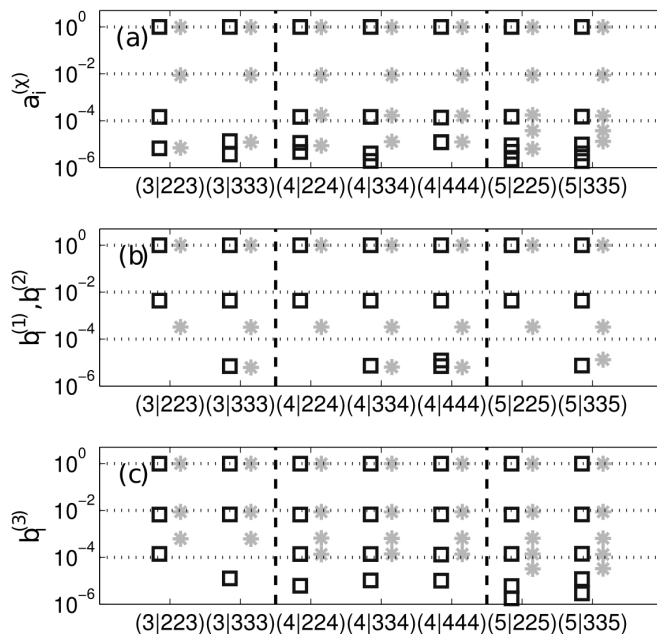
Figure F.1.: Panel (a) shows the natural populations $a_i^{(3D)}$ of $\rho^{(3D)}$, and (b) and (c) presents the natural populations $b_i^{(s)}$ of $\rho^{(s)}$, respectively, for two different aspect ratios $\eta = 2$ (squares) and $\eta = 8$ (stars). The superscript s denotes the dimension. The horizontal axis provides different numerical configurations $\mathcal{C}$, where $M = m_3$ is increased for various $m_1 = m_2$ kept fixed. The black dashed vertical line separates different configurations, where $M = m_3$ is increased by one. Figure is taken from reference [[1]].

figure F.1 b). Finally, figure F.1c shows that the spectrum of $\rho^{(3D)}$ is rather robust w.r.t. adding more 3D- and 1D-SPFs.

Next, we compare the initial population imbalance in dependence of the aspect ratio for different configurations (see figure F.2a). We see that the three configurations $\mathcal{C} = (3; 3, 3, 3)$, $\mathcal{C} = (4; 2, 2, 4)$ and $\mathcal{C} = (4; 3, 3, 4)$ agree well, and we refer to the numerical configuration $\mathcal{C} = (4; 3, 3, 4)$ as the fully converged simulation $\mathcal{C}_{FC}$. In order to ensure the convergence of the dynamical simulations, let us inspect the time evolution of the population imbalance $I_z(t)$ for different configurations $\mathcal{C}$ in two different trap geometries with aspect ratios $\eta = 2$ and $\eta = 8$, respectively. In figures F.2b and F.2c, the population imbalance shows excellent agreement between the tested numerical configurations for both $\eta = 2$ and $\eta = 8$, respectively (the various lines lay on top of each other). We chose again the same numerical configuration as above, $\mathcal{C} = (4; 3, 3, 4) \equiv \mathcal{C}_{FC}$.

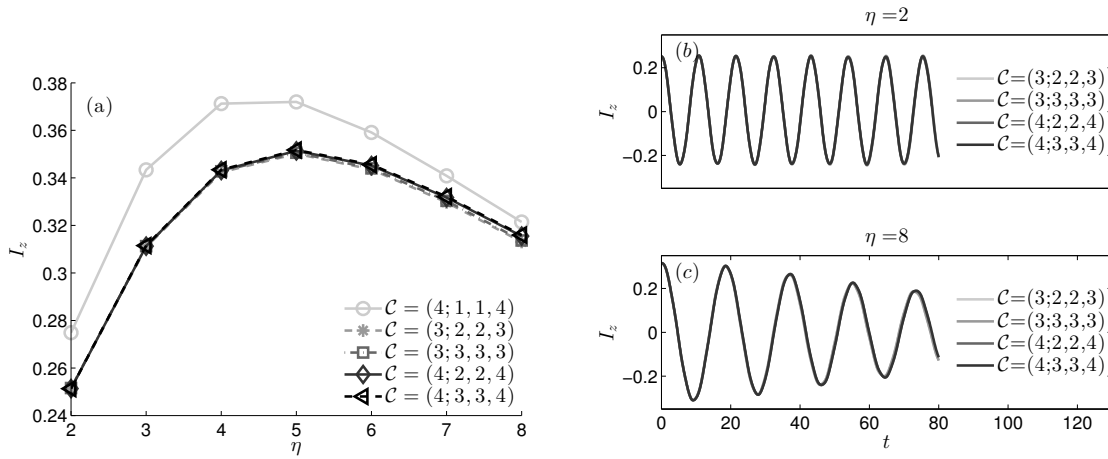**Figure F.2.:** (a) Population imbalances for different numerical configurations $\mathcal{C}$ with respect of the aspect ratio. The lines connecting the points are plotted as a guide to the eye. Temporal evolution of the population imbalance $I_z(t)$ for the two aspect ratios $\eta = 2$ [panel (b)] and for $\eta = 8$ [panel (c)], respectively. The various lines lay on top of each other. Figure is taken from reference [[1]].

APPENDIX

G

APPLICATION: SCATTERING OFF A BARRIER

G.1. Convergence studies

In this section, we discuss the convergence of the simulations performed in chapter 7 (mainly based literally on the paper [[2]]).

The convergence of a (ML-)MCTDHB calculation has to be carefully checked (see e.g. reference [292] and the paper [[3]]), and we consider a numerical simulation converged when an observable of interest does not change to a certain desired accuracy if the numerical control parameters are varied. For the one-dimensional (beyond mean-field) BMF simulations, we have employed five optimized single-particle states.

The numerical results of the simulation in three dimension depend on seven numerical control parameters; the number of 3D-SPFs M, the three numbers of 1D-SPFs $\{m_1, m_2, m_3\}$ as well as the three numbers of grid points $\{q_1, q_2, q_3\}$. In our numerical calculations, we always use a sufficiently large number of grid points, and thus neglect their discussion in the following, reducing the seven dimensional parameter space to a four dimensional one. In the simulations performed, we have used $q_3 = 800$ ($q_1 = q_2 = 200$) grid points for the longitudinal (transversal) direction(s), with an equidistant grid spacing of 0.025. Due to the symmetry of the elongated trap, we set $m_1 = m_2$. We call the set of parameters $\mathcal{C} = (M; m_1, m_2, m_3)$ a numerical configuration $\mathcal{C}$.

For very strongly elongated traps, where the main dynamics takes place in the longitudinal direction ($s = 3$), we can reduce the three-dimensional parameter space further, by setting $m_3 = M > m_1$, for which case the particle correlations, if existent, are handed over to the population of longitudinal 1D-SPFs. However, opposite to this case for nearly isotropic traps, the parameter space can be reduced by choosing $m_1 = m_2 = m_3$.

In the main text, we have mainly focused on two observables: first, the oscillation of the CM $\langle Z \rangle$ and, second, the occupation of the first natural orbital a_1. Their convergence is shown as an example by regarding the integrated difference between two numerical configurations, $\mathcal{E}_1 = \int_0^{T_{max}} |\langle Z \rangle_{\mathcal{C}_1} - \langle Z \rangle_{\mathcal{C}_2}| dt / T_{max}$ and $\mathcal{E}_2 = \int_0^{T_{max}} |a_{1,\mathcal{C}_1} - a_{1,\mathcal{C}_2}| dt / T_{max}$, where the subindex denotes the used numerical configuration $\mathcal{C}$ and T_{max} is the maximal simulation time. We compare the numerical configuration $\mathcal{C}_1 = (5; 3, 3, 5)$ and $\mathcal{C}_2 = (6; 4, 4, 6)$ for the same physical parameters as used in section 7.4 both for $\eta = 2$ and $\eta = 8$, which are the extreme cases for spatial and particle correlations respectively. For $\eta = 2$, we obtain $\mathcal{E}_1 = 5.8 \cdot 10^{-3}$ and $\mathcal{E}_2 = 6.1 \cdot 10^{-4}$ as well as for $\eta = 8$ we get $\mathcal{E}_1 = 3.1 \cdot 10^{-3}$ and $\mathcal{E}_2 = 2.2 \cdot 10^{-3}$. In essence, the integrated error is estimated to be of the order 10^{-3}.

G.2. Co-moving time-dependent basis states

In the first part of this section (based literally on paper [[2]]), we derive a complete set of orthonormal functions $\phi_n(z,t)$, described by displaced harmonic oscillator functions, stiffly oscillating in a harmonic trap, which are used in section 7.3. In the second part of this section, we show that even the displaced stationary ground state of $\varphi_{GP}(z)$ [see equation (7.8)] performs stiff oscillations in a harmonic trap (see also reference [351]), as utilized in section 7.2.2.

First, the orthonormal functions $\phi_n(z,t)$ are assumed to be of the following functional form with the yet unknown real-valued functions $\Theta_n(t)$, $\bar{p}(t)$ and $\bar{z}(t)$.

$$\phi_n(z,t) = e^{-i\Theta_n(t)+i\bar{p}(t)z}\varphi_n^{1D}(z-\bar{z}(t)) \tag{G.1}$$

where φ_n^{1D} is the n-th harmonic oscillator function $\varphi_n^{1D}(z) = 1/\sqrt{2^n n!}\pi^{-1/4}\exp\left(-z^2/2\right)H_n(z)$ with the Hermite polynomial H_n. The ansatz (G.1) is inserted into the time-dependent, one-dimensional, single-particle Schrödinger equation, $i\partial_t\phi_n = [-(1/2)\partial_z^2 + (1/2)z^2]\phi_n$, and we obtain three coupled differential equations by comparing the real and imaginary part as well as equating coefficients

$$\partial_t \bar{z}(t) = \bar{p}(t) \tag{G.2}$$
$$-\partial_t \bar{p}(t) = \bar{z}(t)$$
$$\partial_t \Theta_n(t) - \bar{z}(t)\partial_t \bar{p}(t) = E_n + \frac{1}{2}\left(\bar{z}^2(t) + \bar{p}^2(t)\right)$$

with $E_n = n + 1/2$. With the initial condition that the wave functions is displaced by b, $\phi_n(z,0) = \varphi_n^{1D}(z-b)$, the coupled set of equations can be solved, leading to

$$\bar{z}(t) = b\cos(t) \tag{G.3}$$
$$\bar{p}(t) = -b\sin(t)$$
$$\Theta_n(t) = E_n t + \frac{1}{2}\bar{z}(t)\bar{p}(t)$$

The functions $\phi_n(z,t)$ form a complete and orthonormal set of basis functions at all instants in time. Orthonormality can be checked easily and the proof of completeness follows the same arguments as for the orthogonal Hermite polynomials (see reference [352]).

Second, the initially displaced mean-field ground-state wave functions φ_{GP} performs also stiff oscillations in a harmonic trap. The ground state mean-field orbital obeys the stationary GPE

$$E_{GP}\varphi_{GP}(z) = \left(-\frac{1}{2}\partial_z^2 + \frac{1}{2}z^2\right)\varphi_{GP}(z) + g(N-1)$$
$$\times \int d\mathcal{Z}|\varphi_{GP}(\mathcal{Z})|^2 W(z,\mathcal{Z})\varphi_{GP}(z).$$

Inserting the same approach for the wave function $\phi_{GP}(z,t) = e^{-i\Theta(t)+i\bar{p}(t)z}\varphi_{GP}(z-\bar{z}(t))$ into the corresponding time-dependent GPE, where $W(z_1,z_2) = W(z_2-z_1)$ is assumed, leads again to the three coupled differential equations (G.2) with their solution (G.3), but now with the energy E_n replaced by E_{GP}.

G.3. Stroboscopic perturbation theory

In this section, we sketch the stroboscopic perturbation theory, which we used in section 7.3. There, a single-particle harmonic oscillator Hamiltonian $H_0 = [-(1/2)\nabla_\mathbf{r}^2 + (1/2)\mathbf{r}^2]$, with

harmonic oscillator eigenfunctions $|n\rangle$ and eigenvalues E_n is periodically perturbed in time $V(t) = V_0 f(t)$ with $V_0 = h\exp(\mathbf{r}^2/S^2)$ and $f(t) = \sum_{k=1}^{\infty} \delta(t - kt_0)$ a periodic function. The equation of motion for the total Hamiltonian $H(t) = H_0 + V(t)$ in the interaction picture is given by

$$i\partial_t |\Psi(t)\rangle_I = V_I(t)|\Psi(t)\rangle_I \tag{G.4}$$

$$|\Psi(t)\rangle_I = |\Psi(t_1)\rangle_I + \frac{1}{i}\int_{t_1}^{t} d\tau \, V_I(\tau)|\Psi(\tau)\rangle_I \tag{G.5}$$

with $|\Psi(t)\rangle_I = e^{iH_0 t}|\Psi(t)\rangle$ and $V_I(t) = e^{iH_0 t}V(t)e^{-iH_0 t} = \sum_{n,m} e^{-it(E_m - E_n)}b_{nm}f(t)|n\rangle\langle m|$. The amplitudes b_{nm} can be calculated by $b_{nm} = \langle n|V_0|m\rangle$. If $n + m$ is odd, then $b_{nm} = 0$ due to symmetry and the lowest non-zero amplitudes are $b_{00} = h/\Omega$, $b_{22} = h(S + 2S^5)/(2\sqrt{S^2 + 1}(1 + 2S^2 + S^4))$, $\sim 1/2\Omega$ for small S, as well as $b_{20} = b_{02} = -hS/\sqrt{2}\sqrt{S^2 + 1}(1 + S^2)$.

The initial wave function evolves in time with H_0 until a perturbative 'kick' happens at the time instant t_1. The change in the wave function from $t_i - \epsilon$ to $t_i + \epsilon$ is calculated by using first-order perturbation theory.

$$|\Psi(t_1 + \epsilon)\rangle_I = \int_{t_1-\epsilon}^{t_1+\epsilon} d\tau \sum_{nm} e^{-i\tau(E_m - E_n)}b_{nm}\delta(\tau - t_1)|n\rangle\langle m|\Psi(t_1 - \epsilon)\rangle_I. \tag{G.6}$$

Using as the initial state a harmonic oscillator ground state $|\Psi(0)\rangle_I = |n = 0\rangle = |0\rangle$, applying the limit $\epsilon \to 0$ and making a two mode approximation, we get:

$$|\Psi(t_1)\rangle_I = b_{00}|0\rangle + e^{-it_0(E_0 - E_2)}b_{20}|2\rangle \tag{G.7}$$

This equation describes a breathing excitation. Evolving this wave function until the second 'kick' happens at time instant $t_2 = t_1 + \Delta t$, we get

$$|\Psi(t_2)\rangle_I = (b_{00}b_{00} + b_{20}bg_{02}e^{-i\Delta E\Delta t})|0\rangle + e^{it_1\Delta E}(b_{20}b_{00} + b_{22}b_{20}e^{-i\Delta E\Delta t})|2\rangle$$

with $\Delta E = E_2 - E_0$.

BIBLIOGRAPHY

[1] E. A. Cornell and C. E. Wieman, Nobel lecture: Bose-Einstein condensation in a dilute gas, the first 70 years and some recent experiments, 2002.

[2] W. Ketterle, *When atoms behave as waves: Bose- Einstein condensation and the atom laser*, Le Prix Nobel **74**, 118 (2002).

[3] K. B. Davis, M.-O. Mewes, M. A. Joffe, M. R. Andrews, and W. Ketterle, *Evaporative cooling of sodium atoms*, Phys. Rev. Lett. **74**, 5202 (1995).

[4] M. H. Anderson, J. R. Ensher, M. R. Matthews, C. E. Wieman, and E. A. Cornell, *Observation of bose-einstein condensation in a dilute atomic vapor.*, Science **269**, 198 (1995).

[5] M. R. Andrews, M.-O. Mewes, N. J. van Druten, D. S. Durfee, D. M. Kurn, and W. Ketterle, *Direct, Nondestructive Observation of a Bose Condensate*, Science **273**, 84 (1996).

[6] M.-O. Mewes, M. R. Andrews, N. J. van Druten, D. M. Kurn, D. S. Durfee, C. G. Townsend, and W. Ketterle, *Comment on "Collective Excitations of a Bose-Einstein Condensate in a Magnetic Trap"*, Phys. Rev. Lett. **77**, 988 (1996).

[7] J. Ensher, D. Jin, M. Matthews, C. Wieman, and E. Cornell, *Bose-Einstein Condensation in a Dilute Gas: Measurement of Energy and Ground-State Occupation*, Phys. Rev. Lett. **77**, 4984 (1996).

[8] C. Eric, *Very Cold Indeed: The Nanokelvin Physics of Bose-Einstein Condensation*, NIST **101**, 410 (1996).

[9] Bose, *Plancks Gesetz und Lichtquantenhypothese*, Zeitschrift für Phys. **26**, 178 (1924).

[10] E. Albert, *Quantentheorie des einatomigen idealen Gases*, Sitzungsberichte der Preuss. Akad. der Wiss. **1**, 3 (1925).

[11] T. Lahaye, C. Menotti, L. Santos, M. Lewenstein, and T. Pfau, *The physics of dipolar bosonic quantum gases*, Reports Prog. Phys. **72**, 126401 (2009).

[12] H. Feshbach, *Unified theory of nuclear reactions*, Ann. Phys. (N. Y). **5**, 357 (1958).

[13] C. Chin, R. Grimm, P. Julienne, and E. Tiesinga, *Feshbach resonances in ultracold gases*, Rev. Mod. Phys. **82**, 1225 (2010).

[14] E. Braaten and H. W. Hammer, *Universality in few-body systems with large scattering length*, Phys. Rep. **428**, 259 (2006).

[15] F. Chevy and C. Salomon, *Strongly correlated Bose gases*, J. Phys. B **49**, 192001 (2016).

[16] D. Blume, *Few-body physics with ultracold atomic and molecular systems in traps*, Rep. Prog. Phys. **75**, 046401 (2012).

[17] G. E. Astrakharchik, D. Blume, S. Giorgini, and B. E. Granger, *Quasi-One-Dimensional Bose Gases with a Large Scattering Length*, Phys. Rev. Lett. **92**, 030402 (2004).

[18] H. Metcalf and P. van der Straten, *Laser Cooling and Trapping*, Springer, Berlin, 1999.

[19] A. Griffin, D. W. Snoke, and S. Stringari, *Bose-Einstein Condensation*, Cambridge University Press, Cambridge, 1996.

[20] L. P. Pitaevskii and S. Stringari, *Bose-Einstein Condensation*, Oxford Science Publications, Oxford, 2003.

[21] C. Pethick and H. Smith, *Bose-Einstein Condensation in Dilute Gases*, Cambridge University Press, Cambridge, 2008.

[22] P. Törmä and K. Sengstock, *Quantum Gas Experiments: Exploring Many-Body States of Cold Atoms*, Imperial College Press, London, 2014.

[23] F. Dalfovo, S. Giorgini, L. P. Pitaevskii, and S. Stringari, *Theory of Bose-Einstein condensation in trapped gases*, Rev. Mod. Phys. **71**, 463 (1999).

[24] A. J. Leggett, *Bose-Einstein condensation in the alkali gases: Some fundamental concepts*, Rev. Mod. Phys. **73**, 307 (2001).

[25] J. O. Andersen, *Theory of the weakly interacting Bose gas*, Rev. Mod. Phys. **76**, 599 (2004).

[26] V. Giovannetti, S. Lloyd, and L. Maccone, *Quantum-enhanced measurements: beating the standard quantum limit.*, Science **306**, 1330 (2004).

[27] V. Giovannetti, S. Lloyd, and L. MacCone, *Quantum metrology*, Phys. Rev. Lett. **96**, 010401 (2006).

[28] V. Giovannetti, S. Lloyd, and L. Maccone, *Advances in quantum metrology*, Nat. Photonics **5**, 222 (2011).

[29] C. Orzel, A. K. Tuchman, M. L. Fenselau, M. Yasuda, and M. A. Kasevich, *Squeezed States in a Bose-Einstein Condensate*, Science **291**, 2386 (2001).

[30] B. Gertjerenken and C. Weiss, *Nonlocal quantum superpositions of bright matter-wave solitons and dimers*, J. Phys. B **45**, 165301 (2012).

[31] G. B. Jo, Y. Shin, S. Will, T. A. Pasquini, M. Saba, W. Ketterle, D. E. Pritchard, M. Vengalattore, and M. Prentiss, Long phase coherence time and number squeezing of two Bose-Einstein condensates on an atom chip, Phys. Rev. Lett., **98**, 030407, (2007).

[32] J. Estève, C. Gross, A. Weller, S. Giovanazzi and M. K. Oberthaler, *Squeezing and entanglement in a Bose-Einstein condensate*, Nature **455**, 1216 (2008).

[33] A. D. Cronin, J. J. Schmiedmayer, and D. E. Pritchard, *Optics and interferometry with atoms and molecules*, Rev. Mod. Phys. **81**, 1051 (2009).

[34] T. D. Ladd, F. Jelezko, R. Laflamme, Y. Nakamura, C. Monroe, and J. L. O'Brien, *Quantum computers.*, Nature **464**, 45 (2010).

[35] M. A. Nielsen and I. L. Chuang, *Quantum Computation and Quantum Information*, Cambridge University Press, Cambridge, 2010.

[36] A. Negretti, P. Treutlein, and T. Calarco, *Quantum computing implementations with neutral particles*, Quantum Inf. Process. **10**, 721 (2011).

[37] I. Bloch, *Ultracold quantum gases in optical lattices*, Nat Phys **1**, 23 (2005).

[38] C.-C. Chien, S. Peotta, and M. Di Ventra, *Quantum transport in ultracold atoms*, arXiv **11**, 24 (2015).

[39] W. Hänsel, P. Hommelhoff, T. W. Hänsch, and J. Reichel, *Bose-Einstein condensation on a microelectronic chip.*, Nature **413**, 498 (2001).

[40] D. J. Wineland, C. Monroe, W. M. Itano, D. Leibfried, B. E. King, and D. M. Meekhof, *Experimental Issues in Coherent Quantum-State Manipulation of Trapped Atomic Ions*, J. Res. Natl. Inst. Stand. Technol. **103**, 1689 (1998).

[41] R. Blatt and D. Wineland, *Entangled states of trapped atomic ions*, Nature **453**, 1008 (2008).

[42] O. Morsch and M. Oberthaler, *Dynamics of Bose-Einstein condensates in optical lattices*, Rev. Mod. Phys. **78**, 179 (2006).

[43] M. Anderlini, P. J. Lee, B. L. Brown, J. Sebby-Strabley, W. D. Phillips, and J. V. Porto, *Controlled exchange interaction between pairs of neutral atoms in an optical lattice*, Nature **448**, 452 (2007).

[44] F. Pastawski, L. Clemente, and J. I. Cirac, *Quantum memories based on engineered dissipation*, Phys. Rev. A **83**, 012304 (2011).

[45] F. Verstraete, M. M. Wolf, and J. I. Cirac, *Quantum computation, quantum state engineering, and quantum phase transitions driven by dissipation*, Nat. Phys. **5**, 633 (2009).

[46] J. Struck, C. Olschlager, R. Le Targat, P. Soltan-Panahi, A. Eckardt, M. Lewenstein, P. Windpassinger, and K. Sengstock, *Quantum Simulation of Frustrated Classical Magnetism in Triangular Optical Lattices*, Science **333**, 996 (2011).

[47] J. Struck, M. Weinberg, C. Ölschläger, P. Windpassinger, J. Simonet, K. Sengstock, R. Höppner, P. Hauke, A. Eckardt, M. Lewenstein, and L. Mathey, *Engineering Ising-XY spin-models in a triangular lattice using tunable artificial gauge fields*, Nat. Phys. **9**, 738 (2013).

[48] I. Bloch, J. Dalibard, and S. Nascimbène, *Quantum simulations with ultracold quantum gases*, Nat. Phys. **8**, 267 (2012).

[49] I. Bloch, J. Dalibard, and W. Zwerger, *Many-body physics with ultracold gases*, Rev. Mod. Phys. **80**, 885 (2008).

[50] D. Jaksch, C. Bruder, J. I. Cirac, C. W. Gardiner, and P. Zoller, *Cold bosonic atoms in optical lattices*, Phys. Rev. Lett. **81**, 3108 (1998).

[51] M. Greiner, O. Mandel, T. Esslinger, T. W. Hänsch, and I. Bloch, *Quantum phase transition from a superfluid to a Mott insulator in a gas of ultracold atoms*, Nature **415**, 39 (2002).

[52] M. P. A. Fisher, P. B. Weichman, G. Grinstein, and D. S. Fisher, *Boson localization and the superfluid-insulator transition*, Phys. Rev. B **40**, 546 (1989).

[53] W. Zwerger, *Mott-Hubbard transition of cold atoms in optical lattices*, J. Opt. B **5**, 9 (2003).

[54] W. Zwerger, editor, *The BCS-BEC Crossover and the Unitary Fermi Gas*, Lecture Notes in Physics 836, Springer, Berlin, 2012.

[55] J. Bardeen, L. N. Cooper, and J. R. Schrieffer, *Theory of superconductivity*, Phys. Rev. **108**, 1175 (1957).

[56] J. Dalibard, F. Gerbier, G. Juzeliunas, and P. Öhberg, *Colloquium: Artificial gauge potentials for neutral atoms*, Rev. Mod. Phys. **83**, 1523 (2011).

[57] R. P. Feynman, *Simulating physics with computers*, Int. J. Theor. Phys. **21**, 467 (1982).

[58] P. A. M. Dirac, *Quantum Mechanics of Many-Electron Systems*, Proc. R. Soc. London.

Ser. A **123**, 714 (1929).

[59] R. B. Laughlin and D. Pines, *The theory of everything.*, Proc. Natl. Acad. Sci. U. S. A. **97**, 28 (2000).

[60] O. E. Alon, A. I. Streltsov, and L. S. Cederbaum, *Multiconfigurational time-dependent Hartree method for bosons: Many-body dynamics of bosonic systems*, Phys. Rev. A **77**, 033613 (2008).

[61] S. Krönke, L. Cao, O. Vendrell, and P. Schmelcher, *Non-equilibrium quantum dynamics of ultra-cold atomic mixtures: the multi-layer multi-configuration time-dependent Hartree method for bosons*, New J. Phys. **15**, 63018 (2013).

[62] L. Cao, S. Krönke, O. Vendrell, and P. Schmelcher, *The multi-layer multi-configuration time-dependent Hartree method for bosons: theory, implementation, and applications.*, J. Chem. Phys. **139**, 134103 (2013).

[63] A. Lenard, *Momentum Distribution in the Ground State of the One-Dimensional System of Impenetrable Bosons*, J. Math. Phys. **5**, 930 (1964).

[64] L. Pitaevskii and S. Stringari, *Uncertainty principle, quantum fluctuations, and broken symmetries*, J. Low Temp. Phys. **85**, 377 (1991).

[65] M. D. Girardeau, E. M. Wright, and J. M. Triscari, *Ground-state properties of a one-dimensional system of hard-core bosons in a harmonic trap*, Phys. Rev. A **63**, 33601 (2001).

[66] J. Kane and L. Kadanoff, *Long-Range Order in Superfluid Helium*, Phys. Rev. **155**, 80 (1967).

[67] L. Reatto and G. V. Chester, *Phonons and the properties of a Bose system*, Phys. Rev. **155**, 88 (1967).

[68] M. Schwartz, *Off-diagonal long-range behavior of interacting Bose systems*, Phys. Rev. B **15**, 1399 (1977).

[69] F. D. M. Haldane, *Effective harmonic-Fluid approach to low-energy properties of one-dimensional quantum fluids*, Phys. Rev. Lett. **47**, 1840 (1981).

[70] D. S. Petrov, G. V. Shlyapnikov, and J. T. M. Walraven, *Regimes of quantum degeneracy in trapped 1D gases*, Phys. Rev. Lett. **85**, 3745 (2000).

[71] T. Jacqmin, J. Armijo, T. Berrada, K. V. Kheruntsyan, and I. Bouchoule, *Sub-poissonian fluctuations in a 1D bose gas: From the quantum quasicondensate to the strongly interacting regime*, Phys. Rev. Lett. **106**, 230405 (2011).

[72] M. Greiner, I. Bloch, O. Mandel, T. W. Hänsch, and T. Esslinger, *Exploring phase coherence in a 2D lattice of Bose-Einstein condensates.*, Phys. Rev. Lett. **87**, 160405 (2001).

[73] S. Dettmer, D. Hellweg, P. Ryytty, J. J. Arlt, W. Ertmer, K. Sengstock, D. S. Petrov, G. V. Shlyapnikov, H. Kreutzmann, L. Santos, and M. Lewenstein, *Observation of phase fluctuations in elongated Bose-Einstein condensates.*, Phys. Rev. Lett. **87**, 160406 (2001).

[74] A. Görlitz, J. M. Vogels, A. E. Leanhardt, C. Raman, T. L. Gustavson, J. R. Abo-Shaeer, A. P. Chikkatur, S. Gupta, S. Inouye, T. Rosenband, and W. Ketterle, *Realization of Bose-Einstein condensates in lower dimensions.*, Phys. Rev. Lett. **87**, 130402 (2001).

[75] E. P. Gross, *Structure of a quantized vortex in boson systems*, Nuovo Cimenti **20**, 454 (1961).

[76] L. P. Pitaevskii, *Vortex Lines in an Imperfect Bose Gas*, Sov. Phys. JETP **13**, 451 (1961).

[77] G. Baym and C. Pethick, *Ground-State Properties of Magnetically Trapped Bose-Condensed Rubidium Gas*, Phys. Rev. Lett. **76**, 6 (1996).

[78] M. Marinescu and A. F. Starace, *Elementary excitation spectrum of a trapped weakly interacting Bose-Einstein condensate*, Phys. Rev. A **56**, 570 (1997).

[79] D. S. Jin, J. R. Ensher, M. R. Matthews, C. E. Wieman, and E. A. Cornell, *Collective Excitations of a Bose-Einstein Condensate in a Dilute Gas*, Phys. Rev. Lett. **77**, 420 (1996).

[80] S. Stringari, *Collective Excitations of a Trapped Bose-Condensed Gas*, Phys. Rev. Lett. **77**, 2360 (1996).

[81] M. Edwards, P. Ruprecht, K. Burnett, R. Dodd, and C. Clark, *Collective Excitations of Atomic Bose-Einstein Condensates.*, Phys. Rev. Lett. **77**, 1671 (1996).

[82] F. Dalfovo and S. Stringari, *Bosons in anisotropic traps: ground state and vortices*, Phys. Rev. A **53**, 22 (1995).

[83] A. L. Fetter, *Rotating trapped Bose-Einstein condensates*, Rev. Mod. Phys. **81**, 647 (2009).

[84] E. J. Mueller, T. L. Ho, M. Ueda, and G. Baym, *Fragmentation of Bose-Einstein condensates*, Phys. Rev. A **74**, 033612 (2006).

[85] M. Girardeau, *Relationship between Systems of Impenetrable Bosons and Fermions in One Dimension*, J. Math. Phys. **1**, 516 (1960).

[86] D. Blume, *Fermionization of a bosonic gas under highly elongated confinement: A diffusion quantum Monte Carlo study*, Phys. Rev. A **66**, 053613 (2002).

[87] O. E. Alon and L. S. Cederbaum, *Pathway from Condensation via Fragmentation to Fermionization of Cold Bosonic Systems*, Phys. Rev. Lett. **95**, 140402 (2005).

[88] S. Zöllner, H.-D. Meyer, and P. Schmelcher, *Composite fermionization of one-dimensional Bose-Bose mixtures*, Phys. Rev. A **78**, 13629 (2008).

[89] D. Delande and K. Sacha, *Many-Body Matter-Wave Dark Soliton*, Phys. Rev. Lett. **112**, 040402 (2014).

[90] S. Krönke, J. Knörzer, and P. Schmelcher, *Correlated quantum dynamics of a single atom collisionally coupled to an ultracold finite bosonic ensemble*, New J. Phys. **17**, 053001 (2015).

[91] G. J. Milburn, J. Corney, E. M. Wright, and D. F. Walls, *Quantum dynamics of an atomic Bose-Einstein condensate in a double-well potential*, Phys. Rev. A **55**, 4318 (1997).

[92] S. Zöllner, H.-D. Meyer, and P. Schmelcher, *Tunneling dynamics of a few bosons in a double well*, Phys. Rev. A **78**, 13621 (2008).

[93] K. Sakmann, A. I. Streltsov, O. E. Alon, and L. S. Cederbaum, *Exact Quantum Dynamics of a Bosonic Josephson Junction*, Phys. Rev. Lett. **103**, 220601 (2009).

[94] K. Huang and C. N. Yang, *Quantum-Mechanical Many-Body Problem with Hard-Sphere Interaction*, Phys. Rev. **105**, 767 (1957).

[95] E. H. Lieb and W. Liniger, *Exact analysis of an interacting bose gas. I. the general solution and the ground state*, Phys. Rev. **130**, 1605 (1963).

[96] M. Olshanii, *Atomic Scattering in the Presence of an External Confinement and a Gas of Impenetrable Bosons*, Phys. Rev. Lett. **81**, 938 (1998).

[97] T. Bergeman, M. G. Moore, and M. Olshanii, *Atom-Atom Scattering under Cylindrical Harmonic Confinement: Numerical and Analytic Studies of the Confinement Induced*

Resonance, Phys. Rev. Lett. **91**, 163201 (2003).

[98] L. Tonks, *The complete equation of state of one, two and three-dimensional gases of hard elastic spheres*, Phys. Rev. **50**, 955 (1936).

[99] E. H. Lieb, R. Seiringer, and J. Yngvason, *One-dimensional bosons in three-dimensional traps.*, Phys. Rev. Lett. **91**, 150401 (2003).

[100] E. H. Lieb and W. Liniger, *Exact Analysis of an Interacting Bose Gas. II. The Excitation Spectrum*, Phys. Rev. **130**, 1616 (1963).

[101] J. Armijo, T. Jacqmin, K. Kheruntsyan, and I. Bouchoule, *Mapping out the quasicondensate transition through the dimensional crossover from one to three dimensions*, Phys. Rev. A **83**, 021605 (2011).

[102] T. Yang, A. J. Henning, and K. A. Benedict, *Bogoliubov excitation spectrum of an elongated condensate throughout a transition from quasi-one-dimensional to three-dimensional*, J. Phys. B **47**, 035302 (2014).

[103] M. Fliesser, A. Csordás, P. Szépfalusy, and R. Graham, *Hydrodynamic excitations of Bose condensates in anisotropic traps*, Phys. Rev. A **56**, R2533 (1997).

[104] V. Dunjko, V. Lorent, and M. Olshanii, *Bosons in cigar-shaped traps: Thomas-Fermi regime Tonks-Girardeau regime, and in between*, Phys. Rev. Lett. **86**, 5413 (2001).

[105] D. Guéry-Odelin and S. Stringari, *Scissors Mode and Superfluidity of a Trapped Bose-Einstein Condensed Gas*, Phys. Rev. Lett. **83**, 4452 (1999).

[106] S. Donadello, S. Serafini, M. Tylutki, L. P. Pitaevskii, F. Dalfovo, G. Lamporesi, and G. Ferrari, *Observation of Solitonic Vortices in Bose-Einstein Condensates*, Phys. Rev. Lett. **113**, 65302 (2014).

[107] D. A. W. Hutchinson and E. Zaremba, *Excitations of a Bose-condensed gas in anisotropic traps*, Phys. Rev. A **57**, 1280 (1998).

[108] B. I. Schneider and D. L. Feder, *Numerical approach to the ground and excited states of a Bose-Einstein condensed gas confined in a completely anisotropic trap*, Phys. Rev. A **59**, 2232 (1999).

[109] P. Öhberg, E. L. Surkov, I. Tittonen, S. Stenholm, M. Wilkens, and G. V. Shlyapnikov, *Low-energy elementary excitations of a trapped Bose-condensed gas*, Phys. Rev. A **56**, R3346 (1997).

[110] A. Csordás and R. Graham, *Collective excitations in Bose-Einstein condensates in triaxially anisotropic parabolic traps*, Phys. Rev. A **59**, 1477 (1999).

[111] L. Salasnich, A. Parola, and L. Reatto, *Periodic quantum tunnelling and parametric resonance with cigar-shaped Bose-Einstein condensates*, J. Phys. B **35**, 3205 (2002).

[112] K. K. Das, *Highly anisotropic Bose-Einstein condensates: Crossover to lower dimensionality*, Phys. Rev. A **66**, 053612 (2002).

[113] K. K. Das, M. D. Girardeau, and E. M. Wright, *Crossover from one to three dimensions for a gas of hard-core bosons.*, Phys. Rev. Lett. **89**, 110402 (2002).

[114] A. M. Kamchatnov and V. S. Shchesnovich, *Dynamics of Bose-Einstein condensates in cigar-shaped traps*, Phys. Rev. A **70**, 023604 (2004).

[115] F. Gerbier, *Quasi-1D Bose-Einstein condensates in the dimensional crossover regime*, Europhys. Lett. **66**, 771 (2004).

[116] A. Muñoz Mateo and V. Delgado, *Effective one-dimensional dynamics of elongated Bose-Einstein condensates*, Ann. Phys. (N. Y). **324**, 709 (2009).

[117] A. M. Mateo and V. Delgado, *Effective mean-field equations for cigar-shaped and disk-shaped Bose-Einstein condensates*, Phys. Rev. A **77**, 013617 (2008).

[118] C. Menotti and S. Stringari, *Collective oscillations of a one-dimensional trapped Bose-Einstein gas*, Phys. Rev. A **66**, 043610 (2002).

[119] P. G. Kevrekidis, D. J. Frantzeskakis, and R. Carretero-González, *Emergent Nonlinear Phenomena in Bose-Einstein Condensates*, Springer, Berlin, 2008.

[120] A. B. Tacla and C. M. Caves, *Entanglement-based perturbation theory for highly anisotropic Bose-Einstein condensates*, Phys. Rev. A **84**, 053606 (2011).

[121] A. B. Tacla and C. M. Caves, *Reduced dimensionality and spatial entanglement in highly anisotropic Bose-Einstein condensates*, Phys. Rev. A **90**, 013605 (2014).

[122] E. Schmidt, *Zur Theorie der linearen und nichtlinearen Integralgleichungen*, Math. Ann. **63**, 433 (1907).

[123] D. Dagnino, N. Barberán, M. Lewenstein, and J. Dalibard, *Vortex nucleation as a case study of symmetry breaking in quantum systems*, Nat. Phys. **5**, 431 (2009).

[124] J. C. Cremon, A. D. Jackson, E. O. Karabulut, G. M. Kavoulakis, B. R. Mottelson, and S. M. Reimann, *Rotating Bose-Einstein condensates: Closing the gap between exact and mean-field solutions*, Phys. Rev. A **91**, 033623 (2015).

[125] S. E. Weiner, M. C. Tsatsos, L. S. Cederbaum, and A. U. J. Lode, *Angular momentum in interacting many-body systems hides in phantom vortices* arXiv:1409.7670 (2014).

[126] S. Klaiman and O. E. Alon, *Spatially-partitioned many-body vortices*,

[127] M. C. Tsatsos and A. U. J. Lode, *Resonances and Dynamical Fragmentation in a Stirred BoseEinstein Condensate*, J. Low Temp. Phys. **181**, 171 (2015).

[128] S. Klaiman, A. U. J. Lode, A. I. Streltsov, L. S. Cederbaum, and O. E. Alon, *Breaking the resilience of a two-dimensional Bose-Einstein condensate to fragmentation*, Phys. Rev. A **90**, 043620 (2014).

[129] U. R. Fischer, A. U. J. Lode, and B. Chatterjee, *Condensate fragmentation as a sensitive measure of the quantum many-body behavior of bosons with long-range interactions*, Phys. Rev. A **91**, 063621 (2015).

[130] A. I. Streltsov, *Quantum systems of ultracold bosons with customized interparticle interactions*, Phys. Rev. A **88**, 041602 (2013).

[131] O. I. Streltsova, O. E. Alon, L. S. Cederbaum, and A. I. Streltsov, *Generic regimes of quantum many-body dynamics of trapped bosonic systems with strong repulsive interactions*, Phys. Rev. A **89**, 061602 (2014).

[132] K. B. Davis, M.-O. Mewes, M. R. Andrews, N. J. Van Druten, D. S. Durfee, D. M. Kurn, and W. Ketterle, *Bose-Einstein condensation in a gas of sodium atoms*, Phys. Rev. Lett. **75**, 3969 (1995).

[133] M. H. Anderson, J. R. Ensher, M. R. Matthews, C. E. Wieman, and E. A. Cornell, *Observation of Bose-Einstein Condensation in a Dilute Atomic Vapor*, Science **269**, 198 (1995).

[134] C. C. Bradley, C. A. Sackett, J. J. Tollett, and R. G. Hulet, *Evidence of Bose-Einstein Condensation in an Atomic Gas with Attractive Interactions*, Phys. Rev. Lett. **75**, 1687 (1995).

[135] D. G. Fried, T. C. Killian, L. Willmann, D. Landhuis, S. C. Moss, D. Kleppner, and T. J. Greytak, *Bose-Einstein Condensation of Atomic Hydrogen*, Phys. Rev. Lett. **81**, 3811

(1998).

[136] A. Robert, O. Sirjean, A. Browaeys, J. Poupard, S. Nowak, D. Boiron, C. I. Westbrook, and A. Aspect, *A Bose-Einstein Condensate of Metastable Atoms*, Science **292**, 461 (2001).

[137] G. Modugno, *Bose-Einstein Condensation of Potassium Atoms by Sympathetic Cooling*, Science **294**, 1320 (2001).

[138] T. Weber, J. Herbig, M. Mark, H.-C. N/"agerl, and R. Grimm, *Bose-Einstein Condensation of Cesium*, Science **10**, 232 (2003).

[139] Y. Takasu, K. Maki, K. Komori, T. Takano, K. Honda, M. Kumakura, T. Yabuzaki, and Y. Takahashi, *Spin-Singlet Bose-Einstein Condensation of Two-Electron Atoms*, Phys. Rev. Lett. **91**, 040404 (2003).

[140] A. Griesmaier, J. Werner, S. Hensler, J. Stuhler, and T. Pfau, *Bose-Einstein condensation of chromium*, Phys. Rev. Lett. **94**, 160401 (2005).

[141] S. Kraft, F. Vogt, O. Appel, F. Riehle, and U. Sterr, *Bose-Einstein Condensation of Alkaline Earth Atoms: Ca40*, Phys. Rev. Lett. **103**, 130401 (2009).

[142] S. Stellmer, M. K. Tey, B. Huang, R. Grimm, and F. Schreck, *Bose-Einstein condensation of strontium*, Phys. Rev. Lett. **103**, 200401 (2009).

[143] M. Lu, N. Q. Burdick, and B. L. Lev, *Quantum degenerate dipolar Fermi gas*, Phys. Rev. Lett. **108**, 215301 (2012).

[144] K. Aikawa, A. Frisch, M. Mark, S. Baier, A. Rietzler, R. Grimm, and F. Ferlaino, *Bose-Einstein condensation of erbium*, Phys. Rev. Lett. **108**, 210401 (2012).

[145] S. Chu, *Nobel Lecture: The manipulation of neutral particles*, Rev. Mod. Phys. **70**, 685 (1998).

[146] C. N. Cohen-Tannoudji, *Nobel Lecture: Manipulating atoms with photons*, Rev. Mod. Phys. **70**, 707 (1998).

[147] W. D. Phillips, *Nobel Lecture: Laser cooling and trapping of neutral atoms*, Rev. Mod. Phys. **70**, 721 (1998).

[148] W. Ketterle and N. J. V. Druten, *Evaporative Cooling of Trapped Atoms*, Adv. At. Mol. Opt. Phys. **37**, 181 (1996).

[149] D. E. Pritchard, *Cooling neutral atoms in a magnetic trap for precision spectroscopy*, Phys. Rev. Lett. **51**, 1336 (1983).

[150] T. Esslinger, I. Bloch, and T. W. Hänsch, *Bose-Einstein condensation in a quadrupole-Ioffe-configuration trap*, Phys. Rev. A **58**, R2664 (1998).

[151] R. Folman, P. Krüger, J. Schmiedmayer, J. Denschlag, and C. Henkel, *Microscopic atom optics: From wires to an atom chip*, Adv. At. Mol. Opt. Phys. **48**, 263 (2002).

[152] R. Folman, P. Krüger, D. Cassettari, B. Hessmo, T. Maier, and J. Schmiedmayer, *Controlling Cold Atoms using Nanofabricated Surfaces: Atom Chips*, Phys. Rev. Lett. **84**, 4749 (2000).

[153] P. Krüger, S. Hofferberth, I. E. Mazets, I. Lesanovsky and J. Schmiedmayer *Weakly interacting Bose gas in the one-dimensional limit.*, Phys. Rev. Lett. **105**, 265302 (2010).

[154] H. Moritz, T. Stöferle, M. Köhl, and T. Esslinger, *Exciting collective oscillations in a trapped 1D gas.*, Phys. Rev. Lett. **91**, 250402 (2003).

[155] S. Krönke, *Correlated Quantum Dynamics of Ultracold Bosons and Bosonic Mixtures:*

the Multi-Layer Multi-Configuration Time-Dependent Hartree Method for Bosons, PhD thesis, Universität Hamburg, 2015.

[156] E. Dagotto, *Correlated electrons in high-temperature superconductors*, Rev. Mod. Phys. **66**, 763 (1994).

[157] S. R. White, *Density matrix formulation for quantum renormalization groups*, Phys. Rev. Lett. **69**, 2863 (1992).

[158] S. R. White, *Density-matrix algorithms for quantum renormalization groups*, Phys. Rev. B **48**, 10345 (1993).

[159] A. Daley, C. Kollath, U. Schollwöck, and G. Vidal, *Time-dependent density-matrix renormalization-group using adaptive effective Hilbert spaces*, J. Stat. Mech. , P04004 (2004).

[160] S. R. White and A. E. Feiguin, *Real-time evolution using the density matrix renormalization group*, Phys. Rev. Lett. **93**, 076401 (2004).

[161] U. Schollwöck, *The density-matrix renormalization group*, Rev. Mod. Phys. **77**, 259 (2005).

[162] B. L. Hammond, W. A. Lester, and P. J. Reynolds, *Monte Carlo Methods in Ab Initio Quantum Chemistry*, World Scientific Lecture and Course Notes in Chemistry 1, World Scientific, London, 1994.

[163] S. Giorgini, J. Boronat, and J. Casulleras, *Ground state of a homogeneous Bose gas: a diffusion Monte Carlo calculation*, Phys. Rev. A **60**, 5129 (1999).

[164] K. Sheshadri, H. R. Krishnamurthy, R. Pandit, and T. V. Ramakrishnan, *Superfluid and Insulating Phases in an Interacting-Boson Model: Mean-Field Theory and the RPA*, Europhys. Lett. **22**, 257 (1993).

[165] W. Krauth, M. Caffarel, and J. P. Bouchaud, *Gutzwiller wave function for a model of strongly interacting bosons*, Phys. Rev. B **45**, 3137 (1992).

[166] D. J. Tannor, *Introduction to quantum mechanics - a time-dependent perspective*, University Science Books, Sausalito, 2007.

[167] H. T. Stoof, K. B. Gubbels, and D. B. Dickerscheid, *Ultracold Quantum Fields*, Springer, Berlin, 2009.

[168] D. Raventós, T. Graß, M. Lewenstein, and B. Juliá-Díaz, *Cold bosons in optical lattices: a tutorial for Exact Diagonalization*, J. Phys. B **50**, 113001 (2014).

[169] H.-D. Meyer, F. Gatti, and G. Worth, *Multidimensional quantum dynamics : MCTDH theory and applications*, Wiley-VCH, Weinheim, 2009.

[170] O. Penrose and L. Onsager, *Bose-Einstein Condensation and Liquid Helium*, Phys. Rev. **104**, 576 (1956).

[171] M. Naraschewski and R. J. Glauber, *Spatial coherence and density correlations of trapped Bose gases*, Phys. Rev. A **59**, 4595 (1999).

[172] R. Glauber, *The Quantum Theory of Optical Coherence*, Phys. Rev. **130**, 2529 (1963).

[173] C. N. Yang, *Concept of off-diagonal long-range order and the quantum phases of liquid He and of superconductors*, Rev. Mod. Phys. **34**, 694 (1962).

[174] E. Fermi, *Sopra lo spostamento per pressione delle righe elevate delle serie spettrali*, Ric. Sci. **7**, 13 (1936).

[175] E. Tiesinga, C. J. Williams, F. H. Mies, and P. S. Julienne, *Interacting atoms under strong quantum confinement*, Phys. Rev. A **61**, 063416 (2000).

[176] M. Block and M. Holthaus, *Pseudopotential approximation in a harmonic trap*, Phys. Rev. A **65**, 052102 (2002).

[177] D. Blume and C. H. Greene, *Fermi pseudopotential approximation: Two particles under external confinement*, Phys. Rev. A **65**, 043613 (2002).

[178] E. L. Bolda, E. Tiesinga, and P. S. Julienne, *Effective-scattering-length model of ultracold atomic collisions and Feshbach resonances in tight harmonic traps*, Phys. Rev. A **66**, 013403 (2002).

[179] J. Pade, M. Block, and M. Holthaus, *s -wave pseudopotential for anisotropic traps*, Phys. Rev. A **68**, 063402 (2003).

[180] M. J. Seaton, *Quantum defect theory*, Reports Prog. Phys. **46**, 167 (1983).

[181] C. H. Greene, A. R. P. Rau, and U. Fano, *General form of the quantum-defect theory. II*, Phys. Rev. A **26**, 2441 (1982).

[182] C. Greene, U. Fano, and G. Strinati, *General form of the quantum-defect theory*, Phys. Rev. A **19**, 1485 (1979).

[183] A. Derevianko, J. F. Babb, and A. Dalgarno, *High-precision calculations of van der Waals coefficients for heteronuclear alkali-metal dimers*, Phys. Rev. A **63**, 527041 (2001).

[184] L. D. Landau and E. M. Lifshitz, *Quantum Mechanics*, Elsevier, Oxford, 1973.

[185] J. J. Sakurai, *Modern Quantum Mechanics*, Benjamin Cummings, Menlo Park (California), 1985.

[186] J. R. Taylor, *Scattering Theory*, Dover Publications, Mineola, New York, 2000.

[187] A. G. Sitenko, *Scattering Theory*, Spinger, Berlin, Heidelberg, 1975.

[188] Y. Castin, *Bose-Einstein condensates in atomic gases: simple theoretical results*, Springer, Berlin, 2001.

[189] E. P. Wigner, *On the behavior of cross sections near thresholds*, Phys. Rev. **73**, 1002 (1948).

[190] H. A. Bethe, *Theory of the effective range in nuclear scattering*, Phys. Rev. **76**, 38 (1949).

[191] B. D. Esry and C. H. Greene, *Validity of the shape-independent approximation for Bose-Einstein condensates*, Phys. Rev. A **60**, 1451 (1999).

[192] A. Derevianko, *Revised Huang-Yang multipolar pseudopotential*, Phys. Rev. A **72**, 044701 (2005).

[193] A. Farrell and B. P. van Zyl, *S-Wave Scattering and the Zero-Range Limit of the Finite Square Well in Arbitrary Dimensions*, Can. J. Phys. **88**, 817 (2010).

[194] R. Stock, A. Silberfarb, E. L. Bolda, and I. H. Deutsch, *Generalized Pseudopotentials for Higher Partial Wave Scattering*, Phys. Rev. Lett. **94**, 023202 (2005).

[195] F. Stampfer and P. Wagner, *A mathematically rigorous formulation of the pseudopotential method*, J. Math. Anal. Appl. **342**, 202 (2008).

[196] Z. Idziaszek and T. Calarco, *Pseudopotential method for higher partial wave scattering*, Phys. Rev. Lett. **96**, 013201 (2006).

[197] R. Estrada and R. P. Kanwal, *Regularization, pseudofunction, and hadamard finite part*, J. Math. Anal. Appl. **141**, 195 (1989).

[198] A. A. Khelashvili and T. P. Nadareishvili, *What is the boundary condition for radial wave function of the Schrödinger equation?*, Am. J. Phys. **79**, 15 (2010).

[199] A. A. Khelashvili and T. P. Nadareishvili, *Singular behavior of the Laplace operator in polar spherical coordinates and some of its consequences for the radial wave function at the origin of coordinates*, Phys. Part. Nucl. Lett. **12**, 11 (2015).

[200] B. Numerov, *Note on the numerical integration of d2x/dt2 =f(x,t)*, Astron. Nachrichten **230**, 359 (1927).

[201] T. Busch, B.-G. Englert, K. Rzazewski, and M. Wilkens, *Two Cold Atoms in a Harmonic Trap*, Found. Phys. **28**, 549 (1998).

[202] Z. Idziaszek and T. Calarco, *Analytical solutions for the dynamics of two trapped interacting ultracold atoms*, Phys. Rev. A **74**, 022712 (2006).

[203] A. U. J. Lode, K. Sakmann, O. E. Alon, L. S. Cederbaum, and A. I. Streltsov, *Numerically exact quantum dynamics of bosons with time-dependent interactions of harmonic type*, Phys. Rev. A **86**, 063606 (2012).

[204] M. Zaluska-Kotur, M. Gajda, A. Orlowski, and J. Mostowski, *Soluble model of many interacting quantum particles in a trap*, Phys. Rev. A **61**, 033613 (2000).

[205] L. Cohen and C. Lee, *Exact reduced density matrices for a model problem*, J. Math. Phys. **26**, 3105 (1985).

[206] J. R. Armstrong, N. T. Zinner, D. V. Fedorov, and A. S. Jensen, *Analytic harmonic approach to the N -body problem*, J. Phys. B **44**, 055303 (2011).

[207] J. Yan, *Harmonic Interaction Model and Its Applications in Bose-Einstein Condensation*, J. Stat. Phys. **113**, 623 (2003).

[208] Y. Castin, *Simple theoretical tools for low dimension Bose gases*, J. Phys. IV **116**, 89 (2004).

[209] R. A. Doganov, S. Klaiman, O. E. Alon, A. I. Streltsov, and L. S. Cederbaum, *Two trapped particles interacting by a finite-range two-body potential in two spatial dimensions*, Phys. Rev. A **87**, 33631 (2013).

[210] S. Zöllner, H.-D. Meyer, and P. Schmelcher, *Correlations in ultracold trapped few-boson systems: Transition from condensation to fermionization*, Phys. Rev. A **74**, 53612 (2006).

[211] S. Zöllner, H.-D. Meyer, and P. Schmelcher, *Few-Boson Dynamics in Double Wells: From Single-Atom to Correlated Pair Tunneling*, Phys. Rev. Lett. **100**, 40401 (2008).

[212] R. Schmitz, S. Krönke, L. Cao, and P. Schmelcher, *Quantum breathing dynamics of ultracold bosons in one-dimensional harmonic traps: Unraveling the pathway from few- to many-body systems*, Phys. Rev. A **88**, 043601 (2013).

[213] J. M. Schurer, P. Schmelcher, and A. Negretti, *Ground-state properties of ultracold trapped bosons with an immersed ionic impurity*, Phys. Rev. A **90**, 033601 (2014).

[214] J. M. Schurer, R. Gerritsma, P. Schmelcher, and A. Negretti, *Impact of many-body correlations on the dynamics of an ion-controlled bosonic Josephson junction*, Phys. Rev. A **93**, 063602 (2016).

[215] M. A. Cazalilla, R. Citro, T. Giamarchi, E. Orignac, and M. Rigol, *One dimensional bosons: From condensed matter systems to ultracold gases*, Rev. Mod. Phys. **83**, 1405 (2011).

[216] J. Christensson, C. Forssen, S. Aberg, and S. M. Reimann, *Effective-interaction approach to the many-boson problem*, Phys. Rev. A **79**, 012707 (2009).

[217] E. J. Lindgren, J. Rotureau, C. Forssén, A. G. Volosniev, and N. T. Zinner, *Fermionization of two-component few-fermion systems in a one-dimensional harmonic trap*, New J. Phys.

16, 063003 (2014).

[218] K. G. Wilson, *The renormalization group: Critical phenomena and the Kondo problem*, Rev. Mod. Phys. **47**, 773 (1975).

[219] K. G. Wilson and J. Kogut, The renormalization group and the ϵ expansion, North-Holland Publishing Company, Amsterdam, 1974.

[220] R. Jackiw, *Diverse Topics in Theoretical and Mathematical Physics*, World scientific, London, 1995.

[221] R. M. Cavalcanti, *Exact Green's functions for delta-function potentials and renormalization in quantum mechanics*, Rev. Bras. Ens. Fis. **21**, 336 (1999).

[222] I. Mitra, A. DasGupta, and B. Dutta-Roy, *Regularization and renormalization in scattering from Dirac delta potentials*, Am. J. Phys. **66**, 1101 (1998).

[223] N. T. Zinner, *Universal two-body spectra of ultracold harmonically trapped atoms in two and three dimensions*, J. Phys. A **45**, 205302 (2012).

[224] M. Rontani, S. Aberg, and S. M. Reimann, *Configuration interaction approach to the few-body problem in a two-dimensional harmonic trap with contact interaction.* J. Phys. B **50**, 065301 (2017)

[225] S. Albeverio, F. Gesztesy, R. Høegh-Krohn, and H. Holden, *Solvable Models in Quantum Mechanics*, AMS Chelsea Publishing, Procidence, 1988.

[226] M. Olshanii and L. Pricoupenko, *Rigorous approach to the problem of ultraviolet divergencies in dilute Bose gases*, Phys. Rev. Lett. **88**, 010402 (2001).

[227] P. Gosdzinsky and R. Tarrach, *Learning quantum field theory from elementary quantum mechanics*, Am. J. Phys. **59**, 70 (1991).

[228] S. K. Adhikari and T. Frederico, *Renormalization Group in Potential Scattering*, Phys. Rev. Lett. **74**, 4572 (1995).

[229] T. Ernst, D. W. Hallwood, J. Gulliksen, H.-D. Meyer, and J. Brand, *Simulating strongly correlated multiparticle systems in a truncated Hilbert space*, Phys. Rev. A **84**, 023623 (2011).

[230] M. Rontani, G. Eriksson, S. berg, and S. M. Reimann, *On the renormalization of contact interactions for the configuration-interaction method in two-dimensions*, J. Phys. B **50**, 065301 (2017).

[231] J. G. Cosme, C. Weiss, and J. Brand, *Difficult-to-detect convergence problem of variational multi-mode quantum dynamics with attractive bosons*, Phys. Rev. A **94**, 043603 (2016).

[232] A. Jackle and H.-D. Meyer, *Product representation of potential energy surfaces*, J. Chem. Phys. **104**, 7974 (1996).

[233] A. Jackle and H.-D. Meyer, *Product representation of potential energy surfaces. II*, J. Chem. Phys. **109**, 3772 (1998).

[234] K. Sakmann, *Many-Body Schrödinger Dynamics of Bose-Einstein Condensates*, Springer, Berlin, 2011.

[235] O. E. Alon, A. I. Streltsov, and L. S. Cederbaum, *Many-body theory for systems with particle conversion: Extending the multiconfigurational time-dependent Hartree method*, Phys. Rev. A **79**, 022503 (2009).

[236] S. Zöllner and H.-D. Meyer, *Ultracold few-boson systems in a double-well trap*, Phys. Rev. A **74**, 1 (2006).

[237] S. Zöllner, H. D. Meyer, and P. Schmelcher, *Few-Boson dynamics in double wells: From single-atom to correlated pair tunneling*, Phys. Rev. Lett. **100**, 040401 (2008).

[238] S. Zöllner, H. D. Meyer, and P. Schmelcher, *Tunneling dynamics of a few bosons in a double well*, Phys. Rev. A **78**, 013621 (2008).

[239] K. Sakmann, A. I. Streltsov, O. E. Alon, and L. S. Cederbaum, *Exact quantum dynamics of a bosonic josephson junction*, Phys. Rev. Lett. **103**, 220601 (2009).

[240] A. I. Streltsov, O. E. Alon, and L. S. Cederbaum, *Swift loss of coherence of soliton trains in attractive bose-einstein condensates*, Phys. Rev. Lett. **106**, 240401 (2011).

[241] S. I. Mistakidis, L. Cao, and P. Schmelcher, *Interaction quench induced multimode dynamics of finite atomic ensembles*, J. Phys. B **47**, 225303 (2014).

[242] S. I. Mistakidis, L. Cao, and P. Schmelcher, *Negative-quench-induced excitation dynamics for ultracold bosons in one-dimensional lattices*, Phys. Rev. A **91**, 033611 (2015).

[243] S. Zöllner, G. M. Bruun, C. J. Pethick, and S. M. Reimann, *Bosonic and fermionic dipoles on a ring*, Phys. Rev. Lett. **107**, 035301 (2011).

[244] S. Zöllner, *Ground states of dipolar gases in quasi-one-dimensional ring traps*, Phys. Rev. A **84**, 063619 (2011).

[245] S. Klaiman, A. U. J. Lode, K. Sakmann, O. I. Streltsova, O. E. Alon, L. S. Cederbaum, and A. I. Streltsov, *Quantum many-body dynamics of trapped bosons with the MCTDHB package: Towards new horizons with novel physics*, High Perform. Comput. Sci. Eng. '14 Springer International Publishing, Berlin, 2014.

[246] H.-D. Meyer, U. Manthe, and L. Cederbaum, *The multi-configurational time-dependent Hartree approach*, Chem. Phys. Lett. **165**, 73 (1990).

[247] U. Manthe, H. Meyer, and L. S. Cederbaum, *Wavepacket dynamics within the multiconfiguration Hartree framework: General aspects and application to NOCl*, J. Chem. Phys. **97**, 3199 (1992).

[248] G. A. Worth, *Accurate wave packet propagation for large molecular systems: The multi-configuration time-dependent Hartree (MCTDH) method with selected configurations*, J. Chem. Phys. **112**, 8322 (2000).

[249] H. Wang and M. Thoss, *Multilayer formulation of the multiconfiguration time-dependent Hartree theory*, J. Chem. Phys. **119**, 1289 (2003).

[250] U. Manthe, *A multilayer multiconfigurational time-dependent Hartree approach for quantum dynamics on general potential energy surfaces*, J. Chem. Phys. **128** (2008).

[251] O. Vendrell and H.-D. Meyer, *Multilayer multiconfiguration time-dependent Hartree method: implementation and applications to a Henon-Heiles hamiltonian and to pyrazine.*, J. Chem. Phys. **134**, 044135 (2011).

[252] J. Zanghellini, M. Kitzler, C. Fabian, T. Brabec, and A. Scrinzi, *An MCTDHF approach to multielectron dynamics in laser fields*, Laser Phys **13**, 1046 (2003).

[253] T. Kato and H. Kono, *Time-dependent multiconfiguration theory for electronic dynamics of molecules in an intense laser field*, Chem. Phys. Lett. **392**, 533 (2004).

[254] M. Nest, T. Klamroth, and P. Saalfrank, *The multiconfiguration time-dependent Hartree-Fock method for quantum chemical calculations*, J. Chem. Phys. **122**, 124102 (2005).

[255] A. I. Streltsov, O. E. Alon, and L. S. Cederbaum, *Role of excited states in the splitting of a trapped interacting Bose-Einstein condensate by a time-dependent barrier.*, Phys. Rev. Lett. **99**, 030402 (2007).

[256] O. E. Alon, A. I. Streltsov, and L. S. Cederbaum, *Unified view on multiconfigurational time propagation for systems consisting of identical particles.*, J. Chem. Phys. **127**, 154103 (2007).

[257] O. Alon, A. Streltsov, and L. Cederbaum, *Multiconfigurational time-dependent Hartree method for mixtures consisting of two types of identical particles*, Phys. Rev. A **76**, 062501 (2007).

[258] O. E. Alon, A. I. Streltsov, K. Sakmann, A. U. J. Lode, J. Grond, and L. S. Cederbaum, *Recursive formulation of the multiconfigurational time-dependent Hartree method for fermions, bosons and mixtures thereof in terms of one-body density operators*, Chem. Phys. **401**, 2 (2012).

[259] H. Wang and M. Thoss, *Numerically exact quantum dynamics for indistinguishable particles: the multilayer multiconfiguration time-dependent Hartree theory in second quantization representation.*, J. Chem. Phys. **131**, 024114 (2009).

[260] H. Wang and M. Thoss, *Numerically exact, time-dependent study of correlated electron transport in model molecular junctions.*, J. Chem. Phys. **138**, 134704 (2013).

[261] U. Manthe and T. Weike, *On the multi-layer multi-configurational time-dependent Hartree approach for bosons and fermions*, J. Chem. Phys. **146**, 064117 (2017).

[262] L. Cao, S. Krönke, J. Stockhofe, J. Simonet, K. Sengstock, D. S. Lühmann, and P. Schmelcher, *Beyond-mean-field study of a binary bosonic mixture in a state-dependent honeycomb lattice*, Phys. Rev. A **91**, 043639 (2015).

[263] A. U. J. Lode and C. Bruder, *Dynamics of Hubbard Hamiltonians with the multiconfigurational time-dependent Hartree method for indistinguishable particles*, Phys. Rev. A **94**, 013616 (2016).

[264] A. U. J. Lode, *Multiconfigurational time-dependent Hartree method for bosons with internal degrees of freedom: Theory and composite fragmentation of multicomponent Bose-Einstein condensates*, Phys. Rev. A **93**, 063601 (2016).

[265] J. Grond, A. I. Streltsov, L. S. Cederbaum, and O. E. Alon, *Excitation spectra of fragmented condensates by linear response: General theory and application to a condensate in a double-well potential*, Phys. Rev. A **86**, 063607 (2012).

[266] O. E. Alon, *Many-body excitation spectra of trapped bosons with general interaction by linear response*, J. Phys. Conf. Ser. **594**, 11 (2014).

[267] M. Beck, A. Jäckle, G. Worth, and H.-D. Meyer, *The multiconfiguration time-dependent Hartree (MCTDH) method: a highly efficient algorithm for propagating wavepackets*, Phys. Rep. **324**, 1 (2000).

[268] H.-D. Meyer and G. A. Worth, *Quantum molecular dynamics: propagating wavepackets and density operators using the multiconfiguration time-dependent Hartree method*, Theor. Chem. Acc. **109**, 251 (2003).

[269] U. Manthe, *Accurate calculations of reaction rates: predictive theory based on a rigorous quantum transition state concept*, Mol. Phys. **109**, 1415 (2011).

[270] H. Meyer, *Studying molecular quantum dynamics with the multiconfiguration timedependent Hartree method*, WIREs Comput Mol Sci **2**, 351 (2012).

[271] H. Wang, *Multilayer Multiconfiguration Time-Dependent Hartree Theory*, J. Phys. Chem. A **119**, 7951 (2015).

[272] K. Sakmann, A. I. Streltsov, O. E. Alon, and L. S. Cederbaum, *Universality of fragmentation in the Schrödinger dynamics of bosonic Josephson junctions*, Phys. Rev. A **89**,

023602 (2014).

[273] O. E. Alon, V. S. Bagnato, R. Beinke, I. Brouzos, T. Calarco, T. Caneva, L. S. Cederbaum, M. A. Kasevich, S. Klaiman, A. U. J. Lode, S. Montangero, A. Negretti, R. S. Said, K. Sakmann, O. I. Streltsova, M. Theisen, M. C. Tsatsos, S. E. Weiner, T. Wells, and A. I. Streltsov, *MCTDHB Physics and Technologies: Excitations and Vorticity, Single-Shot Detection, Measurement of Fragmentation, and Optimal Control in Correlated Ultra-Cold Bosonic Many-Body Systems, High Perform. Comput. Sci. Eng. 15 Springer International Publishing, Berlin, 2016.*

[274] J. C. Light, Discrete Variable Representations in Quantum Dynamics, *Springer US, N. Y., 1992.*

[275] D. Kosloff and R. Kosloff, A Fourier Method Solution for the Time Dependent Schrödinger equation as a Tool in Molecular Dynamics, *J. Comp. Phys.* **52**, 35 (1983).

[276] P. A. M. Dirac, Note on Exchange Phenomena in the Thomas Atom, *Math. Proc. Cambridge Philos. Soc.* **26**, 376 (1930).

[277] J. Frenkel, Wave Mechanics: Elementary Theory, *Clarendon Press, Oxford, 1932.*

[278] A. McLachlan, A variational solution of the time-dependent Schrodinger equation, *Mol. Phys.* **8**, 39 (1964).

[279] J. Kucar, H.-D. Meyer, and L. S. Cederbaum, Time-dependent rotated hartree approach, *Chem. Phys. Lett.* **140**, 525 (1987).

[280] J. Broeckhove, L. Lathouwers, E. Kesteloot, and P. Van Leuven, On the equivalence of time-dependent variational principles, *Chem. Phys. Lett.* **149**, 547 (1988).

[281] G. D. Byrne and A. C. Hindmarsh, A Polyalgorithm for the Numerical Solution of Ordinary Differential Equations, *ACM Trans. Math. Softw.* **1**, 71 (1975).

[282] P. N. Brown, G. D. Byrne, and A. C. Hindmarsh, VODE, a variable-coefficient ODE solver, *J. Comput. Phys.* **10**, 1038 (1986).

[283] G. D. Byrne and A. C. Hindmarsh, Stiff ODE Solvers: A Review of current and coming attractions, *J. Comput. Phys.* **8** (1986).

[284] C. Lévêque and L. B. Madsen, Time-dependent restricted-active-space self-consistent-field theory for bosonic many-body systems, *New J. Phys.* **19**, 043007 (2017).

[285] A. Geißler and W. Hofstetter, The infinite occupation number basis of bosons - solving a numerical challenge, *Phys. Rev. B* **95**, 224516 (2017).

[286] *http://www.openmp.org/.*

[287] *https://www.open-mpi.org/.*

[288] *https://software.intel.com/en-us/intel-vtune-amplifier-xe.*

[289] *http://gpelab.math.cnrs.fr/.*

[290] X. Antoine and R. Duboscq, Computer Physics cations GPELab , a Matlab Toolbox to solve Gross-Pitaevskii Equations I : computation of stationary solutions, *Comput. Phys. Commun.* **185**, 1 (2014).

[291] X. Antoine and R. Duboscq, GPELab, a Matlab toolbox to solve Gross-Pitaevskii equations II: Dynamics and stochastic simulations, *Comput. Phys. Commun.* **193**, 95 (2015).

[292] J. G. Cosme, C. Weiss, and J. Brand, Center-of-mass motion as a sensitive convergence test for variational multi-mode quantum dynamics, *Phys. Rev. A* **94**, 1 (2015).

[293] K. J. H. Giesbertz and R. van Leeuwen, Natural occupation numbers: when do they

vanish?, *J. Chem. Phys.* **139**, *104109 (2013).*

[294] *Y. Makhlin, G. Schön, and A. Shnirman,* Quantum-state engineering with Josephson-junction devices, *Rev. Mod. Phys.* **73**, *357 (2001).*

[295] *R. Gati and M. K. Oberthaler,* A bosonic Josephson junction, *J. Phys. B* **40**, *R61 (2007).*

[296] *M. Albiez, R. Gati, J. Fölling, S. Hunsmann, M. Cristiani, and M. K. Oberthaler,* Direct observation of tunneling and nonlinear self-trapping in a single bosonic josephson junction, *Phys. Rev. Lett.* **95**, *010402 (2005).*

[297] *A. Smerzi, S. Fantoni, S. Giovanazzi, and S. R. Shenoy,* Quantum Coherent Atomic Tunneling between Two Trapped Bose-Einstein Condensates, *Phys. Rev. Lett.* **79**, *4950 (1997).*

[298] *S. Raghavan, A. Smerzi, S. Fantoni, and S. R. Shenoy,* Coherent oscillations between two weakly coupled Bose-Einstein condensates: Josephson effects, π oscillations, and macroscopic quantum self-trapping, *Phys. Rev. A* **59**, *620 (1999).*

[299] *D. Ananikian and T. Bergeman,* Gross-Pitaevskii equation for Bose particles in a double-well potential: Two-mode models and beyond, *Phys. Rev. A* **73**, *13604 (2006).*

[300] *J. Gillet, M. A. Garcia-March, T. Busch, and F. Sols,* Tunneling, self-trapping, and manipulation of higher modes of a Bose-Einstein condensate in a double well, *Phys. Rev. A* **89**, *023614 (2014).*

[301] *S. Zöllner, H.-D. Meyer, and P. Schmelcher,* Ultracold few-boson systems in a double-well trap, *Phys. Rev. A* **74**, *53612 (2006).*

[302] *S. Zöllner, H.-D. Meyer, and P. Schmelcher,* Excitations of few-boson systems in one-dimensional harmonic and double wells, *Phys. Rev. A* **75**, *43608 (2007).*

[303] *T. Berrada, S. van Frank, R. Bücker, T. Schumm, J.-F. Schaff, J. Schmiedmayer, B. Juliá-Díaz, and A. Polls,* Matter-wave recombiners for trapped Bose-Einstein condensates, *Phys. Rev. A* **93**, *063620 (2016).*

[304] *A. D. Martin and J. Ruostekoski,* Quantum dynamics of atomic bright solitons under splitting and recollision, and implications for interferometry, *New J. Phys.* **14**, *043040 (2012).*

[305] *Y. J. Wang, D. Z. Anderson, V. M. Bright, E. A. Cornell, Q. Diot, T. Kishimoto, M. Prentiss, R. A. Saravanan, S. R. Segal, and S. Wu,* Atom michelson interferometer on a chip using a Bose-Einstein condensate, *Phys. Rev. Lett.* **94**, *090405 (2005).*

[306] *O. Garcia, B. Deissler, K. J. Hughes, J. M. Reeves, and C. A. Sackett,* Bose-Einstein-condensate interferometer with macroscopic arm separation, *Phys. Rev. A* **74**, *031601 (2006).*

[307] *M. Horikoshi and K. Nakagawa,* Suppression of dephasing due to a trapping potential and atom-atom interactions in a trapped-condensate interferometer, *Phys. Rev. Lett.* **99**, *180401 (2007).*

[308] *R. P. Kafle, D. Z. Anderson, and A. A. Zozulya,* Analysis of a free oscillation atom interferometer, *Phys. Rev. A* **84**, *033639 (2011).*

[309] *R. H. Leonard and C. A. Sackett,* Effect of trap anharmonicity on a free-oscillation atom interferometer, *Phys. Rev. A* **86**, *043613 (2012).*

[310] *T. Fogarty, A. Kiely, S. Campbell, and T. Busch,* Effect of interparticle interaction in a free-oscillation atomic interferometer, *Phys. Rev. A* **87**, *043630 (2013).*

[311] *D. Dries, S. E. Pollack, J. M. Hitchcock, and R. G. Hulet,* Dissipative transport of a

Bose-Einstein condensate, *Phys. Rev. A* **82**, *033603 (2010)*.

[312] *M. Albert, T. Paul, N. Pavloff, and P. Leboeuf,* Dipole oscillations of a Bose-Einstein condensate in the presence of defects and disorder., *Phys. Rev. Lett.* **100**, *250405 (2008)*.

[313] *C. Raman, M. Kohl, R. Onofrio, D. S. Durfee, C. E. Kuklewicz, Z. Hadzibabic, and W. Ketterle,* Evidence for a critical velocity in a Bose-Einstein condensed gas, *Phys. Rev. Lett.* **83**, *4 (1999)*.

[314] *J. Bonart and L. F. Cugliandolo,* Effective potential and polaronic mass shift in a trapped dynamical impurityLuttinger liquid system, *Europhys. Lett.* **101**, *16003 (2013)*.

[315] *J. Catani, G. Lamporesi, D. Naik, M. Gring, M. Inguscio, F. Minardi, A. Kantian, and T. Giamarchi,* Quantum dynamics of impurities in a one-dimensional Bose gas, *Phys. Rev. A* **85**, *023623 (2012)*.

[316] *J. M. Schurer, A. Negretti, and P. Schmelcher,* Capture dynamics of ultracold atoms in the presence of an impurity ion, *New J. Phys.* **17**, *083024 (2015)*.

[317] *L. Salasnich, L. Reatto, A. Parola, and L. Reatto,* Effective wave equations for the dynamics of cigar-shaped and disk-shaped Bose condensates, *Phys. Rev. A* **65**, *43614 (2002)*.

[318] *L. Brey, N. F. Johnson, and B. I. Halperin,* Optical and magneto-optical absorption in parabolic quantum wells, *Phys. Rev. B* **40**, *10647 (1989)*.

[319] *W. Kohn,* Cyclotron resonance and de haas-van alphen oscillations of an interacting electron gas, *Phys. Rev.* **123**, *1242 (1961)*.

[320] *J. F. Dobson,* Harmonic-potential theorem: Implications for approximate many-body theories, *Phys. Rev. Lett.* **73**, *2244 (1994)*.

[321] *A. Fetter and D. Rokhsar,* Excited states of a dilute Bose-Einstein condensate in a harmonic trap, *Phys. Rev. A* **57**, *1191 (1998)*.

[322] *Z. Wu and E. Zaremba,* Dissipative dynamics of a harmonically confined Bose-Einstein condensate., *Phys. Rev. Lett.* **106**, *165301 (2011)*.

[323] *F. Chevy, V. Bretin, P. Rosenbusch, K. W. Madison, and J. Dalibard,* Transverse breathing mode of an elongated Bose-Einstein condensate., *Phys. Rev. Lett.* **88**, *250402 (2002)*.

[324] *J. W. Abraham and M. Bonitz,* Quantum Breathing Mode of Trapped Particles: From Nanoplasmas to Ultracold Gases, *Contrib. to Plasma Phys.* **54**, *27 (2014)*.

[325] *V. A. Yurovsky, M. Olshanii, and D. S. Weiss,* Collisions, correlations, and integrability in atom waveguides, *Adv. At. Mol. Opt. Phys.* **55**, *61 (2008)*.

[326] *Y. E. Shchadilova, R. Schmidt, F. Grusdt, and E. Demler,* Quantum Dynamics of Ultracold Bose Polarons, *Phys. Rev. Lett.* **117**, *113002 (2016)*.

[327] *G. Morigi and S. Fishman,* Dynamics of an ion chain in a harmonic potential, *Phys. Rev. E - Stat. Nonlinear, Soft Matter Phys.* **70**, *066141 (2004)*.

[328] *U. Bissbort, D. Cocks, A. Negretti, Z. Idziaszek, T. Calarco, F. Schmidt-Kaler, W. Hofstetter, and R. Gerritsma,* Emulating solid-state physics with a hybrid system of ultracold ions and atoms, *Phys. Rev. Lett.* **111**, *080501 (2013)*.

[329] *G. Roati, C. D'Errico, L. Fallani, M. Fattori, C. Fort, M. Zaccanti, G. Modugno, M. Modugno, and M. Inguscio,* Anderson localization of a non-interacting Bose-Einstein condensate., *Nature* **453**, *895 (2008)*.

[330] *L. Sanchez-Palencia, D. Clément, P. Lugan, P. Bouyer, G. V. Shlyapnikov, and A. Aspect,* Anderson localization of expanding Bose-Einstein condensates in random potentials,

Phys. Rev. Lett. **98**, *210401 (2007).*

[331] *D. S. Wiersma, P. Bartolini, A. Lagendijk, and R. Righini,* Localization of light in a disordered medium, *Nature* **390**, *671 (1997).*

[332] *P. W. Anderson,* Absence of diffusion in certain random lattices, *Phys. Rev.* **109**, *1492 (1958).*

[333] *M. Grifoni and P. Hänggi,* Driven quantum tunneling, *Phys. Rep.* **304**, *229 (1998).*

[334] *S. I. Mistakidis, T. Wulf, A. Negretti, and P. Schmelcher,* Resonant quantum dynamics of few ultracold bosons in periodically driven finite lattices, *J. Phys. B* **48**, *13 (2015).*

[335] *T. Wulf, B. Liebchen, and P. Schmelcher,* Site-selective particle deposition in periodically driven quantum lattices, *Phys. Rev. A* **91**, *043628 (2015).*

[336] *B. Hess, P. Giannakeas, and P. Schmelcher,* Analytical approach to atomic multichannel collisions in tight harmonic waveguides, *Phys. Rev. A* **92**, *022706 (2015).*

[337] *G. Wang, P. Giannakeas, and P. Schmelcher,* Bound and scattering states in harmonic waveguides in the vicinity of free space Feshbach resonances, *J. Phys. B* **49**, *165302 (2016).*

[338] *J. W. Abraham, K. Balzer, D. Hochstuhl, and M. Bonitz,* Quantum breathing mode of interacting particles in a one-dimensional harmonic trap, *Phys. Rev. B* **86**, *125112 (2012).*

[339] *S. I. Mistakidis, L. Cao, and P. Schmelcher,* Interaction quench induced multimode dynamics of finite atomic ensembles, *J. Phys. B* **47**, *225303 (2014).*

[340] *R. Bücker, U. Hohenester, T. Berrada, S. Van Frank, A. Perrin, S. Manz, T. Betz, J. Grond, T. Schumm, and J. Schmiedmayer,* Dynamics of parametric matter-wave amplification, *Phys. Rev. A* **86**, *013638 (2012).*

[341] *R. Bücker, J. Grond, S. Manz, T. Berrada, T. Betz, C. Koller, U. Hohenester, T. Schumm, A. Perrin, and J. Schmiedmayer,* Twin-atom beams, *Nat. Phys.* **7**, *608 (2011).*

[342] *T. Schumm, P. Krüger, S. Hofferberth, I. Lesanovsky, S. Wildermuth, S. Groth, I. Bar-Joseph, L. M. Andersson, and J. Schmiedmayer,* A double well interferometer on an atom chip, *Quantum Inf. Process.* **5**, *537 (2006).*

[343] *P. Krüger, L. M. Andersson, S. Wildermuth, S. Hofferberth, E. Haller, S. Aigner, S. Groth, I. Bar-Joseph, and J. Schmiedmayer,* Potential roughness near lithographically fabricated atom chips, *Phys. Rev. A* **76** *(2007).*

[344] *Y. Ding and C. H. Greene,* Renormalized contact interaction in degenerate unitary Bose gases, *Phys. Rev. A* **95**, *053602 (2017).*

[345] *M. Abramowitz and I. Stegun,* Handbook of Mathematical Functions, *United States Department of Commerce, National Bureau of Standards, 1964.*

[346] *F. Arickx, J. Broeckhove, P. Van Leuven, V. Vasilevsky, and G. Filippov,* Algebraic method for the quantum theory of scattering, *Am. J. Phys.* **62**, *362 (1994).*

[347] *O. Rubtsova and V. Kukulin,* Green's function and scattering matrix in a discrete oscillator basis, *Phys. At. Nucl.* **64**, *1799 (2001).*

[348] *V. S. Vasilevsky and M. D. Soloha-Klymchak,* T-matrix in discrete oscillator representation, *page 12 (2015).*

[349] *I. Ryzhik and I. Gradshteyn,* Tables of Integrals, Series and Products, *Elsevier, Oxford, 2007.*

[350] *F. Hong-Yi and Z. De-Hui,* New generating function formulae of even- and odd-Hermite polynomials obtained and applied in the context of quantum optics*, Chin. Phys. B **23***, 060301 (2014).*

[351] *S. Moulieras, A. G. Monastra, M. Saraceno, and P. Leboeuf,* Wave-packet dynamics in nonlinear Schrödinger equations*, Phys. Rev. A **85***, 13841 (2012).*

[352] *H. Hochstadt,* The Functions of Mathematical Physics*, Dover Publications, New York, 1971.*